Interference of supports used for ground vehicle wind tunnel testing

Hetherington, Ben

Interference of Supports used for Ground Vehicle Wind Tunnel Testing

Ben Hetherington

A Thesis submitted for the degree of Doctor of Philosophy

Durham University

School of Engineering

2006

ABSTRACT

In order to provide a correct aerodynamic simulation of a vehicle travelling along the ground, models are tested using rotating wheels in a wind tunnel with a moving ground. In the most common of moving ground configurations the model is supported by an overhead strut, usually designed as an aerofoil profile to minimise interference, with the wheels supported by lateral stings hinged to mounts outside the span of the moving ground plane. In using this type of configuration it is assumed that the presence of the intruding supports do not markedly affect the aerodynamic behaviour of the model, but this assumption is not always valid. In order to quantify interference effects from model supports, a range of models were tested over a stationary ground plane mounted to an under floor balance. Each model was tested with and without mock struts and stings, which do not actually support the model. Comparisons were made between configurations with and without the mock supports in order to quantify their aerodynamic effects and investigate any changes in flow structure. Force and moment measurements show significant effects on both drag (up to 25 counts / 7% of total drag) and lift (up to 170 counts) due to a vertical strut for all vehicle types. Motor Sport models, whose performance relies greatly on the underside flow, are largely affected (26 counts / 3% on drag and up to 250 counts on lift) by the presence of lateral stings. Passenger vehicle models with larger ride heights were not as sensitive to the use of stings. Further investigation into the flow mechanisms that create these effects were carried out in the form of pressure and velocity measurements in the model and support wakes, surface oil flow visualisations, and surface static pressure readings. Results showed that the strut wake impinged on the rear wings of the motor sport vehicle models and the backlight of the passenger vehicle models as expected, but its influence was more wide ranging than this, extending to the model under floor. To explore changes in flow structure local to the strut-model junction, the junction is simplified as an aerofoil intersecting a flat plate and modelled in Fluent. Comparisons were made between configurations with and without the presence of six different aerofoil profiles for four different boundary layer thicknesses. Results found a noticeable interference on the plate from the union of the aerofoil, but showed that when the magnitude of the interference effect was recalculated using model frontal area the portion of the interference local to the junction affecting the model was small and in some cases insignificant. It was determined that deficiencies in the wake of the supports and their complex interference flow fields were creating a much greater amount of the overall effect by interfering with vehicle features downstream. Due to the complexity of interactions between struts, stings, and the model, the effect of combining them for a common moving ground configuration was highly vehicle dependent, precluding the possibility of developing a reliable correction for interference effects. The results do, however, lead to suggestions for support-model coupling methods that minimise the magnitude of the effect and offer guidelines for the expected magnitudes of effects for the different vehicle types and struts tested.

NOMENCLATURE

A/A_f	Frontal area.
A_c	Chord area. $= c^2$
b	Base of finite rectangular area (dA).
BF	Bluntness Factor. $= \frac{1}{2} \cdot \frac{R_o}{X_T} \cdot \left[\frac{T}{S_T} + \frac{S_T}{X_T} \right]$
c	Aerofoil chord.
C_D	Drag Coefficient. $= D / (P_{dyn} A_F)$ or $D / (P_{dyn} A_c)$
C_{Di}	Interference drag coefficient. $= \left[(D_{Foil} + D_{Plate})_{Combined} - D_{FoilAlone} - D_{PlateAlone} \right] / (P_{dyn} A_c)$
C_{fx}	Skin friction coefficient. $= \tau_w / P_{dyn}$
C_L	Lift Coefficient. $= L / (P_{dyn} A_F)$
C_{LF}	Front lift coefficient. $= L_F / (P_{dyn} A_F)$
C_{LR}	Rear lift coefficient. $= L_R / (P_{dyn} A_F)$
CNC	Computer Numerical Control.
Count	0.001 on force and moment coefficients.
CP	Pressure coefficient. $= \Delta P / P_{dyn}$
C_{Pitch}/C_{pm}	Pitching moment coefficient. $= P / (P_{dyn} A_F l_c)$, where l_c is the length to the fulcrum.
CP_o	Total pressure coefficient.
CV	Control Volume.

CWR	Closed Wheel Racer.
C_{Yaw}	Yawing moment coefficient. $= Y / \left(P_{dyn} A_F l_c\right)$, where l_c is the length to the fulcrum.
D	Drag force.
f	Gap height between model wheel and tunnel floor.
I_p	Polar moment of inertia (Torsion). $= I_x + I_y$
I_{pfoil}	Polar moment of inertia of aerofoil. $I_{pfoil} = I_p + Ar^2 = I_x + I_y + 2\Delta xyr^2$
$I_{x,y}$	Moment of inertia about x or y-axis (Bending). $I_x = \int_{-h/2}^{h/2} y^2 b dy = \frac{bh^3}{12}$ or $I_y = \int_{-b/2}^{b/2} x^2 h dx = \frac{hb^3}{12}$
$I_{x,y\ foil}$	Moment of inertia of aerofoil about x or y-axis. $I_{xfoil} = \sum I_x$ or $I_{yfoil} = \sum I_y$
$I_{x,p100}$	Moment of inertia either bending or torsion for 100mm chord aerofoils. $= \left(I_{x,p} / \left(c/100mm\right)^4 \right)$
L	Lift force.
L_F	Lift force at vehicle front wheels.
L_R	Lift force at vehicle rear wheels.
m	Meter.
mm	Millimetre.
N	Newton.
NACA	National Advisory Committee for Aeronautics.
OWR	Open Wheel Racer.
P	Static Pressure.
P	Pitching moment.
Pa	Pascal.
P_{dyn}	Dynamic Pressure. $= \frac{1}{2} \rho v^2$
Press.	Pressure drag forces.
R	Rolling moment.

Re	Reynolds Number. $= (\rho V l)/\mu$, where l is the characteristic length.
R_o	Nose radius
S	Side force.
s	Second.
S-A	Spallart Allmaras turbulence model
Sqrt(X)	Square root of a variable X.
S_T	Distance along aerofoil surface to maximum thickness.
T	Thickness.
Tot.	Total drag forces.
u, v, & w	X, Y, and Z velocity components, respectively.
V	Volt.
V_∞/U_∞	Free stream velocity.
Visc.	Viscous drag forces.
X, Y, & Z (x, y, & z)	Cartesian coordinates as defined in text.
X_T	X-coordinate of maximum thickness.
x-vorticity	Stream wise vorticity.
Y	Yawing moment.
y^+/y^+_{max}	Near wall spacing.
δ	Boundary layer disturbance thickness.
δ^*	Boundary layer displacement thickness.
θ	Incidence angle.
θ_m	Momentum thickness.
μ	Dynamic viscosity.
ρ	Density.
τ	Shear stress.
τ_w	Wall shear stress.

TABLE OF CONTENTS

LIST OF TABLES

CHAPTER 2

DECLARATION

I confirm that no part of the material offered has previously been submitted by me for a degree in this or any other University. In all other cases material from the work of others has been acknowledged.

Signed: 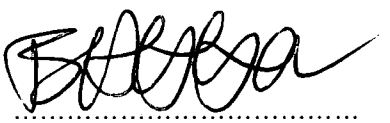

Ben Hetherington

Date: 29/05/2007

COPYRIGHT

ACKNOWLEDGEMENTS

I would like to extend my deepest gratitude to my supervisor, Dr David B Sims-Williams, for the time, support, guidance, and encouragement which he has offered throughout this project.

Also, I am indebted to the staff at the School of Engineering and would like to mention in particular the efforts of Mr Gary Parker in the Thermo-Fluids laboratory, Mr. Colin Wintrip, Mr. Ian Glassford, and Mr. Kevin Longley in the mechanical workshop, Mr Ian Hutchinson in the electronics workshop, and Mr. Trevor Nancarrow and Mr. Michael Wilson for computer support.

Lastly, but by no means least, I would like to thank my mother and father, for their encouragement and giving me this opportunity, as well as my aunts and uncles for making my stay in England as comfortable as possible.

1 INTRODUCTION

1.1 HISTORY OF THE GROUND VEHICLE SHAPE

The history of ground vehicle aerodynamics has been described by numerous authors [Katz, 1995] [Hucho, 1998] [Kieselbach, 1982a,b] [Kieselbach, 1983] [Sumantran & Sovran, 1996]. They are surveyed here once again to show the significance of aerodynamics and aerodynamic research methods that have led to the current vehicles that we see on the road and track today.

Initially, passenger vehicles were modelled directly after the horse carriage, they had high drag coefficients ($C_D \approx 0.80$ [Hucho, 1998]), were boxy, and had most of their components, such as fenders, wheels, headlamps, and the undercarriage exposed to the oncoming flow. Some of the first attempts at streamlining were inspired by aero and marine vehicles such as the boat and airship. Although these basic bodies were well established in their respective fields, they were never intended to be brought near a solid ground and have exposed extremities as would be required for their application as a ground vehicle. Because of this, many of these early vehicles were unsuccessful and still created large amounts of drag [Hucho, 1998]. One landmark vehicle worth mentioning that achieved a low drag ($C_D = 0.28$ [Katz, 1995]), even for today's vehicles, was the 1924 Tropfenwagen developed by E. Rumpler. However, this low drag was achieved with an accompanied sacrifice of other mechanical and stylistic concerns and did not gain the public's popularity [Hucho, 1998].

It was not until W. Klemperer and P. Jaray made use of the fact that the flow around a streamlined body changes and increases its drag as it is brought close to the ground that successful, marketable, streamlined vehicles were produced. These Jaray body types (typical $C_D \approx 0.55$ [Sumantran & Sovran, 1996]), of which some examples can be seen in Figure 1.1, had long sloping rear ends and fused the vehicles main body and wind shielded cockpit to one another to create a more streamlined union. They also featured a cambered windshield and integrated fenders and headlamps, two common characteristics still seen in today's vehicles.

Figure 1.1: Examples of Jaray body types [Hucho, 1998].

Taking one step closer to the present, W. Kamm, W.E. Lay, and Koening-Fachsenfeld began trimming down the large sloping rear end of the Jaray body, converting it to the blunt rear end noticeable in today's hatchback models. They realised that if flow was separating from the vehicle roof anyway, there was no need to keep a streamlined rear end, so the rear portion could be truncated with little change to drag. However, this was not a pioneering idea; it was already known from studies in aeronautics of airfoils that had had their rear quarter removed [Sumantran & Sovran, 1996].

Using the cambered windshields and integrated components fashioned by Klemperer and Jaray along with the recognition that the vehicle rear could be dictated by the effects on the front portion, new notched back vehicle shapes began appearing and were first introduced by H. Darrin in the 1940's [Hucho, 1998]. Observing Figure 1.2, this shape of vehicle, with typical drag coefficient values of about 0.45 [Sumantran & Sovran, 1996], remained with little change until the 1970's. During the 1970's the sharp increase in the price of petroleum created some of the first widespread efficiency concerns and from here on out what has been termed by Hucho [Hucho, 1998] as "detail optimisation" (see Figure 1.3), or the realisation that only local changes not shape changes needed to be made to reduce drag, became popular. This led to numerous refinements in shape and size, creating the familiar passenger vehicle of today.

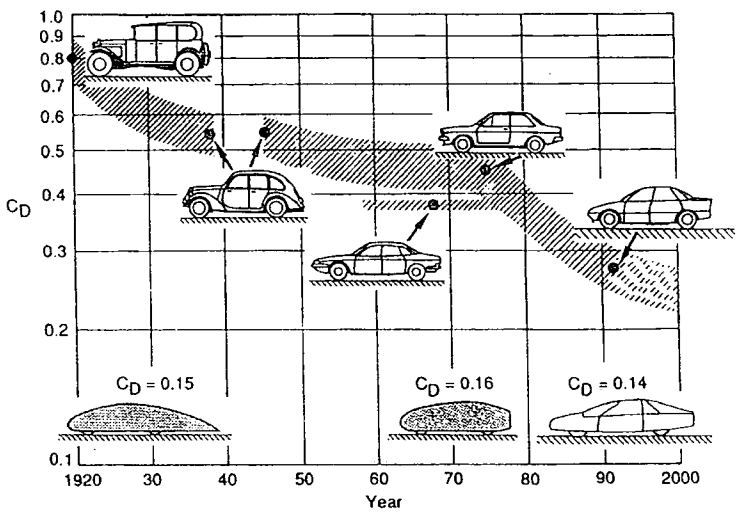

Figure 1.2: Drag coefficient history [Hucho, 1998].

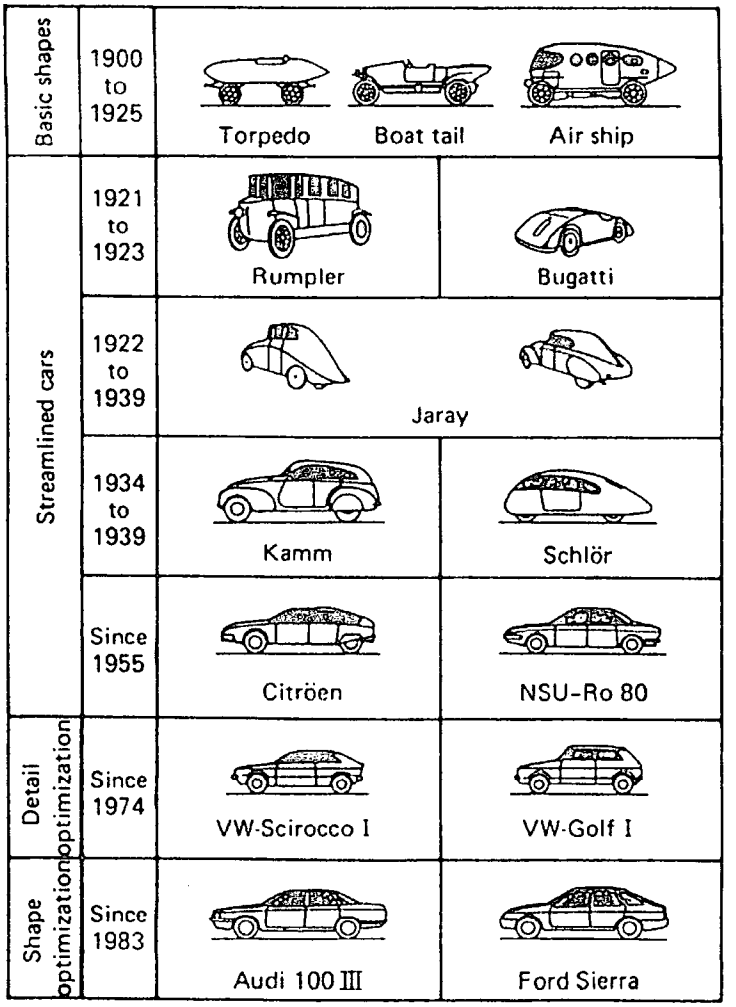

Figure 1.3: Stages of passenger vehicle development [Hucho, 1998]

The 1960's and 1970's also saw some of the most significant changes in motor sport vehicles. In the years leading up to this there were milestones in race vehicle development such as the 1923 Benz Tropfenwagen, similar to the low drag design of Rumpler's Tropfenwagen and the Bugatti Tank that recognised the advantage of encasing the wheels within the vehicle body. However, for the most part, race vehicles maintained their traditional boxed shape, exposing vehicle components and the driver, until after World War II [Hucho, 1998]. Although the importance of streamlining was recognised it was maintained for record vehicles that were intended for high speed straight line driving. During the earlier years more emphasis seems to have been placed on engine and tyre technology, rather than aerodynamics.

In the 1960's, however, aeronautics had become a well established science, and the transfer of technology to motor sport vehicles was at a peak [Katz, 1995]. One of the first concepts to find its place on the ground vehicle was the use of an inverted wing to create down force. This showed up first on vehicles produced by Chaparral.

In 1965 the 2C model used a variable flap at the rear of the vehicle to create down force. The 1966 2E and 1967 2F and 2G models all used inverted wings mounted high above the vehicle in clean flow to create even more of an effect [VintageRPM, 2006] [Petrol Museum, 2006]. From this point, the use of inverted

wings to increase wheel load that would improve handling and stability was introduced to the world of competition driving. Prior to this some attempts were made to control instability using large vertical fins at the rear of the vehicle, however, the increase of wheel traction proved to be a much more effective means.

Another, short lived, innovation to produce down force was seen in the Chaparral 2J and the Brabham BT46B. These vehicles used fans to create a low pressure beneath the vehicle; the low pressure area was then sealed from the surrounding flow using flexible skirts between the vehicle and ground. This method was replaced by the more efficient and effective method of shaping the vehicle underside to make use of the fact that an inverted wing would also create a low pressure area, or increase its down force, when in proximity to the ground. Cars like the 1977 Lotus Type 78 F-1 racer, had wing shaped side pods to create a low pressure area beneath the car, this area was then sealed using flexible skirts to maintain the pressure. This concept of using the body in ground effect quickly became popular and by the 1980's most race vehicles began taking advantage of contoured underbellies to create low pressures beneath the vehicle.

In Figure 1.4 a graph of the handling ability of ground vehicles over the last fifty years shows a sharp increase in the late 1970's that can be associated with these new techniques of developing down force. Since these concepts were employed, developments have been incremental, but continuous; in some cases, improvements in tyre and engine technology along with these aerodynamic abilities have forced regulations to limit the vehicles capabilities.

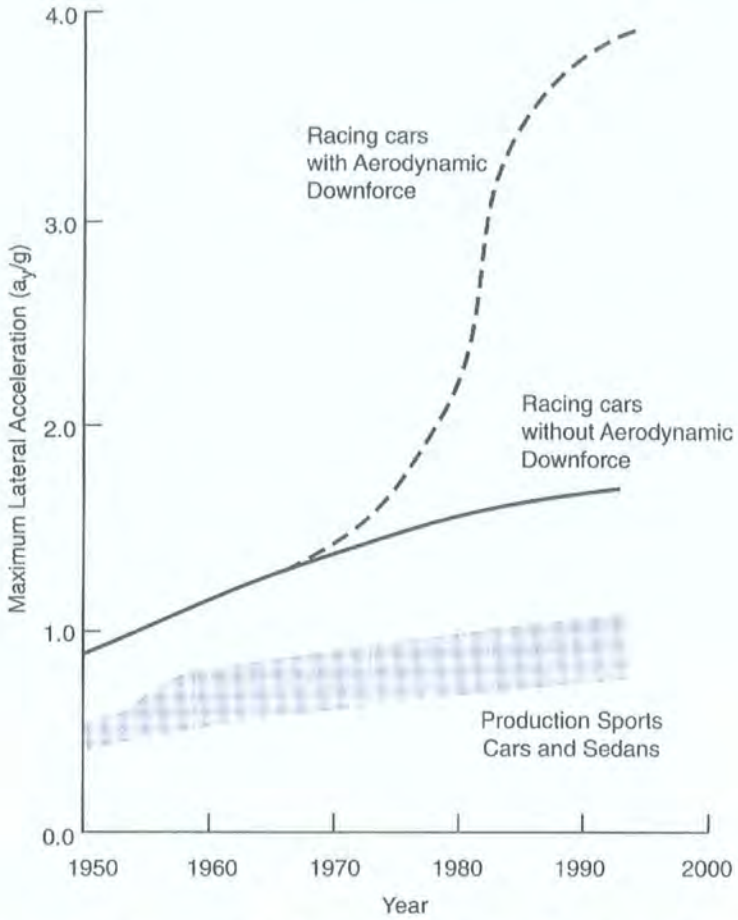

Figure 1.4: Historic development of lateral acceleration [Katz, 1995]

After these noted developments in passenger and motor sport vehicles the process reached a stage where further increase in performance and efficiency could only come from small refinements of the already existing arrangement, not global re-thinking. As an example, one current technique in both fields is the control of flow by re-direction and alteration of separation to produce a desired effect. It's this final milestone development that has led to an increased importance of research methods.

1.2 GROUND VEHICLE AERODYNAMICS

Throughout the evolution of the automobile, aerodynamics has emerged as an important factor in the design and development of the passenger vehicle shape. Engineers and stylists are constantly searching for an efficient, yet practical and aesthetically pleasing form that will place the least amount of load on the power train and provide an acceptable level of stability. The universal problem amongst designs is that the most efficient shapes that minimise flow separation and hence pressure drag, are not aesthetic and in many cases not practical and do not fare well on the market.

This is not, however, the case in the design of specialised vehicles used for motor sport. The aerodynamic design of motor sport vehicles adheres to specific conditions, rules, and regulations and is concerned primarily with function, not form. Ideally, each track or course will dictate an explicit vehicle setup allowing for an optimisation of handling and top speed capabilities. Although each division of motor

sport has its own set of regulations that tend to dictate the vehicle setup more than anything, a general aerodynamic design places emphasis on achieving a high negative lift with low drag and an appropriate and competitive lift balance between front and rear axles. Aesthetics and practicality are not of immediate concern.

One common factor between motor sport and passenger vehicle design is the tools that are used for their development. Thanks to its widespread use in aeronautics the wind tunnel has become a well developed and invaluable tool in the advancement of the ground vehicle. Throughout time, they have become better understood, more affordable, and are now common place in ground vehicle research. Although full scale testing still holds its popularity with passenger vehicles, the low ground clearances of motor sport vehicles commands the use of a moving ground (which will be discussed later) and makes scale model testing a more practical and easily applied option. Because of this model scale wind tunnel testing has begun to emerge as a popular and even more manageable and cost efficient means of exploration than full scale and on-road testing. The advantages of model scale wind tunnel testing are obvious in terms of time and cost, but the validity of the testing depends on the method and instrumentation used. This work aims to assess certain areas of current testing methods, explain the physical aspects and quantify the magnitude of any inaccuracies that are associated with them.

1.3 CURRENT RESEARCH ACTIVITY

As it has become such an important tool, the wind tunnel is used to develop almost every aspect of the ground vehicle from improving its merit as a machine capturing the spirit of motoring to increasing its comfort and ability to treat the driver. The research laid out in this project does not specifically approach topics of vehicle improvement, but concerns itself with improving the fidelity of wind tunnel simulations and creating a more accurate test environment for vehicle development.

Amongst the issues researched, one that has been of paramount importance is the amount of drag generated by the vehicle. Because drag will directly influence fuel consumption and vehicle emissions as well as top speed it has received a lot of attention. This attention has also been the catalyst for the development of new and improved measurement and analytical methods used in wind tunnels throughout the world. Revisiting aerodynamic history; some of the first mainstream passenger vehicles with $C_D \approx 0.36\text{-}0.42$ were produced after the oil crisis in the 1970's [Cogotti, 1989]. Prior to this it was quite common for C_D to average 0.42 to 0.50 and beyond (see Section 1.1). Because the outer body of the ground vehicle has now reached a higher level of efficiency, changing the vehicle shape to lower drag without aesthetic penalties becomes difficult [Tamai, 1999] and it is now widely accepted that a 'gold mine' for future savings in drag will come from underside grooming and cooling flow adaptations. The creation of drag from oil pans, transmissions, drive shafts, suspension components, fuel tanks, exhaust plumbing, and other features that compose a vehicles underside roughness could be largely reduced by appropriate shielding of the components or re-direction of the flow. This is frequently done for costly sports cars and motor sport vehicles; however, doing the same for the average passenger vehicle could have serious practical and marketing consequences. The same is true for vehicle cooling. The average

passenger vehicle requires minimal ducting to cool one or two radiators and the passenger cabin. Cooling of the underside components, if necessary, is usually achieved by flow beneath the vehicle. To introduce low drag ducting that meets the necessary demands would increase overall cost, possibly above the margin of improvement. An efficient, functional, and accepted method to reduce drag through adaptation of these areas could represent the next step in passenger vehicle development [Jama et al., 2006]. The reduction of frictional losses inside cooling ducts is also very important to motor sport vehicles.

Another important issue that has received ample attention is the vehicle's straight line and directional stability. Efforts are made to reduce lifting force in order to maintain dynamic stability at high speeds thereby increasing active safety. However, the lift force of a typical passenger vehicle amounts to only 3% of the vehicle weight at 60 mph and 10% at 120mph [Sumantran & Sovran, 1996] and it is the pitching moment that is usually of greater concern. Because the pitching moment changes the load distribution between front and rear axles, the vehicle will handle differently at higher speeds. Ideally, designs aim to keep the front and rear lift balance close to unity, or even better, close to the vehicle weight balance [Katz, 1995], so the load between front and rear axles will not change with increased speed and the dynamic will remain constant. This condition may be quite different for a motor sport vehicle intended for competition, which will usually require more negative rear lift at any speed to promote the favourable under steering condition [Hucho, 1998].

Part of a vehicle's stability is its sensitivity in crosswinds. Most passenger vehicles' yawing moments tend to twist them away from the wind. Improving the yawing moment coefficient to help turn the vehicle into the wind will not only help improve the passive steering but will also improve crosswind stability. On this same note, reducing the side force coefficient at large yaw angles will make the vehicle less reactive to crosswinds.

Specific to passenger vehicles, the reduction of acoustic noise due to vehicle trim, windshield wipers, wing mirrors, antennas, luggage racks, and other extremities is also finding an important seat amongst the hierarchy of research topics. Other issues include, but are not limited to, visibility due to rain and dirt accumulation as well as appropriate locations for engine air intake and exhaust.

1.4 GENERAL AERODYNAMICS

1.4.1 Boundary Layer Formation

Ideally, inviscid incompressible flow would remain attached to the vehicle shape with all the pressure lost being recovered by the time it reached the rear of the body, creating no drag. From this perfect theoretical view, not incorporating frictional forces, elementary aerodynamic theories such as Bernoulli's equation, relating pressure and velocity along a streamline, are formulated. However, viscous effects within the fluid control the realistic flow condition surrounding a vehicle. In this realistic condition a boundary layer (Figure 1.5) of fluid begins to form along the exposed surfaces of the vehicle parallel to the direction of flow due to the no-slip condition at the walls [Fox & McDonald, 1998]. In the xz-plane (Figure 1.6 shows

the referenced coordinate system) the boundary layer creates an increasing velocity profile starting at the vehicle surface (z=0), where the velocity is zero and extending along the z-axis to the edge of the boundary layer (z=δ) where the velocity matches the free stream velocity.

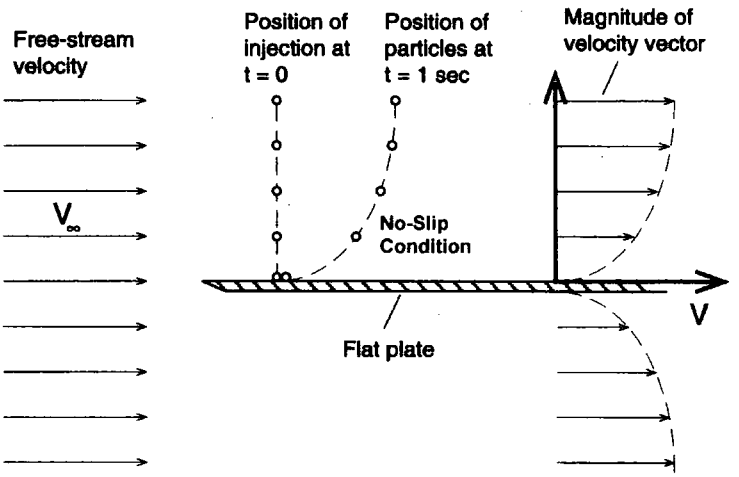

Figure 1.5: Boundary layer formation [Katz, 1995].

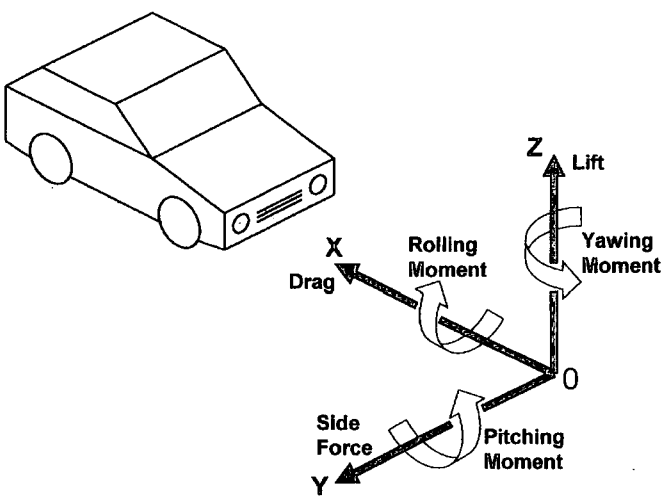

Figure 1.6: Coordinate system used throughout course of the project.

Prandtl's $1/7^{th}$ rule (Equation 1.1) gives an idealised velocity profile typical of a turbulent boundary layer as a function of height above the surface (z):

Equation 1.1

$$\frac{u}{u_\infty} = \left(\frac{z}{\delta}\right)^{1/7}$$

The boundary layer disturbance thickness (Equation 1.2) for this turbulent velocity profile is then determined considering viscous flow growing on a surface from some distance (x in Equation 1.2) upstream. The boundary layer displacement thickness is then determined using Equation 1.3.

Equation 1.2

$$\delta = 0.382 \frac{x}{\left(\frac{ux}{\upsilon}\right)^{1/5}}$$

Equation 1.3

$$\delta^* = \int_0^{\partial} \left(1 - \frac{u}{u_\infty}\right) dz$$

Similarly, the momentum thickness in Equation 1.4 is:

Equation 1.4

$$\theta_m = \int_0^{\delta} \frac{u}{u_\infty}\left(1 - \frac{u}{u_\infty}\right) dz$$

The physical environment within this boundary layer mixed with the effects of the pressure gradient just outside it will either provoke the streamlines to stay attached to or separate from the vehicle body. If the local pressure gradient, determined by vehicle shape, is decreasing in the direction of flow ($\delta p/\delta x<0$), the streamline tendency is to stay attached and the pressure gradient is said to be favourable. If the opposite is true and the local pressure gradient is increasing in the direction of flow ($\delta p/\delta x>0$) the streamline tendency is toward separation and the pressure gradient is said to be adverse [Fox & McDonald, 1998] [Massey, 2006]. In the case of ground vehicles the pressure gradient will be adverse at some point and the flow will eventually detach itself from the vehicle body causing a separation in the form of a wake or longitudinal vortex. This then creates a lower pressure behind the vehicle that is the majority (75-80% [Hucho, 1998]) of resistance to motion that a ground vehicle feels and is termed the Normal Drag. The remaining resistance to motion comes from the tangential shearing effect that the no-slip condition has on the vehicle (Skin Friction Drag).

In a Newtonian fluid skin friction will be directly proportional to the rate of deformation and is defined in Equation 1.5.

Equation 1.5

$$\tau = \mu\left(\frac{du}{dz}\right)_{z=0}$$

For a control volume (Figure 1.7) in incompressible viscous flow over a flat plate u_∞=constant and p=constant meaning that the pressure gradient across the plate will be zero $\left(dp/dx = 0\right)$ and the momentum integral reduces to:

Equation 1.6

$$\tau_w = \rho u_\infty^{\,2} \frac{d\theta_m}{dx}$$

With momentum thickness from Equation 1.4, the shear stress at the surface due to the boundary then becomes:

Equation 1.7

$$\tau_w = \rho u_\infty^{\,2} \frac{d}{dx} \int_0^{\delta} \frac{u}{u_\infty}\left(1 - \frac{u}{u_\infty}\right) dz$$

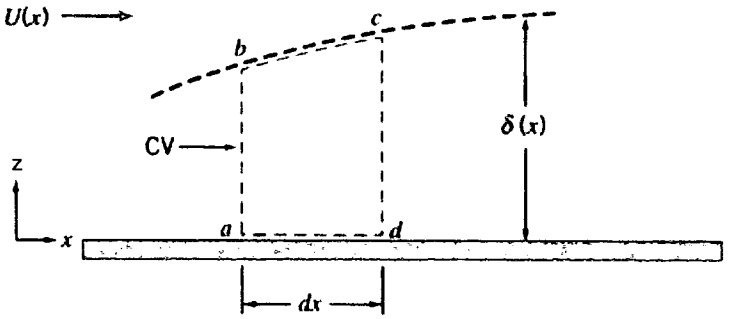

Figure 1.7: Differential control volume in the boundary layer on a flat plate [Fox & McDonald, 1998].

Equation 1.5 through Equation 1.7 illustrate that the shear stress grows with an increase in boundary layer. Also that no matter what the condition of the pressure gradient there is always a net skin friction force acting on the body that brings fluid near the surface to rest. When the condition in Equation 1.8 is met and an adverse pressure gradient is present, the neighbouring fluid will be deflected away from the boundary and the streamlines will begin to separate from the surface. The location at which a separation occurs is largely the responsibility of the type of the boundary layer present [Fox & McDonald, 1998].

Equation 1.8

$$\left.\frac{\delta u}{\delta z}\right)_{z=0} = 0$$

The type of boundary layer, either turbulent or laminar, depends on the local Reynolds number. A laminar boundary layer sees streamlines running adjacent to one another along the surface without mixing, whereas a turbulent boundary layer mixes high momentum fluid away from the surface with low momentum fluid near the surface. A boundary layer starts at the leading edge of a surface as laminar then as the distance from the leading edge increases the Reynolds number also increases until the transitional value (approx. Re=2x10^5) is reached. Here the boundary layer gradually transitions to turbulent. However, this will only occur in a region of negligible or no pressure gradient, if a pressure gradient is present it will affect the transition, either retarding or provoking it. Similarly, surface features, such as roughness will also affect the transition point.

A turbulent boundary layer will delay separation, but create more friction drag and increase boundary layer thickness quicker from the transition point onward. A laminar boundary layer will separate sooner, but not cause as much added friction drag [Katz, 1995]. Since the disadvantage of added skin friction is outweighed by the longer attachment or perhaps re-attachment, turbulent boundary layers are frequently preferred and in some cases provoked [Hucho, 1998].

1.4.2 Separation

An example of flow separation due to an adverse pressure gradient caused by the surface shape can be seen in Figure 1.8. As mentioned, a ground vehicles body shape will create an adverse pressure gradient at some point along its surface in the x direction, which will then provoke a separation. The separation will come in one of two forms: The first is caused by edges perpendicular to the flow direction, and is

visible in the form of a lateral vortex that curls up just past an edge sometimes forming a separation bubble. The second is created by inclined columns and is visible in the form of longitudinal vortices that carry on far behind the vehicle. Both types of separations are illustrated later in Section 1.5 in the descriptions of flow fields particular to different vehicle shapes and both contribute to the wake creating a stagnation pressure deficit behind the vehicle. This low-pressure is contrasted by the high-pressure in front creating a global pressure difference between front and rear. The difference creates the vehicles' pressure drag, which is the majority of the resistance towards vehicle motion. Similar pressure differences caused by velocity distributions and separations also create a difference between the top and bottom and either side of the vehicle creating lift and side forces.

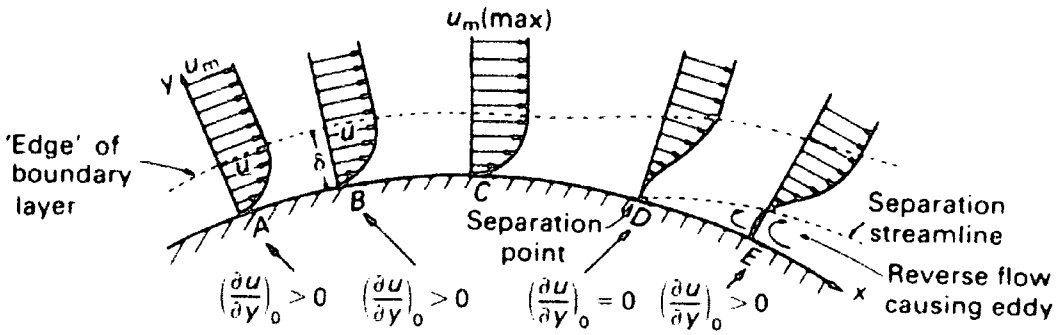

Figure 1.8: Separation of flow due to an adverse pressure gradient created by surface shape [Massey, 2006]. (The coordinate y from Massey in this figure must be replaced with z to make it concurrent with the convention used throughout this report).

1.5 TIME AVERAGED FLOWS PARTICULAR TO VEHICLE SHAPES

1.5.1 Passenger Vehicles

Although there are seemingly more variations of automobile on the road today, commercially produced passenger vehicles will fall into one of four main categories used for wake analysis. They are Fastback, Hatchback, Notchback, and Squareback. For simplification the wake structures of these vehicle rear end types are commonly described as time-averaged flows even though certain features may be unsteady. For all, the flow field surrounding the vehicle is characterised by separations occurring at the top and bottom leading edges of the bonnet, front fenders, windscreen, side view mirrors, A-pillars, side glass, wheels, wheel arches, underside, backlight, C-pillars, and trunk. Depending on the yaw angle of the vehicle some of the separations created at the front of the vehicle, such as the A-pillar vortices, may stretch back to the vehicle wake, but generally separations at the rear of the vehicle are the most defining and will be different for each vehicle type.

1.5.1.1 Fastback

The most noticeable feature that is common to the wake of a Fastback vehicle is a matching pair of stream wise vortices. The vortex structures form at the C-pillars and continue into the wake moving inward to the longitudinal centreline and then toward the ground (Figure 1.9). This rotation creates an area of

downwash between them, a common feature on a lifting body such as a passenger vehicle [Bearman, 1984]. The intensity of the vortices is determined by the slope of the backlight; with a stronger vortex pair being witnessed for a steeper backlight. At the approximate critical angle of 30 degrees (for sharp edged bodies) the vortices are found to create a maximum in drag, beyond this angle the vehicle begins to exemplify a hatchback shape and the separation changes creating an accompanied reduction in drag [Nouzawa et al., 1990].

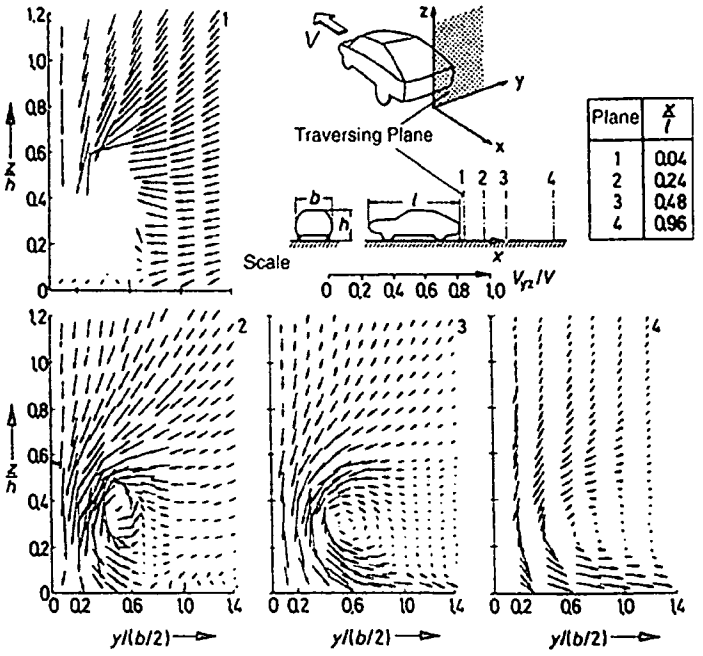

Figure 1.9: Vorticity in the wake of a Fastback vehicle shape [Hucho, 1998].

In order to further explain the behaviour of this and other separations found on a Fastback, the essential geometry was modelled and analysed by Ahmed et al. [Ahmed et al., 1984]. The model created was a car-like bluff body with a rounded front section, straight mid-section, and an angled rear end. This idealised geometry allowed flow structure in the wake to be examined with reference to only one design parameter, the slanted backlight angle. The flow on the remainder of the body stayed attached. For this geometry it was found that up to 85% of the model's total drag is pressure drag, created by separations at the backlight and base, the remaining drag is from friction. The wake structure for this Ahmed bluff body can be seen in Figure 1.10. In this model the shear layer comes from the vehicle side and rolls up at the slanted edges of the backlight creating the stream wise vortices mentioned earlier ('C' in Figure 1.10). The strength of these trailing vortices is directly dependent on the backlight angle, growing as it increases up to the critical 30 degree angle. At backlight angles less than 20 degrees flow from the model roof stays attached to the slanted backlight [Strachan et al., 2004] and energizes one of two horseshoe vortices at the model base as it passes the backlight trailing edge ('A' in Figure 1.10, also seen as a recirculation region in Figure 1.11). Between 20 and 30 degrees the flow will separate at the backlight leading edge, but re-attach further downstream [Strachan et al., 2004] still energising the horseshoe vortex. The second horseshoe vortex ('B' in Figure 1.10, also seen as the lower recirculation region in Figure 1.11), is created by flow coming from the model underside. These two separations, situated one on top of the other, are

then encapsulated in a separation bubble sealed by the flow coming from the backlight and underside. The strength of the upper base separation ('A' in Figure 1.10) is directly related to the backlight angle, while the strength of the lower base separation ('B' in Figure 1.10) depends firstly on the condition of the flow coming from beneath the model, but is indirectly linked to the backlight angle.

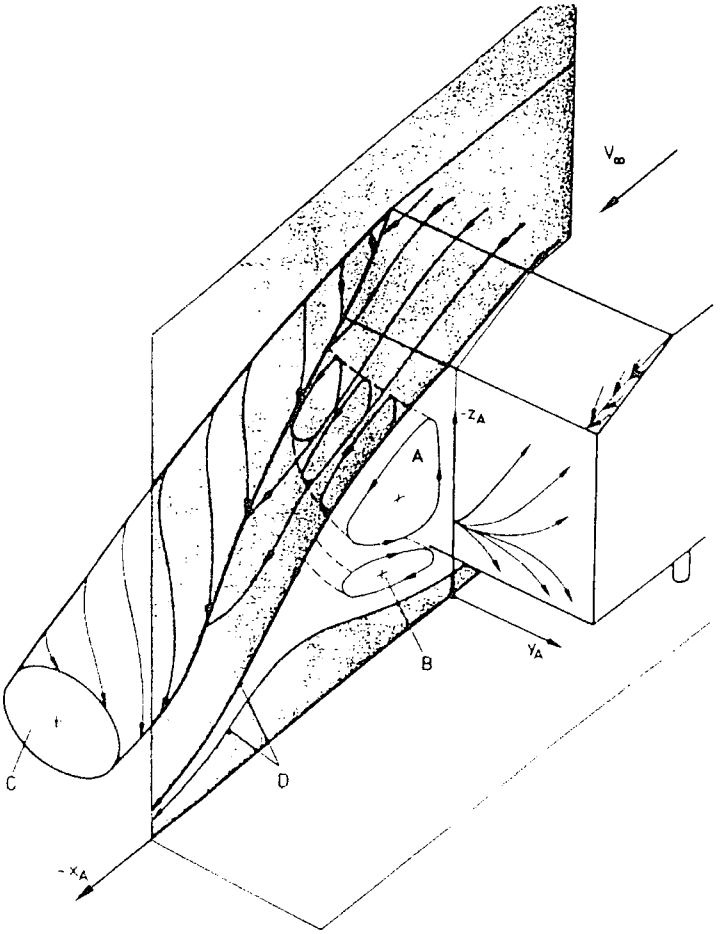

Figure 1.10: Flow structure in the wake of the Ahmed bluff body at small backlight angles below the critical angle [Ahmed et al., 1984].

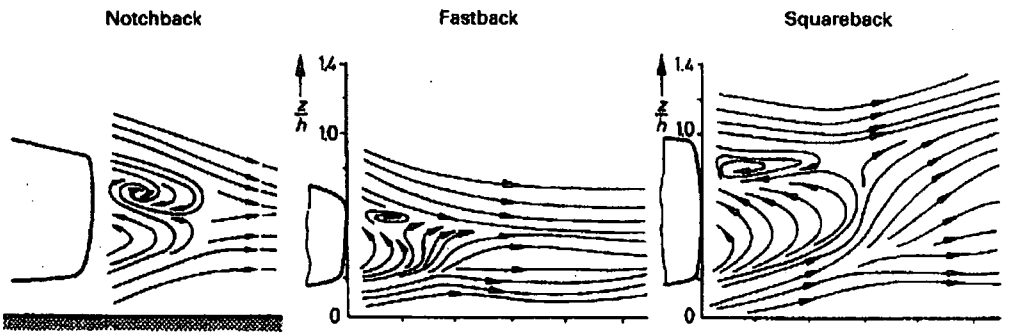

Figure 1.11: Recirculation region in the base of different passenger vehicle types [Hucho, 1998].

At the 30 degree critical angle the model reaches a peak in drag. At this backlight angle the trailing vortices are at their strongest and the backlight separation is present (labelled 'E' in Figure 1.12). The

increased strength of the vortices combined with a lower pressure created by the backlight separation both contribute to the peak in drag. Beyond this angle upstream disturbances encourage the backlight separation bubble to merge with the upper base separation and the trailing vortices no longer exist. Instead, flow coming from the backlight leading edge induces a downward trend to the flow coming from the roof and flow coming from the model sides separates further downstream. The disappearance of the vortex drag creates an overall lower drag on the model as a whole.

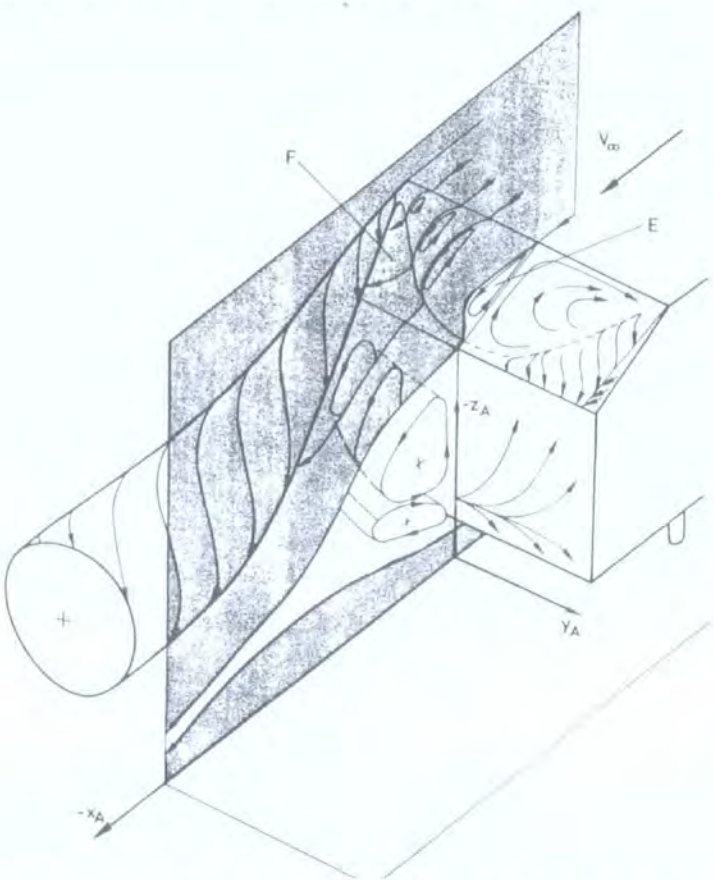

Figure 1.12: Flow structure in the wake of the Ahmed bluff body at 30 degree critical angle [Ahmed et al., 1984].

1.5.1.2 Squareback

In free stream flow, the symmetric shape of a Square back would create opposing separations from the top and bottom surfaces and separations at the two sides. However, the flow around the vehicle is not symmetric due to the proximity of the ground and the wake exhibits a pair of stream wise vortices and two areas of recirculation at the base (see Figure 1.11). The vortices rotate in the opposite direction from that of the Fastback and move upward away from the ground with increasing distance downstream (Figure 1.13). Similar trends were seen by Ahmed et al. [Ahmed et al., 1984] for Fastbacks with backlight angles less than 5 degrees. They observed that the vortices were much weaker exhibiting less cross flow and dissipating sooner.

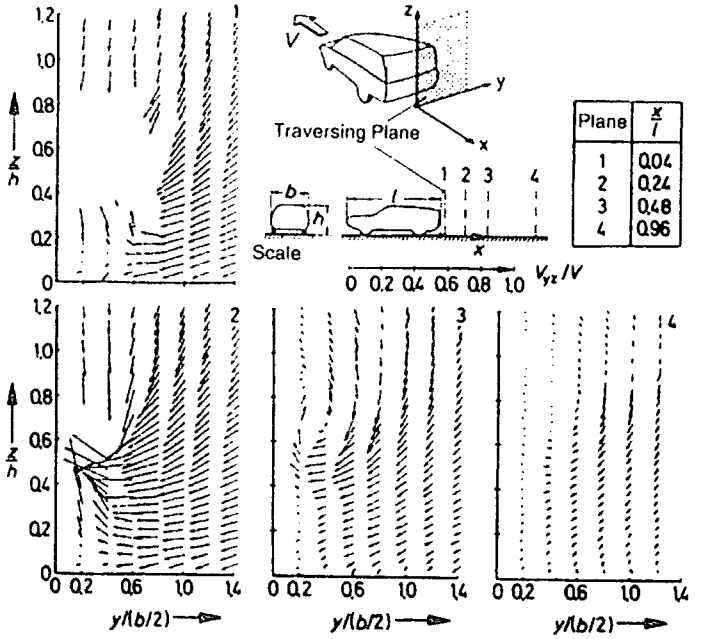

Figure 1.13: Vorticity in the wake of a Hatchback vehicle shape [Hucho, 1998].

1.5.1.3 Notchback

Due to the presence of a trunk and its proximity to the backlight and C-pillars the wake created by a Notchback can be much more complicated than for the Fastback or Hatchback. Moreover, the geometric parameters and their proximity for particular Notchbacks can make the flow unique to that exact vehicle shape, making a generalised flow model difficult to discern. Because of this, different experimenters have come up with varying models to try and explain the flow over the rear of a Notchback shape.

According to Hucho [Hucho, 1998] the vehicle wake (Figure 1.14) is once again dominated by a pair of stream wise vortices formed at the C-pillars, the strength and existence of which are dependent upon the backlight angle and its aspect ratio. The vortices can travel far behind the vehicle, creating a downwash in the region between them. In the notch that is created by the trunk and backlight there is a large area of dead fluid in the form of a lateral vortex that has curled up after flow separates from the roof trailing edge. The downwash greatly affects the flow coming off the roof pulling it down toward the trunk, possibly causing it to re-attach before the base of the vehicle. This will also depend on the length of the trunk in relation to the roof height. If and when the flow does re-attach to the trunk it then continues downstream to separate at the trunk trailing edge. This separation along with a matching separation at the bottom of the trunk created by flow from the vehicle underside creates two contra rolling vortices at the vehicle base (Figure 1.11).

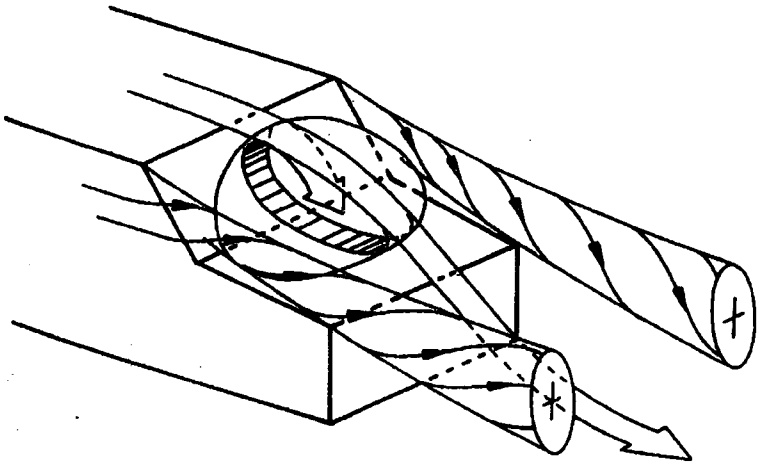

Figure 1.14: Notchback wake according to Hucho [Hucho, 1998].

Carr [Carr, 1974] believed that the C-pillars did not produce longitudinal vortices, but instead thought they contributed to a large transverse vortex above the trunk created by separation from the roof trailing edge. This was further confirmed by flow travelling upstream on the vehicle trunk. The vortex depicted in Figure 1.15 creates downwash above the trunk adding lift to the rear end but also influencing the shear layer from the roof to re-attach to the trunk.

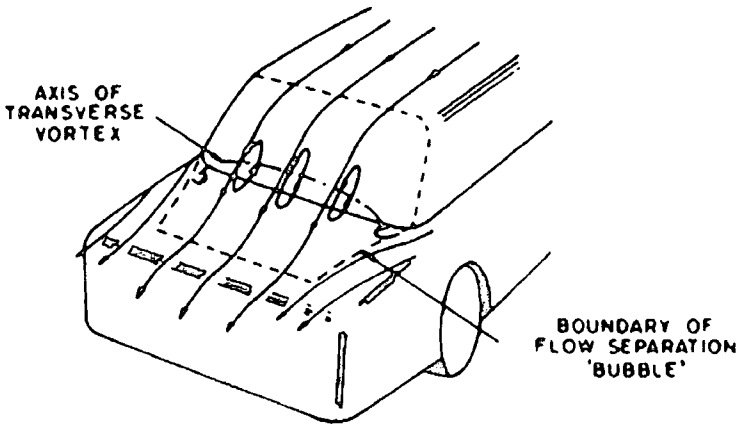

Figure 1.15: Transverse vortex above trunk in the wake of a Notchback vehicle according to Carr [Carr, 1974].

Nouzawa et al. [Nouzawa et al., 1990] recognised the presence of stream wise vortices forming at the C-pillars and their relationship with backlight angle. However, they believed that the transverse vortex seen by Carr [Carr, 1974] and the dead fluid of Hucho [Hucho, 1998] was actually an arch vortex sitting in the notch (Figure 1.17). The transverse portion of the vortex is formed by flow separating at the roof trailing edge, but is then bent into an arch by flow swirling around from the side glass to create the C-pillar vortices. The downwash created by the arch vortex and C-pillar vortices then influences the shear layer to bend and re-attach to the trunk creating a separation bubble in the notch. A critical angle of θ=25 degrees was found (see Figure 1.16 for angle reference), above which the flow would continue into the wake, and below which the flow would re-attach. After re-attaching flow then continues to create similar base recirculation regions to those described by Hucho [Hucho, 1998]. They also postulated that the bending

flow generates downward flow from above the shear layer increasing the circulation of the separations formed at the base.

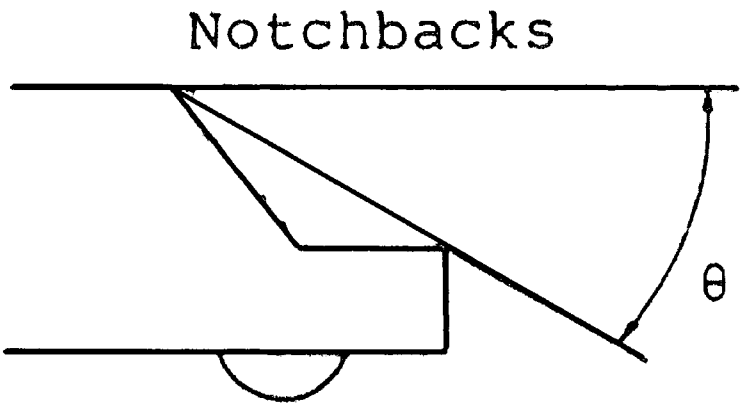

Figure 1.16: Backlight angle as referenced by Nouzawa et al. [Nouzawa et al., 1990].

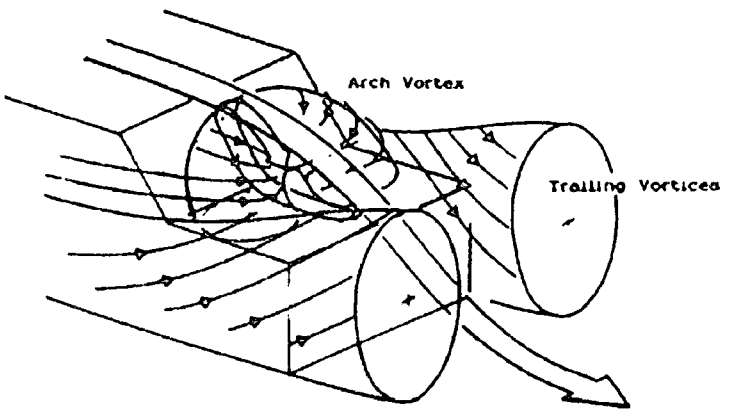

Figure 1.17: Arch vortex above trunk in the wake of a Notchback vehicle according to Nouzawa et al. [Nouzawa et al., 1990].

Another flow model from Jenkins [Jenkins, 2000] does not describe the separation as quasi two dimensional like those previously discussed, but describes a three dimensional flow structure for a more unique Notchback shape seen in Figure 1.18. In this flow model a weak C-pillar separation (labelled G5 in Figure 1.18) is witnessed forming from flow coming from the side glass and corners of the roof and is thought to be the C-pillar vortex seen by other experimenters, but different from the other models, flow coming around the lower portion of the C-pillar creates a column vortex on the trunk (labelled H5 in Figure 1.18). Instead of heading downstream, inflow from the vehicle side forces the column vortices toward the centre plane also bending them in the stream wise direction. At the centreline they create reversed flow and up wash along the majority of the centreline closest to the backlight. The shear layer on either side of the roof centreline merges with the column vortex and is transported to the trunk surface where some of the flow travels toward the backlight and some travels toward the centre plane. At the centre plane the flow converges and travels upstream, downstream, and upward (labelled C5 in Figure 1.18). Upstream fluid joins the other reverse flow, downstream the flow separates at the trunk trailing edge to create the base separation bubble with flow from beneath the vehicle as described earlier in other

models. Upward moving fluid forces the shear layer separating from the roof trailing edge away from the trunk, not allowing it to re-attach to the trunk.

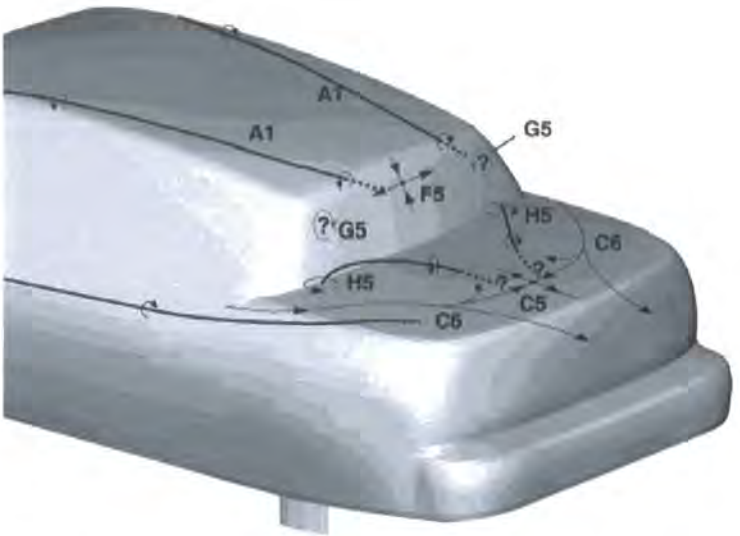

Figure 1.18: Column (boot lid) vortex on the trunk of a Notchback vehicle witnessed by Jenkins [Jenkins, 2000].

Later Gilhome et al. [Gilhome et al., 2001] further analysed and discussed the flow structure found by Jenkins and introduced some other complicated near wake flow patterns of Notchback vehicles. The work contended that the flow structure of a Notchback was very similar to that of a Fastback and identified the existence of an unsteady wake with a hairpin vortex that was shed periodically for Notchbacks with a backlight angle greater than 15 degrees. In this flow model, seen in Figure 1.19, there are the two familiar C-pillar vortices; between them is a pair of contra-rolling secondary vortices. These contra-rolling vortices are formed by the shear layer fluid rolling up in the recirculation area against the backlight and then being turned in the stream wise direction. The legs of these two contra-rolling vortices join at their ends to form what is referred to as the 'hairpin vortex.' The hairpin vortex is then shed periodically as seen in the smoke visualisation of Figure 1.20. In the periodic absence of the hairpin vortex the shear layer from the vehicle roof is thought to flop down and attach to the boot lid, before it begins to roll up and once again form the hairpin vortex. The area of re-attachment is only found on a small area of the boot lid, near the centreline. The impingement of the shear layer occurs at two unstable nodes behind the backlight where the flow moves in every direction. Flow heading toward the centreline from either side intersects at the saddle point and bifurcates up toward the backlight and downstream toward the boot trailing edge.

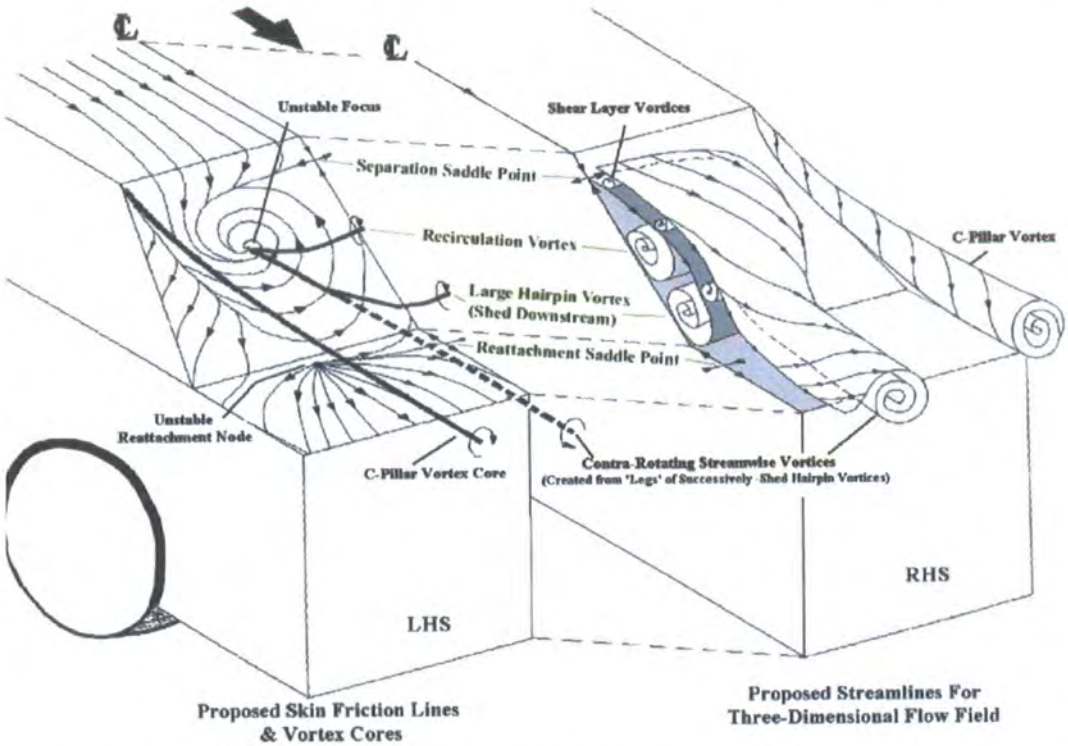

Figure 1.19: Flow structure in the wake of a Notchback vehicle as proposed by Gilhome et al. [Gilhome et al., 2001]

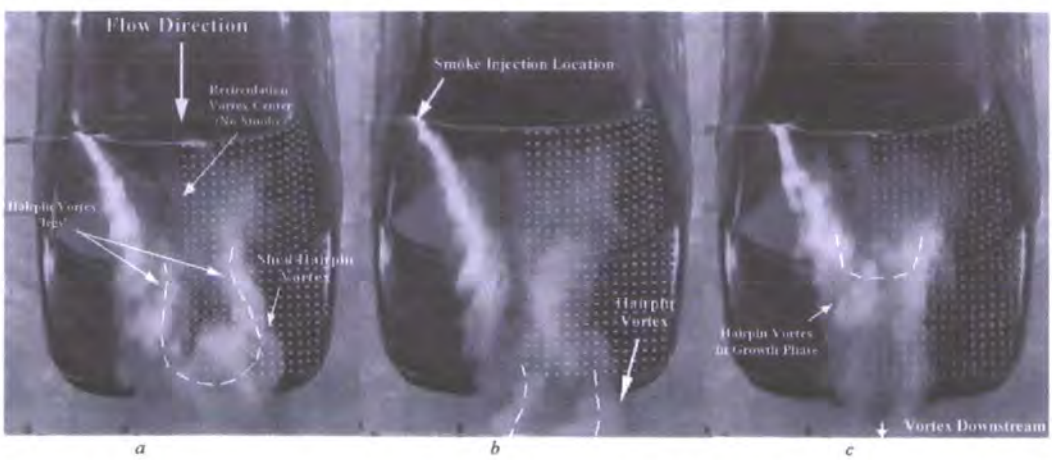

Figure 1.20: Hairpin vortex being shed from the rear of a Notchback vehicle [Gilhome et al., 2001].

1.5.2 Motor Sport Vehicles

Although the world of Motor Sport covers a wide range of vehicles, specifically designed for different racing classes, only the two general categories of open and closed wheel race cars will be used here to explain some of the basic aerodynamics of motor sport vehicles.

1.5.2.1 Open Wheel Racers

Aerodynamically speaking, open wheel race cars are some of the most complex vehicles exhibiting highly separated flow due to their multiple component bodies and large exposed wheels. The wheels alone can be 65% of the frontal area [Katz, 1995] and usually have the flow directed away from them by vanes and

splitters to decrease the large amounts of lift and drag that they create. Common to racing vehicles the shape of the under side will have a large effect on lift and drag. Because of the small under side area of open wheel racers the down force is not only created by the shape of the under pan, but also by shaping the side-pods and the inclusion of wings at both the front and rear of the vehicle.

Figure 1.21 attempts to show the array of vortices and separations created by the vehicle (however, this is a broad view and more focus would reveal many smaller areas of separation). In the wake the most noticeable features are the trailing vortices and up flow from the rear wing, vortices from the under side tunnels, and separations from the wheels. Depicted in Figure 1.21, the cooling flow and engine exhaust are frequently expelled at the rear of the vehicle to help increase the base pressure and may also be visible in the wake [Katz, 1995].

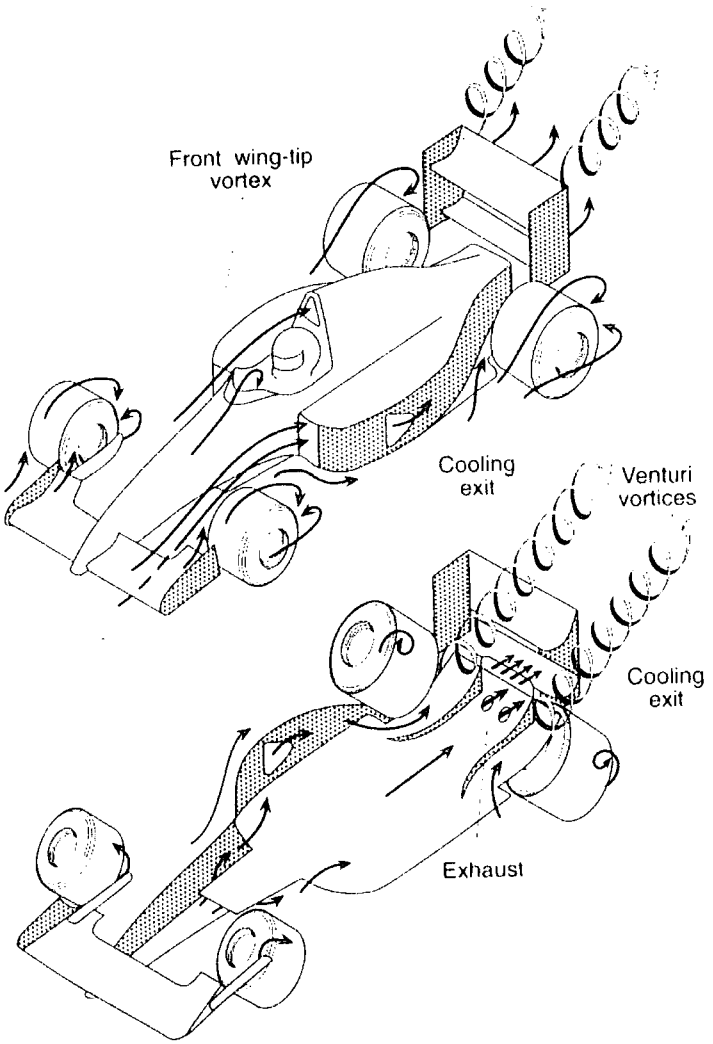

Figure 1.21: Separation around a typical open wheel racer [Katz, 1995].

1.5.2.2 Closed Wheel Racers

Closed wheel race cars have a much smoother body, both top and bottom, which results in mostly attached flow, fewer separations, and less drag than an open wheel racer. Also, because of the larger under side area and lack of exposed wheels, the down force is usually greater [Katz, 1995]. A general

representation of the vehicles' separations is shown in Figure 1.22. At the top of the vehicle the flow will remain attached to the vehicle body with the exception of small separations around wing mirrors and cooling inlets and exits. Beneath the vehicle there will be separation around the wheels but otherwise the flow will cleanly enter the underside beneath the front splitter and along the side skirts. In each of the diffuser tunnels flow entering the vehicle underside from the front and along the side skirts separates over the tunnels' sharp edges and rolls up into a stream wise vortex that continues downstream to the diffuser exit at the vehicle base. Experiments by Katz and Dykstra [Katz & Dykstra, 1992] have shown that the flow beneath the vehicle is a function of the base pressure. Specifically, they determined that proper placement of the rear wing over the body can control the base pressure encouraging more flow through the underside nozzle-diffuser and therefore increasing the down force. Generally, the wake of a closed wheel racer will be dominated by the two pairs of trailing vortices from the rear wing and underside nozzle-diffuser, but in the near wake flow deflected upward by the rear wing camber will also be noticeable.

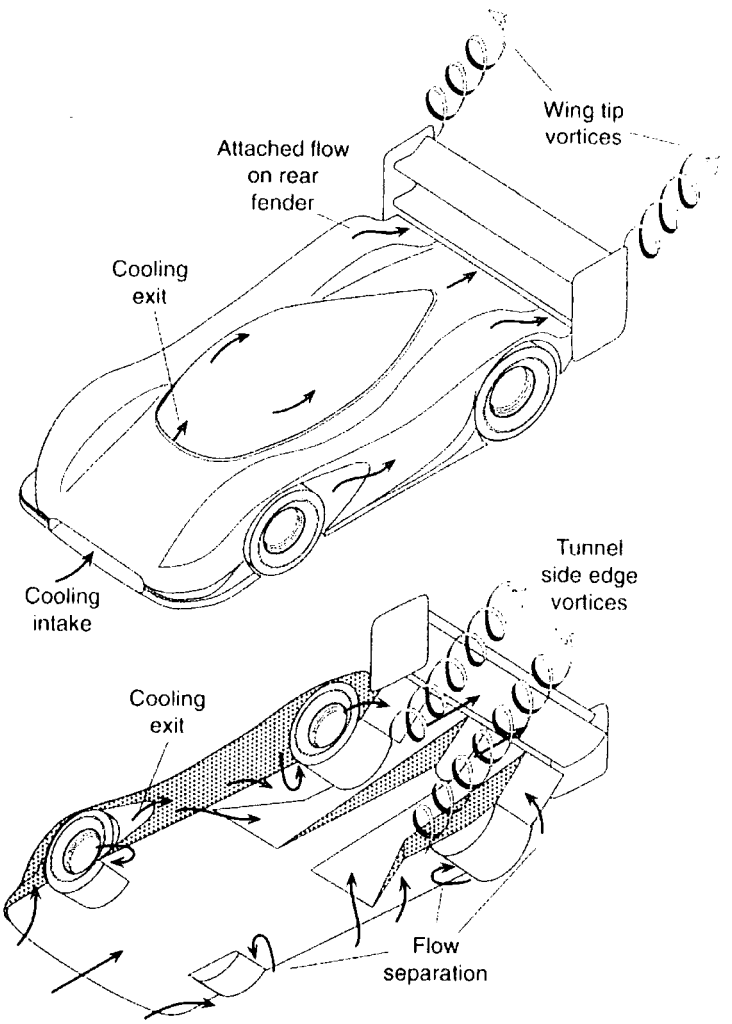

Figure 1.22: Separation around a typical closed wheel racer [Katz, 1995].

1.6 MODEL SCALE WIND TUNNEL TESTING

1.6.1 Tunnel Configuration

Although modern wind tunnels have an infinite number of variations between them, there are only a few categories to define the different types used for vehicle research. A wind tunnel can have an open or closed return circuit. The closed circuit offers greater power savings for a given tunnel size, as well as better flow quality. On the other hand, an open circuit will be less expensive to construct and would be more appropriate if space is of concern or if smoke and exhaust gasses are going to be created within the tunnel. As well as the circuit type, the type of test section boundary is another defining feature. Usually, a test section will have an open or closed jet; however, more recent advancements have seen new derivatives of the closed jet in the form of adaptive and contoured wall test sections. As a final option, slotted or porous wall test sections are also available.

Most modern wind tunnels are capable of accommodating 40% or 50% scale models, but a new generation of wind tunnels for some divisions of motor sport are capable of accommodating 60% and even full scale models for a more precise flow simulation [Carney, 2006]. Of the different wind tunnel types, an open jet will allow a larger blockage ratio when compared to solid wall tunnel types. The amount of drag felt by the model will increase with blockage in a closed wall wind tunnel and decrease in an open jet wind tunnel [Hoffman et al., 2003], but a model of any size will feel the effects of the stream wise pressure gradient created along a finite wind tunnel (termed 'horizontal buoyancy'). A proposed solution is to extend the length of the test section; however, Arnette et al. [Arnette et al, 1999] have shown that at a given length this solution will create low-frequency unsteadiness. Other sources of interference will come from the proximity of the model to the nozzle or collector. Placing the model close to the nozzle will allow the pressure gradient created in front of the model to deflect the flow, creating large amounts of streamline curvature, while placing the model too close to the collector will constrain the vehicle wake. Depending on the models being tested, matching an appropriate test section length with the right model placement can reduce these effects. Although horizontal buoyancy and nozzle and collector blockage are known sources of error, mathematical corrections have been able to resolve these issues with good accuracy. The main source of flow degradation mostly comes from the finite dimension of the jet exiting the nozzle, which is not realistic to the flow a vehicle would witnesses on the road [Arnette & Martindale, 2000]

The closed jet test section, on average, measures lower pressures in the vehicles base region than an open jet test section [Buchheim et al., 1983]. Some of this increased amount of interference is created by the constriction of the flow between the model and wall. With the model in place, an effectively smaller area is created for the same amount of fluid to pass, causing an acceleration of the flow and hence an artificial pressure between the vehicle and wall. In order to minimise this effect the vehicle blockage area should be kept at 5% or less. Using mathematical corrections the blockage ratio can be pushed up to 10%, but the only way to diminish the effect is through increasing the test section size. More interference comes from the proximity of the model to the contraction or diffuser. If the model is allowed to interfere with the

contraction the dynamic pressure measurement can be affected and if the model is too close to the diffuser its wake will interfere with the diffuser causing the base region to see a falsely high static pressure.

As a combination of these two test section types, a slotted wall has been found advantageous by allowing good results with larger blockage ratios (up to 21%) than either an open or closed test section [Barlow et al., 1999]. However, due to the combined open-closed boundary type, appropriate corrections are difficult to determine and have not yet been fully developed.

A derivative of the closed wall test section, the adaptive wall, does not constrict the streamlines. Instead, this system uses actuators to automatically adjust panels and shape the test section walls corresponding to measurements of static pressure to arrive at a shape that accommodates the streamlines that would be present on the vehicle in the open road. Developers of this system at Sverdrup have been able to achieve interference-free results for model blockages up to 30% [Arnette & Martindale, 2000].

With their technology rooted in adaptive walls, contoured wall test sections are another option. This effective, yet simpler method removes the facility for automatic adjustment and uses manual adjustment of fewer panels to achieve an approximate shape of the stream lines. This system comes at a lower expense and is more appropriate for use in wind tunnels that consistently test a similar vehicle shape. Although the adaptive wall system provides the best simulation for a larger scale, the contoured wall system can provide accurate results for blockages up to 20%. Comparison of CFD simulations between solid wall, contoured wall, and infinite wall test sections show that the contoured wall test section provides better aerodynamic simulation than the solid wall test section; even though the solid wall test section is larger [Arnette & Martindale, 2000].

1.6.2 Ground Boundary Layer Control

Independent of the type of tunnel used, the growth of a viscous boundary layer on the test section floor will create a false boundary condition that does not simulate on road conditions. This phenomenon is found to only be significant at low ground clearances when there is a chance that the floor boundary layer may interfere with the vehicle [Howell & Goodwin, 1995] [Istvan & Bearman, 1994] [Eckert et al., 1992]. Because full scale passenger vehicles have a reasonable ground clearance (usually larger than the boundary layer) and a rough underside creating turbulence, replicating the appropriate boundary conditions in a test facility primarily used for passenger vehicles has not always been done [Arnette & Martindale, 2000]. This is also true in some realms of motor sport such as NASCAR, where the vehicles have relatively large ride heights and the ground boundary layer is only important for the development of valence and side skirts [Landman, 2000].

Fago et al.[Fago et al., 1991], Howell & Hickman [Howell & Hickman, 1997], and Katz [Katz, 1995] have all considered the presence of the false boundary condition acceptable for passenger vehicle research, but detrimental to the research of motor sport vehicles due to their smooth underbellies and other components riding close to or in the boundary layer. However, these views are proposed for full scale testing where the ratio of ride height to boundary layer disturbance thickness is high. At model

scales this ratio decreases and the ground boundary layer can be more influential [Mueller et al., 1999]. The increased importance of scale wind tunnel testing as a development tool and changes in research interest to investigate underside flow and wheel rotation has prompted the use of boundary layer removal in passenger, as well as motor sport vehicle research at any scale.

A survey of methods used worldwide reveals several approaches to boundary layer control (Figure 1.23 shows just some of the options): Imaging of the vehicle can be an effective solution, but is impractical at large scale and does not mimic real relative motion. Floor mounted manipulators are another option, but are not widely recommended. A lifted model on a false ground plane is seen by Kessler & Wallis [Kessler & Wallis, 1966] to create the fewest technical problems, but still develops a small boundary layer. Active Suction forward of the vehicle is seen by Landman [Landman, 2000] to have a lower technical risk and practical complication than other methods, but still achieve an acceptable level of simulation. Distributed suction in combination with suction forward of the vehicle has been found effective in the Porsche model and full scale wind tunnels [Eckert et al., 1992]. However, unlike these fixed floor methods, using a moving ground plane to simulate the road moving beneath the vehicle will prevent any unrealistic separation at the vehicle under body [Wildi, 1994], and has been championed as the most promising method of boundary layer control.

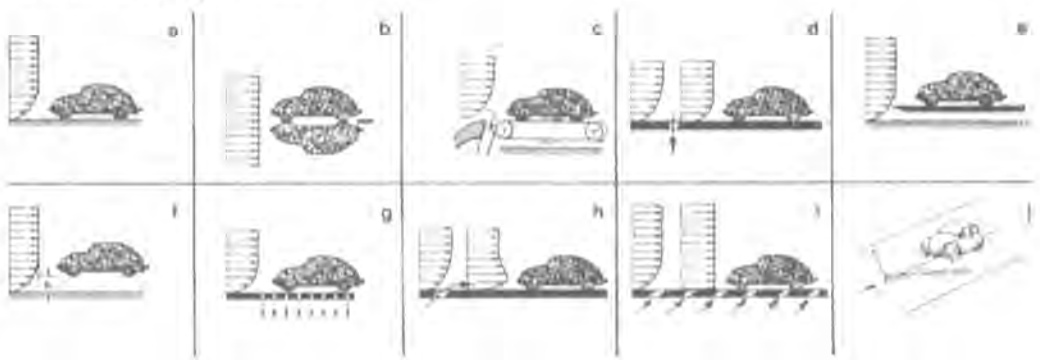

Figure 1.23: Some boundary layer control methods [Hucho, 1998].

1.6.2.1 Rolling Road Systems

Moving ground planes are now instituted in model and full scale wind tunnels worldwide in the form of a rolling belt beneath part or the entire vehicle. This method has been found to improve results, especially in terms of lift coefficient [Borello et al., 1999] and is particularly important for motor sport vehicles with sensitive underside flows, [Landman, 2000], [Eckert et al., 1992], and [Borello et al., 1999].

The two most popular moving ground configurations are a single wide-belt spanning the entire width of the model (Figure 1.24) and a 5-belt system beneath part of the vehicle (Figure 1.25). Of the two, a single wide-belt will provide the highest degree of accuracy [Arnette & Martindale, 2000] and is usually applied at model scale, whereas the limited width of a 5-belt system will be less accurate [Borello et al., 2000], but is much more convenient and preferred for full scale testing. Choosing between the two will usually be an issue of practicality. Using a single wide belt requires alternative means of support other than the traditional method of mounting to an under floor balance. Instead, the vehicle is supported by a strut, usually designed as an aerofoil profile to minimize interference and the force balance is then located

either inside the model or superficially attached to the vertical strut. Alternatively, a 5-belt system, such as the ones described in [Mueller et al., 1999], [Eckert et al., 1992], [Wiedemann & Potthoff, 2003], and [Borello et al., 2000] will allow traditional mounting through the test section floor in the gaps between the belts. This means that fewer changes will have to be made to a test vehicle and preparation time is much less. For facilities looking to upgrade flow quality without altering the existing force measurement equipment, test road worthy vehicles with as few changes as possible, or achieve greater time efficiency, the better than fixed road simulation of a 5-belt system is usually preferred. However, if the best simulation of on road conditions is sought then a single wide belt should be used.

Figure 1.24: Example of a BMW F1 model mounted over a single wide belt in the Sauber-Petronas wind tunnel [Carney, 2006].

Figure 1.25: Example of A 5-belt system at the Pininfarina wind tunnel [Pininfarina, 2006].

1.6.2.2 Wheel Rotation

One aspect of moving ground technology common to both the single and 5-belt systems is the use of wheel rotation. The fact that stationary wheels can contribute between 35% and 50% of the total drag for open wheeled race cars [Mears et al., 1992] and 25% for passenger vehicles [Wickern et al., 1997] justifies them as a valuable component to simulate correctly. Although the effects of wheel rotation are highly configuration dependent [Wiedemann and Potthoff, 2003], the change to the underside flow comes from the contact patch acting as a jet and accelerating the flow [Mears et al., 2002]. This realisation that flow around a wheel in motion can have a significant effect on aerodynamic resistance has been a factor in the increased popularity of rolling roads.

Using a moving ground creates the facility to rotate the wheels beneath the vehicle. In a 5-belt system the wheels are rotated by the four smaller belts which are then attached to the force balance beneath the floor. For a single wide-belt the wheels can be attached to the model using trailing arms to transmit drag but not lift or the wheels can be supported by lateral arms hinged to mounts outside the span of the moving ground plane. For the more usual method using the lateral supports, the wheels rotate in contact with the moving belt separate from the model body. This allows forces on the model to be measured, including the influence of the wheels' wakes. To factor the wheels into the measurement the lateral supports can be equipped to measure drag forces felt by the wheels. Although the supports will not impose a true vertical load on the wheels, it is found to be a far better compromise than stationary wheels [Wickern et al., 1997].

1.6.2.3 *Preferred Method*

The chosen boundary layer control system will ultimately depend on the intended use of the tunnel, the desired degree of accuracy, and any associated cost, which might find some of the other methods more appropriate for a given application, but this research aims to help improve wind tunnel testing beyond its current level and will focus on the single wide-belt system using an internal force balance as the best method for achieving high fidelity flow simulation in the wind tunnel.

1.7 *INTERFERENCE*

According to Lessard [Lessard, 2000] the AIAA Guide for the Verification and Validation of CFD Simulations [AIAA, 1998] states that the degree to which a model is an accurate representation of the real world depends on the perspective of the intended use. Following this philosophy; absolute simulation of the real world in the wind tunnel is not always necessary for every research enquiry, however, it is clear that one of the components leading to the best reproduction of on-road conditions is the use of a single wide-belt, concurrent with Section 1.6.2.3. As part of this configuration the use of intrusive struts and stings to support the model and its wheels above the moving ground and measure aerodynamic loads is necessary. This layout offers good accuracy, but assumes that the supports do not distinctly affect the models aerodynamic behaviour [Borello et al., 2000]. Since the aerodynamic interference of these supports is the deviation between the true result and the actual result obtained in the wind tunnel [Hoffman et al., 2003], as the increment of improvement to ground vehicles gets smaller with further refinement, more accurate simulations will be necessary to find new improvements above and beyond those already made. Because of this, support interference must be included and recognized as a factor in overall road to tunnel comparison error. Neglecting to include this as a contributing factor undermines attempts being made to experimentally model vehicle flow fields.

Traditionally, aeronautical wind tunnels used force balances external to the tunnel with the model mounted by way of struts (or wires). The measurements therefore combined the aerodynamic force acting on the support and model requiring some form of aerodynamic tare or strut fairing to remove the presence of the supports. The introduction of compact technology has made it possible to mount force measurement equipment inside the models thus removing the need for an aerodynamic tare. This approach, now also used in ground vehicle testing, provides a substantial improvement, because the aerodynamic forces acting on the supports are no longer part of the measurement. However, in both fields, the supports still have an impact on the measured forces because their presence interferes with the flow around the model. It is possible for aerodynamicists, experienced in testing a certain vehicle shape, to become familiar with support effects on that particular shape, or its variants, and take into account the presence of the supports in the flow field; but, for ever changing model dimensions and support types it is difficult to determine the exact influences on the model [Borello et al., 2000].

It is well established, from work in aeronautics, that the measured forces on model supports alone differ in the presence of the model [Barlow et al., 1999] and in the same manner the measured forces of the model will be different in the presence of the model supports showing a definite interaction between the

two. However, because the model cannot generally be measured without its supports, de-coupling the effects of the supports and model becomes a difficult task, making the true measurements of the model difficult to discern. If the combination of the model and support has drag $D_{(model+support)}$, it is not equal to $D_{model}+D_{support}$ due to the interaction between the two bodies [Hoerner, 1965]. In most practical applications the interference will mean that the combined force will be larger than the sum of the two. Some proportion of this additional 'interference drag' can be expected to fall on the model.

While model support struts and wheel support stings undoubtedly alter the flow around a ground vehicle, and while there is some anecdotal evidence of significant support strut interference in isolated cases, a very limited amount of work has been published on the correction or extent of support interference in terms of ground vehicles.

In a recent paper by Wickern [Wickern, 2007] intrusive supports are acknowledged as a necessary factor required for the determination and correction of test section interference. Another publication by Strachan et al [Strachan et al., 2004] recognises the downstream wake influence of an overhead strut used for testing an Ahmed model over a moving ground plane. The results show a clear reduction of the stream wise velocity along the model centreline at a traverse plane one model length downstream from the model base. More specifically, in a previous CFD study [Page et al., 2002] using a NASCAR geometry, an overhead strut was found to create an error of –0.1 on CP at one strut chord length before and after the leading and trailing edge respectively. Unfortunately they do not quote changes in global forces on the model. As well as this, experiments performed by Knowles [Knowles, 2002] on an isolated wheel rotating in ground contact showed that the addition of a support sting produced a reduction in wheel lift by 16%, an increase in drag by 2%, an increase in mass flow through the wheel by 83% and a provocation of flow separation on the wheel surface 4 degrees earlier than without the sting.

Although little attention and explanation is given to the degree of interference throughout these publications there are some brief suggestions to future experimenters for avoiding interference. Amongst the results from Page et al. [Page et al., 2002] was the conclusion that a support placed at the roof centre between the A-pillars is the worst possible location for bodied models. They went on to recommend that supporting the model using a horizontal or angled strut approaching from behind, within the vehicle wake, where the flow is already disturbed is preferred and should be advantageous in reducing the amount of interference. Another popular convention for avoiding excessive interference is the use of streamlined struts or stings to reduce the size of a supports wake and therefore the disruption to the vehicles natural flow field.

1.7.1 Junction Flows

Focusing on the junction, local separations begin to explain some of the interference created by model supports. A significant body of work exists on junction flows relevant to aeronautics: [Lessard, 2000], [Thomson and Wentz, 1983], [Walter & Patel, 1996], [Olcmen & Simpson, 1994], [Davenport & Simpson, 1987], [Davenport & Simpson, 1990], [Simpson, 2001], [Shizawa et al., 1996], [Fleming et al., 1993]. Based on this work, support struts can be expected to affect boundary layer flows on the model

and support, vortex formation, and local flow separations. These features are often investigated by simplifying the geometry to an aerofoil intersecting a flat plate, which offers insight into some aspects of the flow associated with more complicated junction geometries. In the case of a streamlined aerofoil joined to a planar surface, there are two areas of separation caused by the union that contribute to an increase of drag.

The first area of separation is created when the boundary layer on the planar surface encounters the aerofoil leading edge. While approaching the stagnation point at the leading edge of the aerofoil pressure gradients produced by the aerofoil re-direct the vortex lines of the boundary layer around the aerofoil in the downstream direction. Adverse pressure gradients ahead of the foil section then pick up this newly directed vorticity causing a three-dimensional separation line around the base of the aerofoil. Figure 1.26 shows a flow visualisation representation of the separation in the xy-plane. This separation allows the newly stream wise vorticity to coil up forming a horseshoe vortex at the leading edge that propagates downstream along the seam of the junction [Moore & Forlini, 1984]. Figure 1.27, from Simpson [Simpson, 2001] illustrates the horseshoe vortex. The vortices are small in scale and usually confined to less than one boundary layer thickness from the plate [Eckerle & Langston, 1987]. Simpson [Simpson, 2001] considers them unsteady, easily changing direction, size, location, and vorticity.

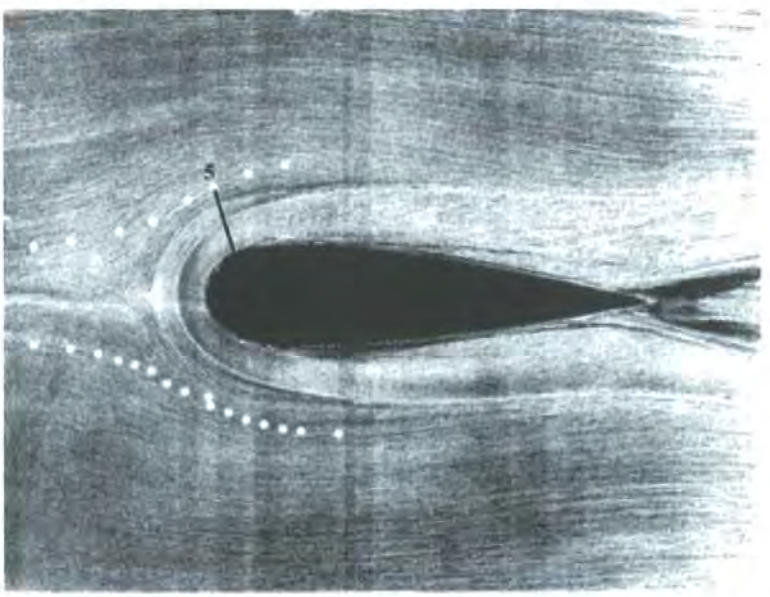

Figure 1.26: Flow visualisation of the separation line in the xy-plane at the junction of an aerofoil intersecting a flat plate [Simpson, 2001]

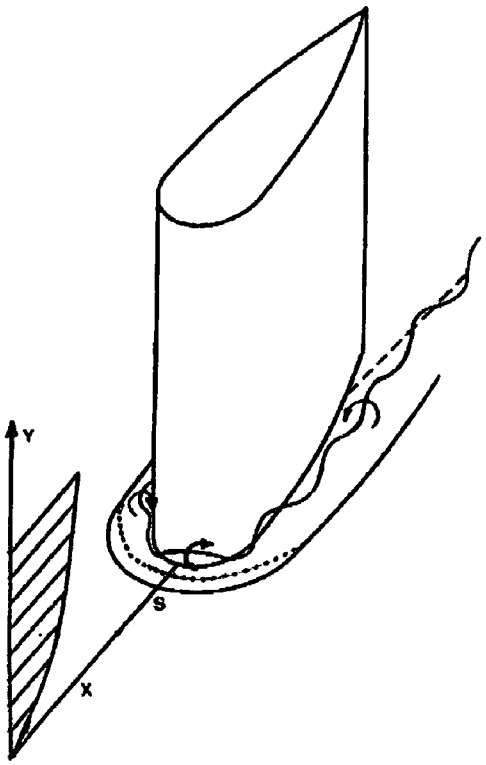

Figure 1.27: Horseshoe vortex separation at the junction of an aerofoil intersecting a flat plate [Simpson, 2001].

The second separation may occur at the trailing edge of the airfoil section. Depending on the momentum of the flow and the shape of the airfoil used, the stagnation pressure deficit behind the airfoil may cause a separation of the flat plate boundary layer downstream from the junction. (Davenport et al., 1992). This separation is illustrated in Figure 1.27 by the dotted line at the rear of the aerofoil on the plate surface and can be seen in the flow visualisation from above in Figure 1.26.

The amount of interference drag will largely depend on the strength of the horseshoe vortex formed at the leading edge and this will increase with the bluntness of the shape intersecting the surface to create the junction [Simpson, 2001]. Accordingly, Fleming et al. [Fleming et al., 1991] developed a Bluntness Factor based on the aerofoil geometry that determines the formation and strength of the vortices.

Equation 1.9

$$BF = \frac{1}{2} \cdot \frac{R_o}{X_T} \cdot \left[\frac{T}{S_T} + \frac{S_T}{X_T} \right]$$

Olcmen & Simpson [Olcmen & Simpson, 1994] and Walter & Patel [Walter & Patel, 1996] found that BF's of 0.029 and 0.019 respectively did not produce horseshoe vortices. However, Olcmen and Simpson [Olcmen & Simpson, 1994] did find vortex formation for BF greater than 0.045, with increasing strength beyond that. The bluntness factor can be used to determine the degree of interference that will be present from the junction. The stiffness required of model support struts will mean that they are likely to have bluntness factors above 0.045.

In order to try and quantify the effects of interference, Hoerner [Hoerner, 1965] created a formula through interpolation of experimental results performed by NACA, Gottingen, Hoerner, Munich, and Junkers for

aerofoils with T/c=0.1 to 0.75 and X_T=0.30 to 0.35. The equation estimates the change in drag of a plate due to the union of an aerofoil shaped strut.

Equation 1.10

$$\Delta C_D = \left[0.8 \cdot \left(\frac{T}{c} \right)^3 - 0.0003 \right]$$

The graph from which this equation was derived was valid for ratios in the order of δ/c of 10%, such as found on wing body junctions. Laminar type sections (X_T=0.5) are expected to have a higher interference drag [Hoerner, 1965]. The equation gives a rough estimate of the interference drag based on the aerofoil geometry. Using this formula can give a rough idea of what sort of drag to expect by the addition of an aerofoil to a planar surface. The interference drag effect is produced by the increased pressure drag of the two separations and the added friction drag produced by the horseshoe vortices pulling the high-speed free stream air into the junction area [Tamai, 1999]. The size and intensity of the vortex is not only a function of nose bluntness (thickness and chord), but also Reynolds number, boundary layer thickness, free stream turbulence, and surface roughness [Simpson, 2001] [Moore & Forlini, 1984] [Hoerner, 1965]. Despite its size, or even if the vortex formation manages to subsist and trail around the entire strut into the wake, the distortions in the axial velocity can proceed well into the wake even after the vortices have diffused [Walter & Patel, 1996]. Controlling the flow condition and geometry can reduce excessive drag, but due to the complicated interactions taking place there is no way to completely remove or account for the changes produced.

1.7.2 Wake Effect

The overall change to the flow field is not only caused by the junction, it is a result of the extending wake of the support as well. In the context of a supported model, a build up of pressure behind the support could induce flow separation instigating further changes in flow at the rear of the vehicle, affecting sensitive areas such as the vehicle backlight, rear wing, or under floor tunnel exits at the vehicle base. In order to try and minimise interference, supports are usually designed as a streamlined shape, however, depending on the model scale and weight, the supports can still be large leaving significant imprints and creating changes downstream that would not otherwise occur.

1.7.3 Potential Influences

Another area of interference can be created by blockage or re-direction of the flow by other, farther off-body components such as support mounts, model manipulation equipment, or measurement paraphernalia. For instance, if mechanical adjustment of the model is required or tubes and/or wires must be run inside the model, some sort of housing would be required to store the equipment within practical proximity of the model. These features of the wind tunnel environment can impinge on the streamlines causing a similar effect to that of the solid wall blockage discussed earlier in Section 1.6.1. These potential influences will be unique to the wind tunnel being used and may cause significant changes in the measured aerodynamic forces of the model.

1.7.4 Practical Support Configurations

In the context of model support above a rolling road the junction geometry can change drastically with vehicle and support type, deviating farther away from the idealised model of an aerofoil intersecting a flat plate. This is especially true when it comes to wheel stings. In terms of supporting the model, a strut will have to penetrate the shell to mount to the balance, leaving a gap around the seam of the junction, as seen in Figure 1.28. These subtle differences as well as strut approach philosophy can have unpredictable effects on the flow field. Some popular methods of strut approach have models held by vertical struts at the roof, struts at an angle through the backlight, or horizontal struts at the vehicle base. Although some [Page et al., 2002] have found that supporting the vehicle in an area of already separated flow will reduce the amount of interference all the support methods will unavoidably interfere with the natural flow field.

Figure 1.28: Strut penetrating model shell to join with interior force balance.

Other attempts at minimising interference have been made by manipulating the geometry of the junction itself. One approach is to introduce a constant radius fillet at the junction. While this may be effective for small fillet radii Davenport et al [Davenport et al., 1990] have shown that this solution makes the nose more blunt adding greater strength to the horseshoe vortices. Another approach is to include a fillet radius only at the leading edge. This can eliminate the leading edge separation and prevent the formation of the horseshoe vortex [Davenport et al, 1992]. Additionally, including a fillet behind the trailing edge up to one chords length can reduce trailing edge separation and interference drag by up to 10% for some configurations [Hoerner, 1965]. Large leading and trailing edge fillets effectively increase the strut chord at the junction, decreasing bluntness. Unfortunately, for setups using internal force balances, the support strut must not make contact with the body shell and the incorporation of effective fillets is not straightforward.

There are also a few other interference drag reduction methods worth mentioning. Lafleur & Langston [Lafleur & Langston, 1993] found that creating a small depression before the wing nose allowed a greater flow area, reducing the flows vorticity and velocity in the region. This method offered a reduction in interference drag of 18%. Unfortunately, in the context of a vehicle support strut, this would imply reshaping the vehicle body to suit the strut.

Experiments performed by Simpson [Simpson, 2001] investigated suction and blowing of the boundary layer but concluded that the vortices were only delayed, usually with secondary vortices being created as

well. Airflow ejection from the strut trailing edge has been shown to be effective in reducing the strut impact on components (eg: wings) far downstream [Akehurst, 2003], but Davenports' swept leading edge remains as the best method for removing separation and reducing the adverse pressure gradient created by the junction.

1.8 SUMMARY

Through numerous environmental, economic, and performance influences the field of automotive aerodynamics has matured to a point where it now upholds an important role in the development of the ground vehicle. As a result the vehicle shape has begun to reach a pinnacle where new improvements can only be made by unpopular changes, or through complex refinement, to the bodies shape. Advancements in model scale wind tunnel testing, in the form of moving ground planes, have made this process more accurate, manageable, affordable, and effective; however, the use of a moving ground plane currently demands the use of intrusive supports, which will inevitably degrade the flow quality around the model. In order for careful examination of a vehicle's elements to be performed an equal if not greater level of flow simulation needs to be achieved and the effects of intrusive supports must be removed in order to achieve a high level of flow simulation.

1.8.1 Objectives and Goal of the Research Project

- Determine the repeatability of the Durham University $2m^2$ wind tunnel.
- Quantify the effects of intruding supports for a range of passenger and motor sport vehicles.
- Explain the physics of interference flow-fields and their impact on the flow structure surrounding a selection from the passenger and motor sport vehicle shapes.
- Determine effects of overhead struts on the rear mounted wings of motor sport vehicles.
- Determine effects of overhead struts on critical backlight angles of passenger vehicles.
- Determine the effects of wheel stings on underside flow.
- Aid in the motivation for research into non-intrusive methods of model support.

1.8.2 Thesis Arrangement

Chapter 1 – Chapter One offers a background into the development of the passenger and motor sport vehicle shape as well as an introduction to model scale wind tunnel testing, the problem of interference, and junction flows.

Chapter 2 – Chapter Two explains the experimental method and the equipment, models, and supports used to explore the problem of support interference.

Chapter 3 – In Chapter Three the experimental results are examined. Force and moment results are provided for all of the tested ground vehicles as well as for the isolated cases of a vertical strut in union with a flat plate and interfering with flow upstream of a motor sport vehicles rear wing. Results of pressure and velocity measurements in the wake of a notchback passenger vehicle shape and a closed wheel motor sport vehicle shape are also presented. Surface oil flow visualisations with and without interference from different support configurations are provided for the same two vehicles. Finally, surface pressure measurements at the top and bottom surfaces of the Closed Wheel Racer are offered.

Chapter 4 – Chapter Four includes results from Computational Fluid Dynamic simulations of a vertical strut intersecting a flat plate. Values for vorticity, velocity, and total pressure are given in planes before and after the junction, perpendicular to the direction of flow. Also included are values of static pressure and skin friction on both the flat plate and aerofoil surfaces. All results are provided for a range of thickness-to-chord ratios as well as boundary layer thicknesses. The amount of interference in the form of changes in forces and moments on the plate by the presence of the vertical aerofoil is provided for all variations of the thickness and boundary layer.

Chapter 5 – Chapter Five offers a discussion of the results from Chapter Three and Chapter Four.

Chapter 6 – Chapter Six concludes the results and discussion and offers ideas for further work.

Chapter 7 – Chapter Seven lists the references used throughout the investigation.

2 EXPERIMENTAL SETUP

2.1 MODELS

In order to investigate the effects of interference a collection of five scale ground vehicle models were used. All of the models were pre-existing and were not purpose built for this investigation. One vehicle was taken from each of the three general passenger vehicle categories and from each of the two motor sport vehicle categories described in Section 1.5. Model dimensions can be found in Table 2.1.

	Length (mm)	Width (mm)	Height (mm)	Track (mm)	Base (mm)	Ride Height (mm)	Area (m^2)	Scale (%)	Blockage (%)
Notchback	1260	450	325	38	700	F:40 R:44	0.125	25	6
Hatchback no deflector	1590	680	545	588	1000	F:60 R:65	0.308	40	15
Hatchback w/deflector	1590	680	545	588	1000	F:60 R:65	0.308	40	15
Ahmed	1044	389	338	327	470	F/R:50	0.308	100	6
Closed Wheel Racer	1680	710	360	551	962	F:11 R:22	0.184	35	9
Open Wheel Racer	1000	465	280	F:414 R:404	644	F:4 R:6	0.094	25	5

Table 2.1: Model dimensions and details.

The models were mounted to the force balance through the wind tunnels stationary ground at each of their four wheels. In the case of the Ahmed bluff body, the model was mounted at locations on the models underside near each of the four corners. The cylindrical mounting stilts were attached to the wheel (for the wheeled models) or model underside (for the Ahmed model) and force balance at either end, passing through a hole in the wind tunnel floor that was larger than the diameter of the stilt to allow clearance between the stilt and stationary ground. Leaving an appropriate clearance insured that no extra forces would be transmitted to the measurement by fouling of the stilt on the tunnel floor. For the same reason the model wheels could not be allowed to contact the stationary ground plane, but a realistic model ride height had to be maintained. To do this, each of the circular wheel cross sections was flattened by an appropriate amount ('f' in Figure 2.1) to allow mounting of the model with a realistic ride height. Figure 2.1 shows the general mounting solution for a wheeled model. Specific values of 'f' removed from the wheel diameter to achieve the flat surface for each of the wheeled models are denoted in the descriptions of the specific models below.

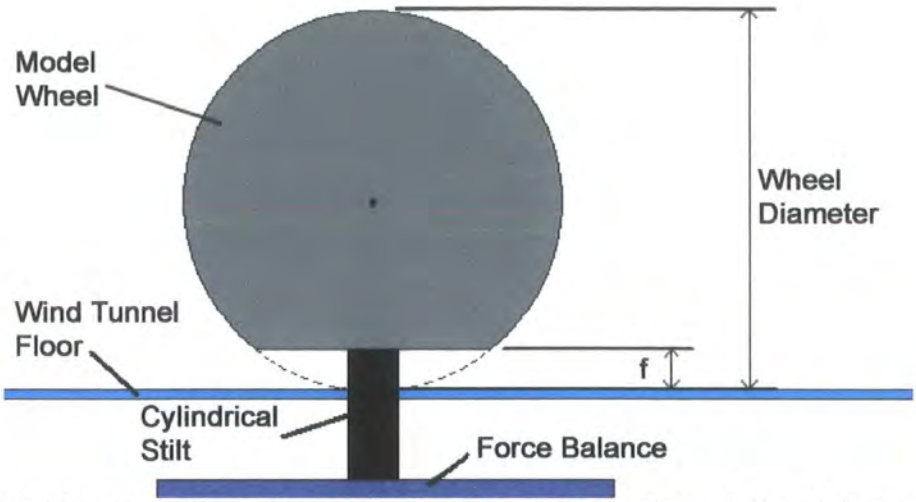

Figure 2.1: Mounting of model wheel to the force balance through the stationary wind tunnel floor.

The Notchback model photographed in Figure 2.2 has stationary wheels, a semi-detailed under floor, simplified engine cooling flow, limited exterior trim, and a slightly boat tailed rear end. Each of the wheels was flattened by 3.5mm from its diameter to allow the model to be mounted at a realistic height without touching the stationary test section floor.

Figure 2.2: 25% scale Notchback model.

The Hatchback model photographed in Figure 2.3 has stationary wheels and limited exterior trim. Each wheel was flattened by 6.0mm from its diameter to allow a realistic ride height without contacting the test section floor. At the roof trailing edge there is a removable deflector seen in Figure 2.4. The model was tested with and without the deflector constituting two different vehicle shapes.

Figure 2.3: 40% scale Hatchback model.

Figure 2.4: Hatchback rear deflector seen in silver.

The Ahmed bluff body represents a Fastback vehicle shape. The model shape, shown in Figure 2.5, is a replica of that described by Ahmed et al. [Ahmed et al., 1984]. In order to provide a range of results for comparison with this work six different backlight angles (0.0, 12.5, 25, 27.5, 30, 32.5 degrees) were used. A smaller increment was chosen around the critical angle for better definition of the change from high to low drag described in Section 1.5.1.1. The model was mounted through the test section floor on four cylindrical stilts attached to the model underside with a ride height of 50.0mm.

Figure 2.5: Ahmed model with interchangeable rear ends (shown in grey) for variable backlight angles representing characteristic shape of a Fastback. Model was 100% scale with an overall length of 1044mm.

The prototype Closed Wheel Race Car is photographed in Figure 2.6. The model has stationary wheels, engine and brake cooling ducts, full exterior trim, an adjustable dual element rear wing, and a detailed under floor with interchangeable front splitter plates and a rear diffuser. The wheels were flattened by 1.5mm from their diameter to allow a realistic ride height with clearance above the test section floor.

Figure 2.6: 35% scale prototype Closed Wheel Race Car.

The generic Open Wheel Race Car is photographed in Figure 2.7. The model has stationary wheels, a detailed under floor, simplified engine cooling, simplified suspension components, full exterior trim, and an adjustable rear wing. Each of the wheels is flattened by 5.0mm from their diameter to allow a realistic ride height without contacting the test section floor.

Figure 2.7: 25% scale generic Open Wheel Race Car.

2.2 Mock Supports

2.2.1 Overhead Struts

In order to introduce interference into the models' flow fields, two different mock overhead struts were designed that did not actually support the models. They were designed for minimal strut drag for a given strut stiffness. Because it was predicted that the strut wake, not the junction flow would dominate interference, the profile was selected based on low drag in order to minimize the impact of the strut wake on motor sport vehicle rear wings and passenger vehicle backlights, rather than minimizing the drag local to the strut-model union. The moments of inertia (bending and torsion) and sectional drag coefficient were considered for a number of established aerofoil profiles and a laminar series NACA 66_4-021 profile was selected. A chord of 100mm was used which would provide a steel strut with an appropriate level of stiffness to support a 25%-40% scale model. The chosen profile corresponds to a Fleming et al. [Fleming et al., 1991] Bluntness Factor (BF) of 0.045, meaning that a significant separation at the junction can be expected. A detailed description of the profile and chord length selection process can be found in Appendix A. The actual struts used were manufactured in Aluminium on a GATE ECM-2 Computer

Numerical Control (CNC) Mill using an ANILAM 3000M controller. The CNC program for the controller was generated in EXCEL. An example of the software input program is offered in Appendix B.

To vary the amount of interference, the strut was designed for use in two different sized configurations. To make this possible the chosen two-dimensional 100mm chord profile was manufactured with a modular design (described in Appendix C) allowing it to be extrapolated into two different span lengths. The 'Small Strut' configuration consisted of the 100mm chord NACA profile extending from the model to a position well outside the jet (z=1510mm). The 'Large Strut' used a smaller portion of the 100mm chord NACA profile strut attached to an overhead support housing actuators for model pitch and ride-height control. The aerofoil profiled strut extended from the model to a position inside the flow (z=750mm) where the actuator housing began, the actuator housing then extended the remaining height until outside the jet at z=1510mm. Figure 2.8 and Figure 2.9 illustrate the 'Small Strut' assembly and Figure 2.10 and Figure 2.11 illustrate the 'Large Strut' assembly. The Aluminium fairing around the 'Large Strut' actuator housing is comprised of the nose and tail of a NACA 0035. The NACA 0035 aerofoil profile is halved at its point of maximum thickness and the nose is placed at the front of the actuator housing. The tail is then placed at the rear of the actuator housing. At the base of the housing (z=750mm) the additional length of 180mm of the housing interrupts the NACA 0035 profile making the overall length of the faired housing 480mm. As the faired actuator housing tapers out the overall length at z=1510mm was 878mm. Figure 2.11 shows cross sectional drawings of the faired actuator housing at both z=750mm and z=1510mm.

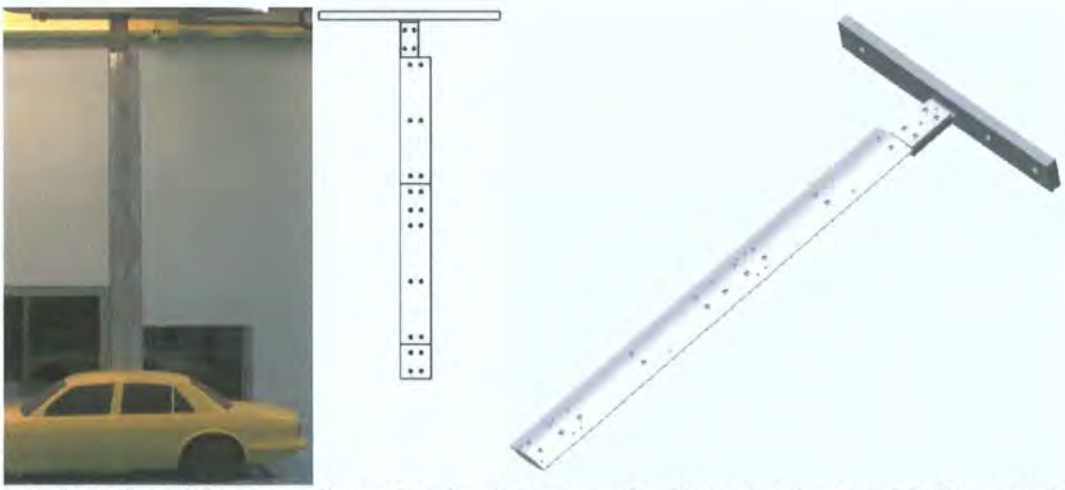

Figure 2.8: Small Strut configuration in place over the Notchback model (left), sketched from a side view (centre), and in an isometric drawing (right).

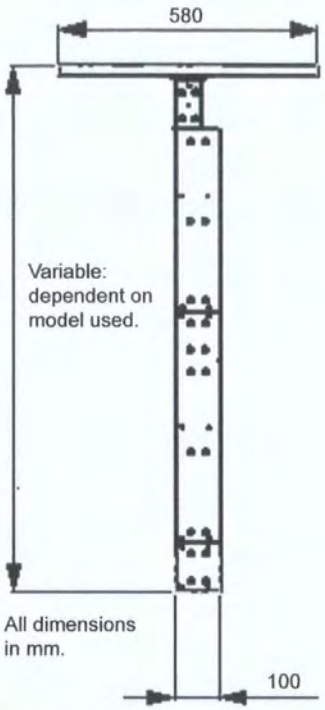

Figure 2.9: Small Strut assembly with key dimensions.

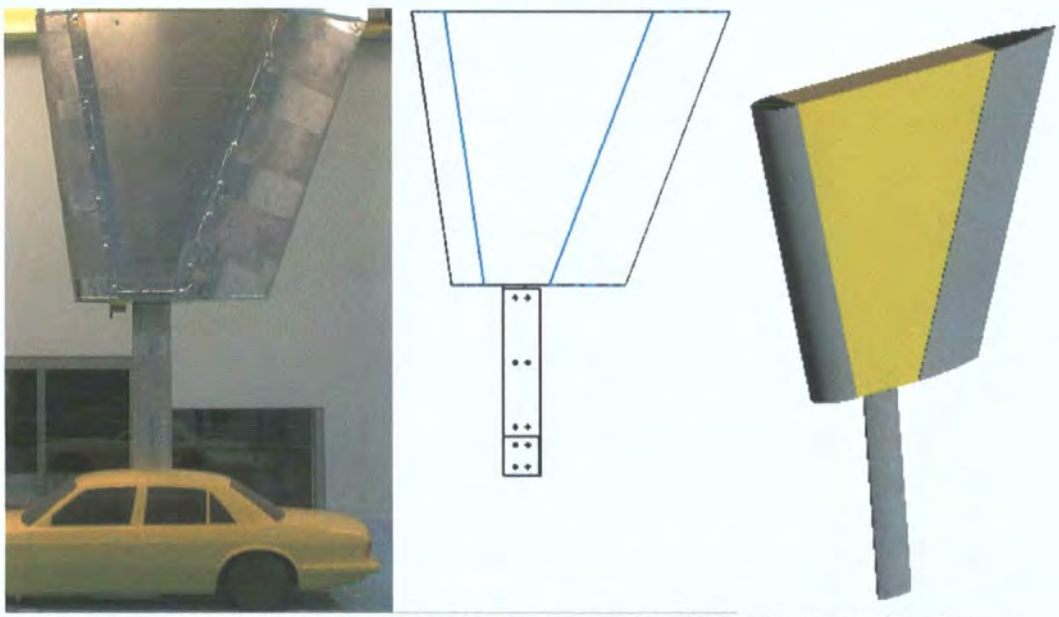

Figure 2.10: Large strut configuration in place over the Notchback model (left), sketched from a side view (centre), and in an isometric drawing showing the NACA 66_4-021 strut, actuator housing, and NACA 0035 fairings nose and tail (right).

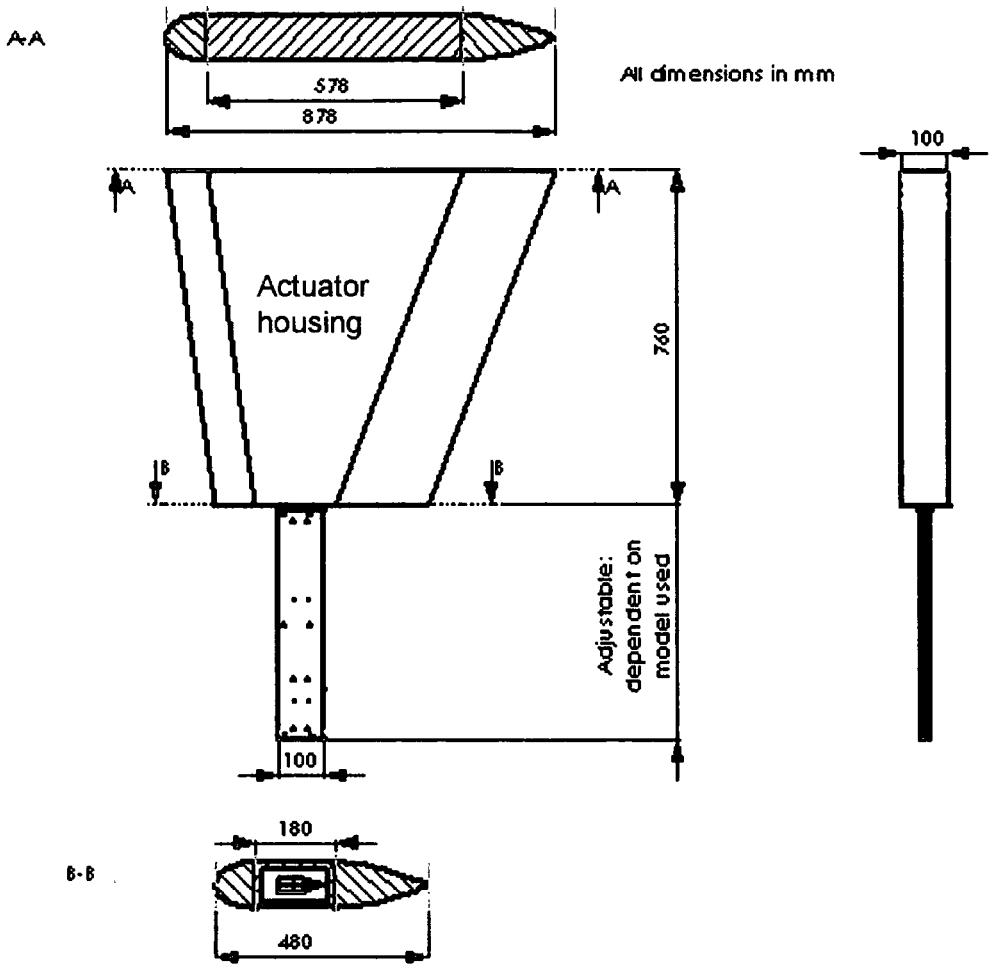

Figure 2.11: Large Strut assembly with key dimensions.

2.2.2 Lateral Stings

The mock lateral wheel stings (Figure 2.12) used were pre-existing, not designed specifically for this experiment, but were found to be an appropriate scale and profile, requiring little modification. They had their stub axles removed, leaving a circular mounting boss (25mm diameter) at the model end which transitioned quickly into an aerofoil shape tapering out at the outboard end. The outboard end was then hinged to a base mounted to the test section floor in the plenum outside the open jet.

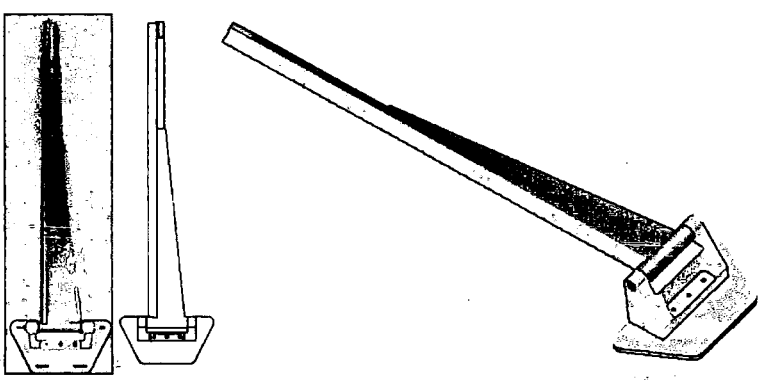

Figure 2.12: Lateral wheel stings with Type 1 mounting base photographed from above (left), sketched from above (centre), and in an isometric drawing (right).

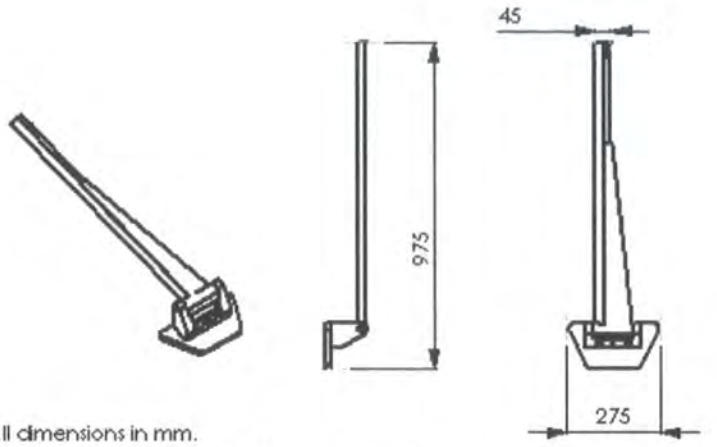

Figure 2.13: Lateral wheel sting with key dimensions.

The mounting bases, photographed in Figure 2.14, had originally been designed in two pairs for use with specific front and rear wheel diameters of a race car model. Accordingly the two different pairs of mounting base (Type 1 and Type 2) were of slightly different geometry to accommodate the front and rear wheel diameters, whilst remaining horizontal to the test section floor. An analysis was carried out to see how placement configuration ('Type 1 at front wheels with Type 2 at rear wheels' or 'Type 1 at rear wheels with Type 2 at front wheels') would affect the amount of interference for the Notchback model.

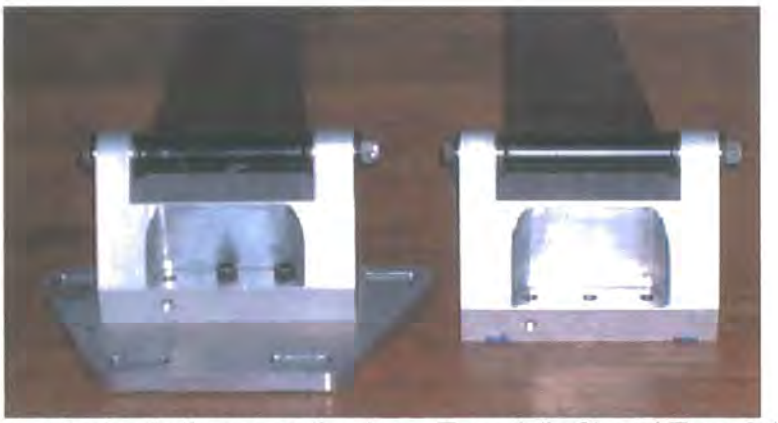

Figure 2.14: Lateral wheel sting mounting base Type 1 (Left) and Type 2 (Right).

Figure 2.15 through Figure 2.18 show comparisons of the two mounting base type's effects on drag and lift for the three strut configurations. The change in coefficient is shown relative to the configuration with no wheel stings but the same strut. This change is then compared between the two different types of wheel sting mounting base to see which causes greater interference on the model and how much greater the interference is over the interference from the other mounting base type.

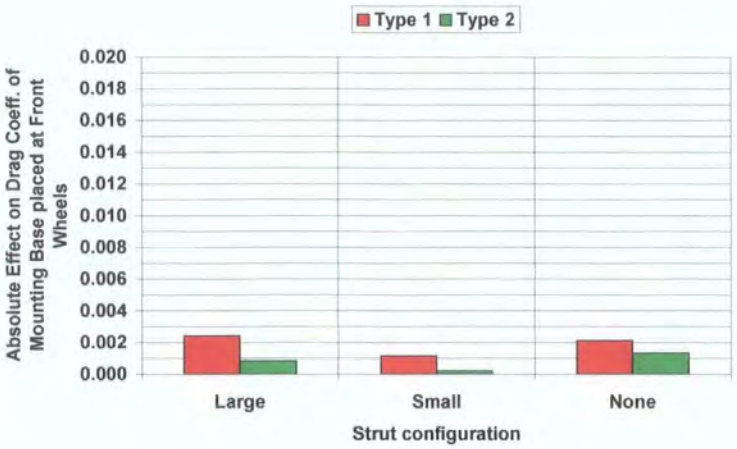

Figure 2.15: Comparison of effects on drag coefficient from mounting base Type 1 & 2 when placed at the front wheels of the Notchback model.

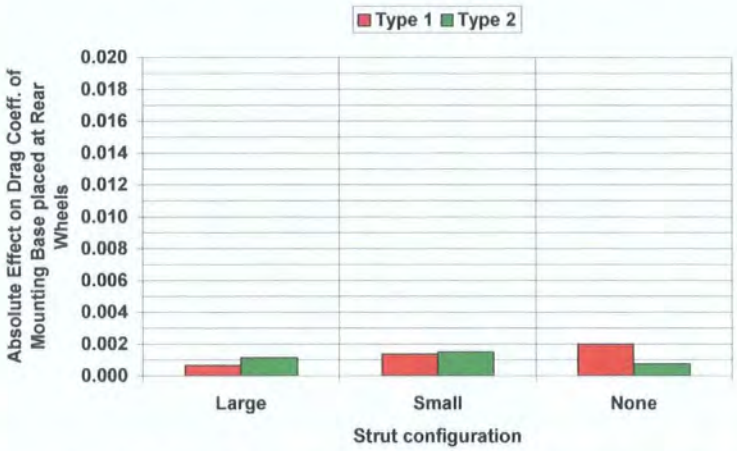

Figure 2.16: Comparison of effects on drag coefficient from mounting base Type 1 & 2 when placed at the rear wheels of the Notchback model.

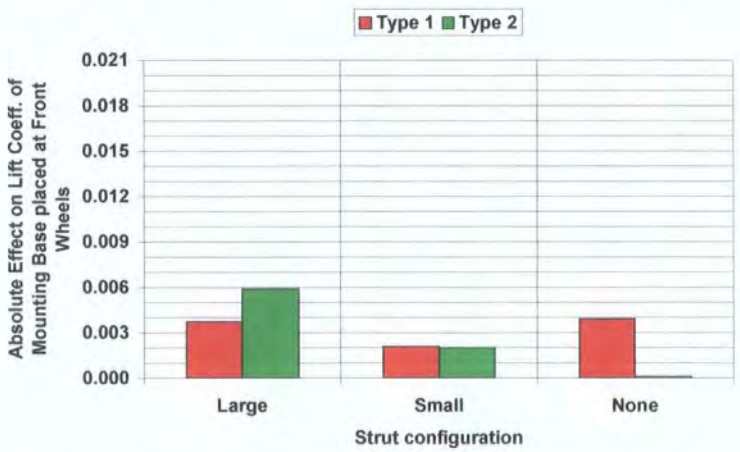

Figure 2.17: Comparison of effects on lift coefficient from mounting base Type 1 & 2 when placed at the front wheels of the Notchback model.

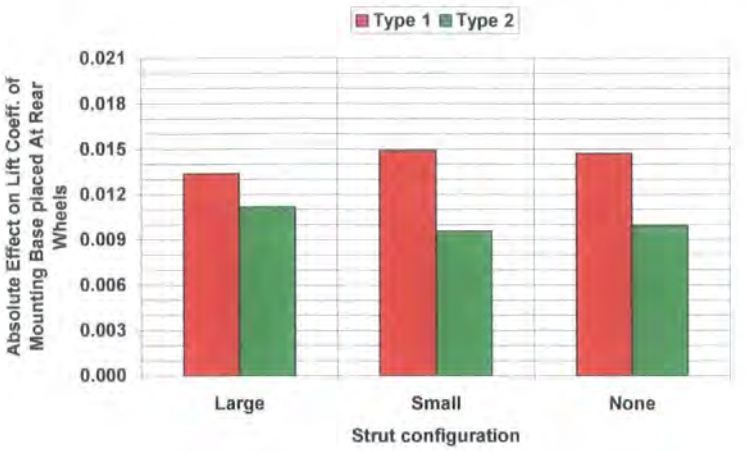

Figure 2.18: Comparison of effects on lift coefficient from mounting base Type 1 & 2 when placed at the rear wheels of the Notchback model.

For all strut configurations neither type of base, when compared with the other, whether placed at the front or rear, creates an effect larger than the balance repeatability of 2 counts on drag. There is only a slight effect larger than balance repeatability of 3 counts on lift for Type 1 when placed at the front wheels, but it is minimal (Figure 2.17). The only effect outside of repeatability is seen on lift in Figure 2.18 when the Type 1 base is placed at the rear wheels. Here, Type 1 creates a surprisingly greater effect (outside of repeatability) on lift than Type 2 when placed at the vehicles rear wheels for the 'Small Strut' and 'No Strut' configurations and has a minimal effect in the 'Large Strut' configuration. Because the Type 1 pair has a greater effect when placed at the rear, the 'Type 1 at rear wheels with Type 2 at front wheels' sting configuration was used throughout the experiment to avoid exaggerating the level of interference.

2.3 Model Test Technique

Tests were performed with both the Small Strut and Large Strut mounted to an overhead support frame. The frame was anchored to the concrete sub floor independent of the rest of the tunnel to provide isolation from vibration. The wheel stings were hinged to mounts on the floor of the test section at their outboard end as discussed in Section 2.2.2. The stings extended from outside the tunnel jet to a position concentric with the axles of the model wheels. A hinge height of 123mm was used for all models with the sting at a different angle to the test section floor for each of the model wheel diameters.

As described in Section 2.1, all wheeled models were mounted to the under floor force balance (described later in Section 2.5.1.2) through the stationary test section floor at their wheels, the only non-wheeled model, the Ahmed model, was mounted with stilts attached to its underside. The models were mounted through a stationary ground to an under floor balance because any struts and stings used to create interference would have to be removed in order to measure a baseline case without intrusion for comparison. This meant that the flow at the under floor would not be the same as it would if a moving ground was used and that the interference effects may be different, but a comparison of this nature gives good insight into the problem.

Because an under floor balance was used it was a requirement that the mock supports approach the models without contact. The configuration for the Notchback left a 1.5mm clearance between the strut base and model roof. For the Hatchback, Ahmed, and Closed Wheel Racer the strut approached the model roof in a fashion similar to that when an internal balance is used (as seen in Figure 1.26), penetrating the model shell into a purpose built cut out leaving a maximum of 3mm clearance gap between the strut and model. The configuration for the Open Wheel Racer was once again typical to the use of an internal force balance leaving the strut sitting in the open air of the driver cockpit. For all wheeled models a 2mm gap was left between the wheels face and sting end. The Ahmed model had the stings placed at a realistic front and rear axle location for a common passenger vehicle, not at the x-position of the mounting stilts, and left the same 2mm gap between the model surface and sting end.

In order to obtain comparative force and moment results from the strut and sting arrangements an array of 12 configurations were tested for the models at zero yaw. Each of the three overhead strut configurations ('No Strut', 'Small Strut', and 'Large Strut') were tested with each of the four wheel sting configurations (no wheel stings, front wheel stings only, rear wheel stings only, and all four wheel stings), combining for a total of 12 experimental configurations. For each configuration a full set of force and moment coefficients was measured.

Because they were found to be more sensitive to support interference than the other models, the Notchback and Closed Wheel Racer were chosen for further experimentation in the form of wake traversing and surface oil flow visualisation for the array of support configurations. From these further experiments it was then decided to explore interference on the Closed Wheel Racer even further by measuring surface static pressures on both the top and under side of the model.

2.4 Isolated Test Cases and Technique

In terms of an aerofoil shaped support intersecting a model roof there are two known areas of interference that can be expected. The first originates from the creation of separations at the model-support junction, the second from momentum deficiencies in the support wake (as described in Section 1.71). In order to explore the local effects of these phenomena two isolated cases were created and tested in the Durham (Plint) 0.46m x 0.46m closed jet wind tunnel (described later in Section 2.5.1.1).

2.4.1 Model-Strut Junction

To explore the effects at the junction the strut and roof are modelled as an aerofoil perpendicularly intersecting a flat plate. The 2.0mm thick plate had a length of 650mm and a width of 275mm. It was mounted to the force balance at either edge half way along its length. Figure 2.19 shows photographs of the top of the plate as well as the edge with the mounting bracket attached.

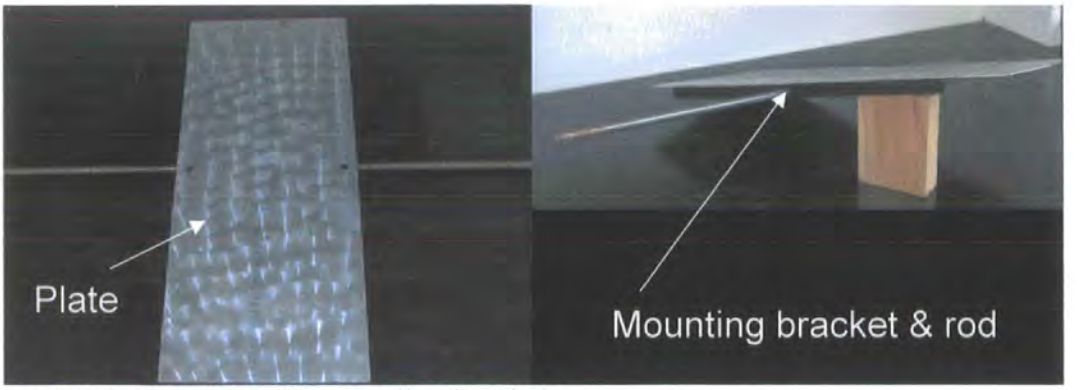

Figure 2.19: Flat plate with mounting brackets.

Two separate aerofoil profiles were used; a 100mm chord NACA 66_4-021 and a 152.4mm chord NACA 0012. Both aerofoils spanned vertically from the plate to a position outside the tunnel where they were securely mounted. A 2.0mm gap was left between the plate and aerofoil base to allow clearance so only the influence of the aerofoil, not the aerodynamic forces were measured on the plate. Tests were performed with the two aerofoils at the centre of the plate width, with the aerofoil leading edge placed at four different positions along the length. Figure 2.20 shows the plate mounted in the wind tunnel with the NACA 0012 aerofoil.

Figure 2.20: Plate mounted in wind tunnel with NACA 0012 aerofoil intersecting.

2.4.2 Strut Wake

To explore the effect that the wake of a vertical overhead support strut may have on the rear wing of a race vehicle, an aerofoil was mounted in the wind tunnel upstream of an isolated rear wing (Figure 2.21). The multi element rear wing, seen in Figure 2.22, was removed from the Open Wheel Race Car model described earlier in Section 2.1 and mounted to the force balance with brackets through its end plates (see Figure 2.23).

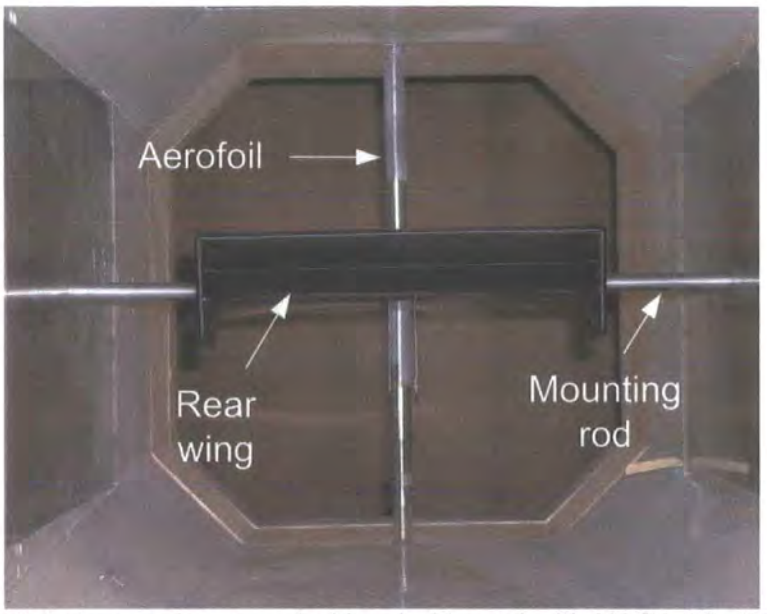

Figure 2.21: Isolated rear wing mounted in wind tunnel with NACA 66_4-021 aerofoil upstream.

Figure 2.22: Rear wing removed from Open Wheeled Race Car.

Figure 2.23: Isolated rear wing with mounting brackets.

Two separate aerofoil profiles were used upstream of the wing to create interference; a 100mm chord NACA 66_4-021 and a 152.4mm chord NACA 0012. The aerofoils spanned the entire vertical height of the test section and mounted to the test section walls upstream at a distance of 500mm matching the distance between the cockpit and wing when in place on the model.

2.5 Experimental Facilities and Instrumentation

2.5.1 Wind Tunnels

2.5.1.1 Durham (Plint) 0.21m^2 Tunnel

The wind tunnel used for the isolated test case experiments was the Plint & Partners TE44 Blower Tunnel [Plint & Partners, 1983] driven by a 36 blade centrifugal fan. The 0.21m^2 tunnel seen in Figure 2.24 is a

closed jet test section with an open return and was operated at a nominal free stream velocity of 20m/s, corresponding to a Reynolds number based on the NACA 66_4-021 aerofoil chord of 8.8 x 10^5. The working test section is 1.22m long with a 0.2m extension for mounting aerofoils upstream as mentioned in Section 2.4.2.

Figure 2.24: Plint & Partners 0.21m^2 closed jet, open return wind tunnel.

2.5.1.1.1 Force Balance

The tunnel uses a three component balance photographed in Figure 2.25 to measure lift, drag, and pitching moment. Models are mounted to the balance by ½ inch diameter stems seen attached to both of the isolated test cases in Figure 2.19 and Figure 2.23. Forces on a model are measured by the reaction of the force plate pulling on one of three wires attached to strain gauge load cells for front lift, rear lift, and drag. The output from each load cell is then taken through an amplifier to a voltmeter. The load cells have a repeatability of 13 counts on lift and drag coefficient based on aerofoil chord area.

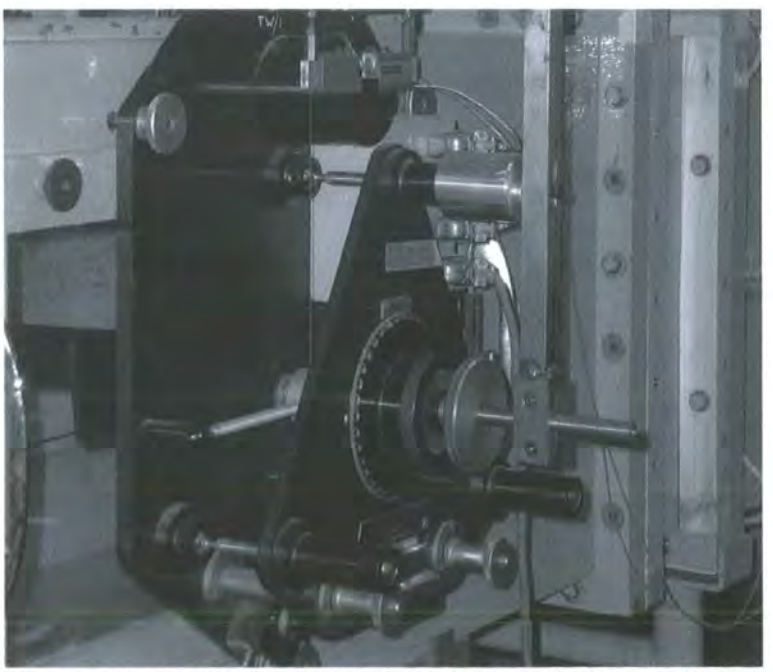

Figure 2.25: Three component force balance for Plint & Partners wind tunnel.

To obtain the strain gauge rates a set of ten voltage readings are taken with and without known weights on the front lift, rear lift, and drag load cells. For each set of ten readings at a given weight an average of the zero and load reading is taken and used in Equation 2.1 to give the strain gauge rate. This can then be

used to find the load on that particular cell. Following the manufacturers advice [Plint & Partners, 1983] the calibration was carried out at weights of 100N and 50N for the lift load cells and 50N and 25N for the drag load cell.

Equation 2.1

$$Rate = \frac{Load(N)}{AvgVoltage(V) - TareVoltage(V)}$$

2.5.1.2 Durham 2m² Tunnel

The wind tunnel used to test the scale ground vehicles was the Durham University 2m² (1.75m x 1.15m) tunnel seen in Figure 2.26. This is a ¾ open jet tunnel and is described in further detail by Sims-Williams & Dominy [2002a,b]. The wind tunnel data was obtained at a nominal free stream velocity of 28m/s, which is achieved after x=100mm, corresponding to a test Reynolds number based on model length of approximately 2.5×10^6. The tunnel was used in fixed ground configuration. Boundary layer removal is performed by suction at the leading edge of the test section with the return injected into the collector.

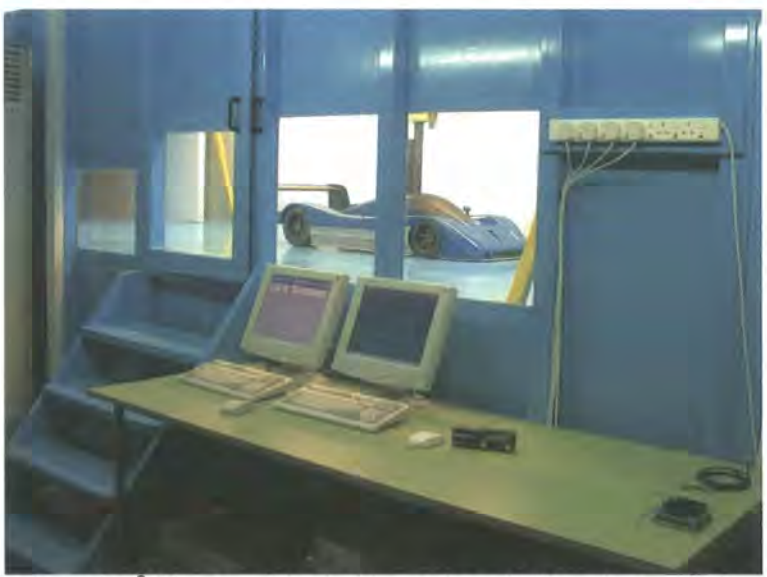

Figure 2.26: Durham 2m² ¾ open jet wind tunnel control centre and observation window.

2.5.1.2.1 Force Balance

Force and Moment measurements are taken through a six component under floor force balance. The balance uses individual strain gauge z-folded load cells (Series 500 QD) and mechanical strain multiplication to achieve a high stiffness without loss of sensitivity. The individual load cells have a quoted accuracy of 0.03% full scale [DSEurope, 2002], which translates to 1 count on C_D. Force and moment measurements were taken at an average of 10 x 2048 samples and a frequency of 800 Hz. This level of data averaging was shown to result in a repeatability of ±2 counts on drag coefficient and ±3 counts on lift coefficient (see Appendix B). The same control model (the Notchback) that was used to discover the levels of repeatability was re-tested at frequent intervals throughout the test programme to confirm the repeatability.

To calibrate, masses were hung from the balance to create known forces on the load cells used to measure the individual forces and moments (Drag, Lift, Side, Yaw, Pitch, and Roll). For each loading arrangement an average of ten load cell voltage outputs were taken from zero load up to a maximum and then from the maximum back down to zero (the increase and then decrease was performed to check for hysteresis). Once the voltages at each load had been read from each of the six load cells, a graph of Voltage (V) vs. Force (N) or Moment (Nm) was created for each of the six forces and moments. An example of the graph created for Drag can be seen in Figure 2.27.

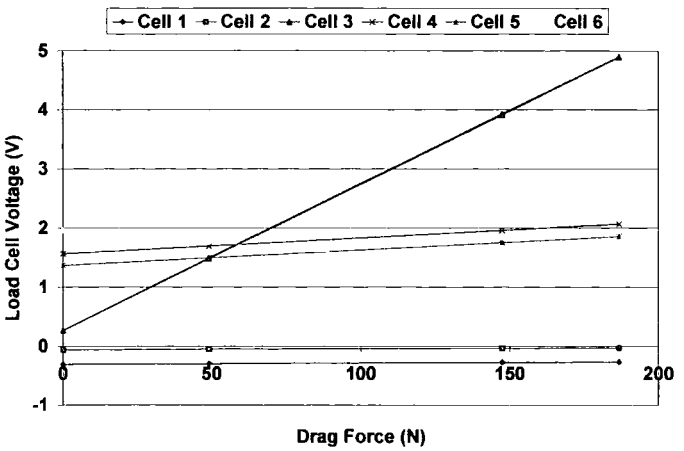

Figure 2.27: Example of load cell calibration graph for calculation of slopes for use in sensitivity matrix.

For each of the six graphs corresponding to the specific force or moment the slopes of the lines were found for each of the six load cells. These 36 slopes (with units of either Volts/N or Volts/Nm) were then put into a 6x6 sensitivity matrix with columns representing a load cell number (1 through 6) and rows representing the force or moment graph they were taken from (Drag, Lift, Side, Yaw, Pitch, and Roll). Equation 2.2 relating voltage to force or moment is:

Equation 2.2

$$\begin{bmatrix} S_{D1} & S_{D2} & S_{D3} & S_{D4} & S_{D5} & S_{D6} \\ S_{L1} & S_{L2} & S_{L3} & S_{L4} & S_{L5} & S_{L6} \\ S_{S1} & S_{S2} & S_{S3} & S_{S4} & S_{S5} & S_{S6} \\ S_{P1} & S_{P2} & S_{P3} & S_{P4} & S_{P5} & S_{P6} \\ S_{Y1} & S_{Y2} & S_{Y3} & S_{Y4} & S_{Y5} & S_{Y6} \\ S_{R1} & S_{R2} & S_{R3} & S_{R4} & S_{R5} & S_{R6} \end{bmatrix} \begin{bmatrix} D \\ L \\ S \\ P \\ Y \\ R \end{bmatrix} = \begin{bmatrix} V_1 \\ V_2 \\ V_3 \\ V_4 \\ V_5 \\ V_6 \end{bmatrix}$$

From Equation 2.2 if we let S equal the sensitivity matrix, FM equal the force and moment matrix, and V equal the voltage matrix:

Equation 2.3

$$S = \begin{bmatrix} S_{D1} & S_{D2} & S_{D3} & S_{D4} & S_{D5} & S_{D6} \\ S_{L1} & S_{L2} & S_{L3} & S_{L4} & S_{L5} & S_{L6} \\ S_{S1} & S_{S2} & S_{S3} & S_{S4} & S_{S5} & S_{S6} \\ S_{P1} & S_{P2} & S_{P3} & S_{P4} & S_{P5} & S_{P6} \\ S_{Y1} & S_{Y2} & S_{Y3} & S_{Y4} & S_{Y5} & S_{Y6} \\ S_{R1} & S_{R2} & S_{R3} & S_{R4} & S_{R5} & S_{R6} \end{bmatrix}$$

Equation 2.4

$$FM = \begin{bmatrix} D \\ L \\ S \\ P \\ Y \\ R \end{bmatrix}$$

Equation 2.5

$$V = \begin{bmatrix} V_1 \\ V_2 \\ V_3 \\ V_4 \\ V_5 \\ V_6 \end{bmatrix}$$

Then the equation can be re-written as:

Equation 2.6

$$[S][FM] = [V]$$

Solving for $[S]^{-1}$ (Calibration Matrix) and multiplying it through the equation yields:

Equation 2.7

$$[S]^{-1}[S][FM] = [V][S]^{-1}$$

Since a matrix multiplied by itself is equal to unity an equation for the forces and moments based on the known slopes and voltage arises:

Equation 2.8

$$[FM] = [V][S]^{-1}$$

The Calibration Matrix is then input into the software used for reading load cell voltages. Together with Equation 2.8 the software can then compute the forces being applied to the load cells.

2.5.2 3-axis Traverse

Pressure and velocity data was measured using a computer controlled three linear axis wake traverse system. The system is capable of traversing 2m in both the stream wise and span wise directions with either a hot-wire or pressure probe. The traverse allowed the probe to be automatically adjusted in the Durham $2m^2$ wind tunnels x, y, and z coordinate system. For the purposes of this project the traverse system was used with a 5-hole pressure probe described in Section 2.5.4.

2.5.3 Pressure Transducers

Pressure data was collected with Sensor Technics series 103LP10D-PCB pressure transducers. These are pressure/vacuum units with a 1.0 to 6.0 Volt output. They have a thermal effect (0-50°C) of ±0.5% full scale and a pressure range of ±1000 Pascal full scale [Sensor Technics, 1994]. The transducers were calibrated periodically using a silicon fluid micromanometer; all sets of transducers were calibrated

simultaneously. A set of five transducers were used to give local flow and reference pressure readings for the 5-hole probe. A set of two transducers were used to read the total and dynamic reference pressures that were used to calculate wind tunnel velocity in the Durham $2m^2$ Tunnel. A single transducer was used to measure static pressures for the surface tappings.

2.5.4 5-Hole Probe

To measure steady, time-averaged, flow structures and observe the sources of some losses in the wake of a model a 5-hole pneumatic probe was used. The 5-hole probe used throughout the course of this work was designed and manufactured at Durham University for specific use in the present work with the 3-axis traverse in the $2m^2$ wind tunnel. The probe, seen in Figure 2.28 and described in Table 2.2, consists of 5 hypodermic tubes assembled to form a forward facing pyramid as described by Dominy & Hodson [Dominy & Hodson, 1992] and shown in Figure 2.29. The probe was specifically designed to be easily interchangeable with the tunnels traverse rig, to maintain the rigs versatility for use with other probes.

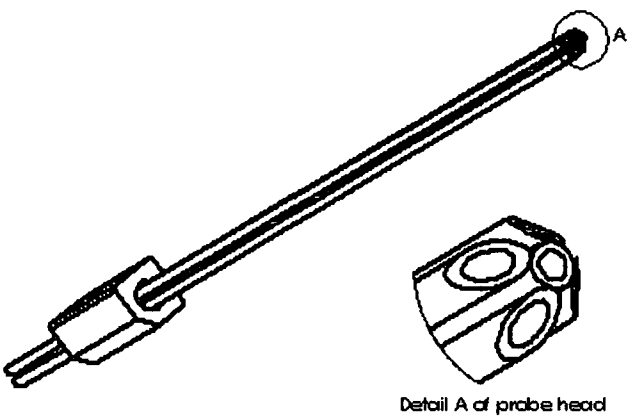

Figure 2.28: 5-hole probe.

	Pitch & Yaw resolution	Calibration speed (m/s)	Head diameter (mm)	Overall Probe Length (mm)	Tube inner diameter (mm)	Tube outer diameter (mm)
5-hole Probe	-44° to +44°	30	3.3	130	1.0	1.1

Table 2.2: 5-hole probe details

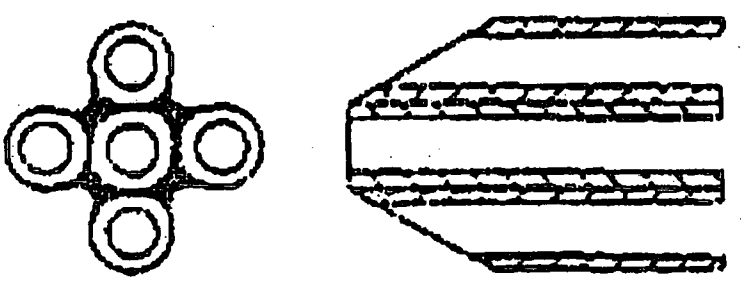

Figure 2.29: 5-hole probe geometry [Dominy & Hodson, 1992]

After the probe geometry and mounting solution were determined, the head of the probe, seen in Figure 2.28, was shaped in order to maximise incidence range. This was done by repeatedly reshaping the head

until an optimum 3 dimensional calibration was achieved. The probe could have been used in a nulled mode, as described by Sims-Williams [Sims-Williams, 2001], which would have been appropriate for the far wake traverses, but the spatial confines of traverses near the model would required that a 3 dimensional calibration be performed [Dominy & Hodson, 1992]. The 5-hole probe was able to capture a suitable range of flow incidences, but could not determine between out of range incidences and areas of reversed flow. To operate at these higher incidences variations of the 5-hole probe such as the 14-hole probe described by Cogotti [Cogotti, 1989] or the 7-hole probe described by Gallington & Sisson [Gallington & Sisson, 1980] can be used, but for the purposes of this experiment the forward facing 5-hole pyramid probe was found to be sufficient.

The probe was calibrated using a computer controlled calibration rig, varying incidence in pitch and yaw in two degree increments at known speed in a small blower tunnel. Tunnel reference speed was determined using a static pressure drop across the nozzle in order to avoid any interference from a Pitot-Static probe and sting. Figure 2.31 to Figure 2.33 show the calibration maps for incidence and total and static pressure coefficients for probe. Maximum repeatability errors of the probe from a comparison of numerous runs at the same tunnel velocity can be found in Table 2.3.

	Pitch (degrees)	Yaw (degrees)	Total pressure (Pa)	Static pressure (Pa)	Dynamic pressure (Pa)
5-hole Probe	0.60	0.59	0.9	0.7	0.8

Table 2.3: Angle and pressure measurement errors from comparison of numerous calibrations at the same wind speed.

The coefficients used to determine flow angle at the probe tip were determined using pressure differences across the tubes numbered in Figure 2.30. The coefficients for yaw, pitch, total pressure, and static pressure are as follows in Equation 2.9 through Equation 2.12.

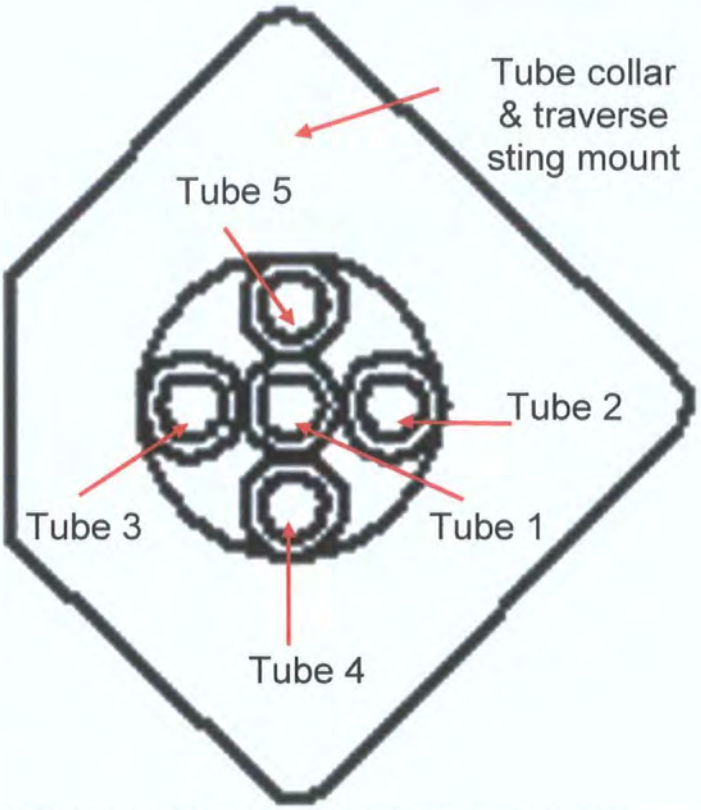

Figure 2.30: Probe head. Looking onto the probe from upstream.

Equation 2.9

$$C_{Pitch} = \frac{P_4 - P_5}{P_1 - P_{avg}}$$

Equation 2.10

$$C_{Yaw} = \frac{P_2 - P_3}{P_1 - P_{avg}}$$

Equation 2.11

$$CP_o = \frac{P_1 - P_{ref}}{P_1 - P_{avg}}$$

Equation 2.12

$$CP = \frac{P_{avg} - P_5}{P_1 - P_{avg}}$$

P_{avg} is the mean of the four pressures from tubes number 2, 3, 4, and 5 (Equation 2.13).

Equation 2.13

$$P_{avg} = \frac{P_2 + P_3 + P_4 + P_5}{4}$$

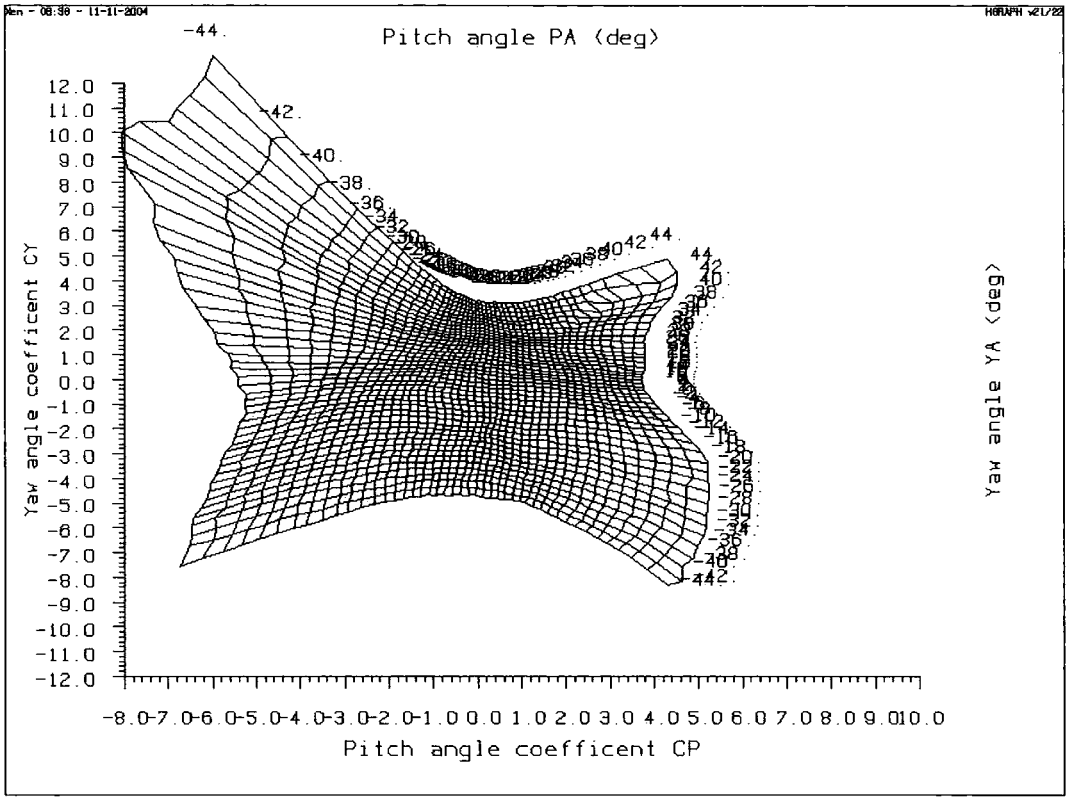

Figure 2.31: Yaw and Pitch incidence range calibration.

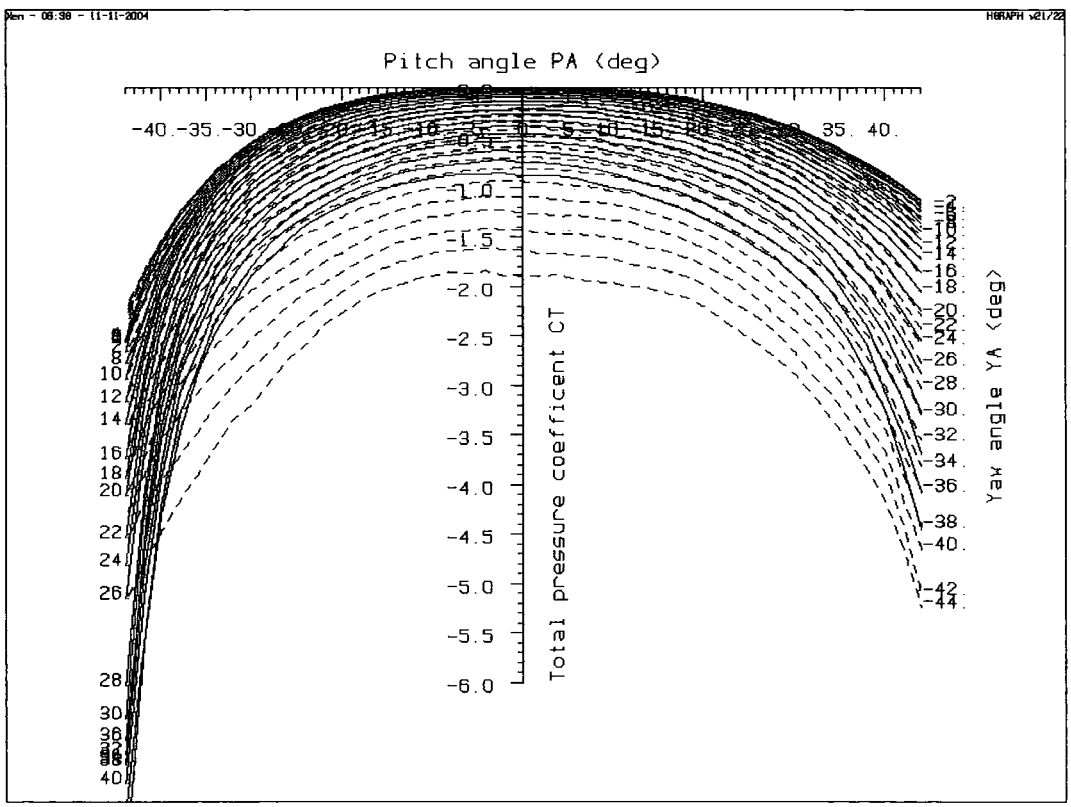

Figure 2.32: Total pressure coefficient calibration.

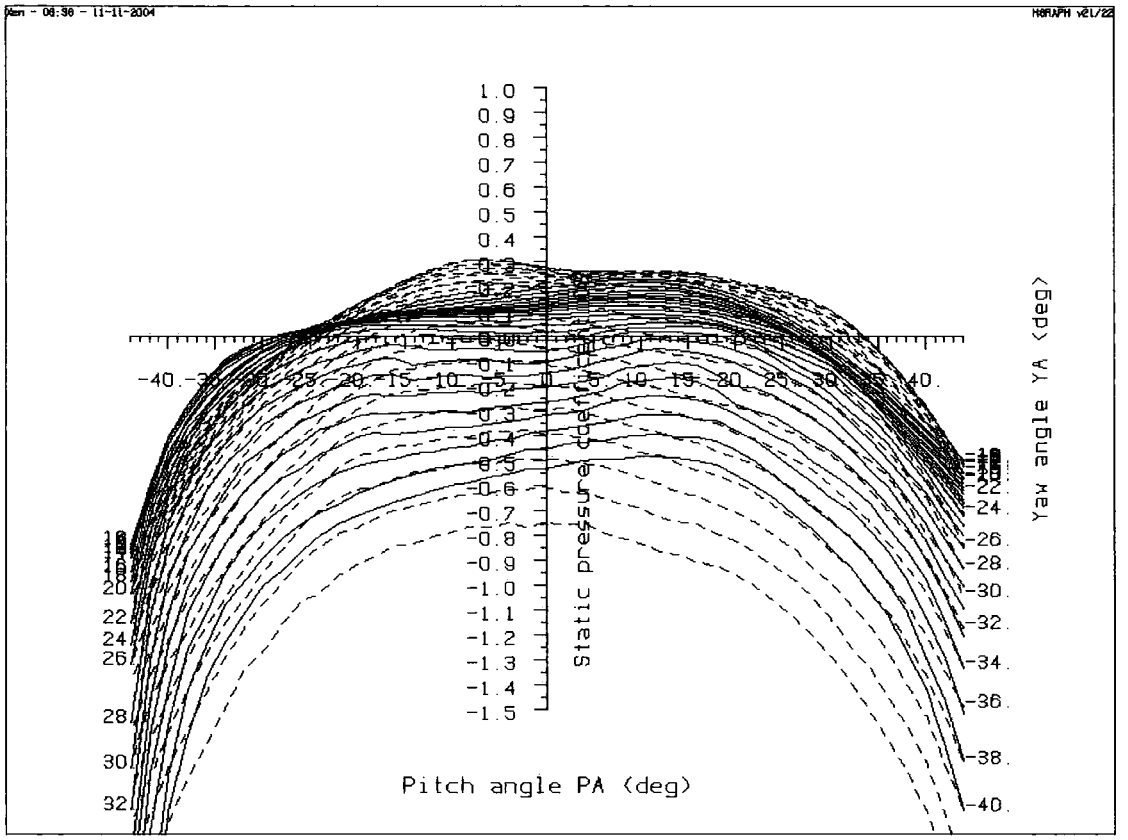

Figure 2.33: Static pressure coefficient calibration.

2.5.5 Surface Static Pressure Measurements

Pressure tappings were drilled on the surface of the model in the desired locations and attached using flexible (1mm inner diameter and 2mm outer diameter) tubing through a Scanivalve, model 48D8-1103, to a central pressure transducer. Usually Scanivalves are supplied and used with their own integrated transducer, however, in this setup a unique blanking plug was placed in the location of the integrated transducer and the tubes were re-routed to one of the Sensor Technics transducers described above. The Scanivalve then steps through the tappings allowing the transducer to take multiple pressure tapping readings in a short period of time. Another advantage of this setup is that it can be contained within the model with minimal tubes and chords exiting the vehicle. For this setup, the Scanivalve signal wire and 12V supply, as well as the pressure transducer reference tube were run through the model wheel well and out of the tunnel working section through the floor at the wheel mount.

2.5.6 Flow Visualisation

The use of on body flow visualisation was employed in the form of a dyed oil to see valuable qualitative information about separation lines and flow direction local to the vehicle surface. The coloured oil used was a mixture of paraffin and fluorescent printing toner. The method employed covered the vehicle surface with the mixture, turned the fans on, and allowed the oil to evaporate, leaving the flow pattern visible in the dye powder. The use of ultraviolet light was also employed in some cases to increase contrast.

2.5.7 Software and Data Collection

Data logging and control was performed using an MS-DOS operating system with a 12-bit Amplicon Win30 card with a 10V range. To control the card for a variety of voltage data collection purposes a compilation of FORTRAN programs were written by Sims-Williams and described in further detail in the DSW Software Manual [Sims-Williams et al., 2000]. A list of the program names and a brief description of their use follows:

ONESHOT – Reports voltages being read on channels 1-8 of the logging card.

LOGBAL6 – Used for taring the force balance, logging load cell voltages, and logging transducer voltages for wind tunnel reference total and dynamic pressures.

SCANIUNS – Used to control the stepping signal for the Scanivalve, logging time-averaged pressure tapping transducer voltages, and logging wind reference total and dynamic pressure transducer voltages.

SUPERLOG – Used for control of the traverse rig with 5-hole probe to log voltages from a bank of 5 pressure transducers used for the probe as well as voltage data to determine wind tunnel reference total and dynamic pressure data.

TRAVTO – Used to move the traverse rig to a desired x, y, & z position.

ZIGZAG – Used to create rectangular grids of a determined spacing for use in Superlog with the traverse rig.

WAKEINT – A data processing program used to plot contributions to drag in a traverse plane.

PLOTCON – A data processing program used to plot pressure contours of readings taken from Superlog.

VECT – A data processing program used to plot velocity vectors of data readings taken from Superlog.

VORT – A data processing program used to plot vorticity of data readings taken from Superlog.

DIFF – A data processing program designed to give the difference between two of the output data files from Superlog.

T5TOTEC – A post processing program that

3 EXPERIMENTAL RESULTS

Undoubtedly the use of struts and stings to support a model over a moving ground plane will alter the airflow around the model. As described in Chapter 2, this is explored using an array of tests comparing the effects on a range of passenger and motor sport ground vehicle models with and without mock overhead support struts and mock wheel support stings over a fixed ground. Measurements of forces and moments, surface pressures, pressures and velocities in the vehicle wake, as well as observations of surface oil flow visualisation are presented for the assortment of model and support configurations.

3.1 DEVELOPMENT OF TEST CONFIGURATION

3.1.1 Interference from Wind Tunnel Components

As part of the support set up it was important to examine any appreciable interference from wind tunnel components used to support the struts and stings from outside the jet. Interference from outboard wind tunnel components will not only add to the interference of struts and stings, but may also interact with them to create secondary effects making the result of the entire support different from a sum of the individual components.

3.1.1.1 Sting Mounts

Section 2.2.2 has already shown that the measured difference between the Type 1 and Type 2 mounting bases when used at the rear wheels with a sting in place, but no overhead support present, was approximately 5 counts on lift coefficient, showing noticeable effects on aerodynamic forces, from small geometric differences. However, this was not an effect from the pair of mounting bases themselves, but rather a change in the effect of the lateral sting pair that was created by the use of the Type 1 mounting bases at the outboard end. Once the configuration had been decided in Section 2.2.2, to see the effects of the mounting bases, tests were performed on the Notchback with the four mounting bases in place, but without the lateral stings attached. The results of these tests show that there is no measurable interference from the mounting bases alone without the stings in place. The increased effect mentioned in Section 2.2.2 is not present until the mounting bases are joined to the lateral stings.

3.1.1.2 Overhead Strut Mounting Base and Stabilising Arms

For moving ground testing models are carried on an overhead strut fastened to a mounting base with stabilising arms seen in Figure 3.1, which is then attached to an overhead steel frame within the wind tunnels plenum to isolate the supports from vibrations. Although no interference was envisaged from these components mounted outside the tunnel jet, tests were performed to report any changes created by their presence. The results in Figure 3.2, show that the mounting base and stabiliser arms do not affect any of the six force and moment coefficients outside of the minimum balance repeatability as they did for the sting mounting bases.

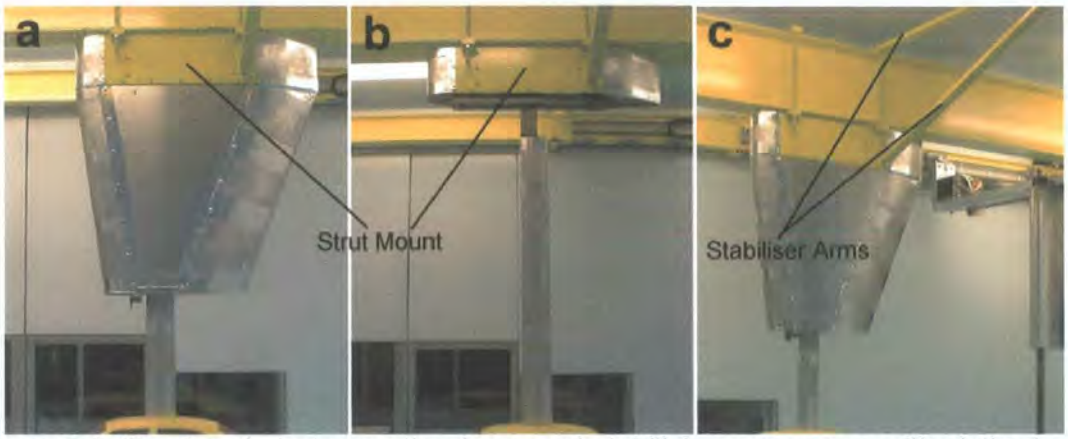

Figure 3.1: Overhead strut mounting base and stabilising arms seen with a) the Large Strut, b) the Small Strut, and c) from an angle with the Large Strut.

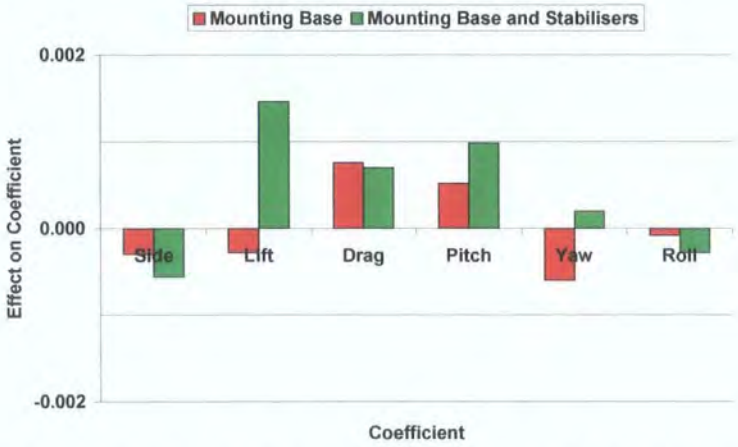

Figure 3.2: Force and moment effects on Notchback model in the presence of the strut mounting base and stabilising arms.

3.1.2 Sting Configurations

In hope of reducing valuable set up time for this project, an investigation into the effects of using just a single pair of wheel stings, either at the front or rear wheels, or at just one side of the model was carried out on the Notchback model. First, tests were performed with a sting pair at only one side of the model and then across the symmetry plane at the other side, and compared to observe the symmetric nature of the sting effects. Next, a sting pair was tested at the front wheels and then at the rear wheels and compared to see if effects would sum to the effect when all four wheel stings were used. The aim was to see if the effects were solely local to junction, reproducing themselves at opposing sides or opposing ends of the model. If so, only a single pair of stings could be used during testing, reducing labour during test preparation and avoiding differences that are present due to the two different mounting base styles (Section 2.2.2).

3.1.2.1 Sting Pairing – Symmetry Plane

Initial tests were performed with stings in isolation and in the presence of the Large Strut. The creation of asymmetric flows by stings placed at only one of the models' four corners or in pairs on only one of the models' sides was found to produce greater effects on drag and lesser effects on lift when compared to the

symmetric case. Therefore, the effects of the stings were not local to the junction, and in order to appropriately measure the interference effects of the stings they had to be used in symmetry; mirroring each other across the vehicle centreline.

3.1.2.2 Sting Pairing – Front and Rear

Subsequent tests were performed with stings in pairs at the front and rear wheels with each of the three overhead strut configurations. The tests compared the effects on both lift and drag coefficient, C_D and C_L of the sum of the two pairs (front and rear) to the measured effects of the two pairs combined (all four stings). In Figure 3.3 through Figure 3.8, the two right most columns for the summed and measured 'All Stings' cases are compared. The differences presented in Figure 3.3 through Figure 3.8 are for each of the wheel sting arrangements relative to the case with no wheel stings and the same overhead strut configuration. The results show that summing the individual effects of the front and rear pairs falls within a magnitude of balance repeatability to that of the measured result for all four stings for both drag and lift coefficient in the presence of all three overhead strut configurations. However, the results of front or rear wheel sting pairs on drag are somewhat ambiguous because they never grow outside of one order of balance repeatability.

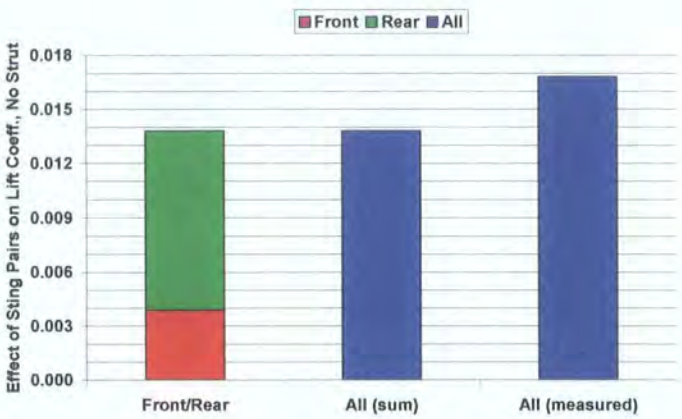

Figure 3.3: Comparison of summed effect from front and rear pairs of stings to measured effect of all stings for lift coefficient without the presence of an overhead strut.

Figure 3.4: Comparison of summed effect from front and rear pairs of stings to measured effect of all stings for lift coefficient when in the presence of the Small Strut.

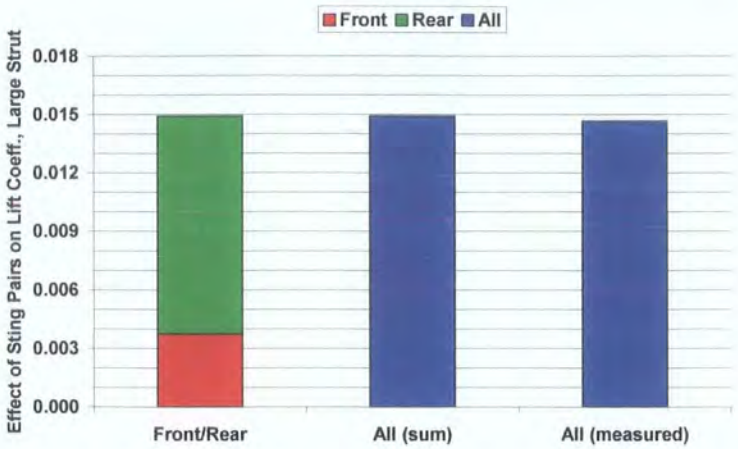

Figure 3.5: Comparison of summed effect from front and rear pairs of stings to measured effect of all stings for lift coefficient in the presence of the Large Strut.

Figure 3.6: Comparison of summed effect from front and rear pairs of stings to measured effect of all stings for drag coefficient without the presence of an overhead strut.

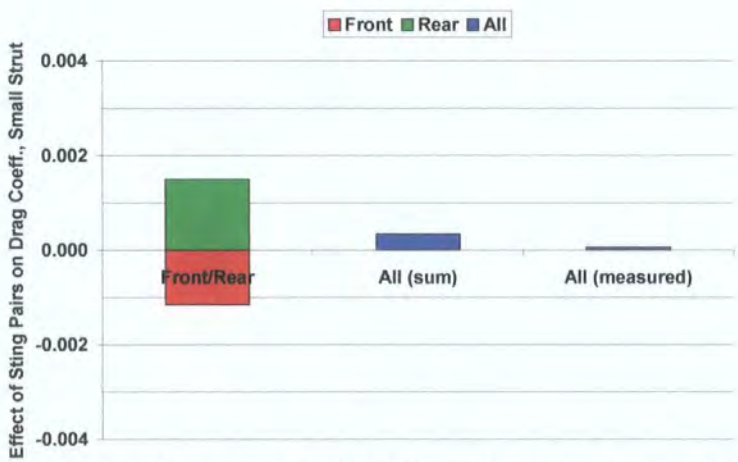

Figure 3.7: Comparison of summed effect from front and rear pairs of stings to measured effect of all stings for drag coefficient in the presence of the Small Strut.

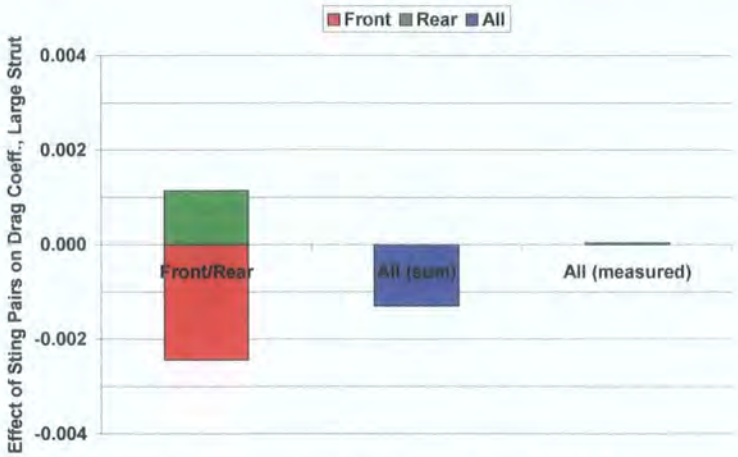

Figure 3.8: Comparison of summed effect from front and rear pairs of stings to measured effect of all stings for drag coefficient in the presence of the Large Strut.

Although the effects of Front and Rear Stings can be added to arrive at the total effect in most cases, they do not each produce equal amounts of the effect. Further observation of Figure 3.3 through Figure 3.5 reveals that placement of a pair of stings at the rear location will always produce a greater effect on lift than placing a pair at the front. Interference tests throughout the project are therefore performed with sting pairs at both the front and rear wheels.

3.1.3 Strut Clearance above Model Roof

When testing with a moving ground and utilising an internal force balance attached to an overhead strut, the strut must penetrate the model shell without contact to attach to the force balance. Fouling of the model shell on the strut would result in an unrealistic transmission of forces between the two, which would then be reflected in the force measurement. In the configuration used throughout this investigation, the use of mock supports that do not actually support the model also required that the strut not touch the model, however, because an external force balance was used, it was not always practical for the support to penetrate the model. In these instances the strut approached the model from above leaving a gap between its base and the model roof. The amount of clearance required above the model to allow for movement due to the aerodynamic lift common to passenger vehicles was investigated by measuring the variation of forces for the Notchback model for different clearances between the base of the Large Strut and model roof. A plot of C_D and C_L versus gap height can be seen in Figure 3.9.

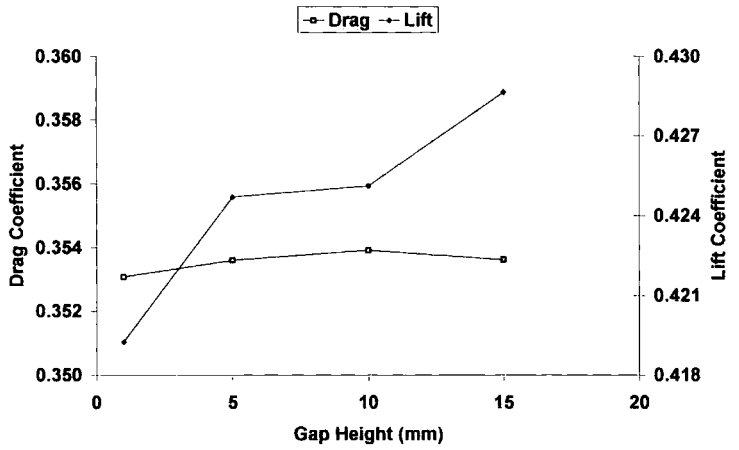

Figure 3.9: Variation of lift and drag coefficient with distance between Large Strut and Notchback roof.

The data shows that C_D does not vary outside of repeatability across the range of gap heights used; however, C_L varies by almost 12 counts over a height change of 15.0mm showing a definite effect caused by the increasing gap between the strut and model roof. In order to keep the mock support test configuration close to that of a rolling road's overhead support configuration and the idealised model of an aerofoil intersecting a flat plate, the smallest possible gap height that does not restrict model movement should be used. Observing the data, it is seen that the largest step occurs for the first 5.0mm gap clearance, but is then non-reactive for the next 5.0mm step. The expectation would be that the gap would cause little change up to a critical height where there would be a sudden impact, which would then fade with further height change. The trend seen in Figure 3.9 leads to a suspicion that perhaps the model is restricted at the lowest gap height of 1.0mm, which then creates a lower lift and the larger jump in C_L between the first two data points. Examining the gap height near 1.0mm in the wind tunnel with the fans turned on using a feeler gauge to test for any collision of the model and strut proves that the model does lift due to the aerodynamic force and intersect the strut for a gap of 1.5mm (measured without any aerodynamic loading), leading to the conclusion that the model was restricted by the support at a gap of 1.0mm and at least a 1.5mm gap must be used to keep the model and strut from colliding during testing. Therefore, at most a gap of approximately 1.5mm was left between the strut base and model roof during interference testing.

This was, however, a test specific to the unique approach of the strut to the Notchback model and cannot be a rule of thumb for mock support testing. As for the other models used in this investigation, the strut approach was different; for these models the strut either sat in an open cockpit (Open Wheel Racer), or penetrated the vehicles outer shell leaving a gap around the strut, but not beneath it (Hatchback, Ahmed, Closed Wheel Racer). Since there was very little lateral movement of the vehicle and the force balance was stiffer in the stream wise direction, movement of the model was minimal in these directions, and no intersection of the model and strut was found. This type of strut approach is analogous to that used in rolling road testing, and was appropriate for the simulation

3.2 BLUFF BODY

To understand the effects that intrusive supports would have on the some of the key separations around a basic vehicle configuration, the well known Ahmed geometry was tested with the array of strut and sting configurations. Without any interfering supports the Ahmed model's [Ahmed, 1984] drag and lift coefficients for a range of backlight angles can be found in Table 3.1. In Figure 3.10, comparing data to experiments performed by Ahmed [Ahmed et al., 1984] shows that the critical backlight angle is found at 27.5 degrees.

	C_D	C_L	C_{LF}	C_{LR}
0°	0.287	-0.103	0.145	-0.248
12.5°	0.265	0.151	0.075	0.076
25°	0.302	0.402	0.026	0.376
27.5°	0.369	0.418	0.023	0.395
30°	0.296	0.063	0.087	-0.024
32.5°	0.296	0.044	0.090	-0.046

Table 3.1: Drag and lift coefficient data for Ahmed model without any interfering supports.

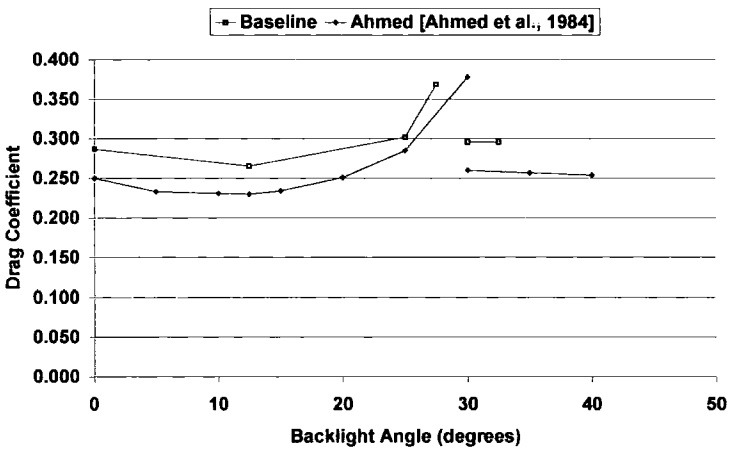

Figure 3.10: Published Ahmed data compared to experimental Ahmed data.

Observing the effects on C_D from the different interfering support configurations in Figure 3.11, the change in drag across the different backlight angles is small from all support configurations. The most interesting effect is the change in critical backlight angle of the model for the most intrusive case with the Large Strut & All Stings. For this support configuration, interference from the supports has allowed the backlight flow to maintain in a high drag state until a backlight angle of 30 degrees.

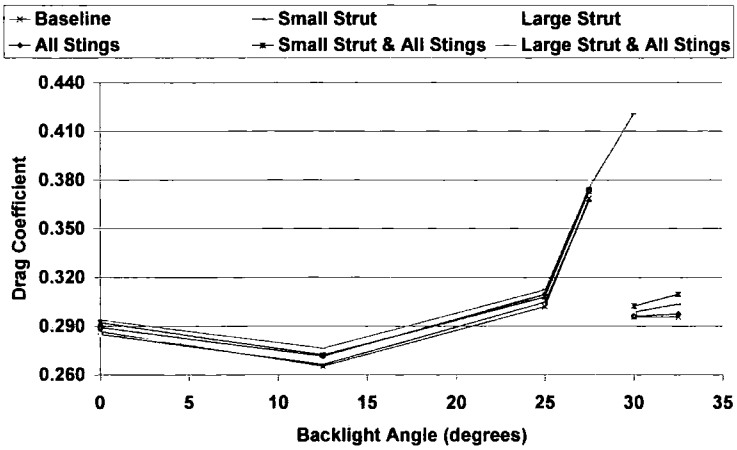

Figure 3.11: Comparison of drag coefficient for all support configurations to baseline across the range of backlight angles.

Figure 3.12 and Figure 3.13 show the effects on C_D and C_L, respectively, from the different support configurations for the range of backlight angles relative to the baseline case. Overall the effects on C_D are at most approximately 10 counts with the exception of the spike in data shown at 30 degrees due to the alteration in critical angle created by the Large Strut & All Stings where the change is 125 counts. At all backlight angles there is an increase in drag created by the interfering supports. The only decreases come from the struts at 0 and then again at 27.5 degrees; however, the magnitude of these changes is small and not outside of repeatability. At backlight angles of 15 degrees and less the effect on drag increases with growing physical intrusion from the supports on the models flow field. Therefore, the most physically intrusive configuration of the Large Strut & All Stings creates the largest effect on C_D (ranging from 7 to 11 counts) and the least intrusive configuration with the Small Strut creates no effect. Between this maximum and minimum, the effects from the Large Strut, All Stings, and the Small Strut & All Stings gradually increase by approximately 2-3 counts.

Between 20 and 27.5 degrees this trend in the drag data disappears. Instead the noticeable effect at this range of backlight angles is the growing influence of the large overhead strut. At 25 degrees, the two support configurations incorporating the Large Strut have the greatest effect when compared to the other support methods and at the critical 27.5 degree backlight angle the Large Strut alone is more influential than the other support methods by approximately 6 counts. This change of influence seen from the Large Strut shows the sensitivity of the models over body and backlight flow at these backlight angles.

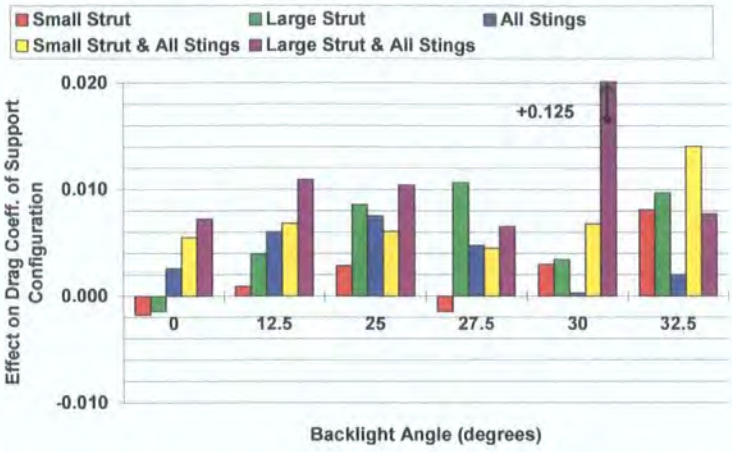

Figure 3.12: Effect on drag coefficient of the different support configurations for all backlight angles.

Observing the lift effects graph in Figure 3.13 across the range of backlight angles, support configurations using the wheel stings consistently reduce the amount of lift in a range of 40 to 80 counts. The struts on the other hand tend to increase lift. Prior to the critical angle the Small Strut has only a small effect on C_L, sometimes negligible. At backlight angles less than 15 degrees there is again a dependable trend in the effects as there was in the previous drag results. As mentioned the Small Strut creates the lowest magnitude of an effect, followed by the Large Strut, the Large Strut & All Stings, All Stings, and surprisingly the Small Strut & All Sting configuration creates the largest effect. Gauging by the drag result, it would be expected to see the Large Strut & All Stings configuration creating the largest effect; however, it now creates the least effect from those configurations that incorporate the stings. Although the stings in general, reduce lift, combining them with the lift-increasing Large Strut has an adverse consequence reducing the overall magnitude.

This trend is maintained for backlight angles between 20 and 27.5 degrees. At the critical backlight angle the influence of the large overhead strut is once again emphasised as the two configurations using the Large Strut increase in magnitude by approximately 20 to 30 counts. Once again there is a large spike in the data (372 counts) from the alteration of the flow and change of critical backlight angle created by the Large Strut & All Stings at 30 degrees. The Small Strut, which does not produce much of an effect at small backlight angles, creates a real and alternating effect beyond 27.5 degrees. These results once again show the sensitivity of the over body and backlight flow at larger backlight angles close to the critical value.

Figure 3.13: Effect on lift coefficient of the different support configurations for all backlight angles.

For all support types there is an increase in drag, the use of the struts typically increases lift, while the configurations using the stings always decrease lift. Looking at the data in Figure 3.12 and Figure 3.13, the effects of the individual support components do not sum and add to the effects of the components when used in combination, showing a definite interaction between the struts and stings for the Ahmed Bluff Body.

3.3 Passenger Vehicles

3.3.1 Aerodynamic Forces of Passenger Vehicles

The Hatchback model has a C_D 0.335 and C_L of 0.333 while the Notchback model has C_D of 0.326 and C_L of 0.411 in the absence of any supports. The high lift of the Notchback occurs largely at the front (C_{LF} = 0.293,Table 3.2), covering the cooling flow inlet to the engine bay shows that this is due to a high flow rate through the empty engine compartment. No significant aerodynamic interaction was envisaged between the support struts and the engine bay flow. Table 3.2 shows measured data for the passenger vehicle models above the fixed ground with and without intruding supports.

Baseline	C_D	C_L	C_{LF}	C_{LR}	**Small Strut & Front Stings**	C_D	C_L	C_{LF}	C_{LR}
Notchback	0.326	0.411	0.293	0.118	*Notchback*	0.000	0.003	0.005	-0.002
Hatchback w/deflector	0.335	0.333	0.052	0.281	*Hatchback w/deflector*	0.001	-0.003	-0.015	-0.018
Hatchback no deflector	0.348	0.451	0.084	0.367	*Hatchback no deflector*	0.004	-0.019	-0.014	-0.005
Small Strut	C_D	C_L	C_{LF}	C_{LR}	**Small Strut & Rear Stings**	C_D	C_L	C_{LF}	C_{LR}
Notchback	0.002	0.001	0.001	0.000	*Notchback*	0.003	0.010	0.006	0.004
Hatchback w/deflector	0.006	0.022	0.008	0.015	*Hatchback w/deflector*	0.015	0.039	0.022	0.017
Hatchback no deflector	0.003	0.002	0.002	0.000	*Hatchback no deflector*	0.010	0.013	0.016	-0.003
Large Strut	C_D	C_L	C_{LF}	C_{LR}	**Large Strut & Front Stings**	C_D	C_L	C_{LF}	C_{LR}
Notchback	0.004	0.016	0.001	0.015	*Notchback*	0.002	0.019	0.007	0.012
Hatchback w/deflector	0.025	0.093	0.026	0.067	*Hatchback w/deflector*	N/A	N/A	N/A	N/A
Hatchback no deflector	0.007	0.033	0.011	0.021	*Hatchback no deflector*	N/A	N/A	N/A	N/A
Front Stings	C_D	C_L	C_{LF}	C_{LR}	**Large Strut & Rear Stings**	C_D	C_L	C_{LF}	C_{LR}
Notchback	-0.002	0.004	0.006	-0.002	*Notchback*	0.005	0.027	0.005	0.022
Hatchback w/deflector	0.000	-0.028	-0.017	-0.011	*Hatchback w/deflector*	N/A	N/A	N/A	N/A
Hatchback no deflector	0.002	-0.022	-0.014	-0.008	*Hatchback no deflector*	N/A	N/A	N/A	N/A
Rear Stings	C_D	C_L	C_{LF}	C_{LR}	**Small Strut & All Stings**	C_D	C_L	C_{LF}	C_{LR}
Notchback	-0.001	0.010	0.003	0.007	*Notchback*	0.002	0.014	0.010	0.004
Hatchback w/deflector	0.011	0.032	0.018	0.013	*Hatchback w/deflector*	0.002	-0.022	-0.020	-0.002
Hatchback no deflector	0.009	0.011	0.015	-0.004	*Hatchback no deflector*	0.001	-0.027	-0.021	-0.007
All Stings	C_D	C_L	C_{LF}	C_{LR}	**Large Strut & All Stings**	C_D	C_L	C_{LF}	C_{LR}
Notchback	0.000	0.017	0.009	0.007	*Notchback*	0.004	0.030	0.010	0.020
Hatchback w/deflector	0.000	-0.028	-0.016	-0.012	*Hatchback w/deflector*	0.020	0.049	0.001	0.048
Hatchback no deflector	0.003	-0.023	-0.017	-0.006	*Hatchback no deflector*	0.008	0.004	-0.009	0.013

Table 3.2: Drag and lift coefficient data with and without interfering support configurations for passenger vehicles.

Figure 3.14 shows effects on C_D, relative to a baseline case without any interfering support, of the overhead struts, all the lateral stings, and different combinations. The most apparent observation is that C_D increases for all models, especially for the configurations including the Large Strut. When compared to the Notchback, the effect on C_D is always greater for the Hatchback model, with and without the rear deflector, but for both passenger vehicles, drag is only affected by the struts, not the stings. When the two are combined, the effect is not much different than with the strut alone, providing proof that there is little interaction between the two types of support for these passenger vehicle types.

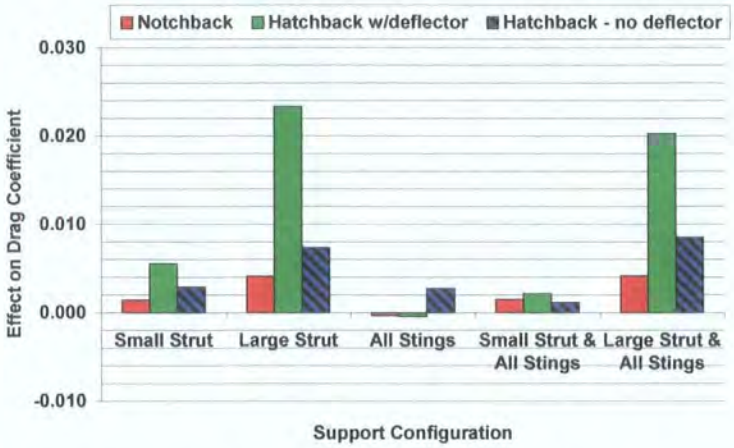

Figure 3.14: Effect on drag coefficient of support configurations for passenger vehicles.

Figure 3.15 shows effects on C_L, relative to baseline for the different support configurations. From these effects the most noticeable is that C_L increases with the use of the Large Strut, and can either decrease or increase, depending on model type with the use of All Stings. The effects are once again more severe for the Hatchback with the exception of the small effect felt from the Large Strut & All Stings for the Hatchback with no deflector. Also notable for the Hatchback, is that the stings cause a decrease in lift, which persists even in combination with the less influential Small Strut. Another noticeable effect common to both vehicles is that for most of the cases the individual effects of the struts and stings can be summed to give the combined effect of the supports when used together. This shows that there is a limited amount of interaction between the two support types for passenger vehicles.

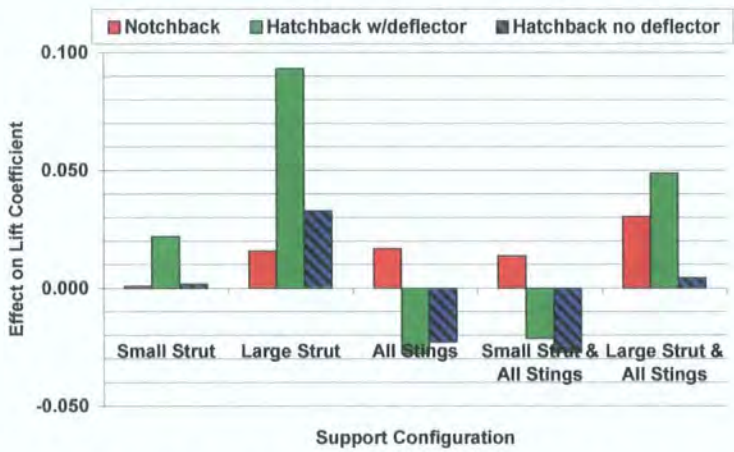

Figure 3.15: Effect on lift coefficient of support configurations for passenger vehicles.

Figure 3.16 shows the effect on C_D of the overhead supports for each of four wheel sting configurations on the Notchback. Differences are presented for each of the wheel sting arrangements relative to the case with the same wheel sting arrangement without the overhead strut. The trend is similar within each wheel sting configuration; adding the more intrusive Large Strut consistently increases C_D. The presence of the Small Strut typically increases C_D by 2 counts, while the Large Strut increases C_D by 4 counts or more.

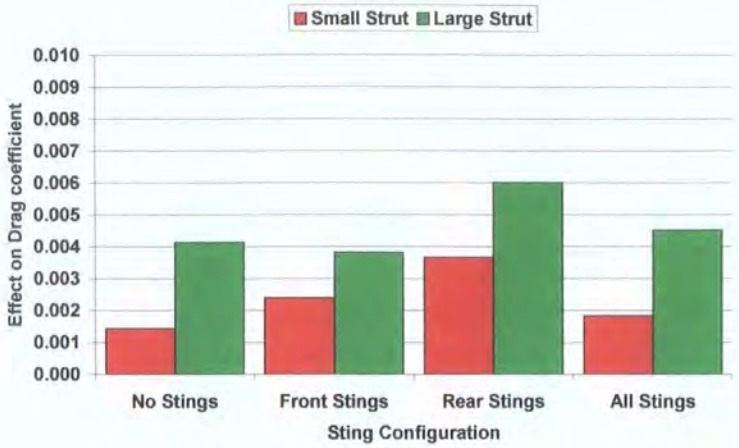

Figure 3.16: Effect on drag coefficient of the overhead struts for the Notchback model.

Figure 3.17 shows the effect of the overhead supports on C_L. Differences are presented for each of the wheel sting arrangements relative to the case with the same wheel sting arrangement without the overhead strut. The small strut does not appear to have any significant effect, its apparent effect changes sign for different wheel sting configurations and is of comparable magnitude to the balance repeatability. The Large Strut always increases C_L by approximately 15 counts, irrespective of the wheel sting configuration, showing that there is no interaction between the struts and stings. It is proposed that the Large Strut's faired actuator housing and its wake creates a solid blockage which increases the velocity above the model. This lowers C_p on the roof and hence generates lift. Looking at Table 3.2, the lift increase was manifest primarily at the rear of the vehicle, which would support the notion of the actuator housing wake creating a blockage and accelerating flow over the rear of the vehicle.

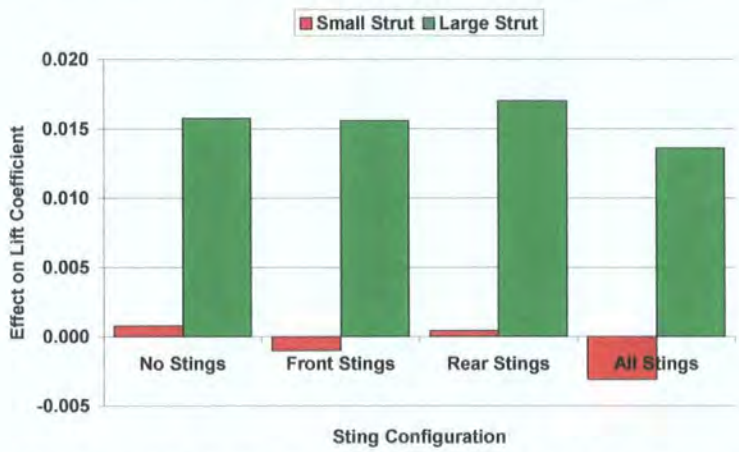

Figure 3.17: Effect on lift coefficient of the overhead strut for the Notchback model

In Figure 3.18 and Figure 3.19 the effects of the struts on C_D and C_L, respectively, are shown relative to the baseline case with the same sting configuration without the strut for the Hatchback model with and without the rear deflector. In both figures the data for the cases with the Large Strut and the individual pairs of Front and Rear Stings was not measured and is not zero as it appears in the charts.

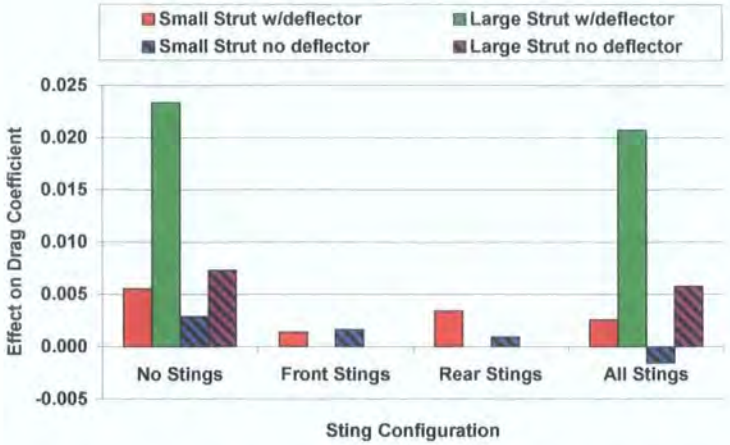

Figure 3.18: Effect on drag coefficient of the overhead struts for the Hatchback model.

In Figure 3.18 it is seen that for both Hatchback model configurations the Large Strut has a consistently greater effect on C_D than the Small Strut. The Small Strut only has a significant effect when there are no stings used and the deflector is in place. In the presence of the sting configurations, the effect of the Small Strut is positive, but then switches sign when All Stings are used without the rear deflector. Comparing the effects of the Large Strut with and without All Stings, the change in C_D for both Hatchback configurations are of the same sign and similar magnitude, generally increasing C_D by 23 counts, the majority of which is witnessed at the rear of the vehicle (Table 3.2). Comparing the models' two configurations; the struts have a greater effect on the model when the deflector is in place (further effects of both struts and stings in the presence of the deflector will be shown later in detail).

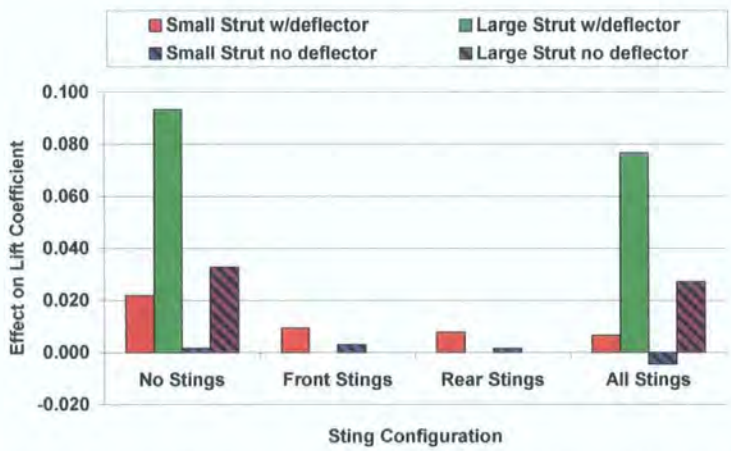

Figure 3.19: Effect on lift coefficient of the overhead struts for the Hatchback model.

Figure 3.19, showing changes on C_L due to the struts, re-enforces the trends of the Large Strut seen on C_D; the Large Strut consistently creates the expected greater effect over the Small Strut. Also, once again the Small Strut only has a significant effect on the model without stings when the deflector is used and the almost negligible effect of the Small Strut still changes sign when in the presence of All Stings as it did for C_D. This suggests that although the effects of the Small Strut in the presence of any of the three sting configurations is similar to the quoted balance repeatability, there is actually an effect taking place that does indeed change sign when All Stings are used. Once again, the effects of the Large Strut are greater for the Hatchback with the deflector in place. Unlike the drag results, the effects on C_L of the struts on

both model configurations are now less in the presence of All Stings and are especially noticeable for the Hatchback with the deflector. Looking back to Figure 3.18, this reduced effect of the struts is noticeable, but its reality is difficult to discern because the difference between the two is so close to repeatability.

Figure 3.20 and Figure 3.21 show the effect of the different sting configurations on C_D and C_L, respectively, for the Notchback model relative to a baseline case with the same strut configuration but no stings. For all sting configurations, changes on C_D were small in Figure 3.20, only just exceeding the range of repeatability. The Front Stings result in a drag decrease and in the presence of a strut the Rear Stings result in a drag increase so that the combination of All Stings results in a negligible total change in drag, showing a possible summative nature, suggesting that there is little interaction between Front and Rear Sting.

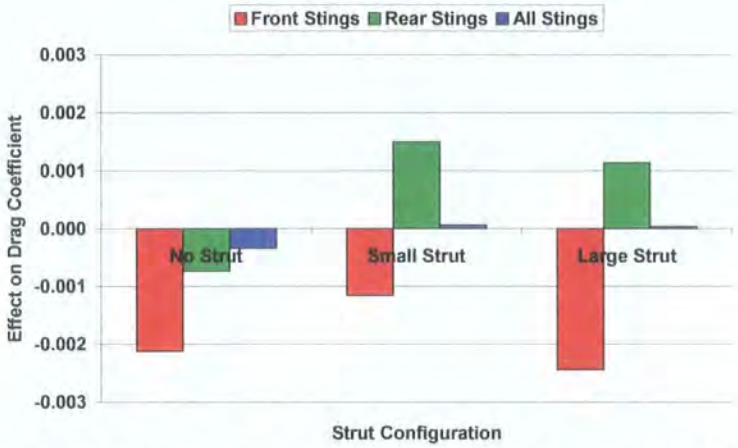

Figure 3.20: Effect on drag coefficient of the lateral stings for the Notchback model.

Figure 3.21 shows the effect of the wheel stings on C_L. While the effect of the Front Stings is relatively small the effect of the Rear Stings is significant, increasing lift by approximately 10 counts. The effect of the Front and Rear Stings, when used alone tends to affect front and rear lift respectively (Table 3.2). Once again, the effect of the Front and Rear Stings appears to sum to the effect of All Stings, suggesting a limited aerodynamic interaction between the two. For C_L, the effects of a given sting configuration, independent of the strut configuration, are similar and do not vary far outside of repeatability, offering further proof to the non-interaction of struts and stings for this model.

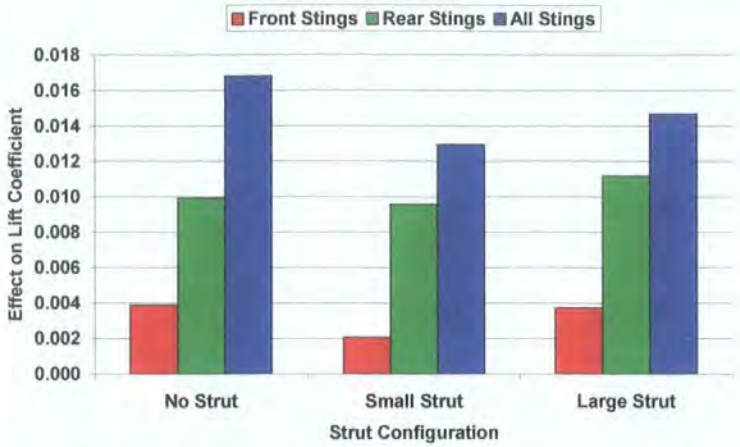

Figure 3.21: Effect on lift coefficient of the lateral stings for the Notchback model.

Figure 3.22 and Figure 3.23 show the same plots as Figure 3.20 and Figure 3.21 of the effects on C_D and C_L for the Hatchback model with and without the rear deflector (as before in Figure 3.18 and Figure 3.19, some data for the Large Strut has been omitted). In Figure 3.22 it is seen that for this model with or without the rear deflector, the Rear Stings create the largest, most significant effect on C_D. The majority of the effects seen from the 'Front Sting' and 'All Sting' configurations are less than repeatability and difficult to discern as real. These configurations do however both create a respectable decrease in drag in the presence of the Small Strut for the Hatchback with the deflector. Without the deflector this effect diminishes to less than repeatability. Worth noting is the reversal in sign of the effect of All Stings for the Hatchback with no deflector in the presence of the Small Strut. Looking at the most noticeable change in drag due to the Rear Stings it can be seen that the effect reduces by 2 counts when the rear deflector is removed. Although, the Rear Stings have a significant effect on drag for all the strut configurations, the effect disappears when they are combined with the Front Stings and the effect of All Stings is not a sum of the two, showing a definite interaction between sting pairs with and without the struts for both Hatchback configurations.

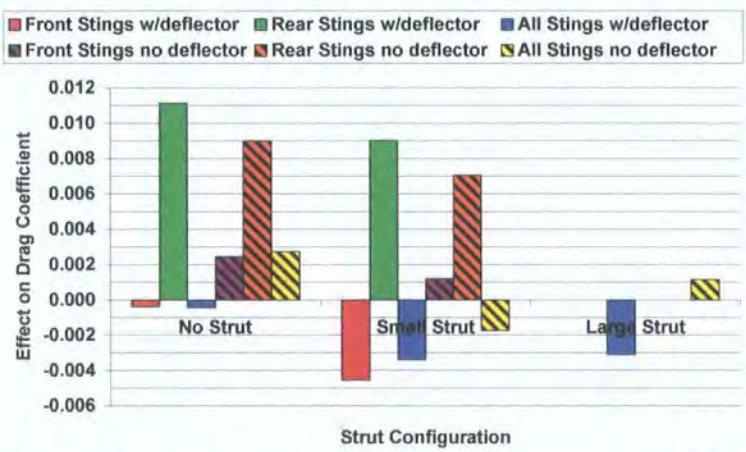

Figure 3.22: Effect on drag coefficient of the lateral stings for the Hatchback model.

Moving to Figure 3.23 the effects of the stings on C_L are much more noticeable than they were for C_D. As in the case of the drag data, the effects of the Front and Rear Stings cannot be collected to create the

effect of the two when combined in the 'All Sting' configuration, proving an interaction. On the other hand, the changes created by the Front Stings and All Stings now register as much more significant.

The Rear Stings increase lift while the Front Sting and All Sting configurations reduce lift and by approximately the same amount. Looking back to Figure 3.22, the same could be said for changes in C_D, however, because the effects were less than repeatability this was ignored, but in fact seems to be real. Unlike the drag results, the effects of all the sting configurations, not just the Rear Stings, reduce in magnitude when the rear deflector is removed, however, the reduction in magnitude of the effect for lift is most easily seen for the Rear Stings. This perhaps provides evidence that the rear stings interact not only with the Front Stings, but also with flow created by the rear deflector. Observing the effects created by the stings across the different strut configurations for lift shows a definite change due to the presence of the struts for the Hatchback with the deflector. This change was noticeable, but not as obvious in earlier figures at a different scale. This shows that there is an interaction of the struts and stings for the Hatchback model when the rear deflector is used.

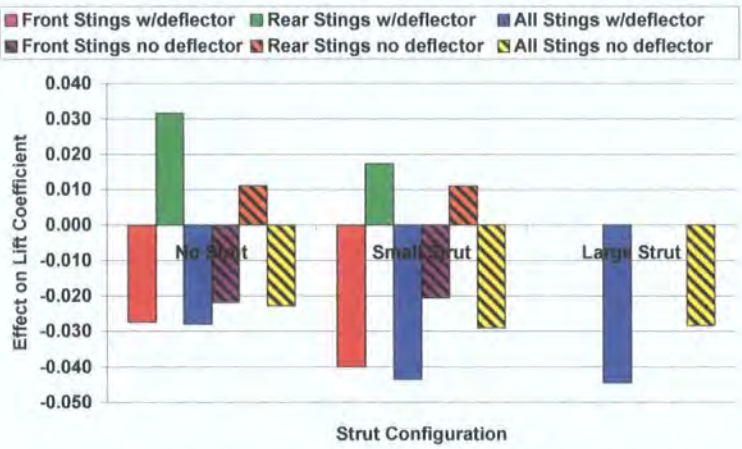

Figure 3.23: Effect on lift coefficient of the lateral stings for the Hatchback model.

Figure 3.24 shows the effect on C_D and C_L of adding the rear deflector when in the presence of the different support configurations. The largest effects created by the use of the deflector are in the baseline configuration; here the deflector causes a decrease of 13 counts on C_D and 118 counts on C_L. As far as support methods are concerned; the next greatest effect is seen in the presence of the struts, specifically the Large Strut. However, in the presence of all the support configurations, except 'All Stings,' the deflector actually increases both drag and lift. Although this effect is only small and just outside of balance repeatability for some of the support methods, it shows that the effect of a shape change (such as the addition of a roof trailing edge deflector) can be different, not only in magnitude, but in sign, in the presence of different support types. In the presence of combinations of struts and stings the effect is a combination of the two, but not a direct sum, showing that there is a definite interaction of the flow from the struts, stings, and rear deflector.

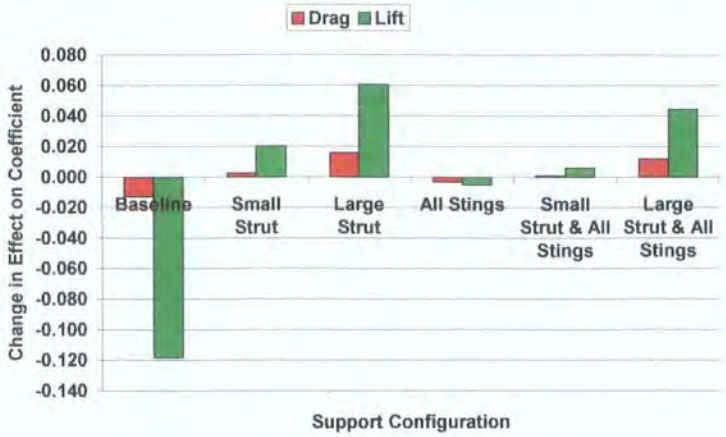

Figure 3.24: Difference between the effects on the hatchback model with and without the rear deflector in the presence of the different support configurations for drag and lift coefficient.

3.3.2 Flow Mechanisms of Passenger Vehicles

To investigate interference effects further and explain some of the underlying mechanisms associated with the changes in force coefficients, flow visualisation and wake traversing was performed for the support configurations with the Large Strut alone and All Stings alone. Figure 3.25 through Figure 3.33 show surface flow visualisations and wake traverses using the 5-hole probe described in Section 2.5.4 performed to identify separation and attachment lines, re-circulating flow regions, and other flow features on the Notchback without interference from the mock supports. In the wake traverse plots, values that were out of the 5-hole probes useful range are shown in white. These areas are largest closer to the vehicle base where the flow exhibits more pitch and yaw and is possibly reversed. Values that are outside of the given scale of the plots are shown in black at the lower end of the scale and in white at the upper end of the scale.

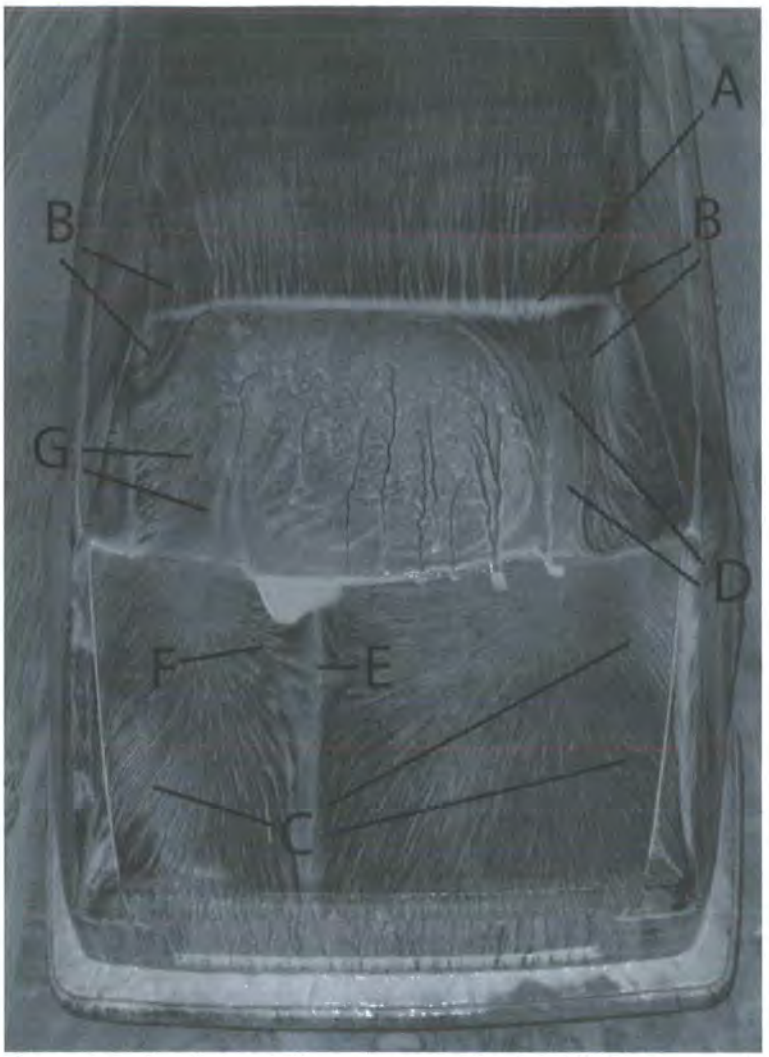

Figure 3.25: Flow visualisation of the asymmetric backlight separation without any interfering supports.

The Notchback wake without any interfering supports demonstrated an asymmetric structure, most obviously seen by the re-attachment of flow at the right side of the roof trailing edge and the off centre saddle point on the boot lid, labelled A and E, respectively, in Figure 3.25. Figure 3.26, Figure 3.28, and Figure 3.30 show CP_o in three planes normal to the direction of flow in the vehicle wake and exemplify the asymmetric imprint left by the vehicle and its time averaged downstream development. Observing the plots of CP_o, the asymmetric imprint left behind by the vehicle does not change drastically as it moves downstream away from the vehicle base. Moving downstream the amount of out of range data, indicating reversed and largely yawed/pitched flow decreases. Also, there is not as much loss behind the vehicle as the wake is mixed with lower loss fluid from the free stream. The overall height of the area of loss and thus the features that create it subtly shift toward the wind tunnel floor. Also present in the images to the sides of the vehicle, pressure loss created by the ground boundary layer on the stationary floor is noticeable.

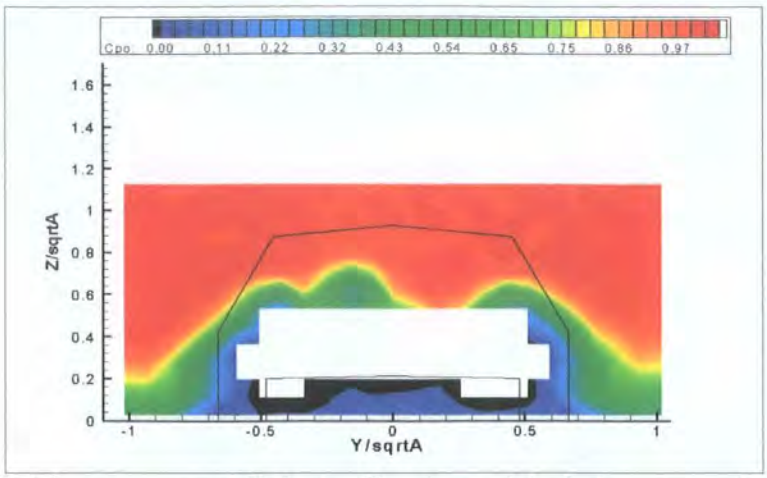

Figure 3.26: Total pressure coefficient without any interfering supports at the vehicle base.

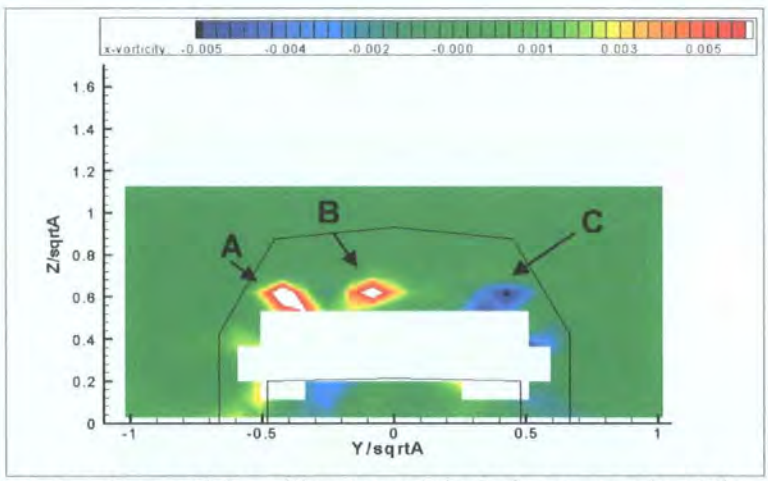

Figure 3.27: Stream wise vorticity without any interfering supports at the vehicle base.

Looking at the vorticity plots at the vehicle base (0mm from the rear bumper) in Figure 3.27, there are three distinct vortices ('A,' 'B,' and 'C') leaving the trunk trailing edge. These vortices are then seen developing in a plane further downstream in Figure 3.29. Already, in this near wake plane (Figure 3.29), the vortices have begun to lose intensity, but have grown in size. By the time they have reached a plane at $1\sqrt{A_F}$ downstream (Figure 3.31) the two outer vortices (labelled 'A' and 'C' in Figure 3.27, Figure 3.29, and Figure 3.31) are still prevalent, but the third, inner vortex (labelled 'B' in Figure 3.27 and Figure 3.29), has begun to dissipate. The two stronger, more symmetric, vortices (A and C in Figure 3.27, Figure 3.29, and Figure 3.31) are generated by flow from the C-pillars and trunk sides similar to a Fastback vehicle. Observing Figure 3.25, proof of this can be seen as the rotation forms over the C-pillars and outside edges of the roof trailing edge (labelled 'B' in Figure 3.25). They can then be witnessed travelling axially along the edges of the trunk (labelled 'C' in Figure 3.25). Judging by the patterns seen in Figure 3.25 and the wake plots of Figure 3.27 the vortices also move in toward the centre plane and down toward the trunk lid before exiting the base plane.

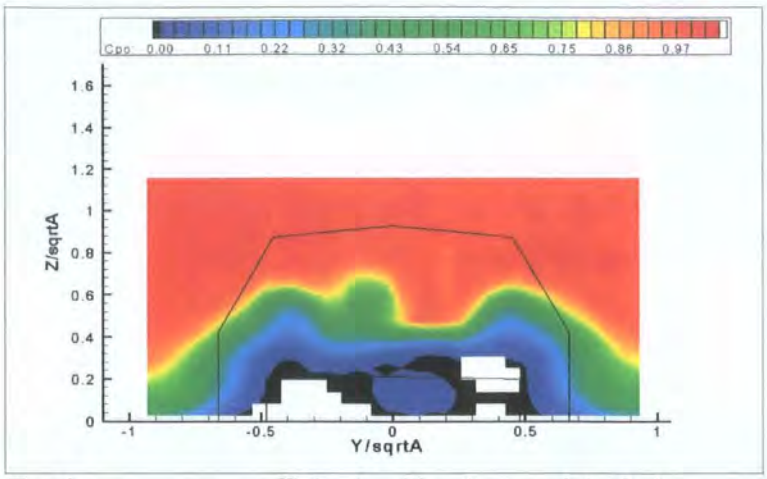

Figure 3.28: Total pressure coefficient without any interfering supports at ½√A_f downstream from the vehicle base.

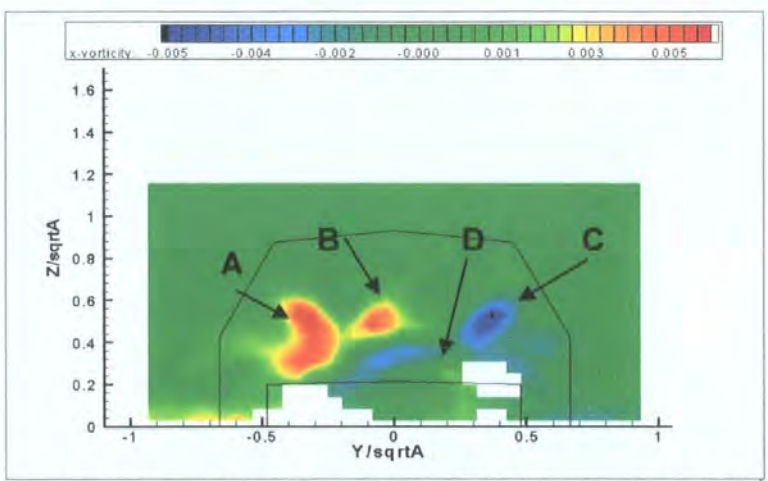

Figure 3.29: Stream wise vorticity without any interfering supports at ½√A_f downstream from the vehicle base.

Observing the time averaged centreline traverse of Figure 3.32, it does not appear that downwash between the C-pillar vortices has forced the shear layer to re-attach to the trunk, at least not at the centre plane. Although it is difficult to discern due to out of range data in this area, it appears that the shear layer extends past the trunk into the wake. Looking back to Figure 3.25, a portion of the flow from the roof has been influenced to re-attach to the backlight just after separation (labelled 'D' in Figure 3.25). This fluid then sweeps down the backlight onto the trunk lid where it is provoked into a third vortex formed at the trunk surface (labelled 'B' in Figure 3.27), counter rotating next to the right side C-pillar vortex at the base of the rear windscreen. After formation, the vortex is bent laterally away from the right side until it intersects the left C-pillar vortex by the time it has reached the trunk trailing edge. As the two vortices intersect they create a saddle point (marked 'E' in Figure 3.25) sending a portion of the flow in the reverse direction to become part of some sort of re-circulation in the separation bubble over the backlight.

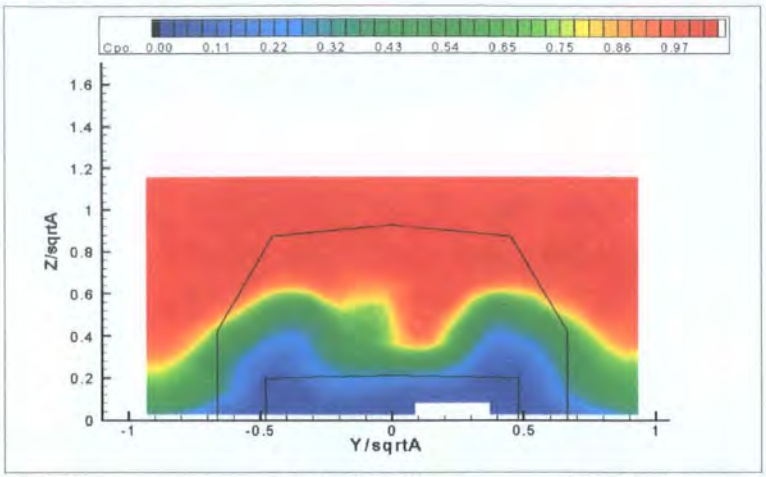

Figure 3.30: Total pressure coefficient without any interfering supports at $1\sqrt{A_f}$ downstream from the vehicle base.

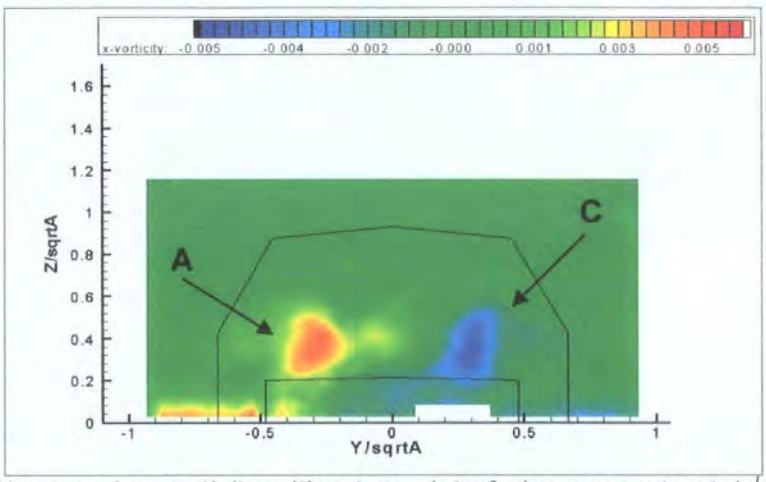

Figure 3.31: Stream wise vorticity without any interfering supports at $1\sqrt{A_f}$ downstream from the vehicle base.

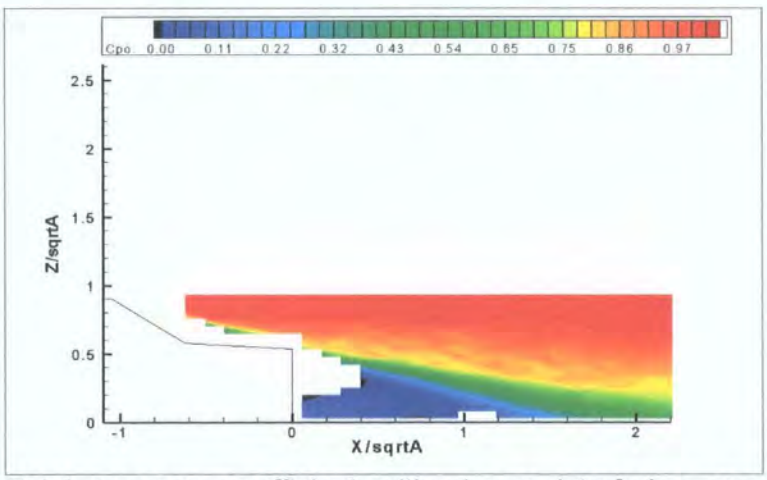

Figure 3.32: Total pressure coefficient without any interfering support along the centreline of the model wake.

Looking at flow visualisations of the vehicle roof in Figure 3.33, the flow coming over the roof and along the side appears to be uniform, not showing any upstream separations or vortices that would influence the re-attachment of fluid on the right side of the rear windscreen. If an equally large portion of flow had re-attached to the backlight at the left side, just as it did on the right, a pair of equally intense vortices inside

the C-pillar vortices would have been created, but in this case the flow coming down the right hand side of the rear windscreen has led to the creation of a stronger trunk vortex on the right than on the left hand side. Looking more closely at the area of flow labelled F in Figure 3.25 counter rotation from the left side trunk vortex is visible. However, this vortex is easily overpowered by the more influential right side trunk vortex and does not appear as strong in the wake traverse planes downstream. The two vortices can be seen in Figure 3.29, one on top of the other between the C-pillar vortices. The stronger influence of the right side trunk vortex has allowed it to move further over to the left side and climb on top of the left side trunk vortex (labelled 'D' in Figure 3.29).

Figure 3.33: Flow visualisations along the vehicle roof from a rear (top left), forward (top right), and side view (bottom) without any interfering supports.

The two inner vortices created on the trunk lid dominate the area over the centre of the trunk. The stronger influence of the right side vortex, due to the larger supply of fluid from the re-attachment of roof flow to the right side of the rear windscreen, has forced the saddle point and vortex seam off centre to the left. After exiting the base plane the weaker left trunk vortex is the first to dissipate and the right side trunk vortex follows dissipating more quickly than the C-pillar vortices. By the time the flow reaches the wake plane at $1\sqrt{A_F}$ in Figure 3.30 and Figure 3.31 the two trunk vortices have become very weak and the C-pillar vortices are the dominant features remaining. Up wash from the stronger, right side trunk vortex near the vehicle base is also the probable reason that the shear layer from the roof centreline did not re-attach to the trunk.

In the presence of the Large Strut the Notchback exhibits an increase in C_D of 4 counts and an increase in C_L of 16 counts (Table 3.2). Observing CP_o at the $\frac{1}{2}\sqrt{A_F}$ plane before and after placement of the Large Strut in Figure 3.28 and Figure 3.34, respectively, it is obvious that the strut creates a more symmetric wake, particularly in the area where losses from the third, trunk vortex were seen in Figure 3.26, Figure 3.28, and Figure 3.30. Plotting the difference of the two cases in Figure 3.35 shows that the strut has created more symmetry by a gain in total pressure at one side of the centre plane and a loss at the other.

There is also an increase in the amount of pressure loss in the wake of the strut, which is the likely cause of the slight increase in drag. Surface flow visualizations with the strut in place (Figure 3.39) compared to the baseline configuration (Figure 3.25), exemplify the increased symmetry created by the presence of the Large Strut, but also show that the decreased velocity behind the strut and strut-model junction has allowed flow from the roof to stay attached to the backlight and that the strut wake has also impinged on the trunk lid at the centreline.

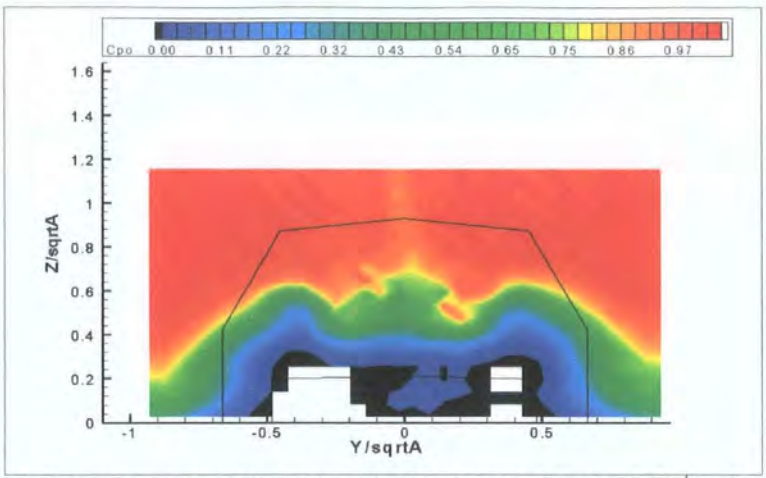

Figure 3.34: Total pressure coefficient with the Large Strut at ½√A_f downstream from the vehicle base.

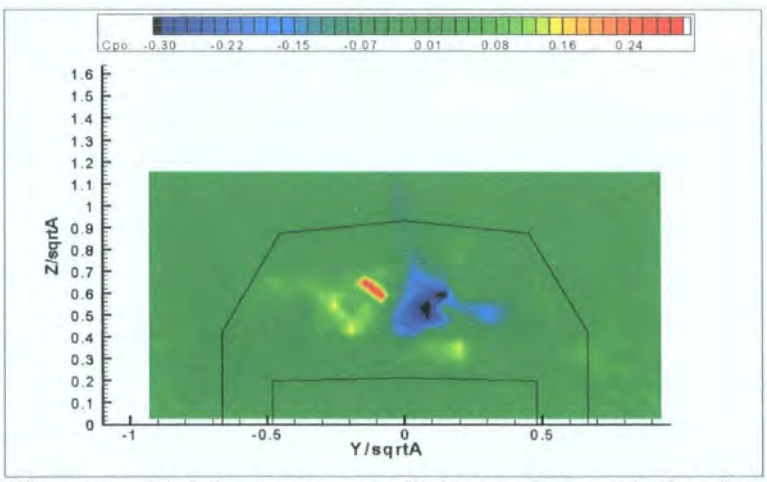

Figure 3.35: Difference of total pressure coefficient before and after the addition of the Large Strut at ½√A_f downstream from the vehicle base.

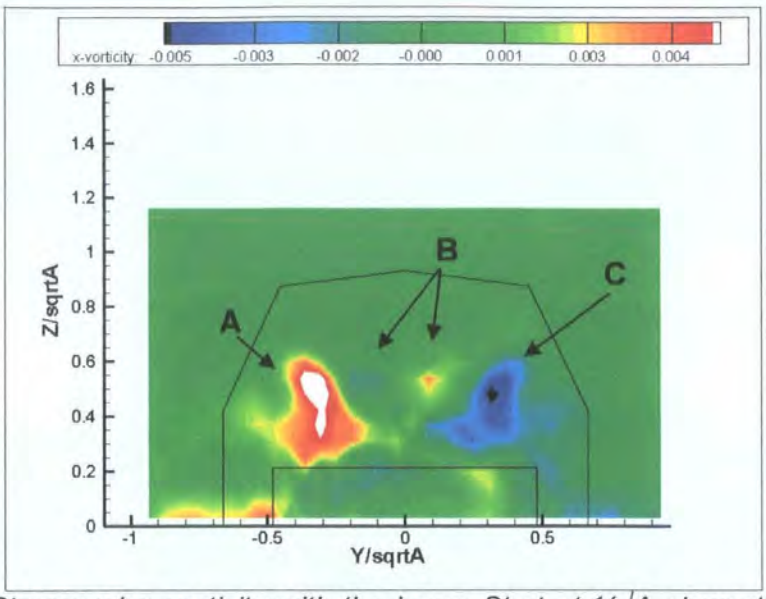

Figure 3.36: Stream wise vorticity with the Large Strut at ½√A_f downstream from the vehicle base.

Looking at Figure 3.36 and Figure 3.38 the trailing vortex system has been altered by the creation of more symmetric flow over the backlight. The two C-pillar vortices ('A' and 'C' in Figure 3.36 and Figure 3.38) are still the most dominant features in the wake. Watching them develop downstream they grow in size, but reduce in intensity, moving toward the ground as they propagate downstream. Because there is not an area of re-attachment on the rear windscreen as there was without any interfering supports, the strong trunk vortex is no longer obvious in the wake traverses.

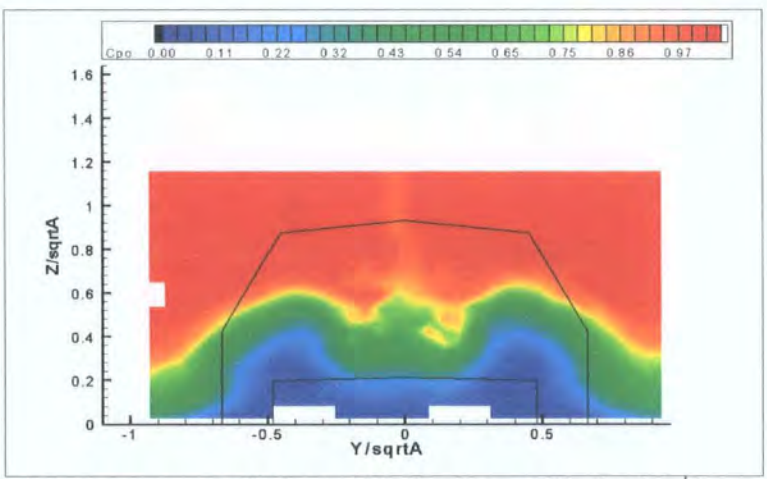

Figure 3.37: Total pressure coefficient with the Large Strut at 1√A_f downstream from the vehicle base.

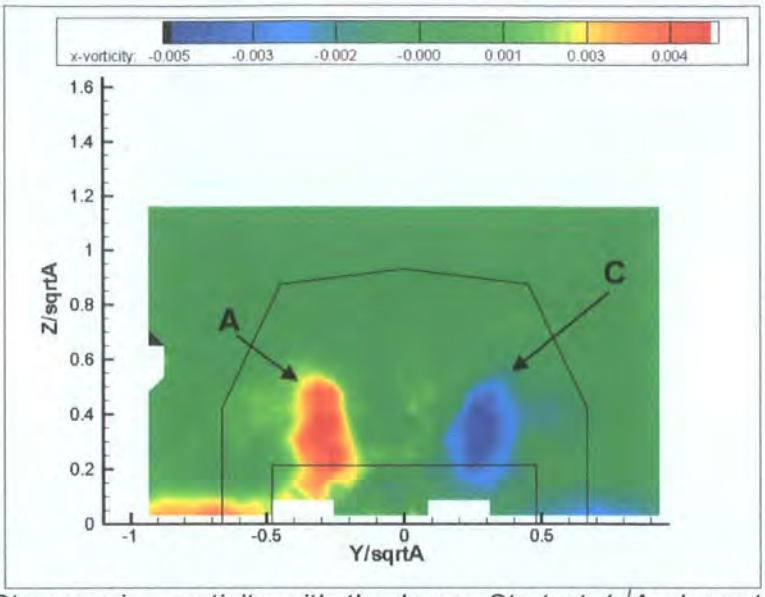

Figure 3.38: Stream wise vorticity with the Large Strut at $1\sqrt{A_f}$ downstream from the vehicle base.

Proof of counter rotation inboard of the C-pillar vortices can be witnessed on the trunk lid in flow visualisations in Figure 3.39 and in vorticity plots $\frac{1}{2}\sqrt{A_F}$ downstream (marked 'B' in Figure 3.36), signifying the existence of a weak pair of trunk vortices. Unlike the baseline case, the symmetric separation from the roof trailing edge has allowed the vortices to form with equal intensities, still both weak relative to the C-pillar vortices. Because they are the same strength neither vortex has forced the other out of the way and they appear next to each other as a pair inside the C-pillar vortices in the wake traverse plot of Figure 3.36. The C-pillar vortices have become more equal in size because the backlight attachment seen before (labelled 'D' in Figure 3.25) is no longer stealing fluid from the right side C-pillar vortex. The wake of the support is now the prevalent feature over the trunk and between the C-pillar vortices above the trunk.

Figure 3.39: Flow visualisation of the backlight separation with the Large Strut.

The effect of All Stings sees no change in C_D and an increase of 17 counts on C_L that is approximately balanced between front and rear axles (Table 3.2), suggesting that the effect is distributed equally over the vehicle. The wake traverse of Figure 3.40 in a plane at $\frac{1}{2}\sqrt{A_F}$ downstream of the vehicle base shows CP_o using All Stings. Comparing the loss in Figure 3.40 to the baseline case without any supports (Figure 3.28) and observing the differences created by the stings at this plane in Figure 3.41, there are small, but equal amounts of increase and decrease, validating the negligible change in drag. Noticeable pressure changes occur behind the model and along the sides of the vehicle, close to the wind tunnel floor, where the sting wakes interfere with the ground boundary layer. The differences of CP_o due to All Stings are on a scale at about half the magnitude of the differences that were witnessed for the Large Strut, showing that the strut has a larger influence in the wake of the vehicle.

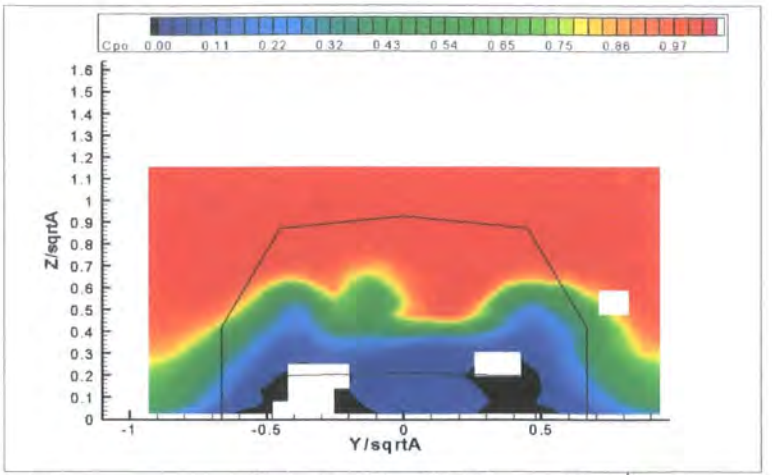

Figure 3.40: Total pressure coefficient with All Stings at ½√A_f downstream from the vehicle base.

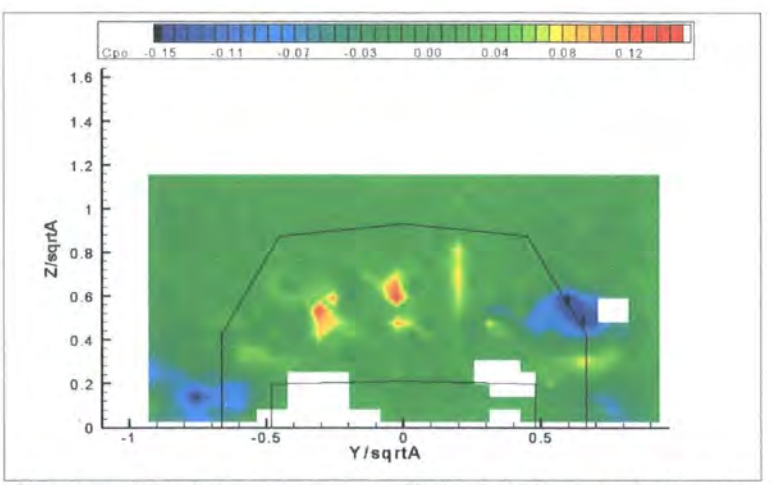

Figure 3.41: Difference of total pressure coefficient before and after the addition of All Stings at ½√A_f downstream from the vehicle base.

Figure 3.42 and Figure 3.44 show little change in the vortices formed at the backlight from the use of the stings. The C-pillar vortices are still the overwhelming features in the wake and the formation of the right side trunk vortex is made stronger by the supply of fluid from the attachment to the rear windscreen at the right side.

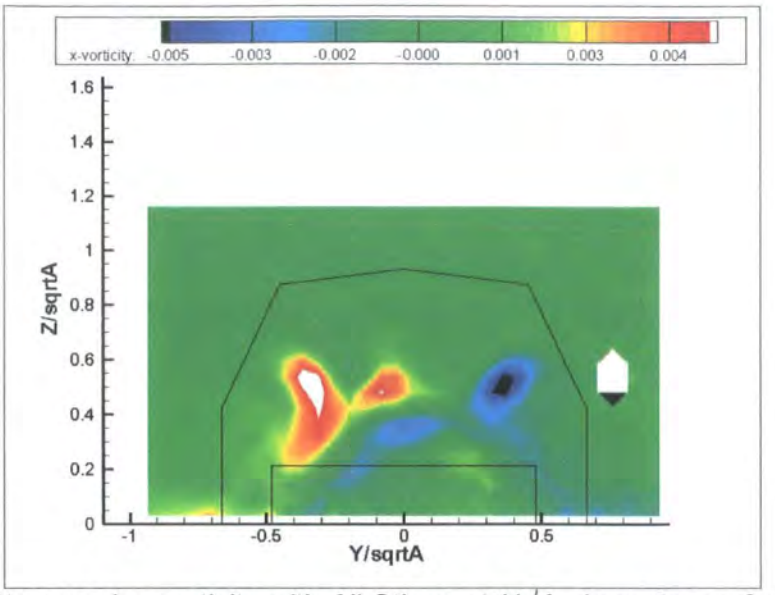

Figure 3.42: Stream wise vorticity with All Stings at ½√A_f downstream from the vehicle base.

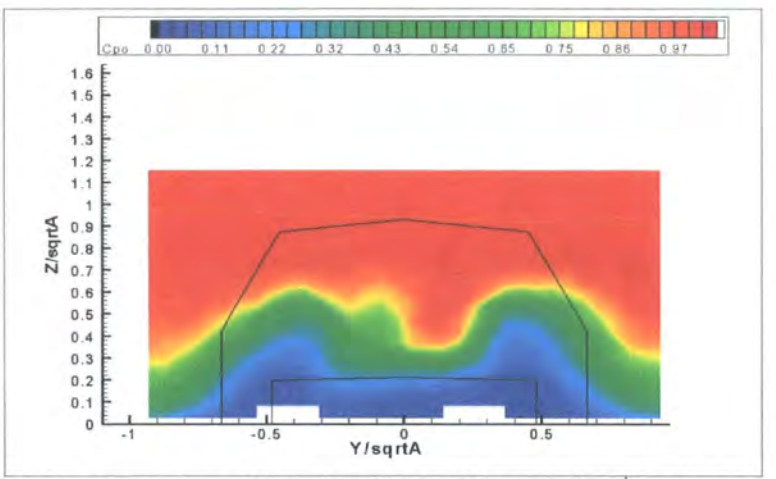

Figure 3.43: Total pressure coefficient with All Stings at 1√A_f downstream from the vehicle base.

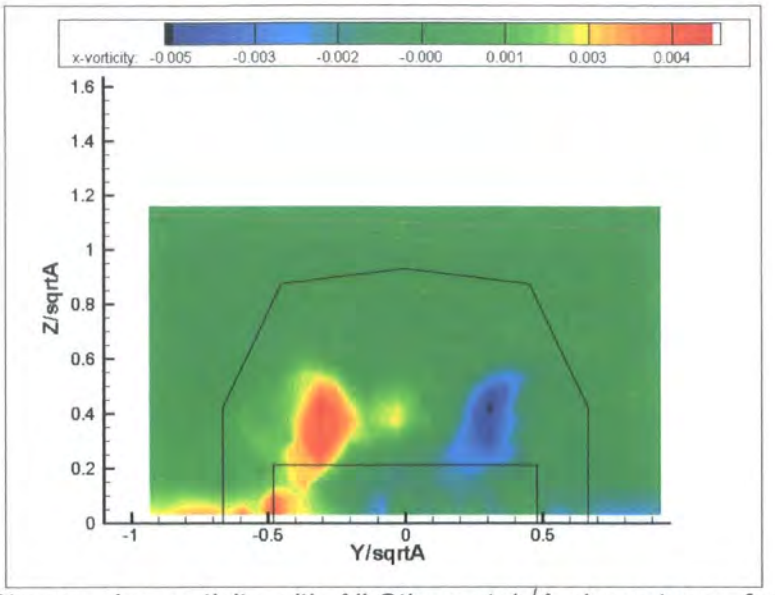

Figure 3.44: Stream wise vorticity with All Stings at $1\sqrt{A_f}$ downstream from the vehicle base.

Figure 3.45 shows the surface flow visualisation of the backlight with placement of the stings. Observing the figure, there is little qualitative change in the flow structure created by the presence of the stings, suggesting that the wheel stings are not altering flow at the top of the vehicle or significantly adding to the vehicle wake and that the change in lift force must be due to an increase in pressure beneath the vehicle, which is concurrent with the changes close to the wind tunnel floor seen in the total pressure change plot of Figure 3.41.

Figure 3.45: Flow visualisation of the backlight separation with All Stings

Figure 3.46, Figure 3.47, and Figure 3.48 show the contributions in the wake to the total drag without any supports, with the Large Strut, and with All Stings, respectively, for the Notchback in the $\frac{1}{2}\sqrt{A_F}$ plane. Although it is difficult to separate the contribution to drag created by the vehicle and the stationary ground, it appears that the majority of the vehicle's drag without any supports is associated with the trailing vortices and the separation bubble behind the trunk. With the supports, the imprint left behind the vehicle has changed slightly, especially in the area behind the Large Strut; however, the areas of maximum contribution to drag appear to be the same.

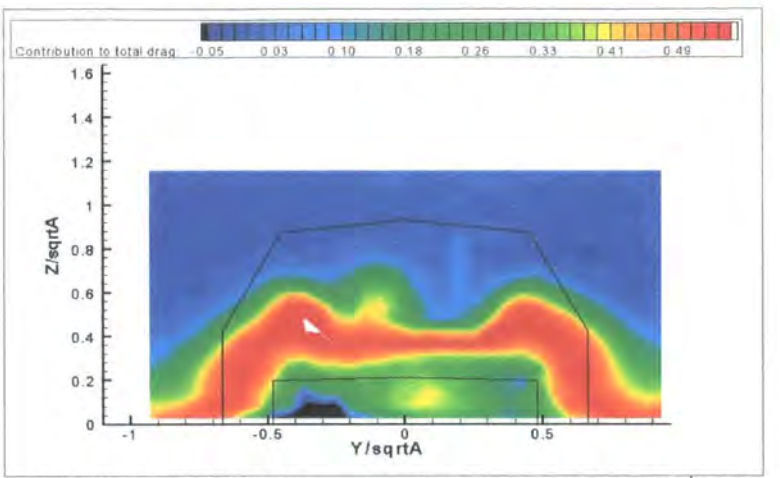

Figure 3.46: Contributions to total drag without any supports at $\frac{1}{2}\sqrt{A_f}$ downstream from the vehicle base.

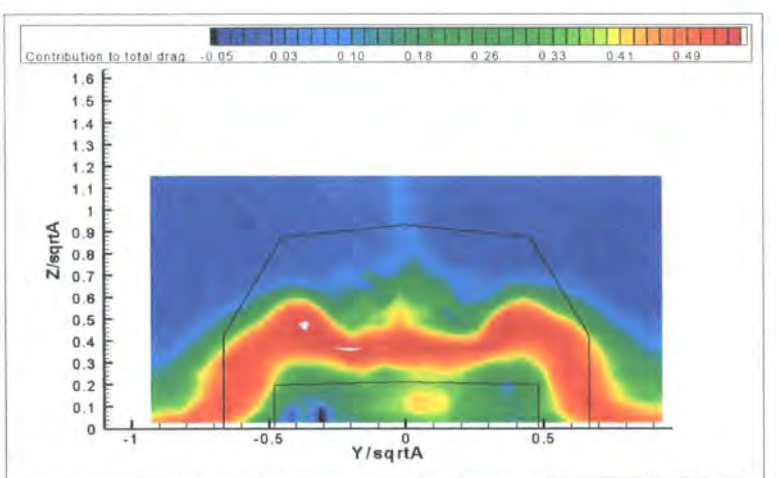

Figure 3.47: Contributions to total drag with the Large Strut at $\frac{1}{2}\sqrt{A_f}$ downstream from the vehicle base.

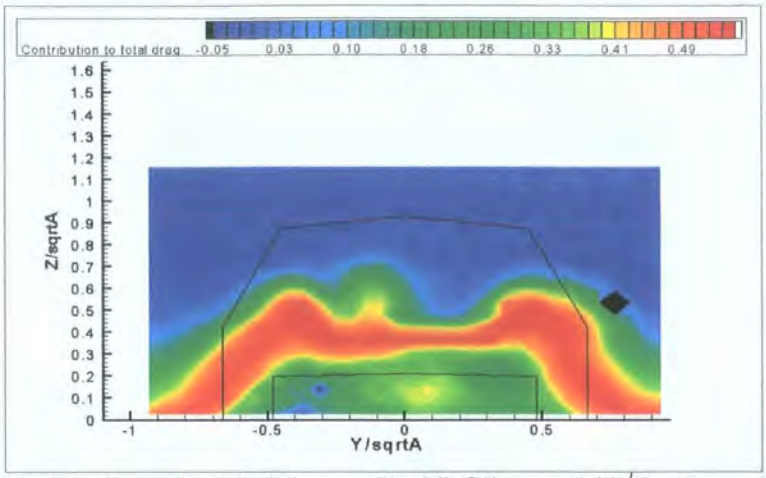

Figure 3.48: Contributions to total drag with All Stings at ½√A_f downstream from the vehicle base.

Looking at the force coefficients in Table 3.2, the overall change in drag due to All Stings is negligible, the change in drag due to the Large Strut is a small 4 counts. Looking at the contributions to drag in Figure 3.49 and Figure 3.50 showing the differences in drag sources for the two support types relative to the baseline case without any supports allows us to ignore the effects of the stationary ground that were present in both plots that the difference was produced from and focus on the drag contribution from the supports alone. Observing Figure 3.50, the changes in the plot due to All Stings are small, and neither of the small positive or negative changes, outweigh the other, confirming the negligible change in C_D. In Figure 3.49 the 4 count increase in C_D due to the Large Strut is created by the strut wake's influence on the C-pillar vortices. The earlier mentioned changes to a more symmetric backlight separation created by the Large Strut have not only affected the intensity and symmetry of the C-pillar vortices, but have also affected the contribution to total drag seen to the sides of the vehicle wake, witnessed in Figure 3.49.

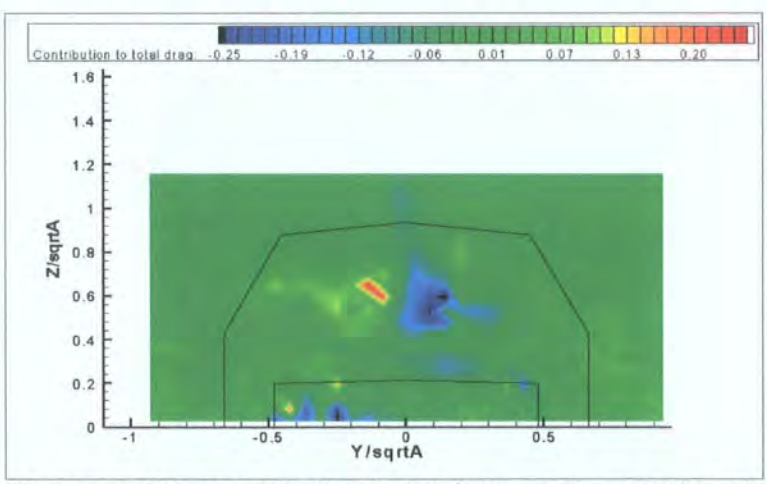

Figure 3.49: Difference of the contribution to total drag with and without the Large Strut at ½√A_f downstream from the vehicle base.

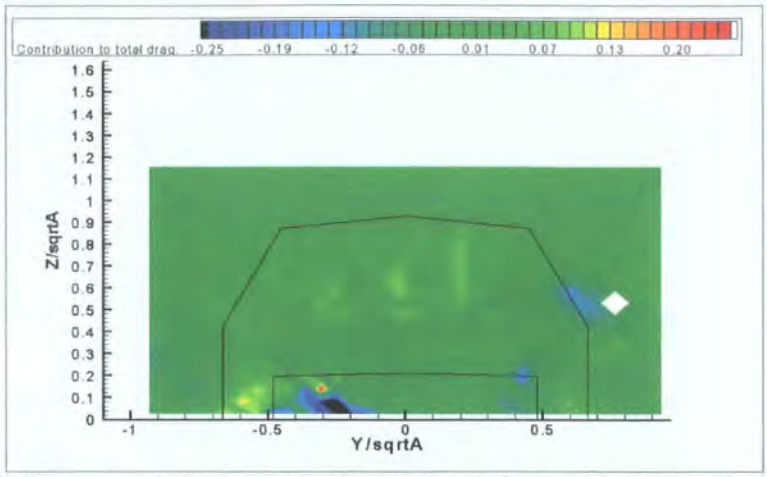

Figure 3.50: Difference of the contribution to total drag with and without All Stings at ½√A_f downstream from the vehicle base.

3.4 Motor Sport Vehicles

3.4.1 Aerodynamic Forces of Motor Sport Vehicles

Aerodynamic forces were taken from both the Open and Closed Wheel Racer models without any interfering support at different rear wing incidences. The sweep of rear wing incidences was then performed in the presence of the different support configurations to see the effects. For each model the wings incidence is defined as the angle between a line tangent to the nose and trailing edge and a line parallel to the direction of flow (see Figure 3.51). The aim was to see if racing car rear wings, which are usually already close to stall, would be forced into a stall by the presence of an intruding support.

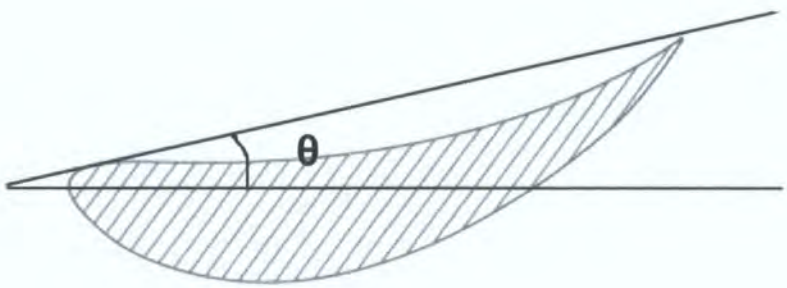

Figure 3.51: Rear wing incidence.

Figure 3.52 through Figure 3.57 show the results from the rear wing sweeps on lift and drag for the two models. For the generic Open Wheel Racer (OWR) comparison of the rear wing sweeps with and without supports shows that they are similar, having almost no noticeable effect on C_D and only altering the magnitude, not the shape of the curve for C_L. The drag increases gradually with an increased incidence, while C_L decreases. Interfering with the flow by the use of the Large Strut with or without the stings

causes the largest increase in C_L (loss of down force) by about 50 counts. Other support configurations alter C_L, but not by as much, and at smaller wing incidences, all differences created by the supports seem to diminish towards zero, offering some proof that it is interference with the wing that is the important effect taking place.

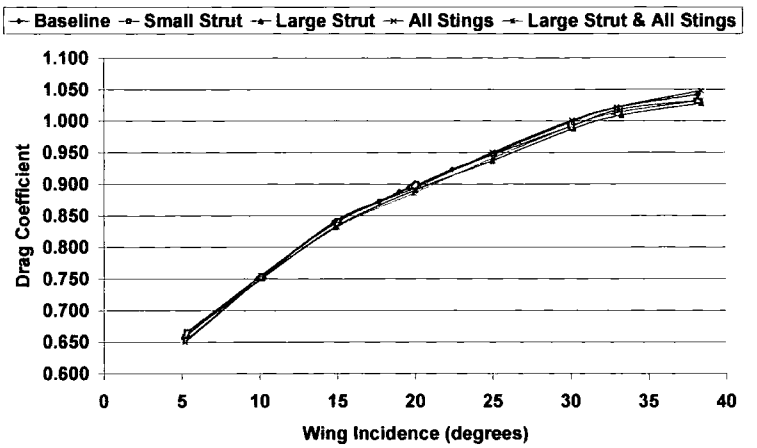

Figure 3.52: Drag coefficient for the Open Wheel Racer for different rear wing incidences in the presence of the different support configurations.

Looking at the change in lift over the different rear wing incidences in Figure 3.53, the wing did not immediately stall. For inviscid flow C_L would be linear, the first sign of non-linear behaviour in the plot starts at 15 degrees, but arguably there is a more abrupt change from linear behaviour indicating a gradual stall at about 30 degrees. The rear wing angle of 30 degrees was therefore used for extended testing of the model and was the chosen angle from which force measurements were taken to compare to other models. This general stall behaviour remains the same for all the curves despite the use of an interfering support.

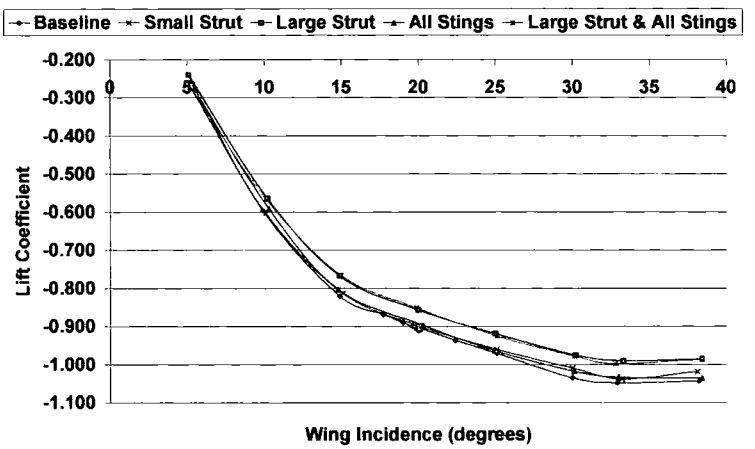

Figure 3.53: Lift coefficient for the Open Wheel Racer for different rear wing incidences in the presence of the different support configurations.

The Closed Wheel Prototype Racer (CWR) had a multi element adjustable rear wing. Both the upper and lower elements were adjustable through a range of angles. To see the effects on lift and drag for the different lower element incidences (Figure 3.54 and Figure 3.56, respectively), the upper element was used at a middle of its range incidence of 10.0 degrees. Taking a quick glance ahead to Figure 3.56, the lift stops reducing at 18 degrees when the lower element is adjusted. This will be used as the effective

stall angle of the lower element and used to sweep through the upper element incidences. For the lower element range of incidences for all the support configurations the shapes of the graphs in Figure 3.54 and Figure 3.56 are similar, the graphs are simply shifted according to the effect of the interfering object. Despite the configuration, C_D does not deviate by more than ±10 counts from the baseline.

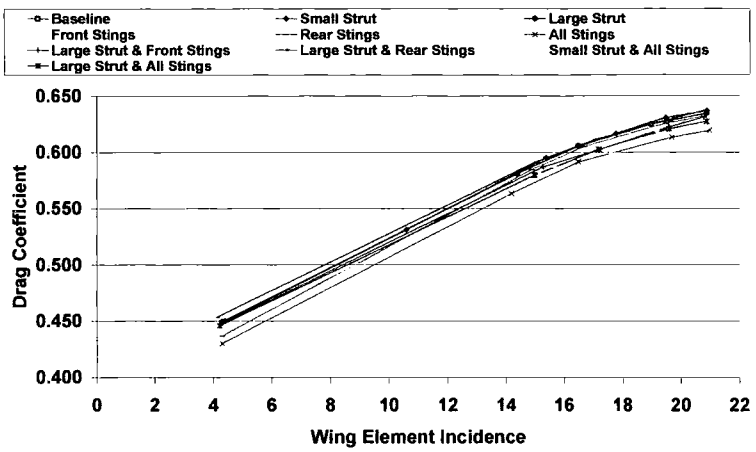

Figure 3.54: Drag coefficient for the Closed Wheel Racer for different rear wing lower element incidences in the presence of the different support configurations.

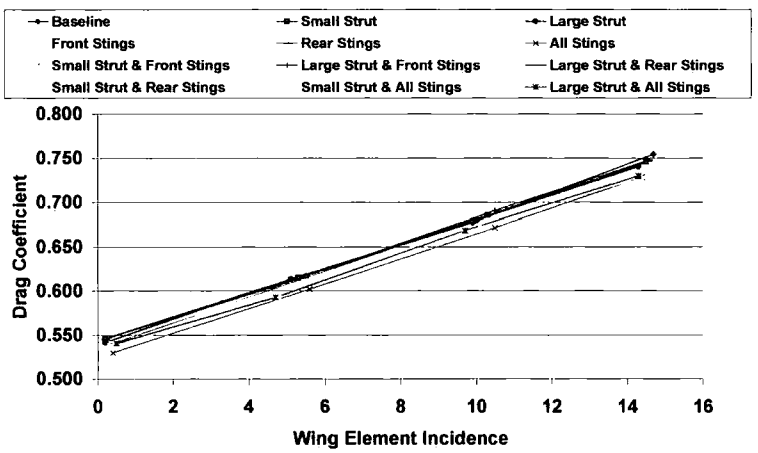

Figure 3.55: Drag coefficient for the Closed Wheel Racer for different rear wing upper element incidences in the presence of the different support configurations.

The curves for the upper element sweeps in Figure 3.55 and Figure 3.57 show the same characteristics despite the support configuration and there is no critical stall angle to use to compare differences. The differences due to the supports simply cause a shift in the graphs with a variation of C_D within –30 counts of baseline. Gurney flaps were used at the upper element trailing edge to effectively give the wing more camber and perhaps force a stall, however, both the drag and down force continued to increase not achieving a stall for any gurney height up to 4% of the chord. Because no obvious stall was seen, further tests were carried out at the highest down force configuration with the lower rear wing element at the optimum value of 18 degrees just before its gradual stall and the upper rear wing element at its maximum incidence of 14.5 degrees.

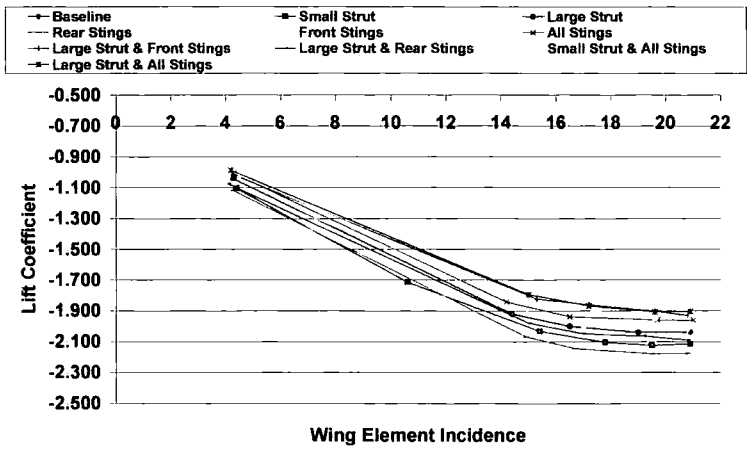

Figure 3.56: Lift coefficient for the Closed Wheel Racer for different rear wing lower element incidences in the presence of the different support configurations.

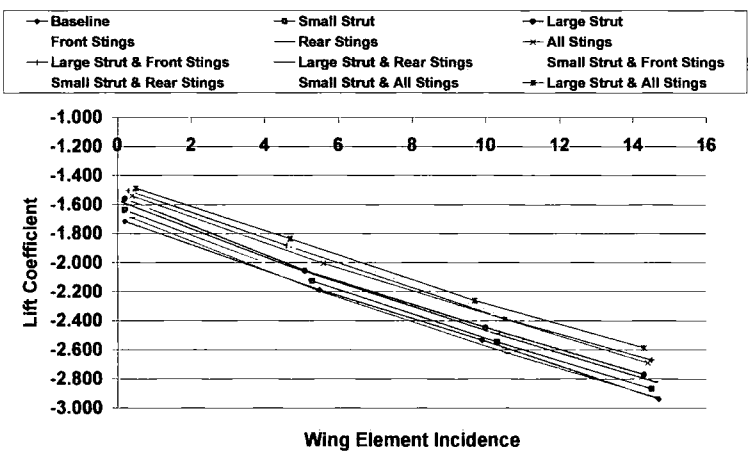

Figure 3.57: Lift coefficient for the Closed Wheel Racer for different rear wing upper element incidences in the presence of the different support configurations.

The OWR had a C_D of 1.021 and a C_L of –1.048 without any intruding supports (Table 3.3). Common to open wheel racers the model achieves down force using front and rear wings as well as profiled side pods and creates large amounts of drag with the exposed wheels. The CWR had C_D of 0.755 and a C_L of –2.938 in the absence of any supports. In its baseline condition the lift balance was at an un realistic value of 80% at the rear due to the absence of a rolling road. Typical to a closed wheel race car, the flow stays mostly attached to the body on the upper and lower surfaces.

Baseline	C_D	C_L	C_{LF}	C_{LR}	**Small Strut & Front Stings**	C_D	C_L	C_{LF}	C_{LR}
Open Wheel Racer	1.021	-1.048	0.125	-1.173	*Open Wheel Racer*	N/A	N/A	N/A	N/A
Closed Wheel Racer	0.755	-2.938	-0.533	-2.405	*Closed Wheel Racer*	-0.015	0.257	0.105	0.152
Small Strut	C_D	C_L	C_{LF}	C_{LR}	**Small Strut & Rear Stings**	C_D	C_L	C_{LF}	C_{LR}
Open Wheel Racer	-0.002	0.010	0.001	0.009	*Open Wheel Racer*	N/A	N/A	N/A	N/A
Closed Wheel Racer	-0.009	0.073	-0.007	0.080	*Closed Wheel Racer*	-0.012	0.083	0.008	0.075
Large Strut	C_D	C_L	C_{LF}	C_{LR}	**Large Strut & Front Stings**	C_D	C_L	C_{LF}	C_{LR}
Open Wheel Racer	-0.011	0.058	0.007	0.052	*Open Wheel Racer*	N/A	N/A	N/A	N/A
Closed Wheel Racer	-0.015	0.169	0.023	0.146	*Closed Wheel Racer*	-0.008	0.269	0.089	0.180
Front Stings	C_D	C_L	C_{LF}	C_{LR}	**Large Strut & Rear Stings**	C_D	C_L	C_{LF}	C_{LR}
Open Wheel Racer	N/A	N/A	N/A	N/A	*Open Wheel Racer*	N/A	N/A	N/A	N/A
Closed Wheel Racer	-0.013	0.175	0.090	0.085	*Closed Wheel Racer*	-0.008	0.120	0.005	0.116
Rear Stings	C_D	C_L	C_{LF}	C_{LR}	**Small Strut & All Stings**	C_D	C_L	C_{LF}	C_{LR}
Open Wheel Racer	N/A	N/A	N/A	N/A	*Open Wheel Racer*	N/A	N/A	N/A	N/A
Closed Wheel Racer	-0.007	0.016	-0.009	0.025	*Closed Wheel Racer*	-0.027	0.322	0.107	0.204
All Stings	C_D	C_L	C_{LF}	C_{LR}	**Large Strut & All Stings**	C_D	C_L	C_{LF}	C_{LR}
Open Wheel Racer	0.001	0.015	0.001	0.013	*Open Wheel Racer*	-0.008	0.051	0.012	0.039
Closed Wheel Racer	-0.026	0.249	0.114	0.136	*Closed Wheel Racer*	-0.025	0.352	0.122	0.231

Table 3.3: Drag and Lift coefficient data with and without interfering supports for the motor sport vehicles.

Figure 3.58 shows effects, relative to a baseline case without any interference, on C_D of both of the struts, the lateral wheel stings, and combinations of the two (data for the OWR in the presence of the Small Strut was not measured and has not been included in this chart or the upcoming chart for the effects on C_L). One of the most noteworthy effects is that all of the configurations cause a decrease in drag. For both racing vehicles drag is reduced by the overhead struts, with the Large Strut having the expected greater effect. The stings on the other hand only appreciably reduce drag for the CWR and do not change drag outside of balance repeatability for the OWR. In an investigation into interference effects on bodied and open wheeled vehicles at the Swift Rolling Road Wind Tunnel (Page et al., 2002), it was found that support interference on open wheel vehicles at zero yaw was small. This was because the supports approach in areas of already separated flow. The lack of an effect of the wheel stings for the OWR in this case is no doubt due to a similar effect in which the pre-existence of largely separated flow in the region of the wheels does not allow wake impingement on components further downstream. When the two support types are combined, the effect on drag is comparable to the effect from the Large Strut for the OWR, showing again the lack of an effect from the stings. For the CWR, the effect of the combined supports is similar to the effect from the wheel stings alone; however, it is not equal to a sum of the effects from the individual supports, proving that there is an interaction between the two types of support for the prototype race car.

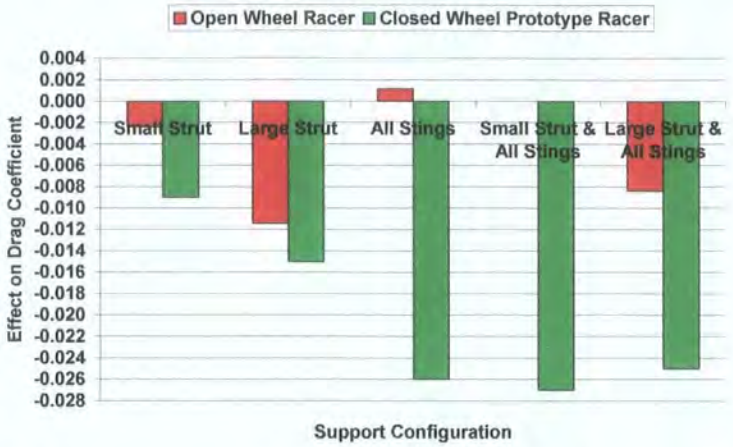

Figure 3.58: Effect on drag coefficient of support configurations for motor sport vehicles.

Figure 3.59 shows effects, relative to a baseline case without any interference, on C_L of the different support configurations. The most noticeable effect common to both vehicles is that there is always an increase in lift (loss of down force) created by the use of a support, with a much more substantial effect seen on the CWR (up to 360 counts). For both vehicles the effect on lift grows with an increase in strut size, however, for the OWR, the effect of the stings is once again smaller than the struts (as it was for C_D) and for the CWR the effect of the stings is once again greater than the struts. Unlike the plot of C_D, the combined effects of struts and stings on C_L for the CWR continue to increase beyond the effects of All Stings, but they are not equal to a sum, still showing proof of an interaction. It is speculated here that the wake of the Front Stings interferes with flow entering the underside tunnels at the side skirt. For the OWR the stings have a real, but lesser effect on lift when used alone and when combined with the Large Strut, the effect is still close to the case with the strut alone, confirming the lack of influence from the stings seen in C_D.

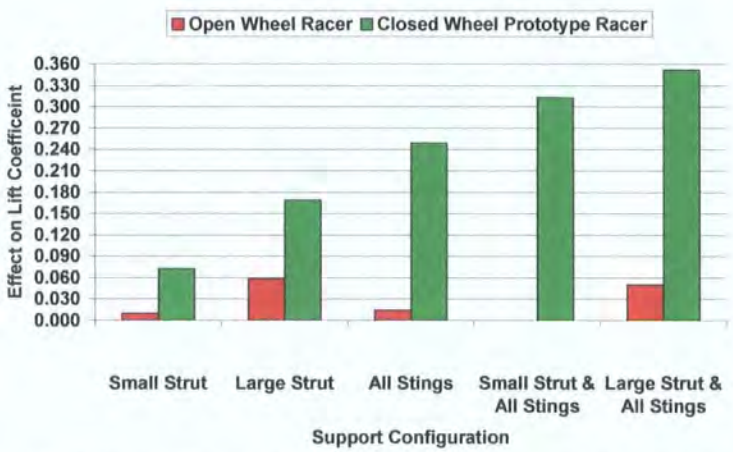

Figure 3.59: Effect on lift coefficient of support configurations for motor sport vehicles.

Although, also important for the stability of passenger vehicles, the distribution of the aerodynamic lift between the front and rear of a motor sport vehicle is very important to vehicle performance. Figure 3.60 shows the effect on C_{PM} relative to a baseline case for each of the support configurations. The data shows that for both of the motor sport vehicles the Large Strut has a much greater lifting effect on the rear of the

vehicle, pitching the models toward their front wheels. This is concurrent with interference and an effect of the down forcing capability of the rear wing. The same is true of the Small Strut for the CWR. The All Stings configuration was shown earlier to be less influential for the OWR, but had a largely noticeable effect on drag and lift for the CWR. From Figure 3.60, it can be seen that although the stings still pitch the model forward, the effect is smallest for both vehicle types, and the sometimes large effects of the stings on lift are close to being evenly distributed between the front and rear of the vehicle, making them the most favourable support method for maintaining the lift balance. However, they would also make a realistic lift measurement more difficult to distinguish. Combining struts and stings for both models shows that the effects of the overhead struts on the rear of the vehicle, maintains their influence even in the presence of the stings.

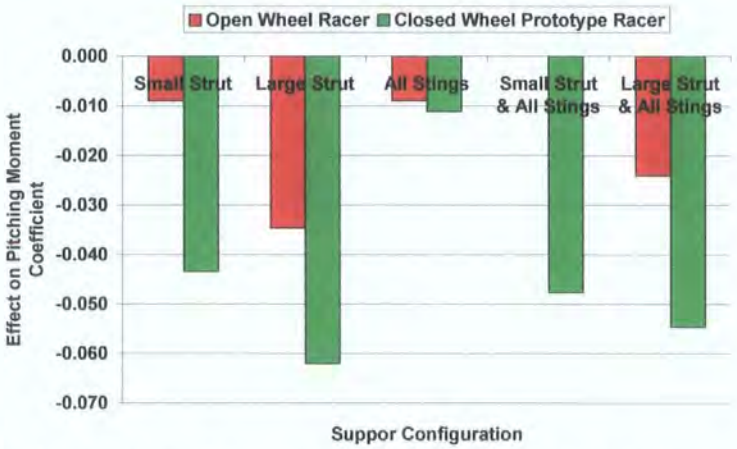

Figure 3.60: Effect on pitching moment coefficient of support configurations for motor sport vehicles.

As seen in Table 3.3, the effect of the struts on lift and drag is always more substantial for the bodied CWR. However, the decrease of 11 counts on C_D and increase of 58 counts on C_L felt by the OWR in the presence of the Large Strut is still significant. Figure 3.61 and Figure 3.62 show the effects of the struts on C_D and C_L, respectively, relative to a baseline case with the same wheel sting configuration, but without the overhead strut. The effects on C_D show a decrease for both the 'Small Strut' and 'Large Strut' configurations, which is consistent with interference of the drag producing rear wing. The only observation that can be made regarding combinations of the supports is that the Large Strut has a comparable effect with and without the stings, showing only a small interaction between the two support types.

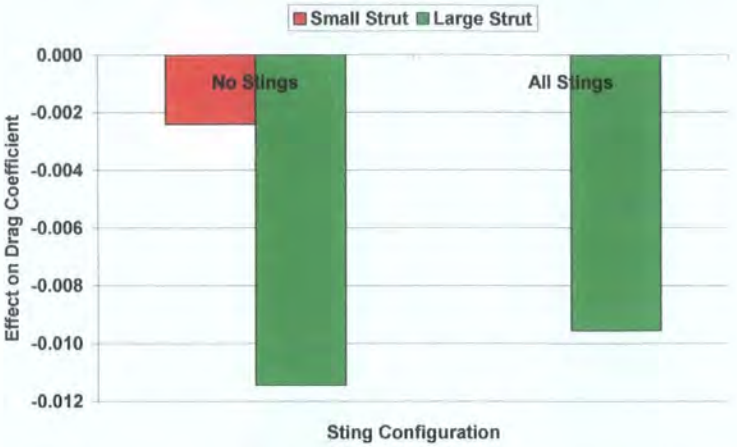

Figure 3.61: Effect on drag coefficient of the overhead struts for the Open Wheel Racer.

The effects on C_L in Figure 3.62 shows an increase from the struts with the greater effect coming from the use of the Large Strut. When used in the presence of the 'All Stings' configuration, the effect of the Large Strut is still positive, but is less than its effect without the stings. This change in the effect of the Large Strut confirms the assumption made earlier with the observation of C_D that there is a small interaction between the support types that is in favour of reducing the amount of interference created by the Large Strut.

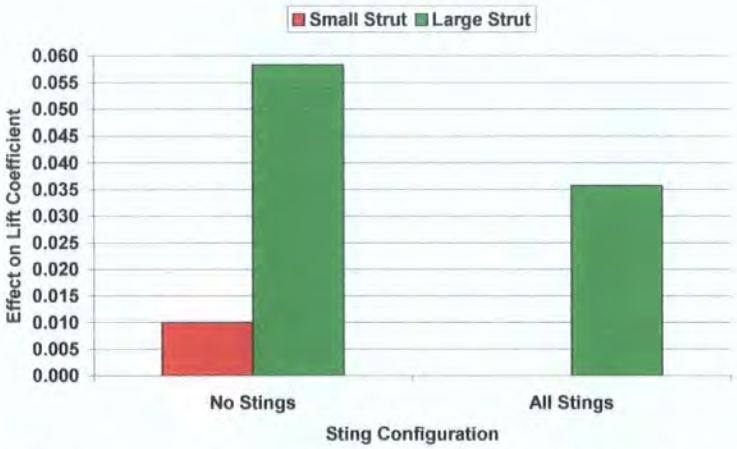

Figure 3.62: Effect on lift coefficient of the overhead struts for the Open Wheel Racer.

The larger effects of the CWR on drag and lift due to the struts are plotted in Figure 3.63 and Figure 3.64, respectively. Differences are shown for the struts relative to a baseline case with the same sting configuration, but no overhead strut. Without any stings the Small Strut and Large strut have a negative effect, with the Large Strut decreasing drag further. This is once again in keeping with a reduction of the effect of the drag producing rear wing. However, in the presence of the stings the struts' effects start to diminish to within repeatability. In the presence of the Front Stings, the Large Strut actually increases drag, but only by a small amount. These effects show the influence that the stings have on the CWR drag production and that the extent of the interaction is powerful enough to negate the effects that the struts have when used alone.

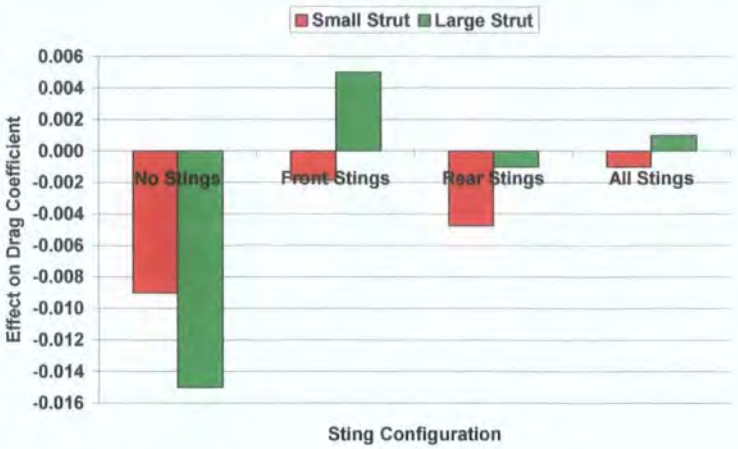

Figure 3.63: Effect on drag coefficient of the overhead struts for the Closed Wheel Racer.

Looking to Figure 3.64 it is easy to see that the interference of the supports on lift is much greater than it was for drag. The Large Strut once again has the greater effect than the Small Strut, but by a smaller margin in the presence of any of the sting configurations. The effects of the small strut are least changed when adding a sting configuration showing a smaller interaction between this strut and the stings when compared to the Large Strut. However, the effects of the Large Strut do remain comparable across all of the configurations incorporating the stings, showing not only the over bearing interference of the stings, but also the similar effect that the 'Front Sting,' 'Rear Sting,' and 'All Sting' configurations have.

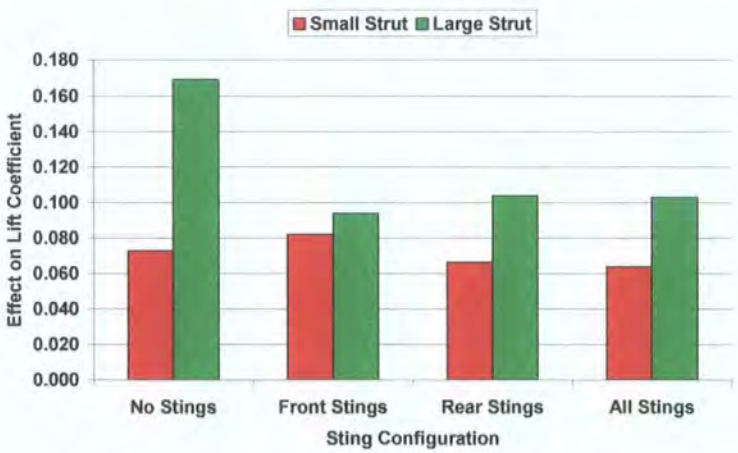

Figure 3.64: Effect on lift coefficient of the overhead struts for the Closed Wheel Racer.

Figure 3.65 and Figure 3.66 show the effects on drag and lift of the stings relative to a baseline case with the same strut configuration, but no stings for the OWR. The effects on drag in Figure 3.65 are small, showing very little effect that is greater than repeatability. However, the apparent trend seems to create an increase in drag. On the other hand, the effect on lift in Figure 3.66 shows a much more appreciable change in measurement due to the stings. Without a strut present, the stings cause an increase in lift of just under 15 counts; with the Large Strut in place above the model, the stings create an opposing, negative effect, of approximately 8 counts. Although the data for this model is limited, the provided results do offer some insight to the fact that there is an interaction between the stings and the Large Strut.

This interaction not only increases the effect on drag, but also changes the sign of the effect on lift when it is compared to the configuration with the stings alone.

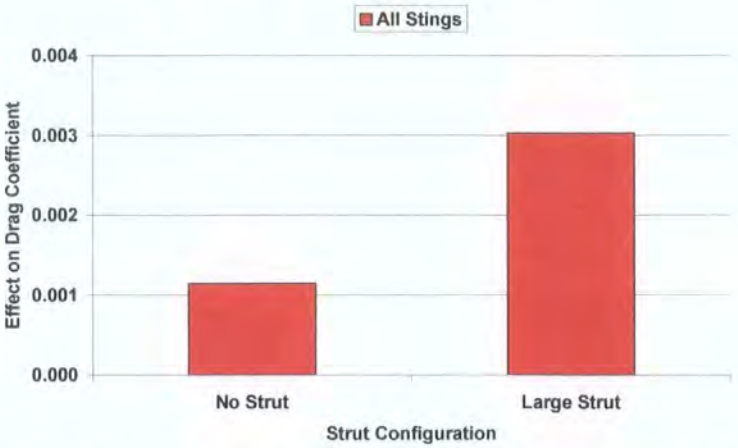

Figure 3.65: Effect on drag coefficient of the lateral stings for the Open Wheel Racer.

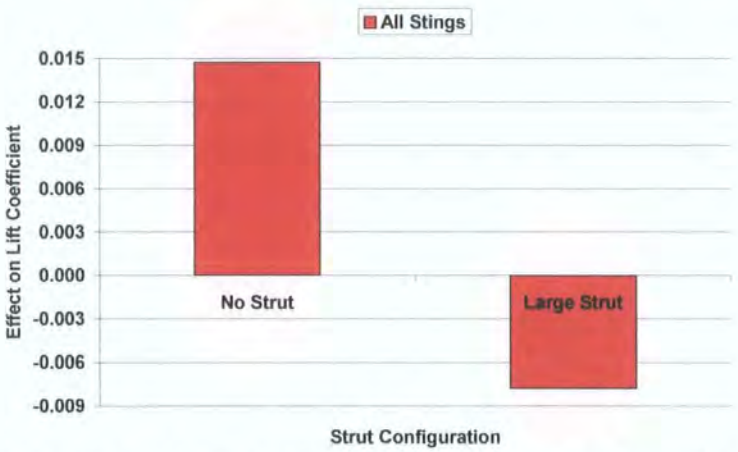

Figure 3.66: Effect on lift coefficient of the lateral stings for the Open Wheel Racer.

Figure 3.67 and Figure 3.68 show the effects of the stings on drag and lift for the CWR. For the most part the sting configurations cause a decrease in C_D in Figure 3.67, except for the case of the Front and Rear Stings when used in the presence of the Large Strut. Here the effect is an increase of about 7 counts. 'All Stings' used together creates the most interference independent of which strut configuration is used, followed by the Front Stings and then the Rear Stings. The largest change in drag is not from an individual sting configuration, but from an interaction of the stings when they are combined. This effect is seen to the greatest extent when All Stings are used without a strut present. None of the sting effects are the same in the presence of the struts, in fact the effects of the stings are greatest when there is no strut present, which shows an interaction between the struts and stings for this model.

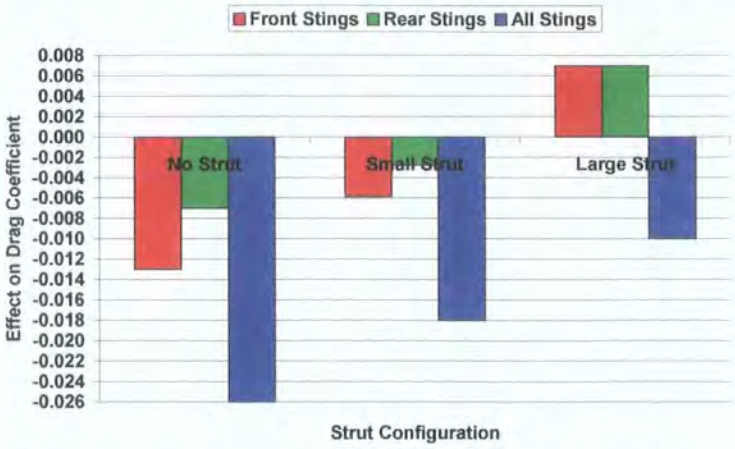

Figure 3.67: Effect on drag coefficient of the lateral stings for the Closed Wheel Racer.

Looking at Figure 3.68 the lift is once again much more sensitive to the use of supports. In particular, lift is most sensitive to All Stings without a strut present. Looking at Table 3.3, the effects of All stings is felt to a similar degree at both the front and rear of the vehicle, use of the front and rear pairs of stings tends to principally affect the front and rear lift, respectively. Following in the trends of the drag chart, the Front Stings have a greater effect on the model than the Rear Stings; however, for lift, the margin is much larger. The effect of the Front Stings is approximately 150 counts greater than the rear, and the effect of both pairs together is another 70 counts beyond that. The additional 70 count effect created by the combination of the two pairs is not greater than the effect of the Front Stings as it was in the drag chart, but is still significant.

Once again the interaction between struts and stings is seen in the lack of a consistent effect of any given sting configuration in the presence of the struts. The effects of the individual sting pairs in the presence of the Large Strut show the interesting effect of increasing drag in Figure 3.67 when all other configurations decrease drag and an equally unintuitive effect is seen here on lift. The effect of the Front Stings is considerably reduced and the effect of the Rear Stings changes sign and is then taken to a magnitude far greater than their effect without a strut or with the Small Strut. The effect of All Stings is also reduced in the presence of the Large Strut, showing a definite influence of the Large Strut on this model.

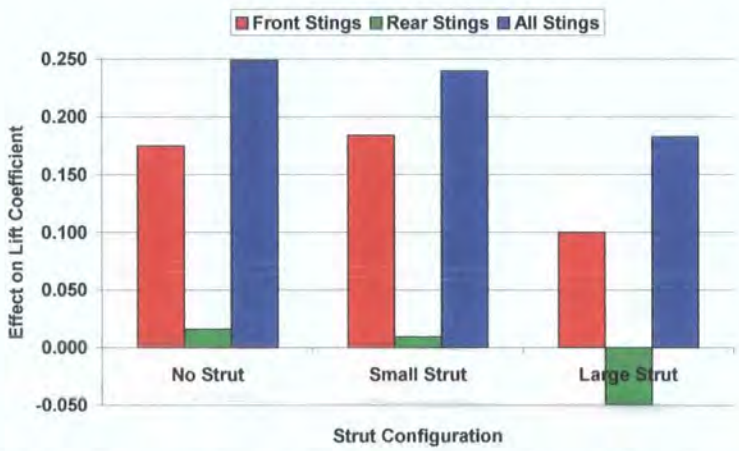

Figure 3.68: Effect on lift coefficient of the lateral stings for the Closed Wheel Racer.

3.4.2 Flow Mechanisms of Motor Sport Vehicles

As a reference to understand the location of traverse planes relative to the model, Figure 3.69 has been prepared showing the location of the planes at X/sqrtA=1.0 (red), X/sqrtA=-2.1(blue), and Y/sqrtA=0.0 (green). Note that the perspective drawing is not to scale.

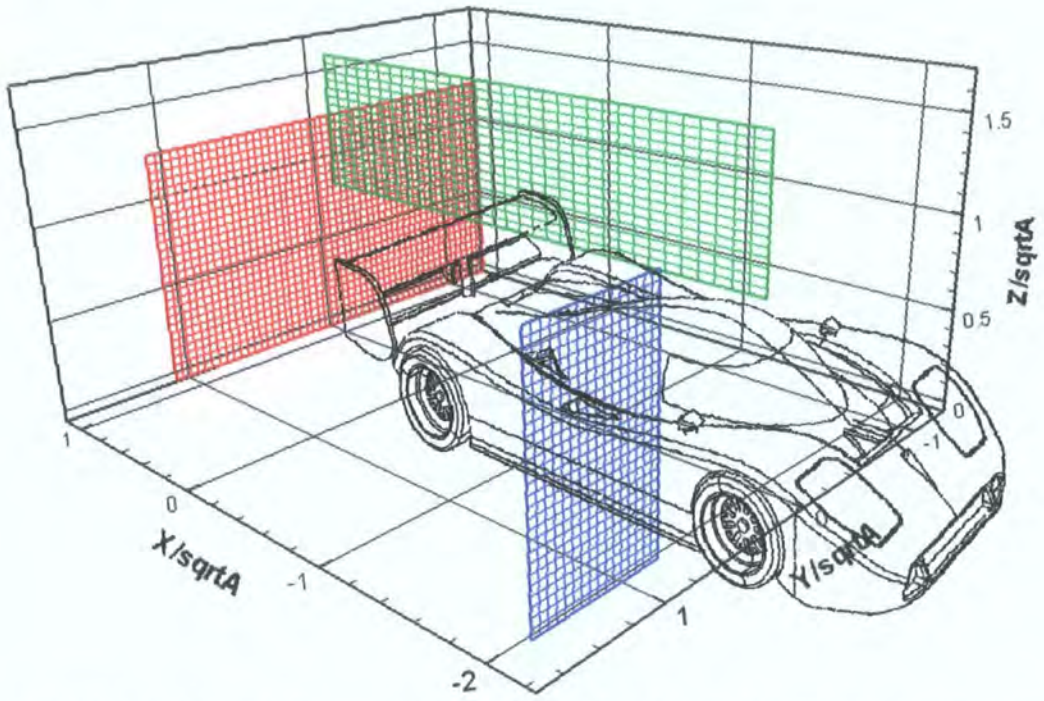

Figure 3.69: Locations of traverse planes around the Closed Wheel Racer. X/sqrtA=1.0 (red), X/sqrtA=-2.1(blue), and Y/sqrtA=0.0 (green). Drawing not to scale.

Figure 3.70 illustrates that without any interference the flow over the top of the CWR stays mostly attached to the vehicle with the exception of some localised separations near the cooling duct inlets and outlets and around the side view mirrors. On the bottom, flow enters the developed underside between the floor and front splitter and between the floor and side skirts (Figure 3.71) where it is accelerated creating a low pressure region before it enters one of two diffuser that slow the fluid allowing it to regain some pressure before exiting the rear of the vehicle beneath the rear wing and between the rear wheels.

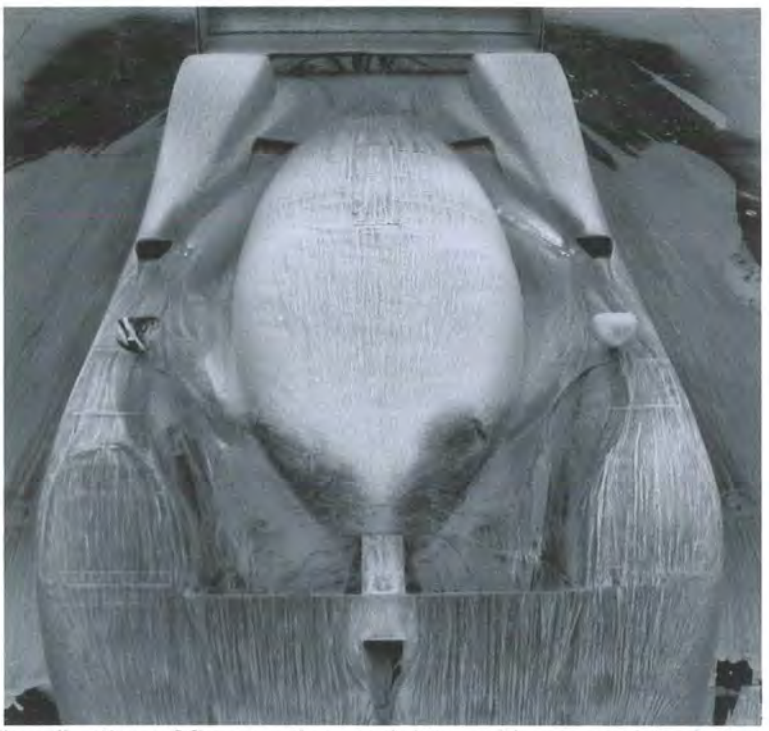

Figure 3.70: Visualisation of flow on the model top without any interfering supports.

In Figure 3.71, without any interference, the flow can be seen entering the vehicle underside between the floor and side skirt. Flow enters the gap from the point marked 'A' in Figure 3.71, up until the rear wheel. Just behind the front wheels, to the left of the point marked 'A' in Figure 3.71, the stationary wheel and mounting stem wake rejects flow from entering the vehicle underside and causes it to arch around the wake until point 'A.'

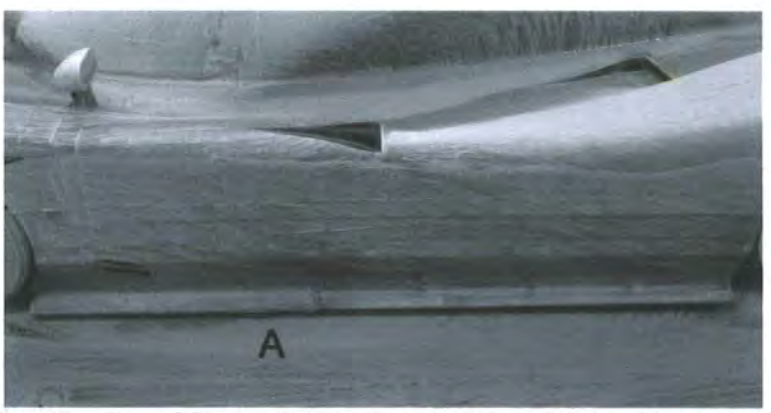

Figure 3.71: Visualisation of flow entering the model underside beneath the side skirt.

Total pressure loss in the un-interfered vehicle wake can be seen in Figure 3.72. The wake is dominated by a pair of vortices seen in Figure 3.73 and labelled 'A,' generated at the outboard tips of the large rear wing. Other features include two less intense vortical regions spread over larger areas (also seen in Figure 3.73 and labelled 'B') and a large area of loss, and possible re-circulation, in the area behind the model (seen as the large black out of range area in Figure 3.72).

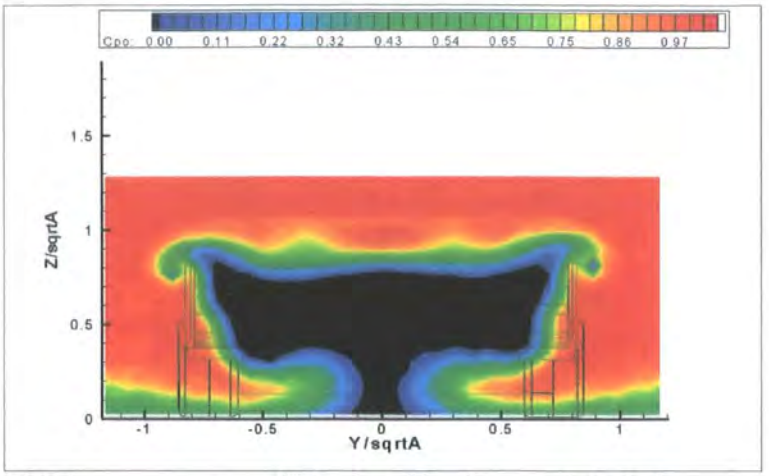

Figure 3.72: Total pressure coefficient without any interfering supports at $1\sqrt{A_f}$ downstream from the vehicle base.

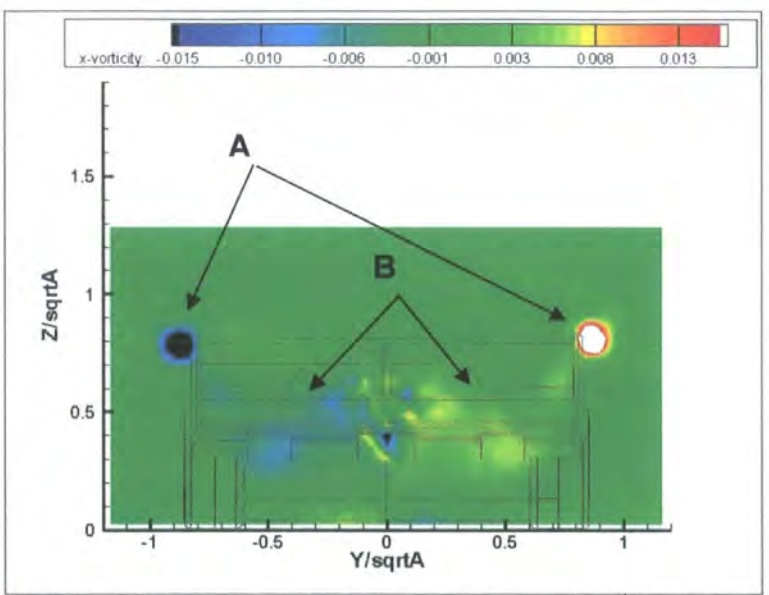

Figure 3.73: Vorticity without any interfering supports at $1\sqrt{A_f}$ downstream from the vehicle base.

Figure 3.74: Visualisation of the under floor tunnel vortex formation without any interfering supports.

The two smaller vortices originate from flow separating in the under floor tunnels. Surface flow visualizations show the flow entering the tunnel at 'A' in Figure 3.74, turning around the edge of the tunnel, rolling into a vortex and then brushing against the roof of the tunnel at 'B' of the same figure. Judging by the velocity vectors of Figure 3.75, the tunnel separations are given encouragement by the larger wing vortices before they reach the traverse plane. The narrow area of loss at the centreline near the tunnel floor that creates a 'bottle neck' in Figure 3.72 is created by the system of vortices entraining low

loss free stream fluid into the wake (as shown by the vector plot of Figure 3.75) and by the increased amount of axial flow leaving the under floor tunnels in this region.

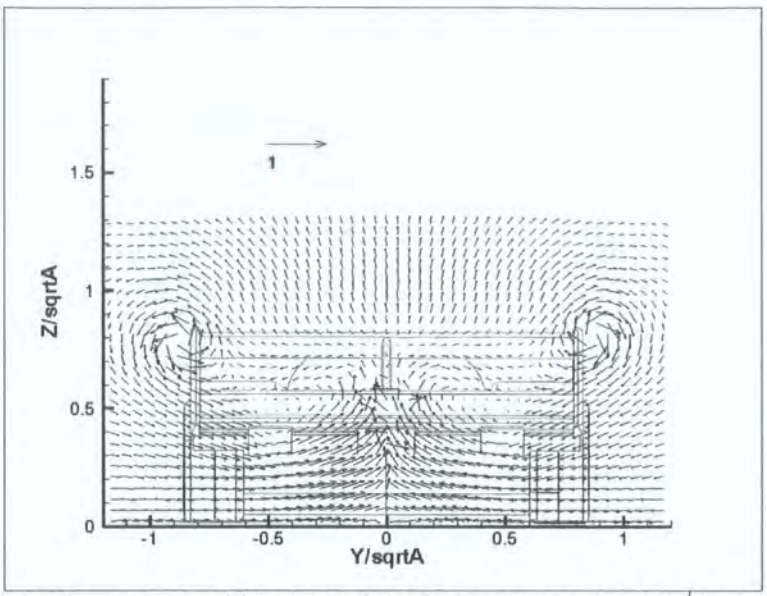

Figure 3.75: Velocity vectors without any interfering supports at $1\sqrt{A_f}$ downstream from the vehicle base.

A traverse along the vehicle centreline in Figure 3.76 shows only small amounts of loss above the model in its baseline configuration. The largest noticeable area of loss after X/sqrtA=0.0 occurs due to the upward deflection of fluid from the rear wing. There is also an appreciable amount of up wash at the centreline of Figure 3.75 created by the vortex system. The vortex rotation and hence large amount of up wash at the centreline that helps create the vehicle down force is opposite to that seen earlier for the passenger vehicles, which create a positive lift.

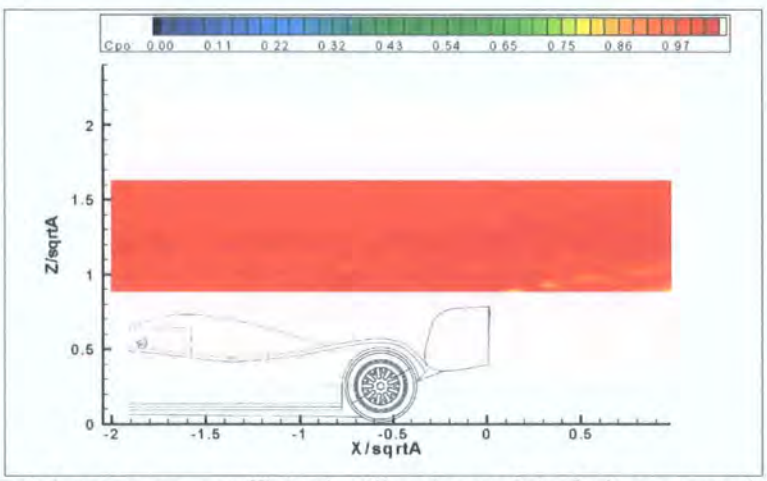

Figure 3.76: Total pressure coefficient without any interfering supports at the model centreline.

Looking at pressures along the vehicle side without any supports in Figure 3.77 shows very little loss created by the model. Instead, the largest area of loss is created by the stationary ground boundary layer, which grows thicker as the traverse plane nears the edge of the tunnel jet. The loss in the corner of the model and ground is created by an interaction of fluid entering the vehicle underside (beneath the side

skirt) and the boundary layer, but judging by the vectors in Figure 3.77, the fluid entering the under floor tunnel will be entraining lower loss fluid from the free stream, keeping the level of loss lower than that at the outboard end of the plot. Only small effects on CP_o can be seen in the remaining area of the plot.

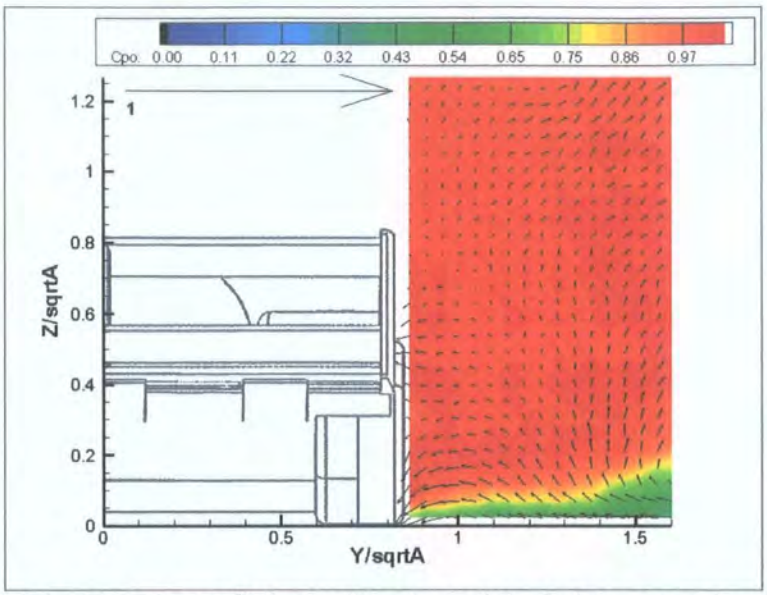

Figure 3.77: Total pressure coefficient without any interfering supports along the model side in a plane at X/sqrtA=-2.1.

In the presence of the Large Strut the model feels a decrease in drag coefficient of 15 counts and an increase in lift coefficient of 169 counts, with the majority of the increase in lift occurring at the rear of the vehicle (Table 3.3). It is believed that these effects are created by interference with flow over the influential rear wing. In Figure 3.78 the wake of the support can be seen impinging on the wings upper element. Other than this noticeable change in the flow, looking at the rear of the models top surface in Figure 3.79, there is little other noticeable change in the attached flow on the models surface. The wake of the support is only noticeable on the rear wing element.

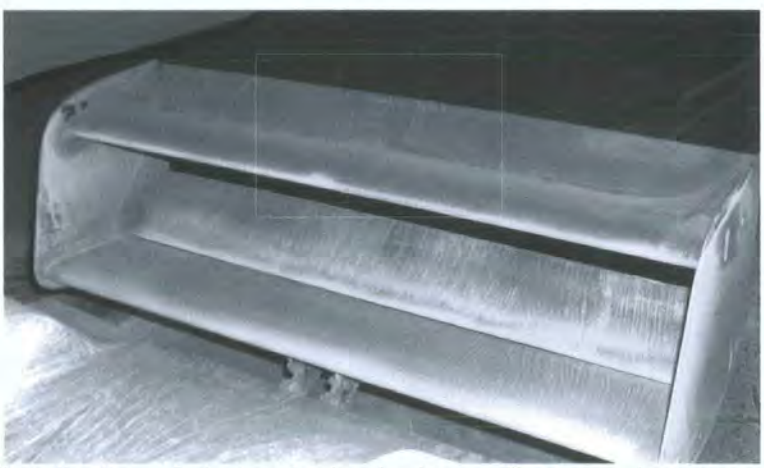

Figure 3.78: Visualisation of strut wake impinging on the rear wings upper element.

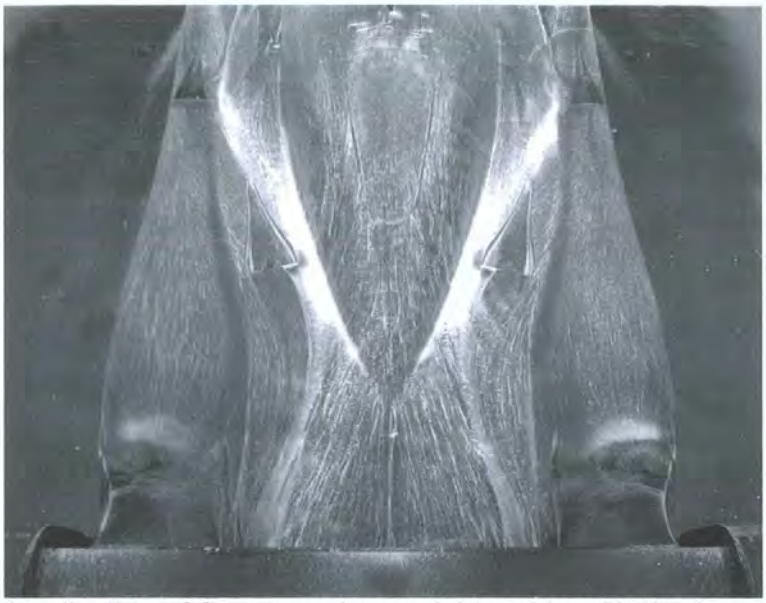

Figure 3.79: Visualisation of flow over the model topside with the Large Strut (viewed from the rear of the vehicle).

Total pressure losses along the model centreline in Figure 3.80 show that the presence of the faired actuator housing from the Large Strut configuration has created a noticeable wake in the area above the model, but has not noticeably increased the area of up wash above and behind the rear wing, suggesting that there is not much change to the post rear wing wake structure caused by the Large Strut.

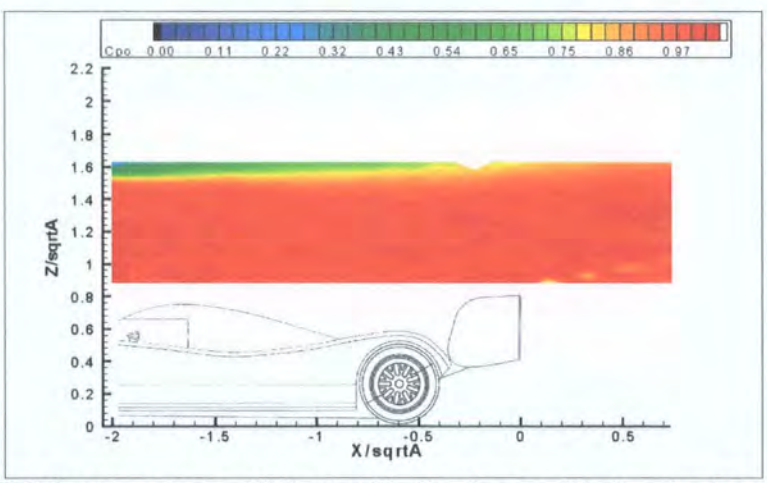

Figure 3.80: Total pressure coefficient with the Large Strut actuator housing at the model centreline.

For further evidence to the effects of the Large Strut Figure 3.81 and Figure 3.82 have been prepared showing CP_o and a difference of CP_o with and without the strut, respectively. Figure 3.81 shows little noticeable change in the overall wake structure caused by the strut. This makes the point that the effect of the strut on the flow around the vehicle is more significant than the strut wake itself and that the flow structure created by the rear wing is strong enough to allow the strut wake to propagate to the traverse plane. The wake is still dominated by the large amount of loss at the vortex cores and in the area behind the rear wing. Looking at Figure 3.82 the differences created by the Large Strut are mainly in the amount of loss and therefore strength of the two vortex pairs.

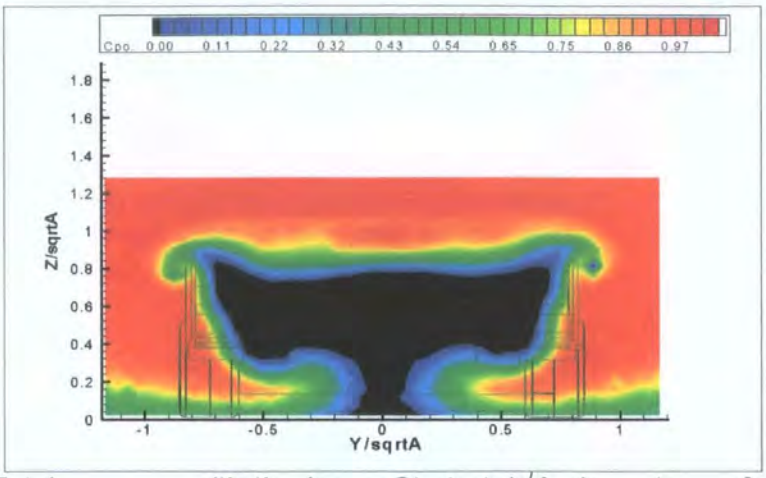

Figure 3.81: Total pressure with the Large Strut at $1\sqrt{A_f}$ downstream from the vehicle base.

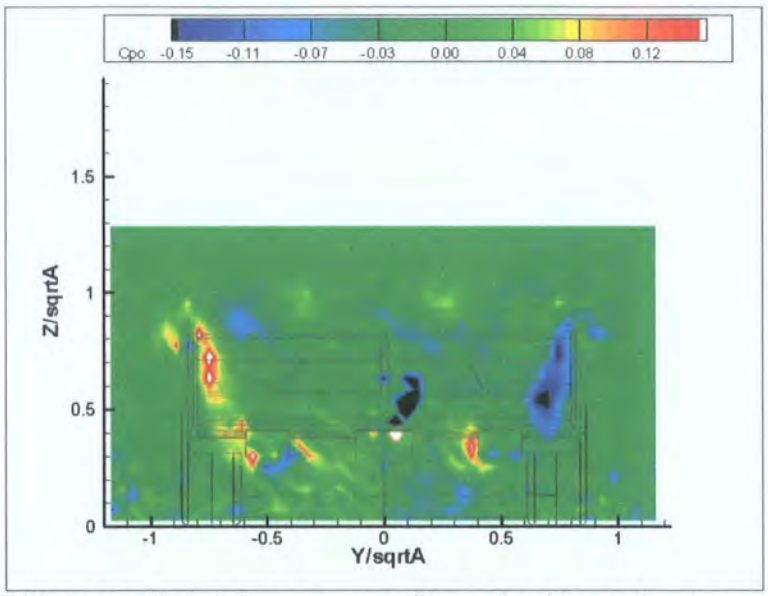

Figure 3.82: Difference in total pressure with and without the Large Strut at $1\sqrt{A_f}$ downstream from the vehicle base.

The force measurements of Figure 3.58 and Figure 3.59 show that there is a much larger effect from the wheel stings when compared to either of the struts. Due to the Front Stings the model feels a decrease in C_D of 13 counts and an increase in C_L of 175 counts (Table 3.3). Once again there were very few changes seen in a comparison of the topside flow patterns with the stings present (Figure 3.83) when compared to the flow visualisation without the stings (Figure 3.70). However, the wake of the Front Stings were noticeable along the vehicle side in both flow visualizations of the vehicle side (Figure 3.84) and traverse planes directly behind the support (Figure 3.85).

Figure 3.83: Visualisation of flow on the model top with All Stings.

The wake of the Front Stings seen in Figure 3.84 on the wheel surface immediately behind the junction of the sting and model wheel, then stretches in the stream wise direction and transfers to the model side where it is swept down toward the skirt. It is here where the support is thought to interfere with fluid entering the underside tunnels beneath the side skirt.

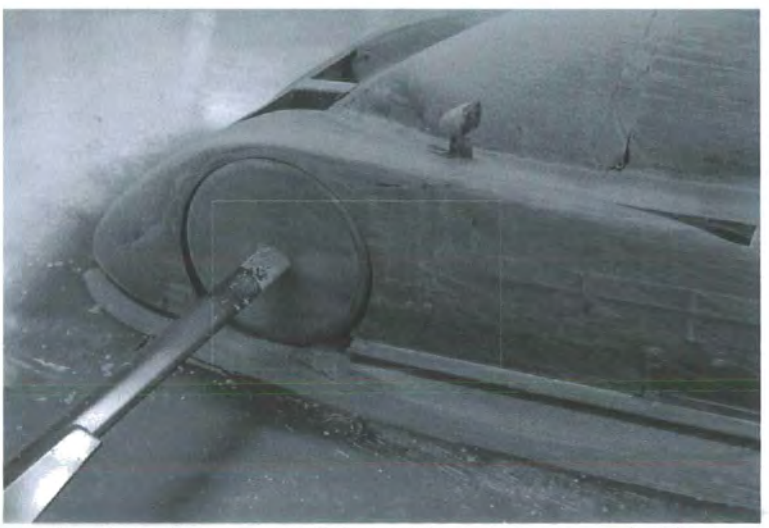

Figure 3.84: Visualisation of the Front Sting wake on the model side.

The wake created by the presence of the stings does not only affect the area immediately next to the model, but is noticeable in Figure 3.85 across the entire side traverse plane. The wake also interacts with the ground boundary layer. A difference of the total pressures with and without the stings in Figure 3.86 shows the significant increase in loss behind the sting. This area of increased loss is accompanied by a small reduction of loss beneath the stings in the ground boundary layer.

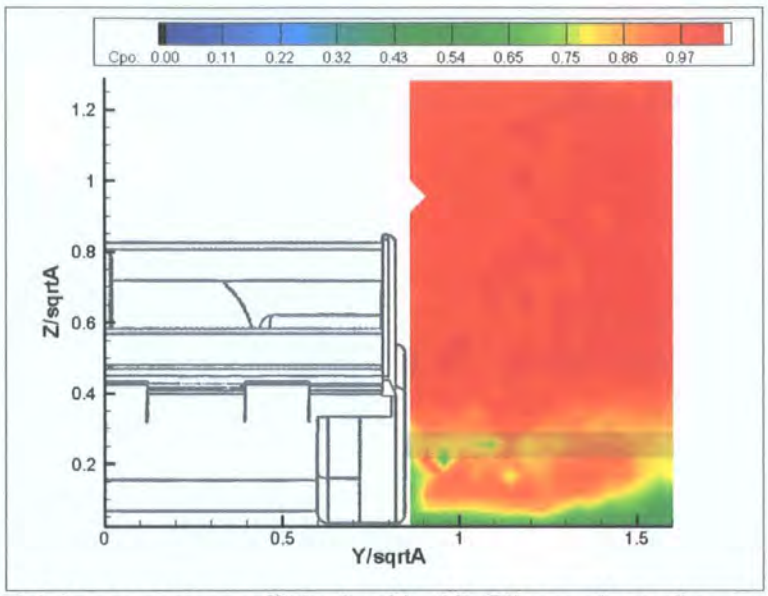

Figure 3.85: Total pressure coefficient with All Stings along the model side at X/sqrtA=-2.1.

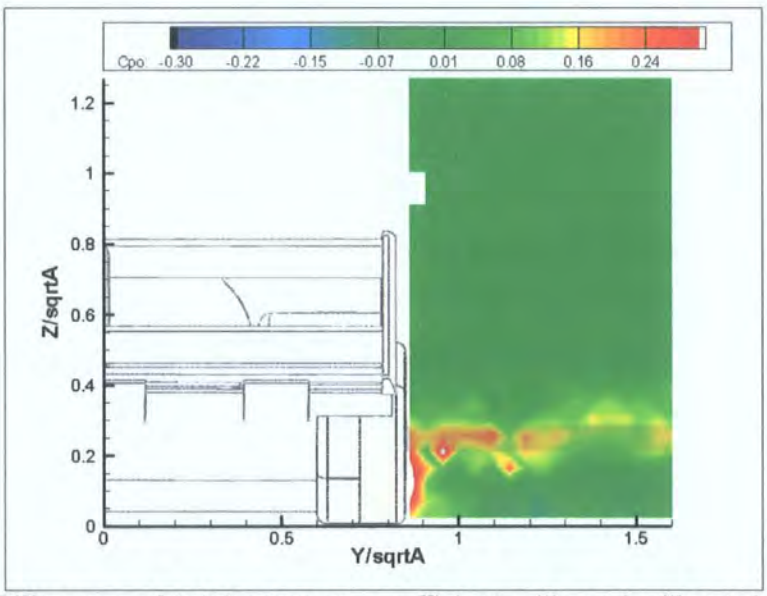

Figure 3.86: Difference of total pressure coefficient with and without All Stings along the model side at X/sqrtA=-2.1.

The disruption created by the wake of the stings, seen along the side of the model in Figure 3.84 through Figure 3.86, does not easily dissipate as it moves downstream and is still noticeable in the wake traverse behind the vehicle (Figure 3.87). Looking at the difference in CP_o with and without the stings at X/sqrtA=1.0 in Figure 3.88 shows that the stings reduce the amount of loss near the under floor tunnel

exits at the test section floor. There is then an increased amount of loss near the cores of the under floor tunnel vortices. The effects also extend behind the rear wing at the cores of the pair of wing tip vortices.

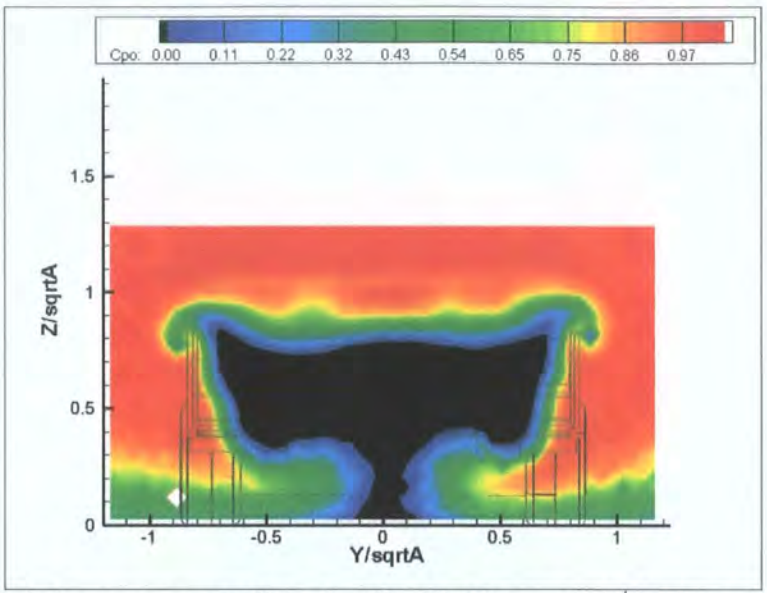

Figure 3.87: Total pressure coefficient with All Stings at $1\sqrt{A_f}$ downstream from the vehicle base.

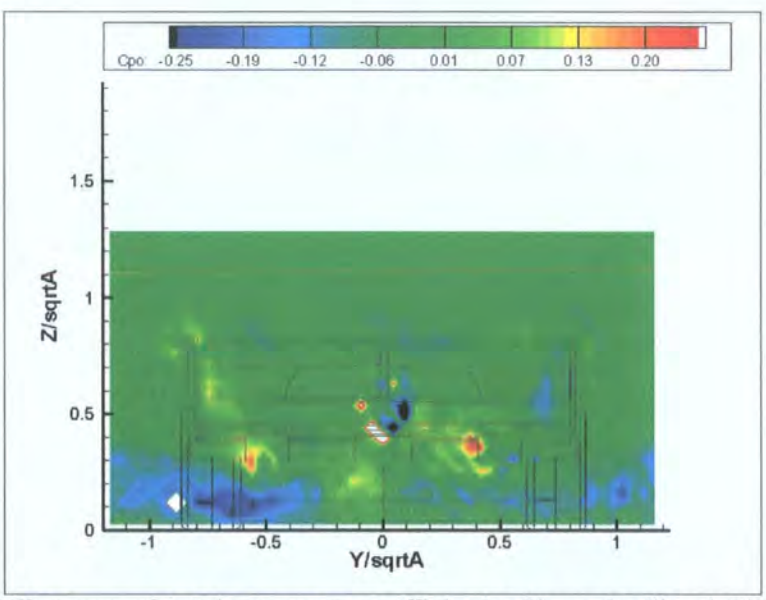

Figure 3.88: Difference of total pressure coefficient with and without All Stings at $1\sqrt{A_f}$ downstream from the vehicle base.

To further demonstrate the effects of the different support methods, surface pressures were taken on both the top and bottom surfaces of the model with and without the supports. The approximate locations of the tapping strings are shown in Figure 3.89. On the top surface a string of 14 tappings and on the bottom surface a string of 13 tappings were placed along the model centreline (Y/sqrtA=0.0). The tappings local to the strut junction on the model roof deviated slightly from the centreline to allow for the support to penetrate the model shell. Moving outboard, away from the centreline the next string of tappings, dubbed the mid-line, is located along the channel between the drivers cockpit fairing and the front/rear wheel coverings on the top (9 tappings), and along the centreline of an under floor tunnel on the bottom side (12

tappings). The third string is called the side line and runs along the wheel coverings on the top with 14 tappings and just beneath the side skirt on the bottom with 10 tappings.

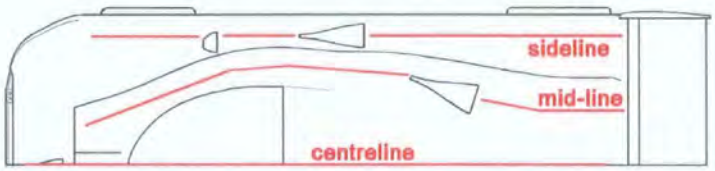

Figure 3.89: Approximate locations of the three surface pressure tapping strings (shown in red).

Figure 3.90 through Figure 3.92 show the pressure distribution along the top surface strings while Figure 3.93 through Figure 3.95 show the pressure distribution along the bottom surface strings, each for the configurations with and without the different supports.

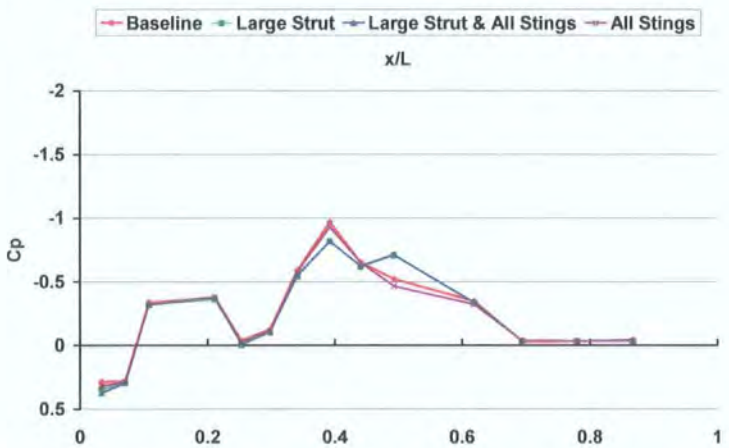

Figure 3.90: Pressure coefficient with and without supports along models upper centreline.

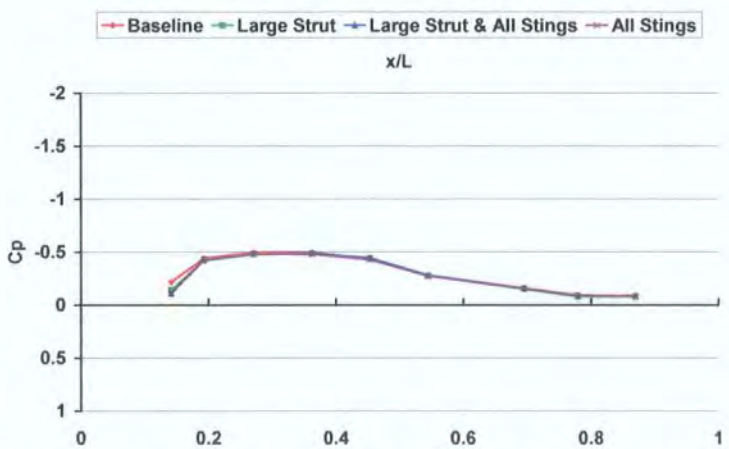

Figure 3.91: Pressure coefficient with and without supports along a mid-line on the models upper surface.

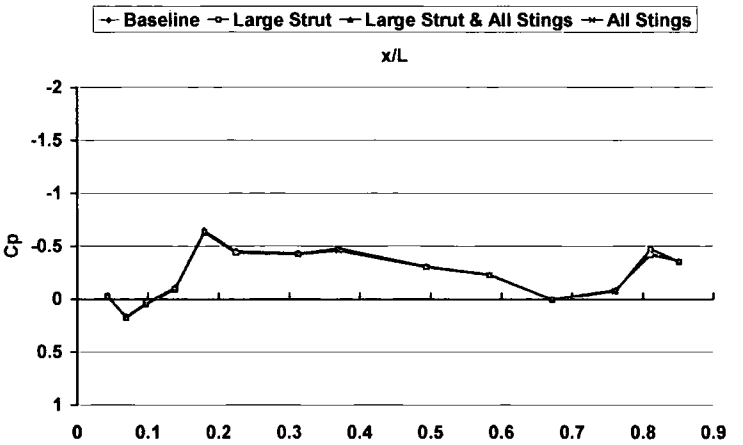

Figure 3.92: Pressure coefficient with and without supports along a side line on the models upper surface.

Looking at plots for the top surface strings, no appreciable changes from the baseline pressure distribution are noticeable in either the mid-line or sideline in their respective plots of Figure 3.91 and Figure 3.92 for any of the three support configurations. This supports the lack of effect that was seen in the surface flow visualisations of Figure 3.79 and Figure 3.83. The centreline distribution in Figure 3.90 also shows little appreciable change due to All Stings, however, looking at the two configurations involving the Large Strut there is a noticeable increase in C_p at x/L=0.4, near the maximum thickness of the strut and a decrease in C_p at x/L=0.5 near the strut trailing edge. Beyond these effects local to the junction there are no changes in the pressure distribution created by the Large Strut or its wake on the models upper surface.

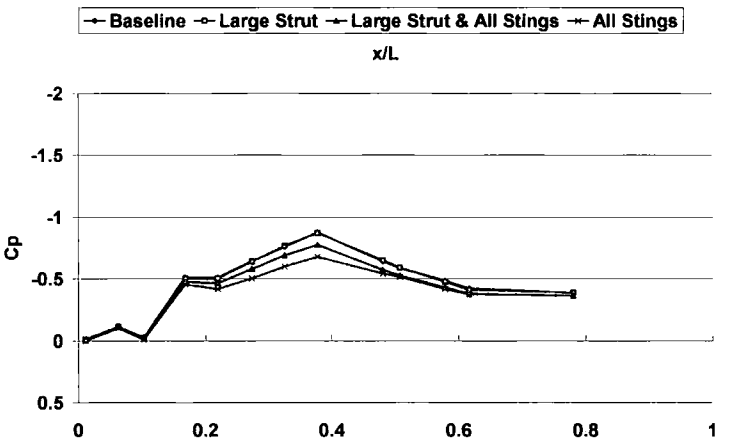

Figure 3.93: Pressure coefficient with and without supports along models lower centreline.

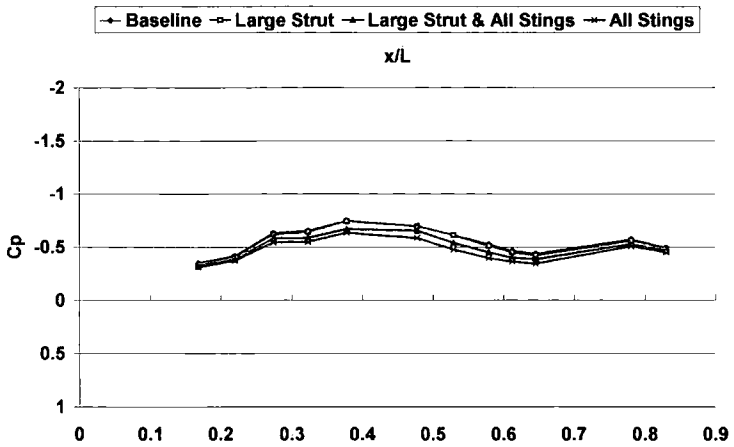

Figure 3.94: Pressure coefficient with and without supports along a mid-line on the models lower surface.

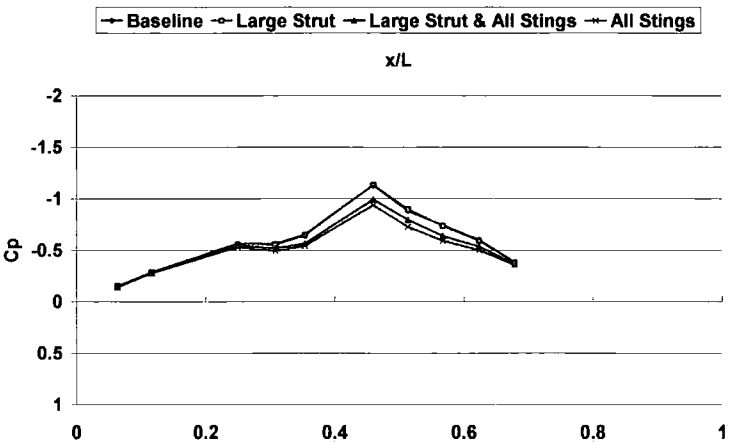

Figure 3.95: Pressure coefficient with and without supports along a side line on the models lower surface.

Due to the Large Strut, changes in average pressure coefficient on the lower surface ($\Delta[-C_{pavg}]$=-0.021) were slightly larger than changes at the upper surface ($\Delta[-C_{pavg}]$=-0.015). The further increase in pressure on the bottom accounts for some of the 169 count increase on C_L, the remainder occurs by interference with the rear wing. Overall changes in the surface pressures due to the 'All Stings' configuration on the lower surface ($\Delta[-C_{pavg}]$=-0.099) were larger than changes at the upper surface ($\Delta[-C_{pavg}]$=-0.0145). The further increase of pressure on the lower surface created a lifting force due to the lateral supports that agrees with force measurements.

On the models under side very little deviation from the baseline distribution is created by the presence of the Large Strut. However, for all three plots between x/L=0.2 to 0.7 there is an increase in C_p, showing a reduction in velocity, due to interference created by the configurations including the stings All three plots in Figure 3.93 through Figure 3.95 show a similar trend with 'All Stings' alone increasing C_p more than the Large Strut & All Stings. The interaction of the Large Strut and All Stings that is seen here and was witnessed earlier in the force measurements is caused by the effects of the strut wake impinging on the rear wing (seen in the flow visualisation of Figure 3.78) and the sting wake extending down stream (seen in Figure 3.84 through Figure 3.88) combining to alter the vehicles base pressure.

Although there was not much of a noticeable effect on the lower surface due to the Large Strut in Figure 3.93 through Figure 3.95, the change in average pressure coefficient was slightly larger on the bottom surface when compared to the upper surface. This leads to a change in pressure that adds a lifting force to the model. Because the increase of C_p at x/L=0.4 and accompanying decrease at x/L=0.5 in Figure 3.90 made the average on the upper surface arrive closer to the baseline, the average change from baseline on the lower surface is greater. This means that although differences on the lower surface are not readily noticeable in the pressure distribution plots, there is a real effect from many small differences adding up. The fact that the strut is affecting pressures on the lower surface and that there are few visible changes in flow on the upper surface (Figure 3.79) leads to the notion that the support is interfering with the wing and therefore the positive wing-body interaction that favours flow through the model underside.

3.5 Plate-Strut Junction

3.5.1 Junction Flow Visualisation

In order to provide some physical evidence of the flow structure to be expected in the computational simulations discussed later in Chapter 4, flow visualisation was performed on an aerofoil intersecting the roof of the Notchback model. The model was tested in the Durham $2m^2$ tunnel with the dummy strut protruding vertically from the centre of the roof. The strut used was the 100mm chord NACA 66_4-021 profile. Figure 3.96 shows photographs of the surface oil flow visualisation of the junction of the dummy support strut and model roof. Figure 3.96a shows the three-dimensional separation line created around the base of the aerofoil. The separated region in the seam of the junction is clear when looking at the surface of the vehicle roof in the photograph, however, evidence of the horseshoe vortex rotation or its continuation downstream of the support is not quite as obvious. The extent of the supports influence on the streamlines is noticeable in Figure 3.96a up until a distance of approximately y/c=±0.8 perpendicular to the direction of flow, where the streamlines begin to straighten back to the free stream direction.

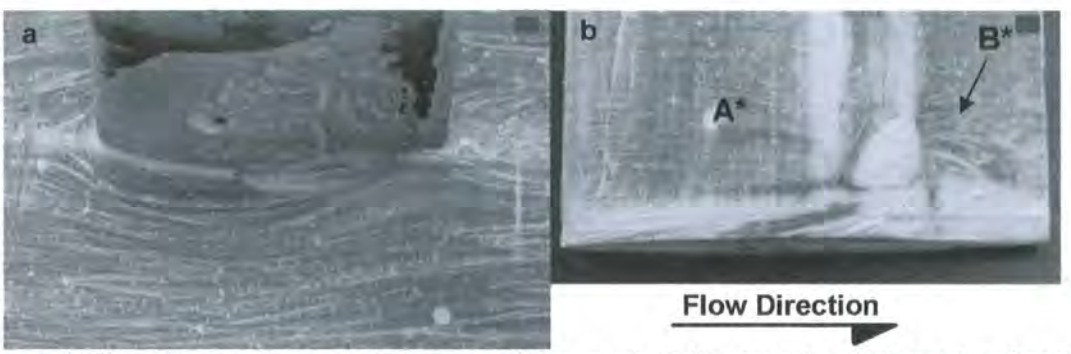

Figure 3.96: a)Separation on plate around the strut at the junction b)flow visualisation of strut once removed from the model roof.

Figure 3.96b shows a close view of the separation on the aerofoil. The horseshoe vortex rotation (described in Section 1.7.1) forces dye to collect along the base of the aerofoil and mixes with the separation at the foil trailing edge. Further up the page, along the span of the aerofoil in the area labelled 'A*' the streamlines on the foil surface just before the maximum thickness begin to bend down, in the –z-

direction. This is because this area of highly rotational flow, created by the horseshoe vortex, is entraining free stream fluid down the aerofoil span and into the corner of the junction. Near the base of the aerofoil, after the maximum thickness where, a region of reversed flow indicated by 'B*' is caused by a combination of the horseshoe vortex rotation and trailing edge separation.

3.5.2 Aerodynamic Forces

To compliment the computational simulations presented later in Chapter 4 changes in aerodynamic forces on a flat plate due to the introduction of an aerofoil shaped strut were measured. The experiment was performed in the Durham (Plint) 0.46m x 0.46m tunnel. Two different aerofoil profiles were used to intersect the plate and create the junction; the first was a 152.4mm chord NACA 0012, the second a 100.0mm chord NACA 66_4-021. Because the aerodynamic forces of the plate alone, not the forces on the plate with the strut in contact, were important, a small (approximately 1.5mm) gap was left beneath the aerofoil base and above the plate surface to separate the two. This size gap allowed for a union realistic enough to simulate a strut intersecting the roof of a model, but also allowed for movement of the plate on the force balance under its aerodynamic load. The setup can be seen in Section 2.4.1.

Figure 3.97 shows the effect on the plates' (L=650mm) drag coefficient due to the proximity of the struts. The change in C_D due to the strut is plotted against the position, in percentage of overall plate length (L), of the strut leading edge for each profile. The force balance resolution, mentioned in Section 2.5.1.1.1 was 13 counts. The results show a decrease in drag on the plate for both aerofoil profiles at any distance along the plate.

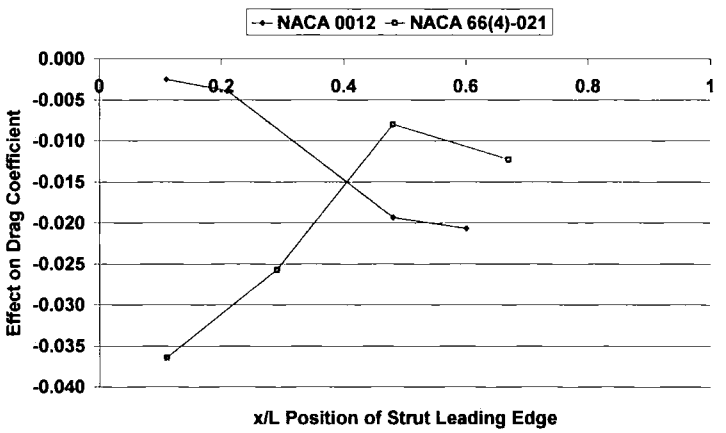

Figure 3.97: Effect on the flat plate drag coefficient with intersection of the NACA 0012 and 66_4-021 aerofoils.

The effect on C_D from the NACA 0012 aerofoil grows increasingly negative as the strut reaches the rear of the plate, with the largest change after about x/L=0.2. In a small boundary layer, such as was present at the leading edge of the plate there will be little or only weak formation of secondary flow to alter the plates drag. However, after a given distance along the plate, when the plate boundary layer begins to mature and thicken, the adverse pressure gradient created by the strut wake will begin to interact with the plate boundary layer, increasing the effect, and formation of secondary flow. After x/L=0.5 the further effect of moving the strut toward the plate trailing edge is only small. This is likely due to the further

development of the plate boundary layer at this point, not creating any more opportunity for an increased interaction of plate and strut.

Observing the effects of the NACA 66_4-021 aerofoil in Figure 3.97, near the plate leading edge and the following trend as the strut is moved downstream is opposite from that of the NACA 0012. Due to the differences between NACA series and chord length of the two struts used, the effective trend on the plate of the NACA 66_4-021 opposes that seen from the NACA 0012 aerofoil and decreases as the strut is moved downstream. The initial change up until x/L=0.5 is quite abrupt. The plate then sees a slight increase in the effect as the aerofoil leading edge is moved past this point. Once again, the more rapid change in effect near the front of the plate will be due to the growth of the plate boundary layer in this region.

As the two struts are moved downstream, there is less surface aft the strut to effect, as proof of this Figure 3.97 shows that the graphs are tending towards converging with each other, it stands to reason that the effect would decrease as the strut leading edge reached x/L=1.0.

The results witnessed here for this isolated case are surprising in that they decrease the drag of the plate. Whereas, literature reviewed in Section 1.7 expects to see an increase in drag created by interference., Hoerner [Hoerner, 1965] does predict a negative interference drag for T/c<8% in Equation 1.10, but nothing less than 12% was used here. There is a gap between the strut and plate creating imperfect junction geometry, but a similar gap was evaluated in Section 3.1.3 and was not found to be significant. The maximum drag changes observed here would correspond to less than 3 counts on C_D based on the frontal area of the Notchback model. The interference drag due to the overhead strut for the Notchback (Section 3.3.1) was 2 counts on C_D. The effects for the complete model and junction in isolation are opposite in sign and this could be due to a local drag decrease at the junction coupled with a drag increase further downstream caused by the strut wake, which would show that the effect of the strut wake, not the junction is more influential on the overall change in drag. However, the changes in force in both cases are very small (in the region of balance repeatability).

3.6 ISOLATED REAR WING

Because a motor sport vehicles rear wing has been proven to be a significant location for support interference, tests were performed measuring aerodynamic forces on an isolated rear wing downstream from an aerofoil shaped strut. The experiment was performed in the Durham (Plint) 0.46m x 0.46m tunnel. The 152.4mm chord NACA 0012 and the 100.0mm chord NACA 66_4-021 were used to create interference. The rear wing was removed from the OWR and mounted at a realistic distance from the strut, as would be seen when the strut and wing where in position on the full model in the wind tunnel. The setup of the wing and strut was described earlier in Section 2.4.2.

Looking at the incidence range for drag and lift in Figure 3.98 and Figure 3.99, the rear wing alone without interference begins a gradual stall at approximately 12 degrees incidence. In comparison to the

idealised lift of a wing in 2D potential flow assumptions, the wing seems to compare well at incidences less than 9 degrees, however, it is surprising that the measured slope is actually steeper at incidences greater than this.

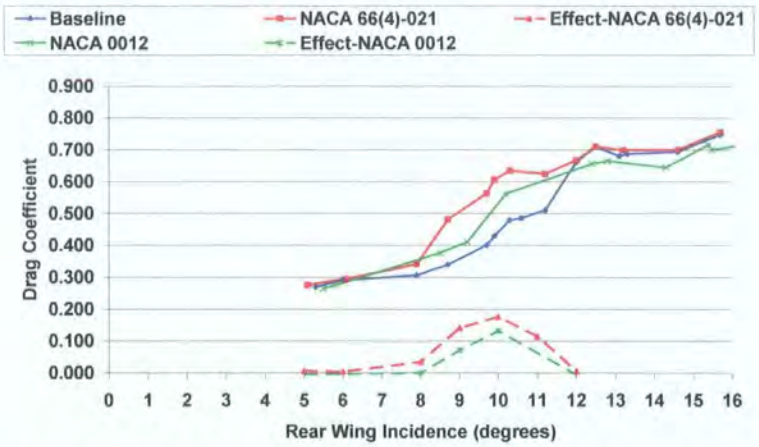

Figure 3.98: Incidence sweep showing drag coefficient of the isolated rear wing with and without interference.

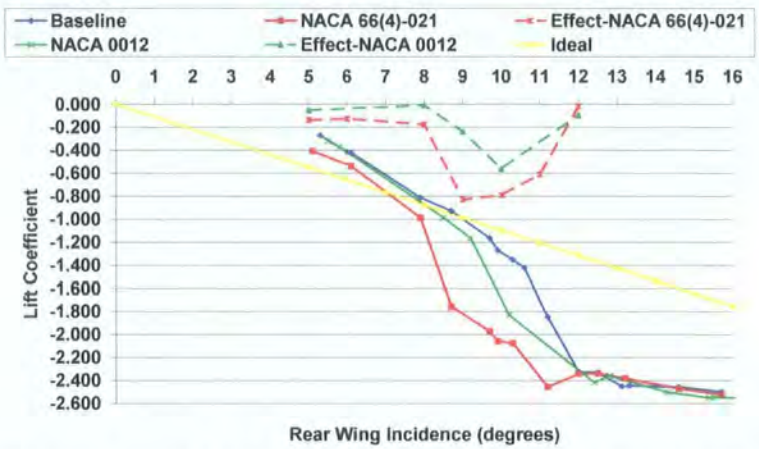

Figure 3.99: Incidence sweep showing lift coefficient of the isolated rear wing with and without interference.

Comparing the drag and lift, respectively, of the interfered case to the baseline case in Figure 3.98 and Figure 3.99 it is seen that the NACA 66_4-021 strut can create an increase in C_D of 175 counts at 10 degrees incidence and a reduction in C_L of 830 counts at 9 degrees. At 12 degrees incidence the difference dropped to approximately 0 counts for both lift and drag. This approximate 0 count difference remains for incidences greater than 12 degrees. At the lower end of the sweep the difference is approximately 0 at both 5 and 6 degrees incidence for drag. For lift the strut causes a change of approximately 130 counts at these lower incidences. The NACA 0012 strut creates a maximum effect on drag and lift at 10 degrees. At this incidence there is an increase of C_D of 132 counts and a decrease of C_L of 559 counts. At incidences below 6 degrees on drag and 8 degrees on lift the effect of the strut on the wing is almost zero. At higher incidences greater than 12 degrees there is a relatively small decrease in drag, but no considerable change in the lift coefficient. Looking at the common trends, a strut placed upstream of this multi element rear wing can be expected to increase its down force whilst increasing the amount of drag it generates and the most noticeable effects occur between 8 and 12 degrees incidence. The increase in down force and drag in

this region suggests that the strut wake could be reducing the extent of the stall. In Figure 3.100 the effect of the NACA 66_4-021 on the isolated rear wing has been recalculated using the OWR model frontal area and compared to the effect from the Small Strut on the full model at different rear wing incidences. A comparison shows that for both lift and drag between 5 and 12 degrees incidence the effect on the full model bears no resemblance to the effect on the rear wing alone.

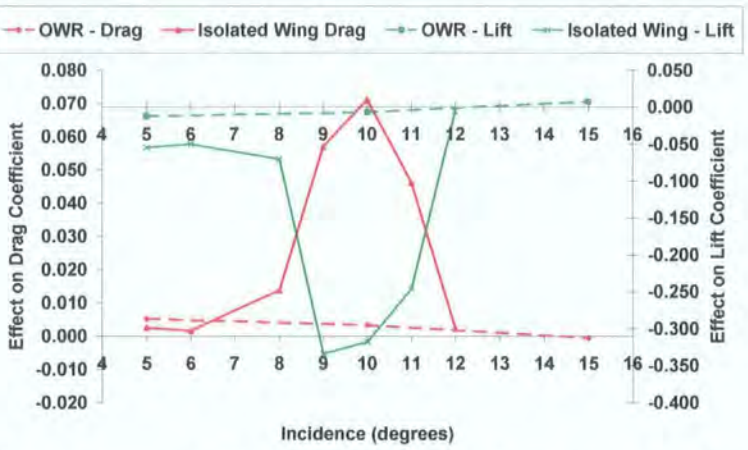

Figure 3.100: Comparison of effects on the isolated rear wing and the Open Wheel Racer of the NACA 66_4-021.

Katz & Dykstra [Katz & Dykstra, 1992] outline the importance of the wing-body interaction for racing style vehicles in the context of the wing placement and the improvements it can have on vehicle performance. They also outline the importance of designing the wing with the complex flow field created by the model in mind. Similarly, the results seen here indicate that the sensitivity of the rear wing to a strut wake is dependent on the flow around the model.

3.7 SUMMARY

The results have shown a maximum effect on C_D of 25 counts (7% of the total drag for the Hatchback with the deflector) and C_L of 350 counts (CWR) from the use of the Large Strut and Large Strut & All Stings, respectively. They have also shown that a vehicle's lift (or down force) is affected most by interference. However, despite these significant effects, interference is highly model/configuration dependent and the effects will depend on the vehicle type: For the Notchback there was a rearrangement of flow structure, but not much change in magnitude of the drag forces. For the Hatchback there was a reversal of an effect from a shape change (with and without the rear deflector). The CWR had its down force destroyed by interference with its sensitive underside flow and showed that both an overhead strut and lateral stings can affect flow beneath a motor sport vehicle. The OWR on the other hand saw little effect due to large regions of already separated flow. Lastly, for most of the models, the effects of different support types, cannot be summed to arrive at their overall effect.

4 COMPUTATIONAL APPROACH AND RESULTS

4.1 INTRODUCTION

It is undisputed that the use of an overhead strut positioned between the A-pillars perpendicular to a vehicles roof will disrupt the flow quality around a model; however, the portion of this interference effect that is created by an interaction of the two bodies' flow fields at the junction and the portion that is created by the support wake is not understood. Research in other engineering disciplines has shown that understanding and control of interference at a wing-body junction, blade-hub assembly, appendage-hull junction, bridge pillar-river bed junction, in turbo machines, in the case of a building subject to wind, or for a vortex generator designed to prevent boundary layer separation or to enhance heat transfer can be critical to a successful design [Apsley & Leschziner, 2001]. In the same manner understanding the effects local to a strut-model junction is essential to improving the reliability of wind tunnel testing using intrusive supports above a moving ground. Furthermore, research in aeronautics has discovered that when the T/c ratio of a strut is reduced the flow field tends to be disturbed only locally at the intersection of the strut and surface [Tetrault et al, 2001] with fewer disturbances reaching downstream to interfere with other components. Discovering the amount of the interference effects measured in Chapter 3 that are local to the junction will not only identify the origin of the greater amount of interference, but also determine if reducing the T/c ratio or re-defining the junction geometry to suppress certain flow features is of greater importance.

To compliment the experiments performed in the wind tunnel, a further Computational Fluid Dynamics (CFD) investigation was carried out and the local geometry of the intersection of the strut and model roof was simplified as an aerofoil normal to a planar surface and modelled in Fluent. With this computer generated model the specific interaction of the flow surrounding the two individual components is of interest. Paramount is the amount of additional interference drag created by the presence of the aerofoil that falls on the plate (as it represents the model in this setup) thus affecting its force measurement.

This simplified model suffices in exemplifying the junction of a roof and support for a closed, flat roofed vehicle, such as the Hatchback and Notchback models used. It will also bear some insight toward a closed, but curved roof and strut junction, such as is the case for the Closed Wheel Race Car. It may even provide understanding of the flow at the junction of the lateral stings and model wheels, but experience has shown that separations in this area created by the wheels and/or wheel arches will make the region more difficult to simplify and model in this manner. For this same reason, the separations surrounding an open cockpit will make this model inaccurate for the strut approach on the OWR.

The CFD simulation was performed with varying inlet boundary layer, thickness-to-chord ratio, and the axial position of maximum aerofoil thickness. The result is a better understanding of the process taking place at the foil-plate junction through a collection of pressure, vorticity, velocity, and skin friction data from numerous surfaces and planes surrounding the junction.

4.2 APPROACH

4.2.1 Boundary Layer and Aerofoil Variations

To examine how interference drag is affected by the thickness of the support and boundary layer thickness at the support, the configuration is modelled as an aerofoil intersecting a flat plate. Figure 4.1 shows the sign convention used throughout the simulation.

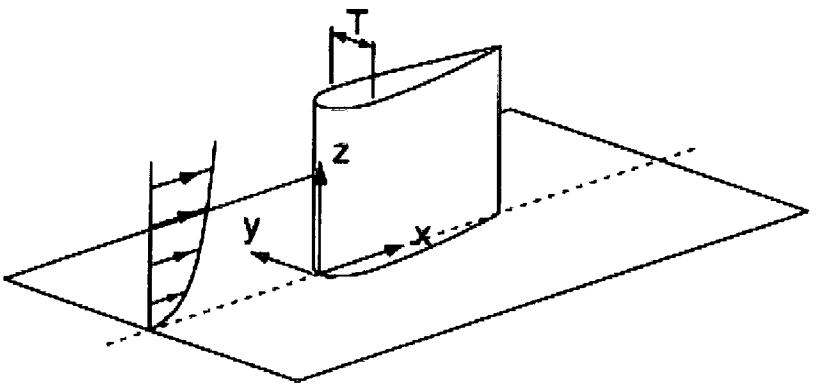

Figure 4.1: Sign convention used throughout simulation.

Four different boundary layer disturbance thicknesses (δ) of 6.1mm, 12.0mm, 16.6mm, and 22.9mm were used. The velocity profiles as a function of height above the plate (z) for the four boundary layers were determined using the idealised Prandtl $1/7^{th}$ rule described earlier in Equation 1.1.

Each of the four boundary layer disturbance thicknesses was determined considering viscous flow growing from a distance of 250mm, 500mm, 750mm, and 1000mm, respectively, upstream from the velocity inlet to the test section. From these four boundary layer disturbance thicknesses, boundary layer displacement thicknesses (δ*) of 0.86mm, 1.51mm, 2.08mm, and 2.86mm, were determined using Equation 1.3. Non-dimensionalising using the 100mm aerofoil chord gives δ*/c=0.009, 0.015, 0.021 and 0.029.

An approximate value of the boundary layer disturbance thickness at the location of the strut-model junction as tested on the models in Chapter 3 is (δ*) 1.80mm, making the growth of a viscous boundary layer from a distance of up to a meter upstream ample for comparison to those that would grow on the roof of a 25-40% scale model, however, flow upstream of the junction on a model vehicle would be more complex depending on the detailed geometry. In order to explore the effects of a changing boundary layer on interference, four different boundary layer disturbance thicknesses were tested.

As well as varying the plate boundary layer, the aerofoil thickness and section were also varied. A collection of six different aerofoil profiles from two different NACA series' were used. The first set were NACA 4-digit aerofoils with their maximum thickness at 30% of the chord and included thickness-to-chord (T/c) ratios of 6%, 12%, and 21%. The second set was from the NACA 66-series. The NACA 66-series aerofoils are a laminar series aerofoil. The fundamental difference of these aerofoils from the NACA 4-digit series is the movement of the point of maximum thickness (to 50%) and the centre of

pressure (to 60%) further aft along the chord in order to keep a favourable pressure gradient and maintain laminar flow further along the aerofoil surface thus creating minimal drag [Abbot & Von Doenhoff, 1959]. This allows the aerofoils to exhibit a lower drag for a similar T/c ratio when compared to the NACA 4-digit series. The two 66-series aerofoils used for this investigation had a T/c ratio of 12% and 21%. Although not an aerofoil at all, the sixth 'profile' used to complete the range of T/c ratios for each set was a zero width aerofoil (0width), or essentially a vertical flat plate. The T/c ratios of 21% were chosen to compare with the struts used throughout the experimental model wind tunnel tests of Chapter 3.

The results of this approach method aim to provide guidelines towards appropriate combinations of boundary layer thickness and aerofoil T/c ratio that will result in a low or acceptable amount of interference a model during testing.

4.2.2 Simulation Technique

Each of the six profiles was tested with each of the four boundary layer displacement thicknesses, creating an array of 24 test cases. The flow simulations were then performed for each test case on the aerofoil and plate in union (Foil-Plate), the plate alone (Plate Alone), and the aerofoil alone (Foil Alone). The amount of interference was then determined by taking the difference of the sum of the forces on the aerofoil and plate in combination and the sum of the forces on the aerofoil and plate alone (Equation 4.1).

Equation 4.1

$$Interference = \left(Foil_{Combined} + Plate_{Combined}\right) - Foil_{Alone} - Plate_{Alone}$$

When testing the 'Foil-Plate' combination and the 'Plate Alone' a free stream velocity of 30m/s was set outside the boundary layer. In the 'Foil Alone,' case there was no plate present, and hence, no boundary layer. This configuration was run with a uniform inlet velocity chosen to match the average momentum in the other cases.

To solve for the uniform velocity of the 'Foil Alone' case the momentum of the two different scenarios was equated to arrive at Equation 4.2. The result yields slightly slower free stream velocities (u_∞) of 29.77m/s, 29.60m/s, 29.44m/s, and 29.30m/s, for each of the previously mentioned boundary layer thicknesses, respectively.

Equation 4.2

$$u_\infty = \sqrt{\frac{1}{z}\int u^2(z)dz}$$

Each of these velocities was then used as the free stream velocity for the 'Foil Alone' configuration allowing it to be related to the appropriate 'Foil-Plate' combination and 'Plate Alone' configuration to solve for the interference in Equation 4.1 at a given boundary layer thickness.

4.2.3 Geometry and Mesh

To appropriately simulate the flow around the desired test cases the CFD solver Fluent 6.1 was used. The geometry was created using its pre-processing counterpart Gambit. The two-dimensional geometry in the xy-plane (shown in Figure 4.2) consisted of a 100mm chord aerofoil profile with its leading edge at the

co-ordinate origin. The velocity inlet was situated at one chords length upstream from the leading edge (x=-100mm). The outflow from the section is placed at one chords length downstream from the foil trailing edge (x=200mm). Because the test case is symmetrical about the aerofoil centreline, only half the test case is modelled, classifying the y=0 plane as a symmetry plane in Fluent. The far field wall is then placed at y=100mm from the symmetry plane. The two dimensional surface has been split into five separate surfaces: 'Plate Front,' 'Plate Mid-Front,' 'Plate Mid-Rear,' 'Plate Rear,' and 'Foil.' This was done so an analysis of effects on specific areas of the plate could be carried out.

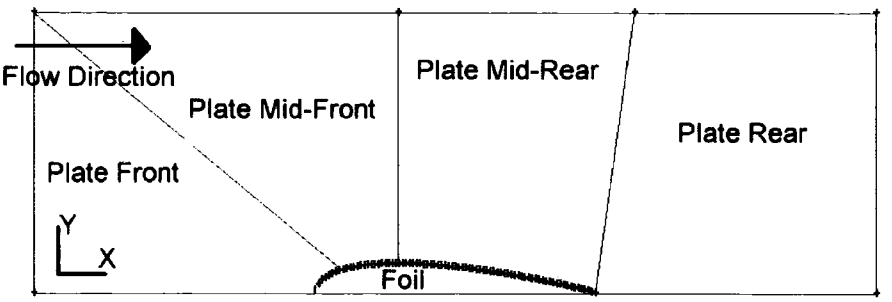

Figure 4.2: Two dimensional geometry and area subdivisions (NACA 0021 aerofoil section shown).

The adopted grid spacing for this two-dimensional case was determined in a pilot study by Wilson [Wilson, 2004]. Wilson refined the grid to achieve the best solution performance while minimising computational time. The mesh was analysed for the optimum value of y^+ near the wall to achieve an appropriate value for use with the Spallart-Allmaras (S-A) turbulence model. Refinement of the node spacing for the grid was first carried out in the two-dimensional plane of Figure 4.2, this plane was then extruded in the third dimension and the z-direction node spacing was defined.

The final grid refinement is shown in Figure 4.3 for the NACA 0021 aerofoil. The figure shows the number of nodes and growth factor along each edge of the two dimensional area subdivisions. The node spacing determined by the growth factors is growing with distance from the aerofoil section, making the mesh more dense at the junction for better definition of the flow in this region.

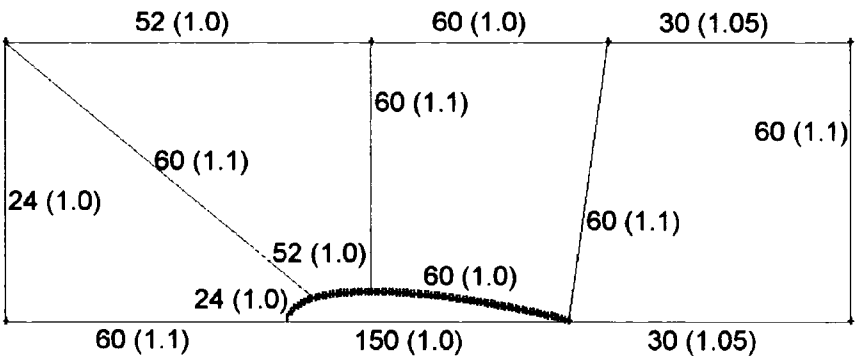

Figure 4.3: Final refinement of two dimensional mesh showing the node count and Growth Factor with a NACA 0021 aerofoil profile [Wilson, 2004].

According to the Fluent Users Manual [Fluent, 2006] a value of y^+ close to unity must be used in order for the S-A model to give good resolution of the wall boundary layer. To achieve this value,

approximately 17,000 cells were required in two dimensions, which when expanded to three dimensions would be very expensive in terms of computational time. In order to save time a sacrifice on y^+ is made in the final refinement by reducing the number of cells along the edges that are normal to the aerofoils profile. This final refinement has approximately 14,000 cells and a value of y^+=4.5. Looking at Figure 4.4, this converges on a drag coefficient value of about C_D=0.72, this same drag value could be achieved using fewer cells (as shown by the graph), but an increased number was required to achieve an appropriate y^+ value for use with the S-A turbulence model.

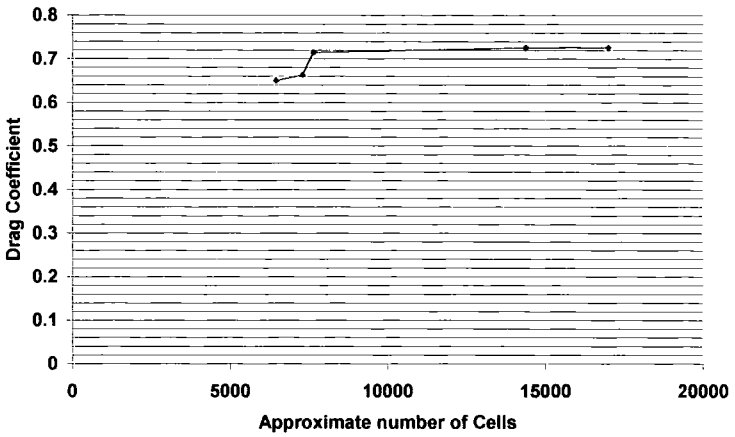

Figure 4.4: Graph of drag convergence for data derived from Wilson [Wilson, 2004].

To create the three-dimensional grid the edges in two dimensions were extruded to a height of z=100mm. The number of nodes was determined by observing the value of y^+ and convergence of C_D near and on the two dimensional surface. Once again the computational time and the suggested y^+ value of the Fluent users manual [Fluent, 2006] were the design criteria. The final grid refinement along the z=100mm edge results in a y^+ value of 6 with 70 nodes.

As mentioned, the 'Foil-Plate' combination, 'Plate Alone,' and 'Foil Alone' will all be used in comparison to find interference on the plate. Because of this the three-dimensional cases for a particular aerofoil section were all derived from the same two-dimensional grid so that there would be no discrepancies during comparison due to changes in grid structure. This meant that only one two-dimensional grid had to be developed and then the three, three-dimensional test cases could be defined by simply changing the surface classification in Fluent. This also meant that the area inside the two dimensional aerofoil section of Figure 4.3 had to be meshed. Because the same two dimensional surface would be used for the plate with ('Foil-Plate') and without ('Plate Alone') the aerofoil present, a mesh had to be placed inside the aerofoil section so that when the aerofoil surface (in the third dimension) was removed and classed as 'Interior' in Fluent, the portion of the plate that it uncovered was meshed.

The created two-dimensional mesh can be seen in full view in Figure 4.5. The mesh on the inside of the aerofoil section was resolved using a triangular pave to accommodate the uneven number of nodes on its edges and the remaining surface used a quadrilateral map. A closer view of the mesh surrounding the aerofoil can be found in Figure 4.6, and a view of the mesh around the aerofoil leading edge is seen in Figure 4.7.

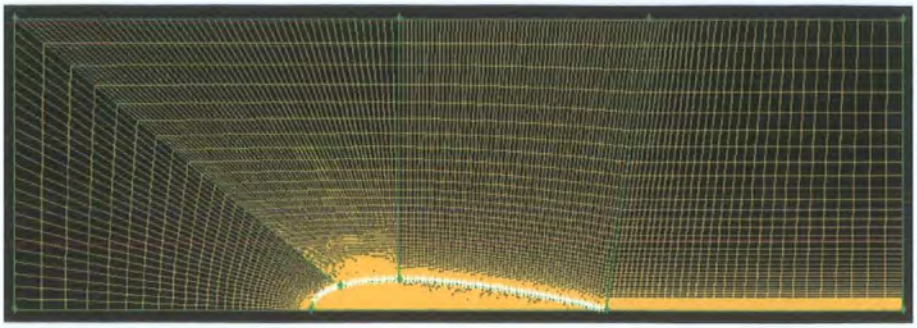

Figure 4.5: Full view of two-dimensional mesh from x: -100mm to 200mm and y: 0 to 100mm for NACA 0021 profile.

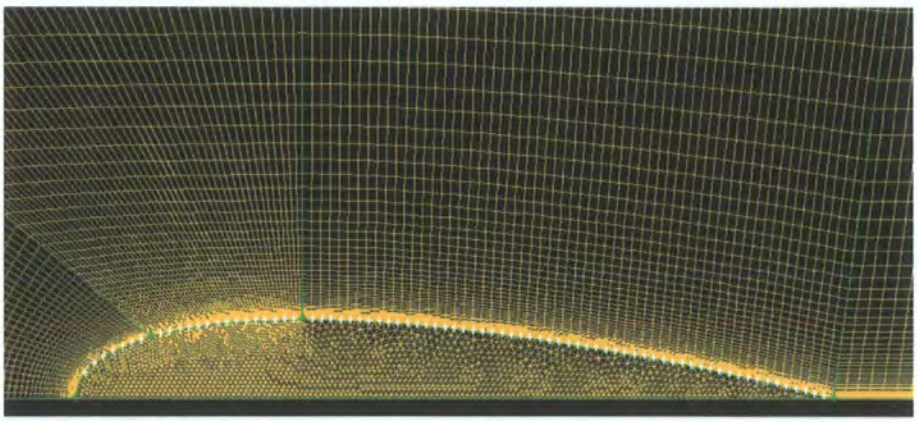

Figure 4.6: Two dimensional mesh inside and surrounding the aerofoil for the NACA 0021 profile.

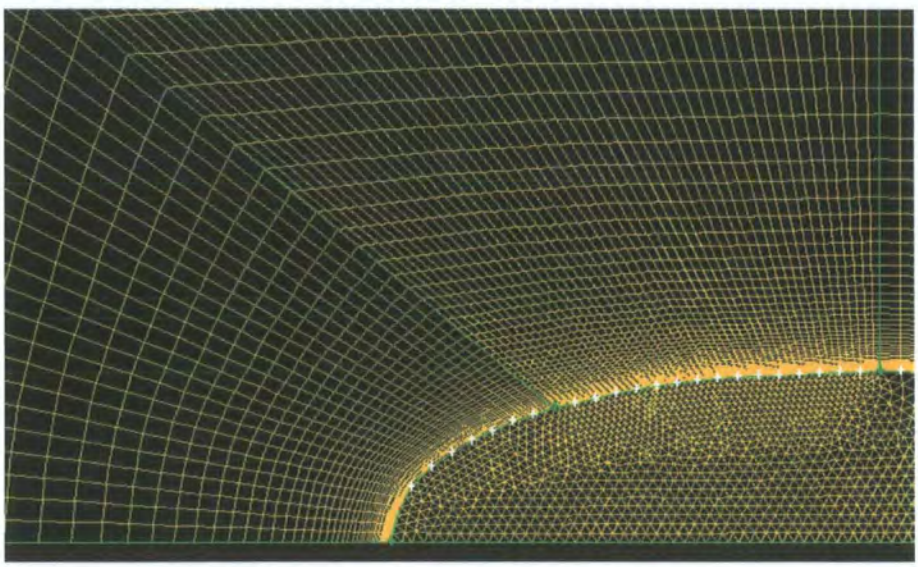

Figure 4.7: Two dimensional mesh at leading edge of NACA 0021 profile.

4.2.4 Solution Controls

Initially, for the first one hundred iterations, the solution controls were left at their default values for all test cases. The default settings were:

Pressure-Velocity Coupling:	SIMPLE
Discretization:	Pressure – Standard Momentum/Modified Turbulent Viscosity – First Order Upwind
Under-Relaxation Factors:	Pressure – 0.3 Density – 1.0 Body Forces – 1.0 Momentum – 0.7 Modified Turbulent Viscosity – 0.8 Turbulent Viscosity – 1.0

After the first one hundred iterations the solution controls were adjusted on a case by case basis to achieve an improved solution. With the exception of the 0width and NACA 0006 'Foil Alone' case, which had their under relaxation factors halved after the first one hundred iterations to achieve better accuracy, the values for the under relaxation factors were left at their default settings throughout all the iterations for all cases.

The discretisation of the pressure equations was changed to 2^{nd} order after the first hundred iterations and the pressure-velocity coupling was left at the default setting throughout the entire simulation. For the 'Foil-Plate' combination and 'Foil Alone' configurations for all aerofoil profiles, the tri-paved mesh inside aerofoil section was considered a solid and only the quad paved mesh on and above the plate was used in the computation. This uniform structuring of the grid and its alignment with the flow meant the QUICK scheme would be best used for the momentum and modified turbulent viscosity equations and was altered from the default after the first one hundred iterations.

As mentioned, the simpler one equation S-A model was chosen to represent viscous turbulence in the flow. Although this model has been criticised for its ability to calculate the shear layer length scale in areas such as the aerofoil trailing edge where the flow boundary changes from a solid to free shear, the model was designed specifically for aerospace applications involving wall bounded flows. It provides good results for boundary layers in adverse pressure gradients [Fluent, 2006], and is suggested over the two equation k-ε model by Paciorri et al [Paciorri et al., 2002].

4.3 RESULTS

4.3.1 Solution Convergence and number of iterations

The residual computed by Fluent's segregated solver is the amount of imbalance from the conservation of mass equation summed over all the computational cells. To judge convergence, the residual is scaled using a factor representative of the flow rate through the domain and then observed over each of the iterations to see when it converges to a value below 10^{-3}. For the continuity equation, the scaling factor is the absolute value of the continuity residual from the first five iterations [Fluent, 2006]. Observing the

residual histories for all of the different test cases, it was noticed that the simulations using the smallest boundary layer thicknesses took the longest to converge on a solution. Because of this, only these cases were used as a guideline to determine the appropriate number of iterations that each simulation must perform in order to converge on an appropriate solution.

Figure 4.8 through Figure 4.10 show the residual convergence history for the 'Foil-Plate', 'Plate Alone', and 'Foil Alone' test cases for each of the aerofoils tested. Observing Figure 4.8, the slowest convergence occurs for the 0 width case where the continuity equation does not drop below 10^{-3} until approximately 1000 iterations, all the other aerofoil cases from this figure drop below the prescribed value prior to this. Observing Figure 4.9 for the 'Plate Alone' case, the continuity equation barely asymptotes at 10^{-3} for all aerofoil profiles except the NACA 66-021, which asymptotes at a slightly smaller value. Running the simulations out to 1200 iterations does not noticeably improve the convergence. The consistency amongst these cases was expected because they are essentially simulating the same geometry, but each with a slightly different mesh due to the different shaped aerofoil profiled triangular paves incorporated into the plate. For the 'Foil Alone' cases in Figure 4.10 convergence occurs quickly (within 400 iterations) for all cases except the 0width, which does not converge to a value below 10^{-3}. For more easily solved cases such as the 0width 'Foil Alone' and the 'Plate Alone' cases, which are only simulating viscous flow over a flat plate, this method of observing scaled residuals to judge convergence can fail. Because the simulated case is simple, the initial 5 iterations from which the scaling factor is derived are too accurate, resulting in a large scaled residual for the continuity equation that does not approach the prescribed scaled value of 10^{-3}. In these cases it was best to look at the un-scaled residual or another relevant integrated quantity to judge convergence. For this reason C_D on the rear of the plate after the trailing edge was also monitored to judge convergence. Results from 1200 iterations showed a maximum fluctuation from all cases and configurations of 7.0×10^{-5}, 0.5% of the measured drag coefficient for the monitored surface. The analysis led to the decision that 1200 iterations would safely allow solution convergence for all test configurations, boundary layer thicknesses, T/c ratios, and axial position of maximum thickness.

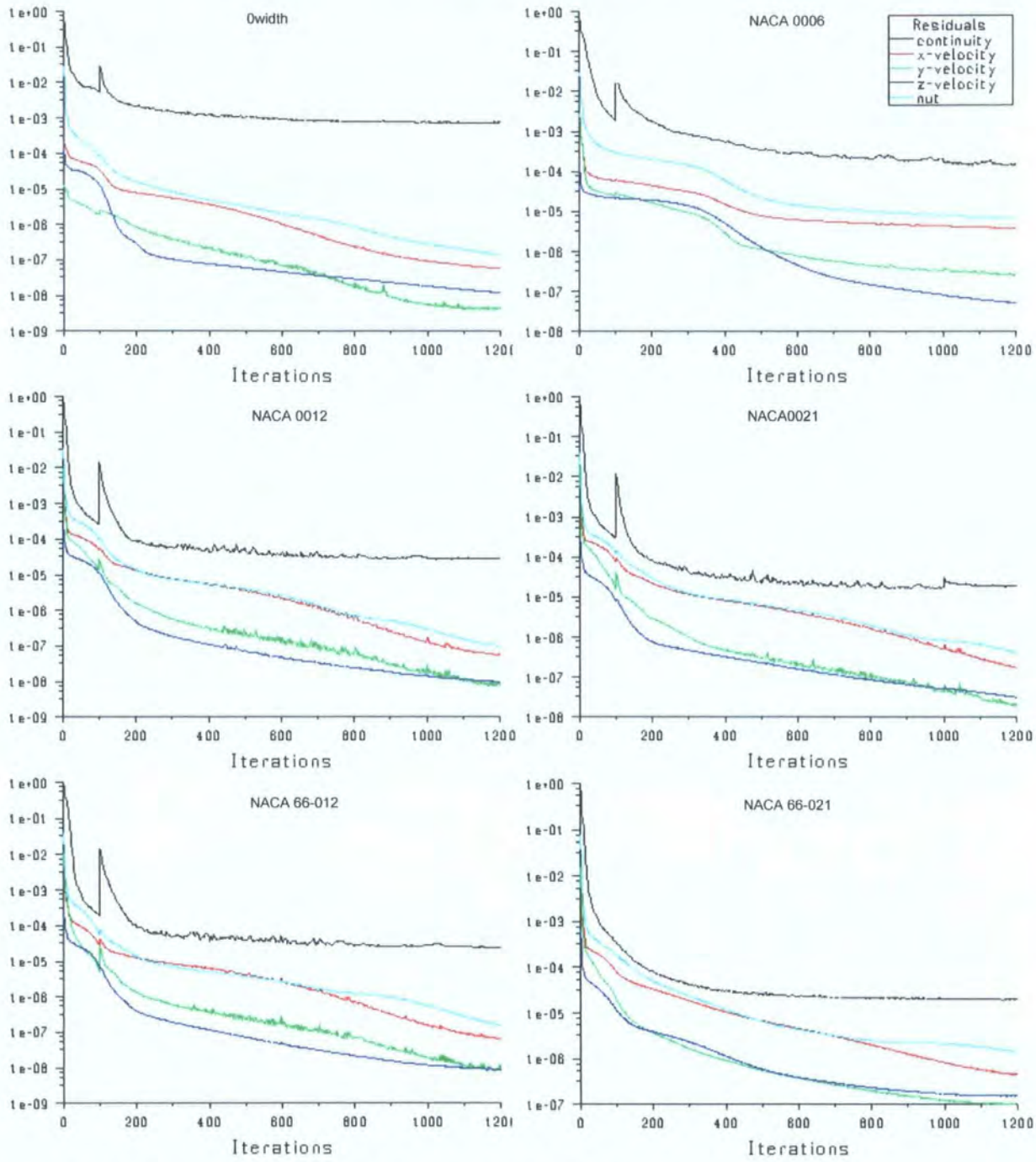

Figure 4.8: Residual convergence for Foil-Plate. δ/c=0.009.*

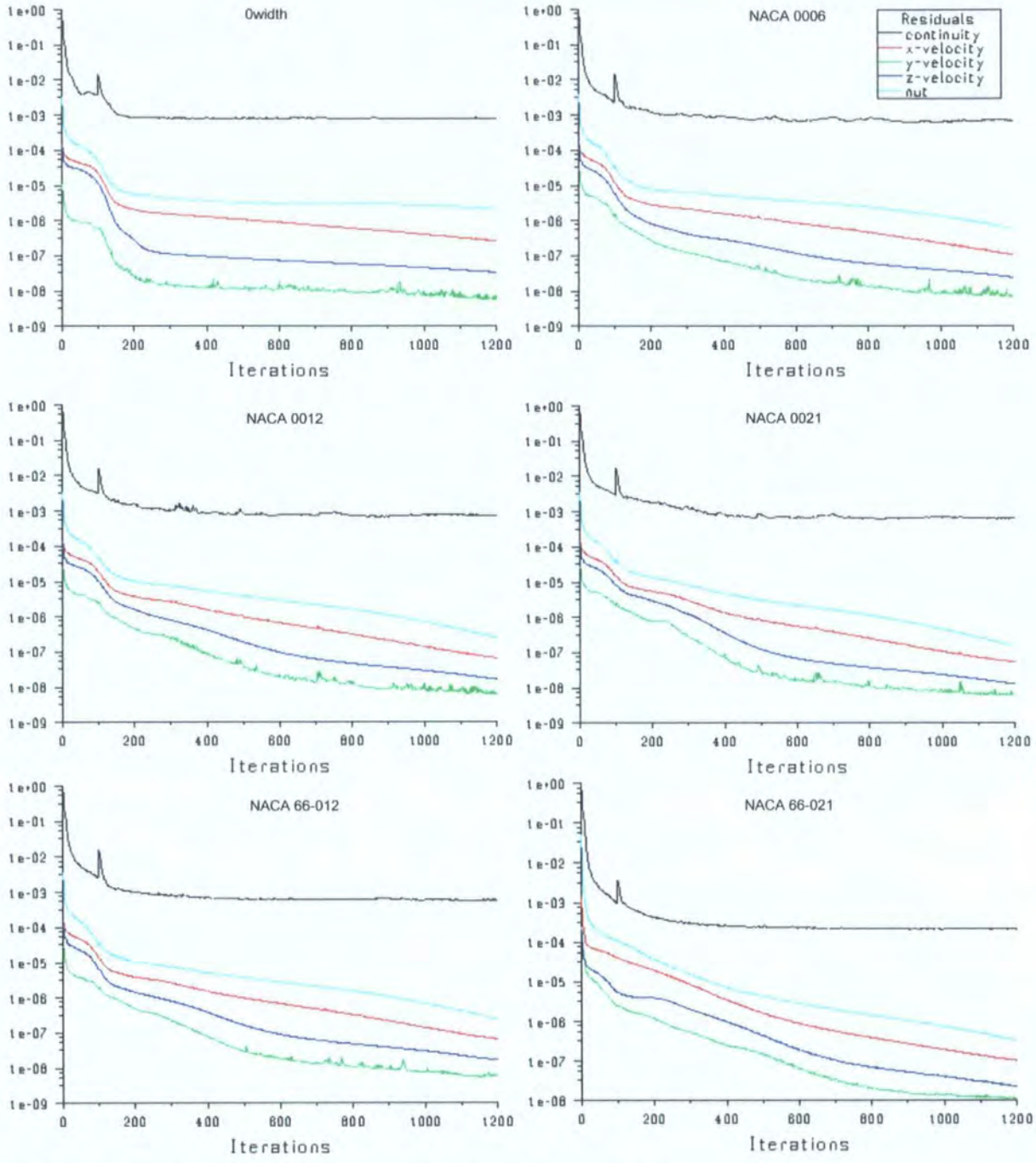

Figure 4.9: Residual convergence for Plate Alone. δ/c=0.009.*

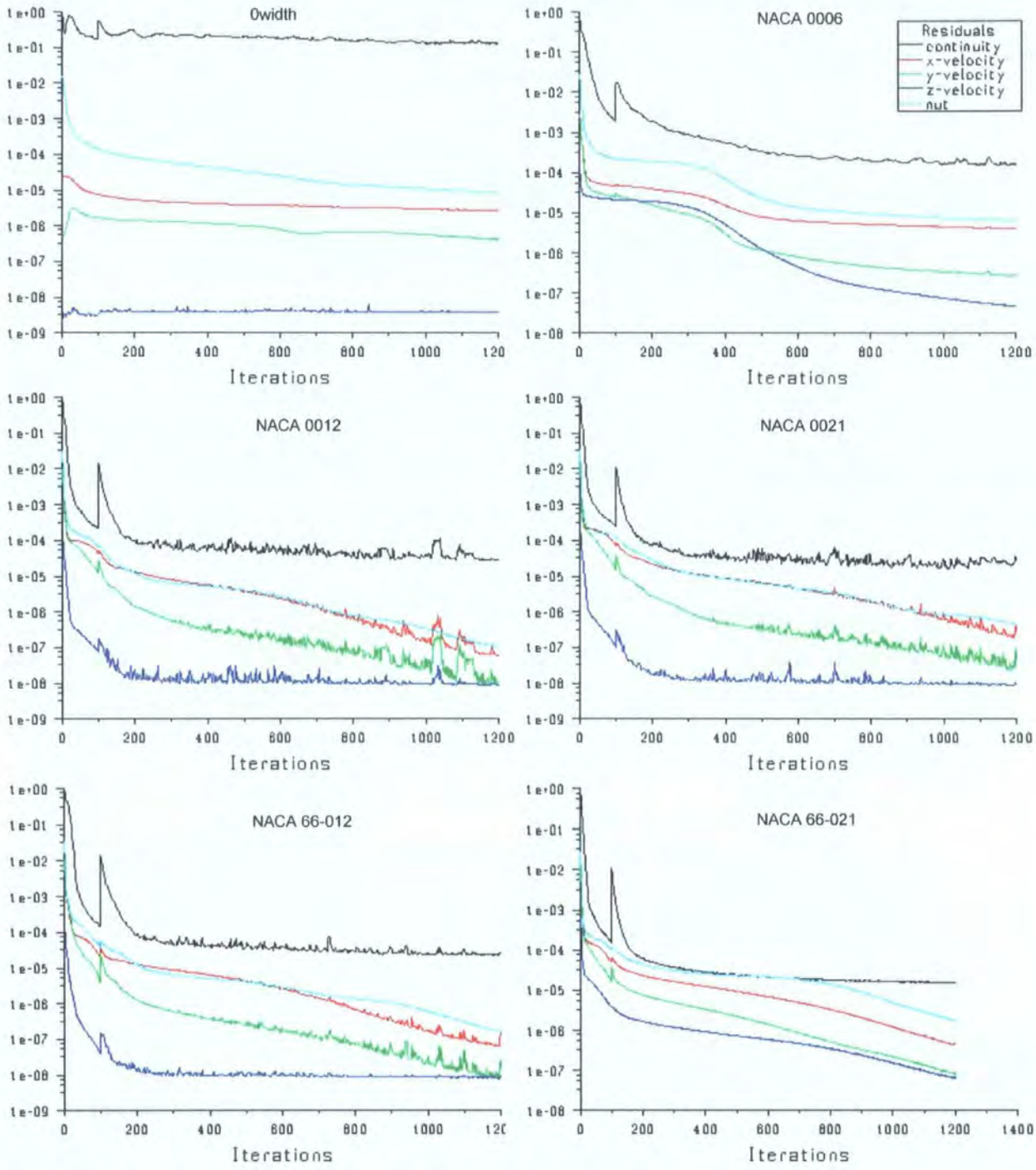

Figure 4.10: Residual convergence for Foil Alone. δ/c=0.009.*

4.3.2 Interference Drag

Figure 4.11 and Figure 4.12 show the interference drag coefficient (C_{Di}) produced from the interference forces calculated by Equation 4.1. The coefficients were non-dimensionalised using the chord area (c^2) and the free stream velocity outside of the boundary layer (30 m/s). The graphs compare C_{Di} and T/c for each of the NACA series and boundary layer thicknesses. Observing Figure 4.11 an increase in boundary layer provides a small increase in C_{Di} for all NACA 4-digit aerofoil T/c ratios above 0%, however, it is obvious that an increase in T/c ratio has the greatest impact. For the laminar series, in Figure 4.12, a

change in boundary layer has almost no effect for T/c ratios less than 12%. Above this, the effect due to a change in boundary layer is still small, but greater than the change that was seen for the 4-digit aerofoils. Once again a change in T/c ratio has the larger effect.

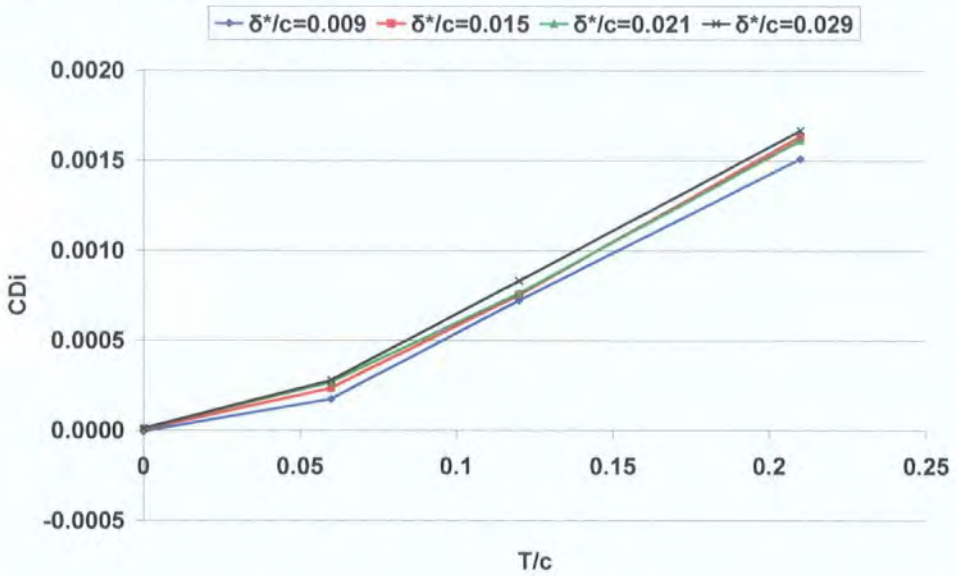

Figure 4.11: Interference drag coefficient vs. thickness-to-chord ratio for the NACA 4-digit series aerofoils at δ/c=0.009, 0.015, 0.021, and 0.029.*

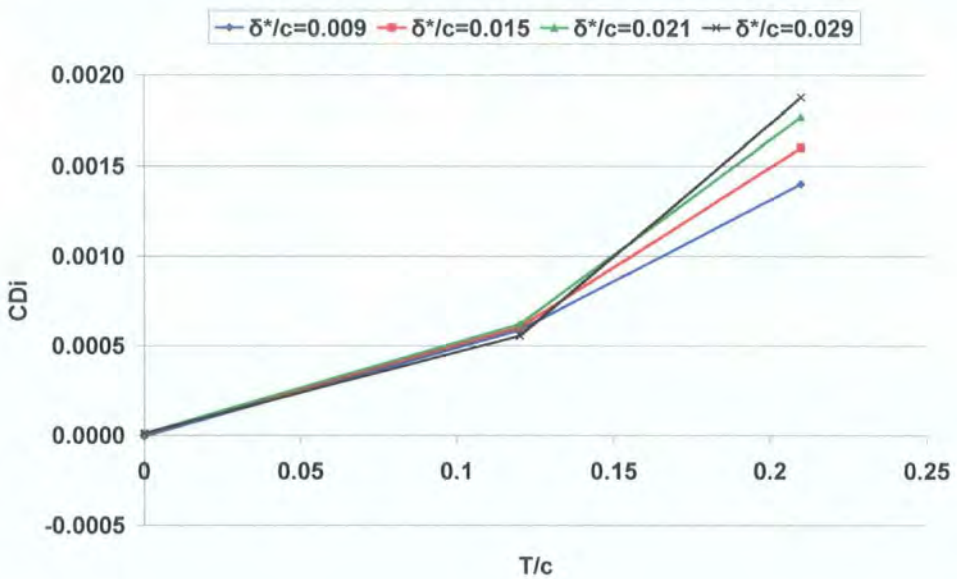

Figure 4.12: Interference drag coefficient vs. thickness-to-chord ratio for the NACA 66-series aerofoils at δ/c=0.009, 0.015, 0.021, and 0.029.*

Hoerner [Hoerner, 1965] predicted that interference drag would be negative for T/c<8% and that laminar type sections with their point of maximum thickness at 50% of the chord would produce a higher interference drag than sections with their point of maximum thickness at 30% of the chord. Despite these predictions, the findings of this investigation do not show an appreciably greater interference for the laminar series aerofoils and the interference for T/c ratios less than 8% does not go negative. When plotting Equation 1.10 against the results of Figure 4.11 in Figure 4.13 there is good agreement for small

T/c ratios, but at T/c ratios above 12%, these results do not agree with the amount of interference predicted by Hoerner.

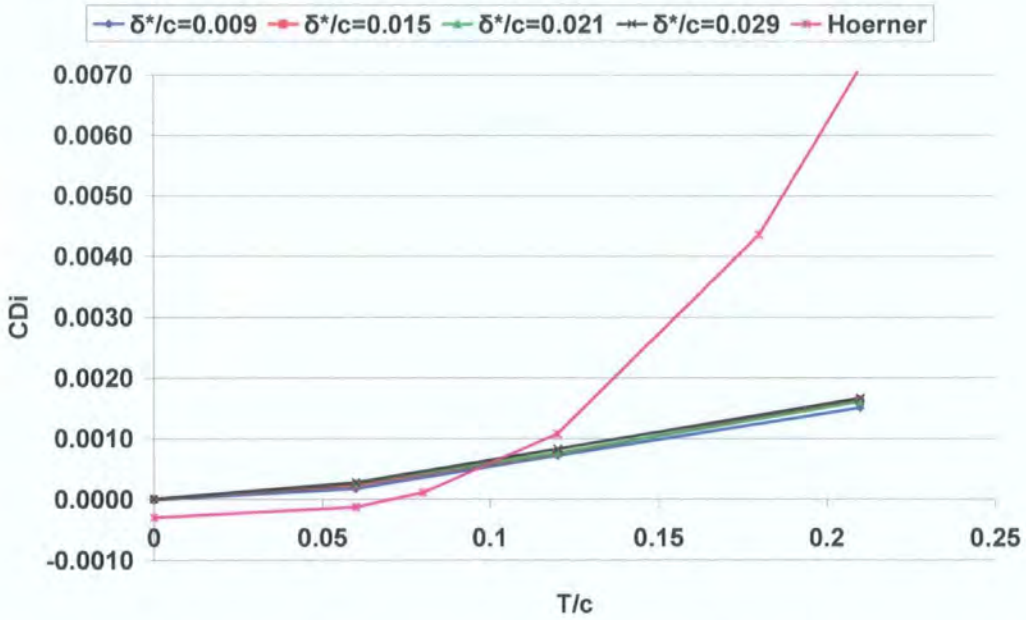

Figure 4.13: Comparison of NACA 4-digit data to Hoerner's formula.

C_{Di} of Figure 4.11 and Figure 4.12 above is on the simulated model as a whole, not indicative of which surface, or part thereof, the extra drag is created. In terms of model testing in wind tunnels, the interest is the change in force on the planar surface that represents the vehicle. In order to see where the majority of the change in forces falls the surfaces of the junction have been segregated and labelled in Figure 4.14. A portion of the plate that is not visible in Figure 4.14, but is included in the surface dubbed 'PlateF' when it is used in Equation 4.1 is found beneath the aerofoil, on the plate and was seen in the two-dimensional representation of the plate of Figure 4.2 as 'Foil'. Pressure, viscous, and total forces are presented for the individual surfaces of the junction in Table 4.1 and Table 4.2.

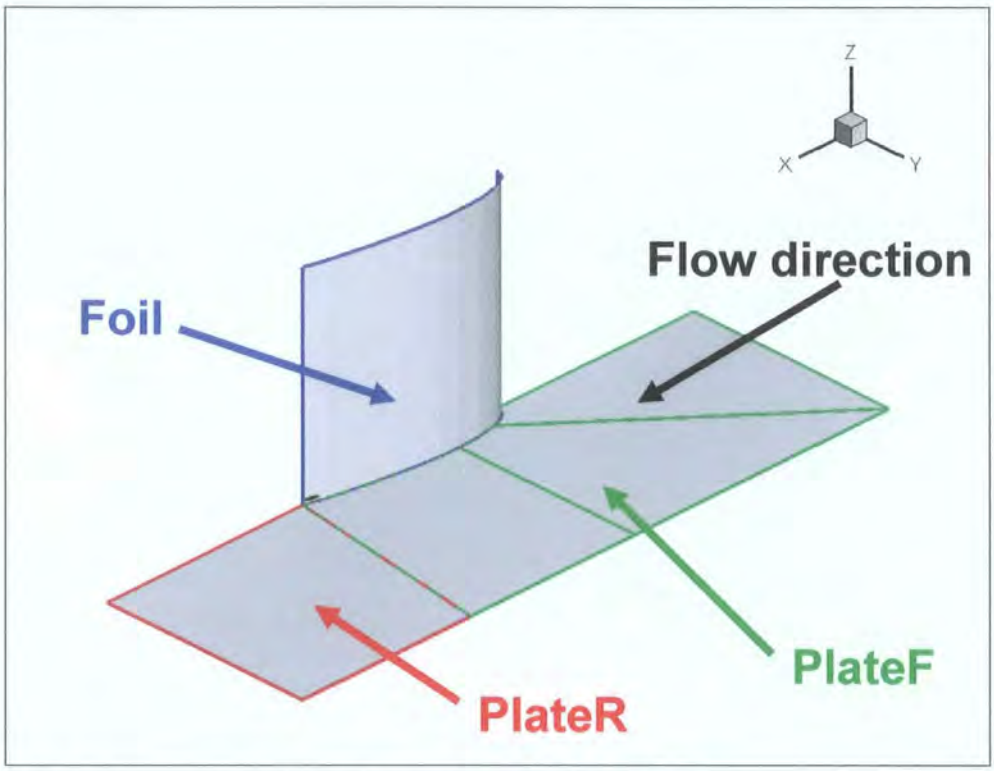

Figure 4.14: Segregation of junction surfaces for force breakdown.

For both NACA series the values in Table 4.1 and Table 4.2 show that interference forces responsible for the extra drag fall predominantly on the aerofoil and are mostly the effect of increased pressure drag. The remainder of the interference drag falls on the plate in the form of viscous drag. Looking at the force breakdown for the two regions of the plate ('PlateF' and 'PlateR') shows that the interfering aerofoil actually decreases drag on the plate behind the aerofoil trailing edge, but causes a larger increase of drag on the front portion of the plate making the overall interference effect on the plate positive.

Observing Table 4.1 and Table 4.2 the largest interference magnitude is the Total Drag value (0.0019) for the NACA 66_4-021 aerofoil in the thickest boundary layer. Translating this value from the chord area of the aerofoil used (A_c=0.01m^2) to a typical frontal area of a 25-40% scale model (A_f=0.1-0.3m^2) results in approximately 0.000063-0.00019 on drag coefficient. Assuming that the overhead strut and each of the four wheel stings would produce this effect alone and multiplying by five supports; the maximum amount of interference for the smallest frontal area results in only 1 count. Although this is an unrealistic assumption to make because the wheel stings with their blunt profile would undoubtedly result in a greater interference effect, the overall effect that originates at the junction would still be small relative to that seen from the use of all five supports seen in Chapter 3.

	0021			0012			0006		
δ*/c=0.009	*Press.*	*Visc.*	*Total*	*Press.*	*Visc.*	*Tot.*	*Press.*	*Visc.*	*Tot.*
Foil	0.0010	0.0001	0.0011	0.0005	0.0001	0.0005	0.0001	0.0000	0.0001
PlateF.	0.0000	0.0006	0.0006	0.0000	0.0003	0.0003	0.0000	0.0002	0.0002
PlateR.	0.0000	-0.0002	-0.0002	0.0000	-0.0001	-0.0001	0.0000	-0.0001	-0.0001
Total	0.0010	0.0005	0.0015	0.0005	0.0003	0.0007	0.0001	0.0001	0.0002
δ*/c=0.015	*Press.*	*Visc.*	*Tot.*	*Press.*	*Visc.*	*Tot.*	*Press.*	*Visc.*	*Tot.*
Foil	0.0011	0.0001	0.0012	0.0004	0.0001	0.0005	0.0001	0.0000	0.0001
PlateF.	0.0000	0.0006	0.0006	0.0000	0.0003	0.0003	0.0000	0.0002	0.0002
PlateR.	0.0000	-0.0002	-0.0002	0.0000	-0.0001	-0.0001	0.0000	-0.0001	-0.0001
Total	0.0011	0.0006	0.0016	0.0004	0.0003	0.0008	0.0001	0.0001	0.0002
δ*/c=0.021	*Press.*	*Visc.*	*Tot.*	*Press.*	*Visc.*	*Tot.*	*Press.*	*Visc.*	*Tot.*
Foil	0.0010	0.0001	0.0012	0.0004	0.0001	0.0005	0.0001	0.0000	0.0001
PlateF.	0.0000	0.0007	0.0007	0.0000	0.0003	0.0003	0.0000	0.0000	0.0002
PlateR.	0.0000	-0.0002	-0.0002	0.0000	-0.0001	-0.0001	0.0000	-0.0001	-0.0001
Total	0.0010	0.0006	0.0016	0.0004	0.0003	0.0008	0.0001	0.0001	0.0003
δ*/c=0.029	*Press.*	*Visc.*	*Tot.*	*Press.*	*Visc.*	*Tot.*	*Press.*	*Visc.*	*Tot.*
Foil	0.0011	0.0002	0.0012	0.0005	0.0001	0.0006	0.0001	0.0000	0.0002
PlateF.	0.0000	0.0005	0.0003	0.0000	0.0004	0.0004	0.0000	0.0002	0.0002
PlateR.	0.0000	-0.0002	-0.0002	0.0000	-0.0001	-0.0001	0.0000	-0.0001	-0.0001
Total	0.0011	0.0006	0.0017	0.0005	0.0003	0.0008	0.0001	0.0001	0.0003

Table 4.1: Pressure, viscous, and total drag coefficient breakdown for the surfaces of the junction for the NACA 4-digit series aerofoils.

	66-021			66-012		
δ*/c=0.009	*Press.*	*Visc.*	*Tot.*	*Press.*	*Visc.*	*Tot.*
Foil	0.0011	0.0000	0.0012	0.0003	0.0001	0.0004
PlateF.	0.0000	0.0005	0.0005	0.0000	0.0003	0.0003
PlateR.	0.0000	-0.0003	-0.0003	0.0000	-0.0001	-0.0001
Total	0.0011	0.0003	0.0014	0.0003	0.0002	0.0006
δ*/c=0.015	*Press.*	*Visc.*	*Tot.*	*Press.*	*Visc.*	*Tot.*
Foil	0.0013	0.0001	0.0013	0.0003	0.0001	0.0004
PlateF.	0.0000	0.0005	0.0005	0.0000	0.0003	0.0003
PlateR.	0.0000	-0.0003	-0.0003	0.0000	-0.0001	-0.0001
Total	0.0013	0.0003	0.0016	0.0003	0.0003	0.0006
δ*/c=0.021	*Press.*	*Visc.*	*Tot.*	*Press.*	*Visc.*	*Tot.*
Foil	0.0014	0.0001	0.0015	0.0003	0.0001	0.0004
PlateF.	0.0000	0.0005	0.0005	0.0000	0.0004	0.0004
PlateR.	0.0000	-0.0002	-0.0002	0.0000	-0.0001	-0.0001
Total	0.0014	0.0004	0.0018	0.0003	0.0003	0.0006
δ*/c=0.029	*Press.*	*Visc.*	*Tot.*	*Press.*	*Visc.*	*Tot.*
Foil	0.0015	0.0001	0.0016	0.0002	0.0001	0.0003
PlateF.	0.0000	0.0005	0.0005	0.0000	0.0004	0.0004
PlateR.	0.0000	-0.0002	-0.0002	0.0000	-0.0001	-0.0001
Total	0.0015	0.0004	0.0019	0.0002	0.0003	0.0006

Table 4.2: Pressure, viscous, and total drag coefficient breakdown for the surfaces of the junction for the NACA 66-series aerofoils.

4.3.3 Flow Mechanisms

Despite the fact that the magnitude of the interference effects are small when compared to that of the full model, the flow structure at the junction is still analysed to see the size and stream wise extent of the horseshoe vortex system. Although the added pressure and viscous force to the plate surface is small, the down stream extension of flow features from the junction and support wake were proven earlier to be influential on the amount of interference seen on a full model vehicle.

For an aerofoil shaped appendage normal to a planar surface, two separations at the junction are well known and described in the literature review of Section 1.7.1. The first is produced by an interaction of the plate boundary layer and aerofoil leading edge. The initial rotation is created when the span wise velocity gradient in the plate boundary layer is turned at the leading edge stagnation point. This rotation is then picked up by oncoming flow and protracted around both sides of the aerofoil nose in the seam of the junction creating what is referred to as the horseshoe or necklace vortex.

The second separation occurs at the rear of the aerofoil where an interaction of the boundary layers creates a momentum deficiency that causes a trailing edge separation similar to that seen on an aerofoil in free air. Although this type of separation can be witnessed on an aerofoil in free air, an aerofoil that may not have a separation in free air can easily be provoked into one by the presence of the plate. Both of these separations are witnessed here within the computational work. The size, intensity, and interference of which are dependent on both the thickness of the plate boundary layer intersecting the aerofoil and the bluntness of the aerofoil joined to the plate.

4.3.3.1 Flow Mechanisms of the Flat Plate Alone

Figure 4.15 and Figure 4.16 showing C_{fx} and C_p, respectively, on the plate in isolation have been prepared so that the extent of change created by the aerofoil on the plate can be seen and comparisons can be made. Although they all represent the same plate surface, there are four sub-figures (a, b, c, and d) in both Figure 4.15 and Figure 4.16 to show the four different plate meshes that are used for the 0width, NACA 0006, NACA 0012, and NACA 0021 aerofoil sections. As described earlier in Section 4.2.3 the two-dimensional 'Plate Alone' surface is a hybrid of two mesh types; a quad map on the 'Plate Front,' 'Plate Mid-Front,' 'Plate Mid-Rear,' and 'Plate Rear' (from Figure 4.2) and a tri pave on the 'Foil' surface. When the T/c ratio or position of maximum thickness is changed, the tri paved mesh area will change accordingly to accommodate the new section profile, thus changing the overall composition of the 'Plate Alone' mesh. Four separate figures have been shown to observe any differences that may be present due to the alteration of the mesh and to use for comparison with changes that will occur when the 'Plate-Foil' case is examined. Each of the four figures (a through d) are also plotted at different scales, this is so they will coincide and directly compare with the scales used on their counterparts of the 'Foil-Plate' cases shown later.

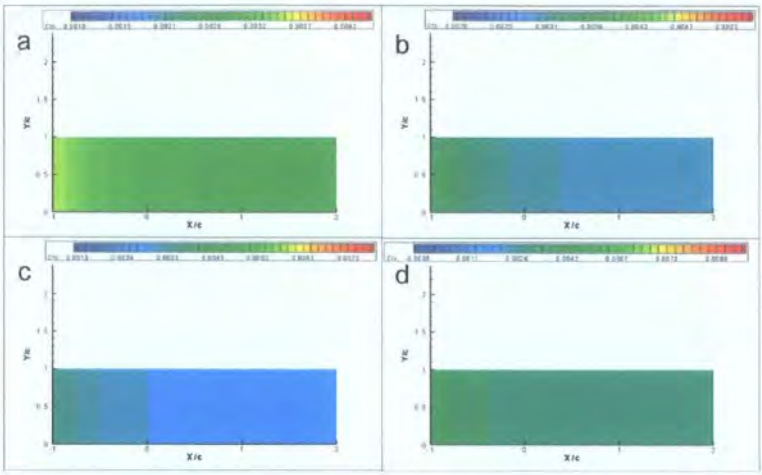

Figure 4.15: Skin friction coefficient on the Plate Alone with δ/c=0.029 for the a)0width, b)NACA 0006, c)NACA 0012, and d)NACA0021 meshes.*

On the plate alone without the presence of the aerofoil there is a general decrease in C_{fx} and C_p moving downstream along the plate, due to the developing boundary layer. However, at this scale these changes are small and insignificant, making the effects of aerofoil placement easily recognisable. On the larger scales used in Figure 4.15c&d and Figure 4.16c&d to capture the range of effects from the thicker aerofoils, very little change is noticeable. The same trends were witnessed for the NACA 66-series aerofoils and therefore not necessary to plot.

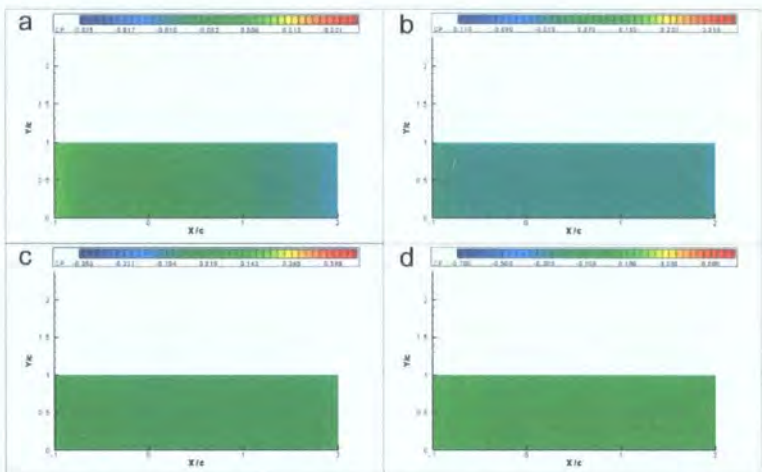

Figure 4.16: Pressure coefficient on the Plate Alone with δ/c=0.029 for the a)0width, b)NACA 0006, c)NACA 0012, and d)NACA0021 meshes.*

4.3.3.2 Flow Mechanisms of the 0width Aerofoil

Without any finite thickness, the 'Foil-Plate' case has no reversed flow in front of the aerofoil signifying formation of a horseshoe vortex nor is there a trailing edge separation. Furthermore, the small scale separation created by an interaction of the boundary layers that is present, is not influential enough to inspire free stream air into the junction. This makes the overall separation at the junction small and any interference on the plate insignificant as the previous drag data suggested in Figure 4.12 and Figure 4.13.

Figure 4.17 for the 0width aerofoil shows what little effect there is on the plate created by the aerofoil. There is a low positive skin friction across the entire plate, which decreases at the rear just as it did for the

'Plate Alone' in Figure 4.15. Proof of the weak interaction of the boundary layers on the two surfaces can be seen by a sliver of low skin friction, in the corner of the junction starting at x/c≈0.5 and extending to the outlet plane at x/c=2.0 just along the plots x-axis in Figure 4.17a. This is most easily visible in the inset, 'A' from Figure 4.17c at a different scale in Figure 4.18. In Figure 4.17b the variation of skin friction caused by the formation is more easily seen on the aerofoil surface, not on the plate. In fact, when placed on the same scale as the aerofoil surface in Figure 4.17a, the visible formation on the plate becomes less obvious suggesting that the majority of a change in force will fall on the aerofoil and not the plate for this configuration as predicted by the interference data for thicker aerofoils in Table 4.1 and Table 4.2.

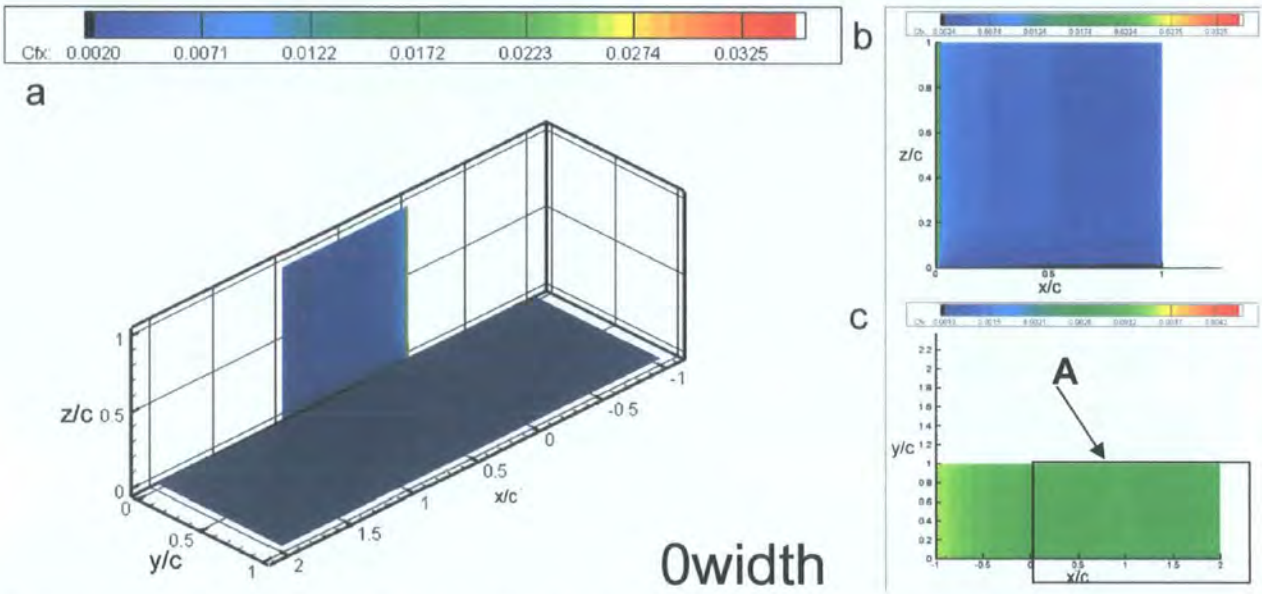

Figure 4.17: Skin friction coefficient of the 0width Foil-Plate case at δ/c=0.029 showing a)a three dimensional view of the junction, b)a two dimensional view of the aerofoil surface, and c)a two dimensional view of the flat plate.*

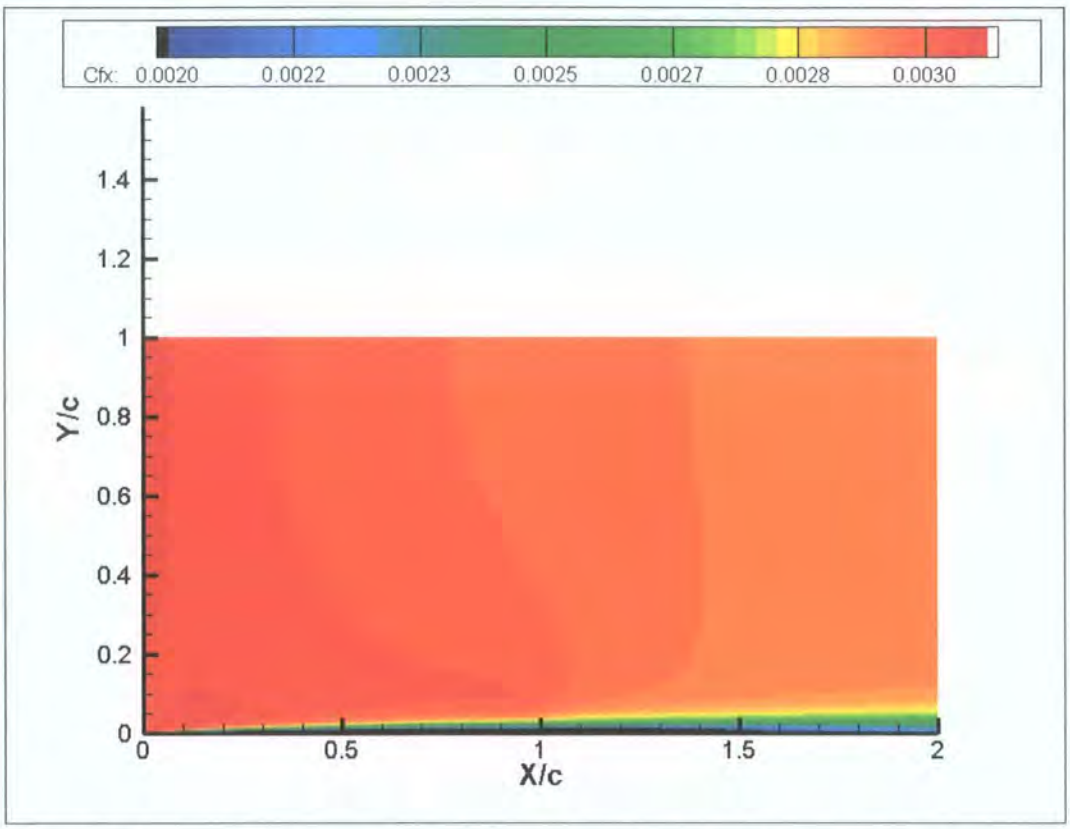

Figure 4.18: Inset A, showing skin friction coefficient on the plate when in junction with the 0width aerofoil for δ/c=0.029.*

4.3.3.3 Flow Mechanisms of the NACA 4-Digit Aerofoils

Figure 4.19 and Figure 4.20 show C_{fx} on the surfaces of the junction allowing the formation and passage of the horseshoe vortex to be determined. Starting at the leading edge of the aerofoil in Figure 4.19a and Figure 4.20 there is a negative skin friction area (marked 'A') where streamlines from the boundary layer roll up and head in the upstream direction. Following the vortex around the seam of the junction, the skin friction quickly becomes positive and increases to a maximum just before the point of maximum thickness at x/c≈0.2 as the vortex is stretched around the aerofoil nose. As the vortex propagates downstream from the maximum thickness along the aerofoil surface C_{fx} reduces, indicating a dispersion of vortex intensity. As the aerofoil thickness decreases the second, trailing edge separation (marked 'B'), shown as the area of negative skin friction at the aerofoil trailing edge, begins at about x/c≈0.75. Adjacent to the trailing edge separation an area of low skin friction (marked 'C' in Figure 4.20) is found on the outboard side of the horseshoe vortex passage. This low skin friction area is the result of the plate boundary layer outside the separation line and the horseshoe vortex interacting and slowing the fluid in this region. Between the trailing edge separation and the adjacent area of low skin friction the passage of the horseshoe vortex as it is deflected away from the symmetry plane by the trailing edge separation can clearly be seen. In keeping with the results seen in Section 4.3.2 the majority of effects seen on both the plate and aerofoil are an increased skin friction resulting in the increase in drag created by the junction of the two components.

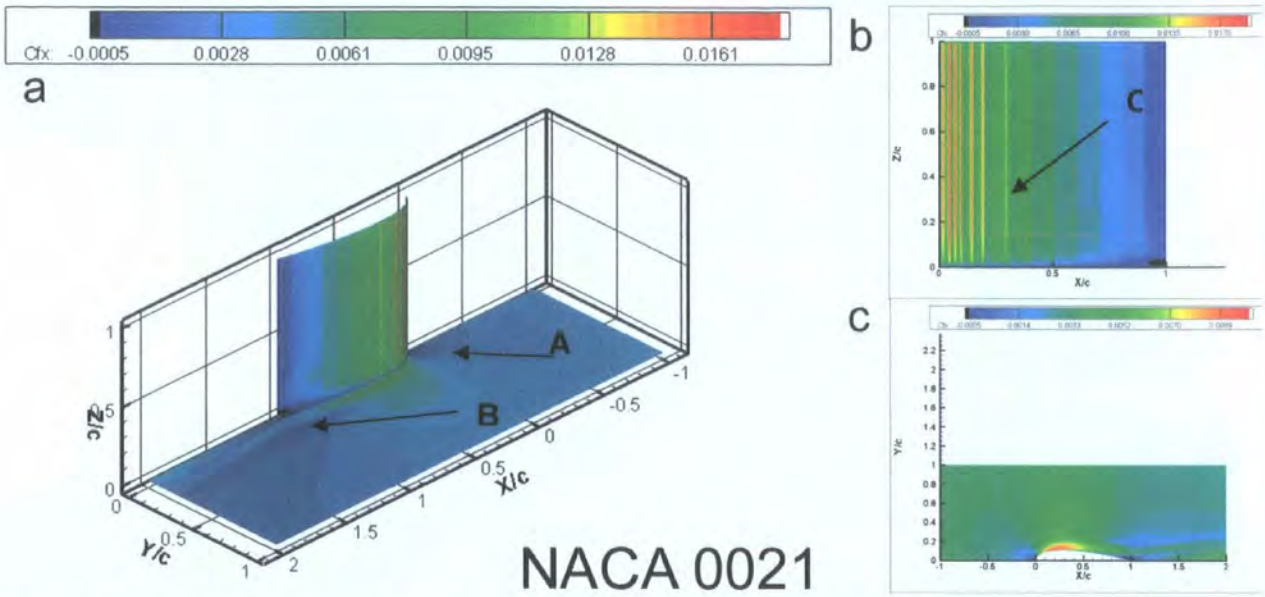

Figure 4.19: Skin friction coefficient contours of the NACA 0021 Foil-Plate case at δ/c=0.029 showing a) a three dimensional view of the junction, b) a two dimensional view of the aerofoil surface, and c) a two dimensional view of the flat plate.*

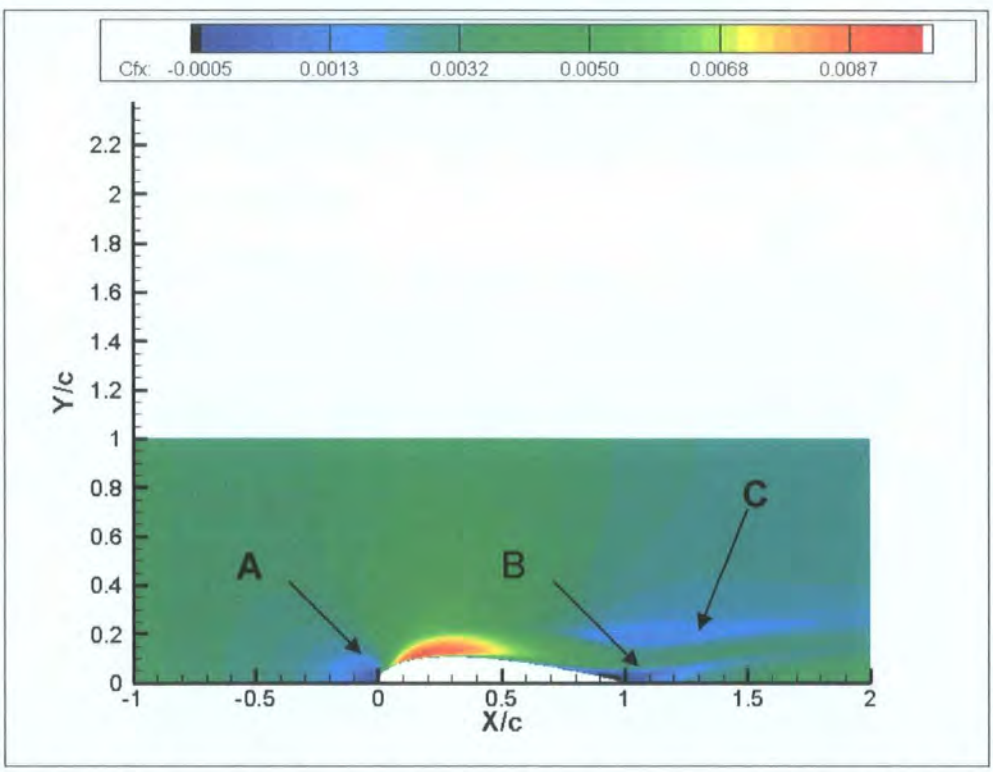

Figure 4.20: Skin friction coefficient on the plate when in junction with a NACA 0021 aerofoil for δ/c=0.029.*

Another feature that has come to life since the addition of a finite thickness to the aerofoil is the abrupt stepping of contours on the aerofoil surface. This appears most clearly in Figure 4.19b as unblended vertical lines of different contour levels labelled 'C' in Figure 4.19b. This effect is not a feature of the junction flow, but is a by-product of the way in which the aerofoil surface was created in Fluent. In two

dimensions the aerofoil surfaces were created by a collection of coordinates each connected with a straight line, thus the three dimensional extrusion of the profile creates an aerofoil surface with numerous flats, and is not smooth. The abrupt change in contours is an effect of the flow passing over the angled intersection of one flat surface and the next.

To examine the stream wise development of the horseshoe vortex and trailing edge separation for the NACA 4-digit series aerofoils, three planes normal to the free stream direction were observed for the NACA 0021 aerofoil. One at the aerofoils point of maximum thickness (x/c=0.30), one at 90% of the aerofoil chord (x/c=0.90) and another at the outlet plane (x/c=2.0).

In Figure 4.21 CP_o is plotted in the three parallel planes of the test section for each of the three NACA 4-digit aerofoils. In Figure 4.21a, at the maximum thickness (x/c=0.30), the largest areas of loss are adjacent to the solid surfaces, with a larger region seen above the plate due to the more mature boundary layer on that surface. A contribution of low loss fluid to feed the horseshoe vortex bends the horizontal contours near the aerofoil surface toward the corner. The largest amount of loss is then found in the corner of the plate and aerofoil where the strongest interaction of the two boundary layers occurs. Moving downstream to x/c=0.90 in Figure 4.21b there is a noticeable increase of loss along the aerofoil surface caused by flow separation at the aerofoils trailing edge. Looking down the z-axis toward the plate, effects from the trailing edge separation and horseshoe vortex have combined to significantly increase the amount of loss in the corner of the plate and aerofoil. However, by the time flow reaches the outlet plane (x/c=2.0) in Figure 4.21c these areas of loss behind the aerofoil and in the corner are mixed with lower loss fluid being pulled in from the free stream.

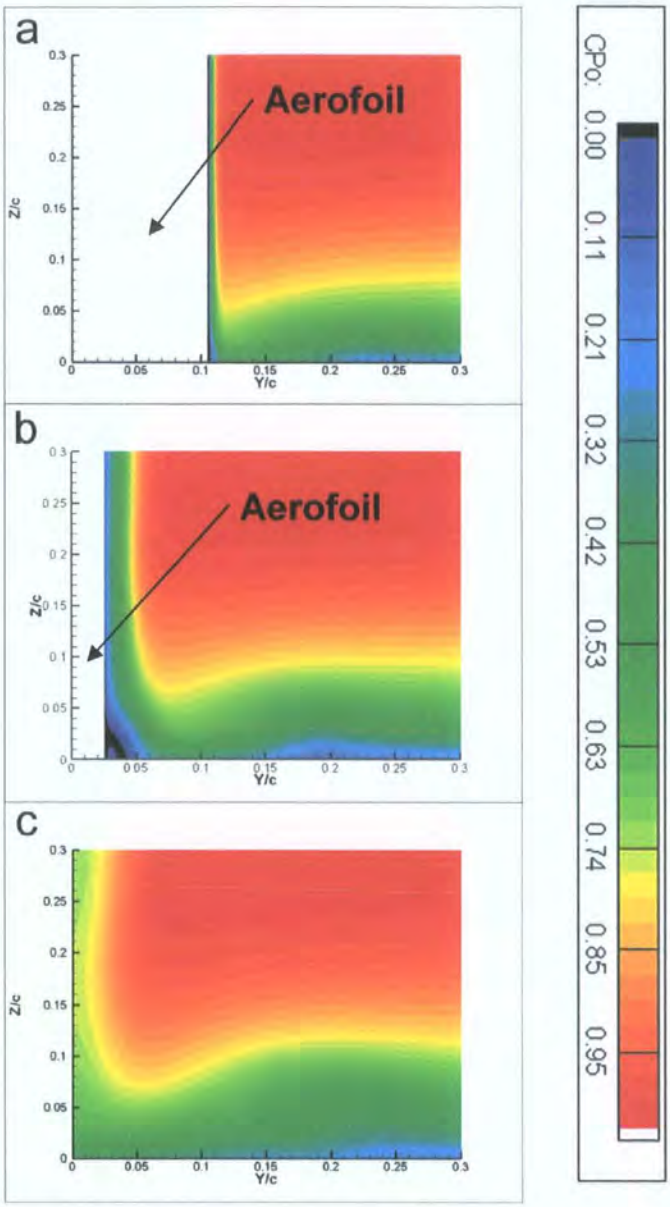

Figure 4.21: Stream wise development of total pressure coefficient through the test section in planes normal to the free stream direction at a) x/c=0.30, b) x/c=0.90, and x/c=2.0 for the NACA 0021 aerofoil with δ/c=0.029.*

Looking at vorticity in the same three planes in Figure 4.22 shows the development of the horseshoe vortex. From Figure 4.22a it can be seen that out of the presented planes the horseshoe vortex (marked A in Figure 4.22) is strongest just after formation at the aerofoils maximum thickness (x/c=0.30). At this point it is found in the corner of the aerofoil and plate, flattened against the plate, rotating in a counter clockwise direction. Looking at the vector plots in Figure 4.23a; the vortex is entraining flow into and out of the corner creating opposing vorticity along the aerofoil surface (marked B in Figure 4.22a) and accounting for the bending of the low loss contours toward the corner. The largest area of loss in this plane (from Figure 4.21a) was seen in this area, where entrained fluid from the vortex coming down the span of the aerofoil is being turned in the corner. In the vector plots of Figure 4.23a, the general direction

of the flow being deflected by the increasing width of the aerofoil nose, up to its maximum thickness, is outward away from the symmetry plane.

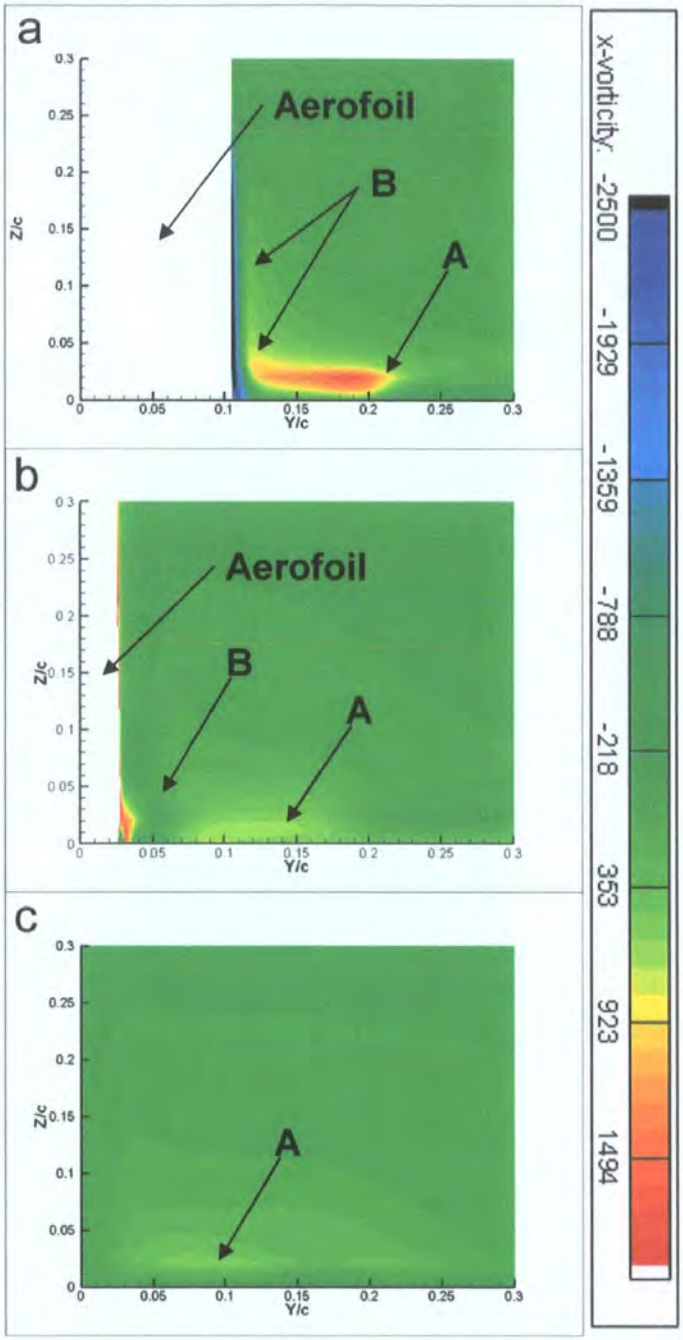

Figure 4.22: Stream wise development of vorticity through the test section in planes normal to the free stream direction at a) x/c=0.30, b) x/c=0.90, and x/c=2.0 for the NACA 0021t aerofoil with δ/c=0.029.*

Moving downstream to x/c=0.90 in Figure 4.23b the general outward direction of the vectors in the plane is reversed and pointed inwards as the flow attempts to remain attached to the aerofoil surface; the magnitude of the flow increases between these two planes and the flow is directed upward, away from the plate. This newly directed flow changes the direction of rotation of the fluid along the aerofoil surface and affects flow being expelled by the horseshoe vortex from the corner. As a result, the horseshoe vortex (marked A in Figure 4.22b) loses strength as is noticeable in Figure 4.22b and the skin friction plots of

Figure 4.19 and Figure 4.20. At this point, the vortex core has been overwhelmed by the inward flow and has moved toward the symmetry plane in the –y-direction, following the aerofoil surface. The reduction of vortex strength provides a testimony to the notion that the trailing edge separation, not the horseshoe vortex is creating the majority of loss in the corner that was seen in Figure 4.21b. It can also be seen that a new rotational formation (marked B in Figure 4.22b and Figure 4.24) has appeared in the corner due to the trailing edge separation, also adding to the loss. Looking at closer view of the corner in Figure 4.24, the vectors are a superposition of the horseshoe vortex from upstream with the inward flow trying to stay attached to the aerofoil surface giving them an upward (z) deflection component that curves in the –z-direction as the flow continues inward toward the aerofoil surface. This then creates the counter-clockwise rotation along the aerofoil surface seen in Figure 4.24. By the time the horseshoe vortex has reached the outlet plane (x/c=2.0) its core has not been moved again, but it is weak. The circulation of the vortex is the same, but the intensity is dispersed over a larger area, as shown by the increase in size of the vortex in Figure 4.22c. At this point there is also little transverse velocity in Figure 4.23c and thus, little rotation in the surface boundary layer of Figure 4.22c.

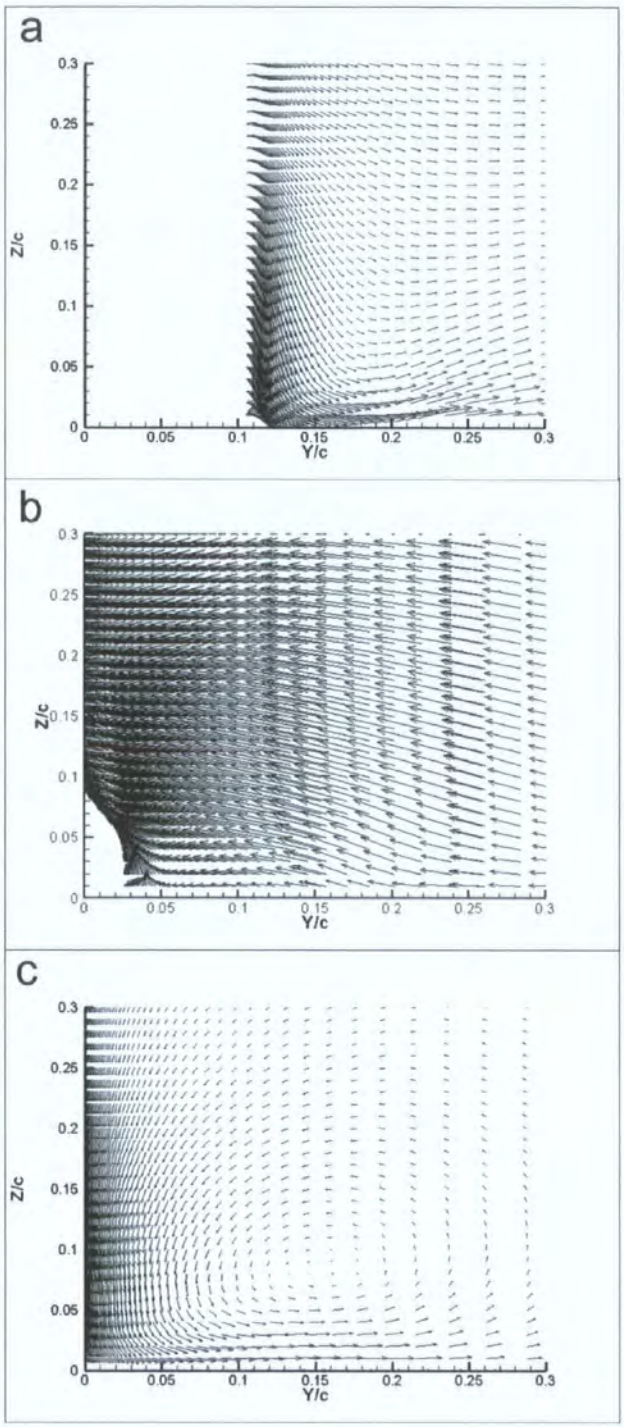

Figure 4.23: Stream wise developments of velocity vectors through test section in planes normal to the free stream direction at a) x/c=0.30, b) x/c=0.90, and x/c=2.0 for the NACA 4-digit aerofoils with δ/c=0.029.*

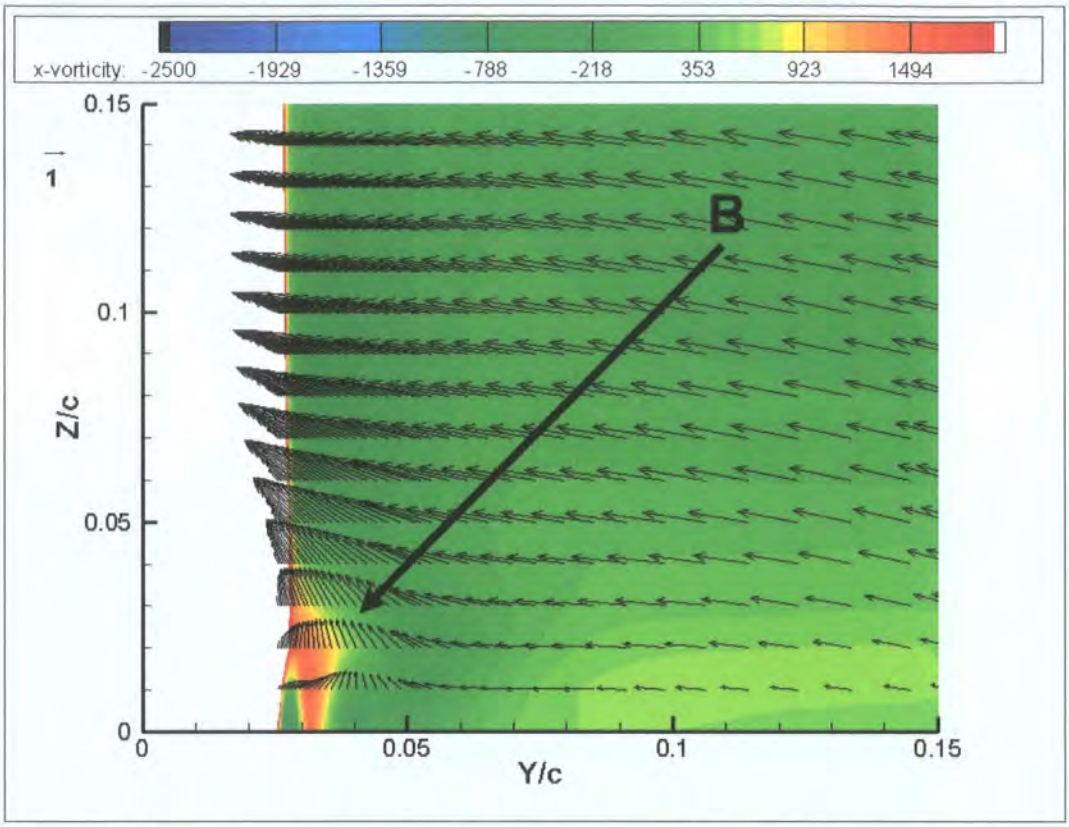

Figure 4.24: Stream wise vorticity and velocity vectors in a plane normal to the free stream at x/c=0.90 for the NACA 0021 aerofoil with δ/c=0.029.*

4.3.3.4 *Flow Mechanisms of the NACA 66-Series Aerofoils*

In order to understand the fundamental differences of the flow surrounding the junction that are created by the use of a laminar flow aerofoil intersecting a flat plate, the same surfaces and planes of the test section that were observed in Section 4.3.3.3 for the NACA 4-digit series are observed for the NACA 66-series aerofoils.

Figure 4.25 and Figure 4.26 show C_{fx} on the surfaces of the junction allowing the formation and passage of the horseshoe vortex to be determined. Starting at the leading edge of the aerofoil the negative skin friction area (marked 'A') where the vortex rolls up from the boundary layer can still be seen, however, this time it is less pronounced than it was for the 4-digit aerofoils, implying a smaller vortex. Following the vortex around the seam of the junction there is a skin friction increase as before where the vortex reaches a maximum before the point of maximum thickness. This high skin friction area has a higher magnitude than for the 4-digit series, but covers a smaller area. Surprisingly, it occurs at approximately the same x/c value as it did for the NACA 4-digit series, showing that it is independent of the position of maximum thickness. One of the most noticeable changes that has occurred with the shift of the maximum thickness further aft, is the increase in size and strength of the negative skin friction area of the trailing edge separation. The separation (marked 'B' in the figures) now also begins earlier at x/c≈0.60. Also notable is the virtual disappearance of the low skin friction area adjacent to the trailing edge separation.

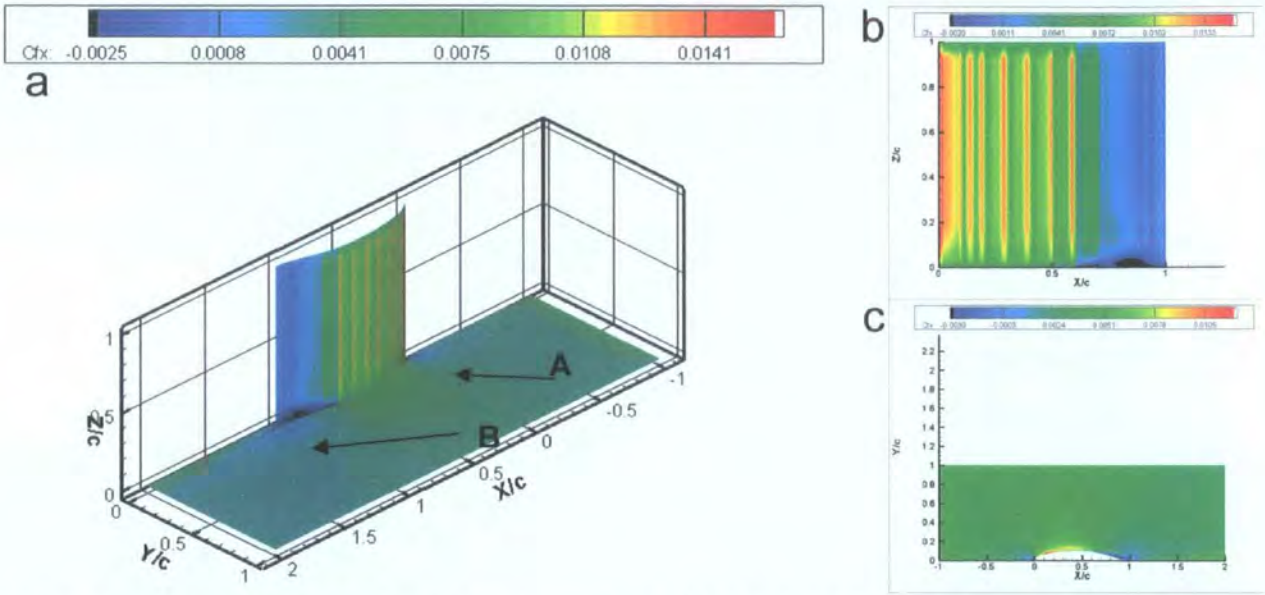

Figure 4.25: Skin friction coefficient contours of the NACA 66$_4$-021 Foil-Plate case at δ/c=0.029 showing a) a three dimensional view of the junction, b) a two dimensional view of the aerofoil surface, and c) a two dimensional view of the flat plate.*

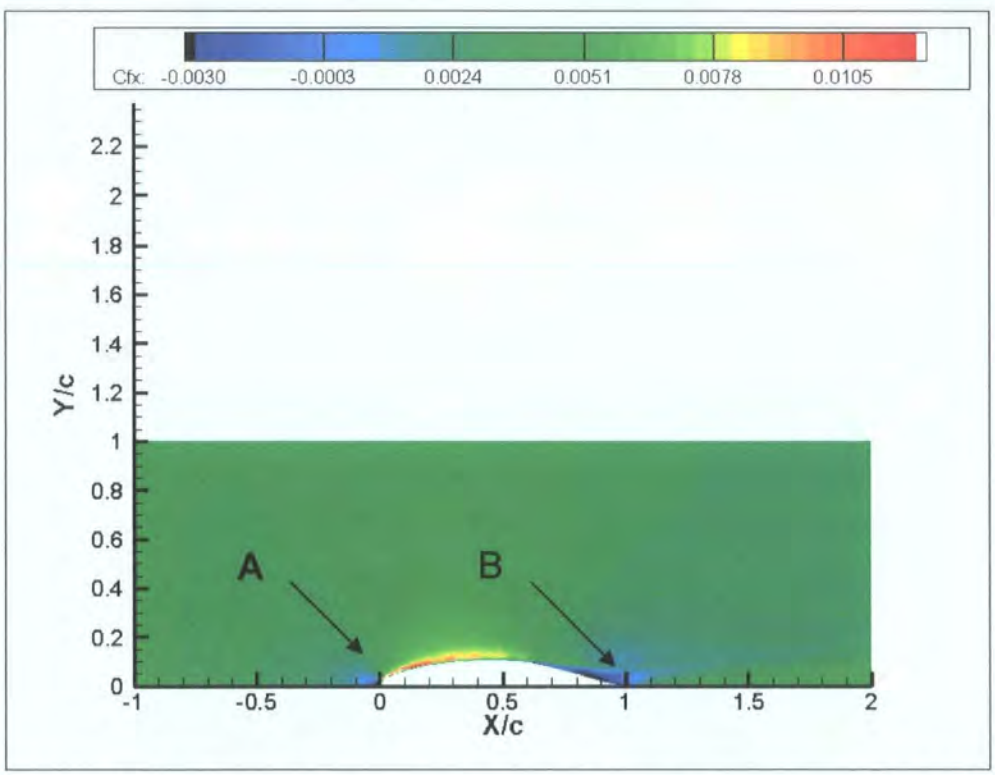

Figure 4.26: Skin friction coefficient on the plate when in junction with a NACA 66$_4$-0021 aerofoil for δ/c=0.029.*

As expected, the stream wise development of the horseshoe vortex and trailing edge separation are similar to those for the NACA 4-digit series aerofoils shown earlier. At the maximum thickness plane (x/c=0.50) in Figure 4.27a the largest areas of loss are still adjacent to the solid surfaces, with a much larger area seen above the plate due to the more mature boundary layer. Also, lower loss contours once again bend in toward the corner, where the vortex is entraining fluid from the free stream. The largest amount of loss is

then found in the corner of the junction and along the plate surface. Looking at Figure 4.27b further downstream at x/c=0.90 there is an increase in the amount of loss next to the aerofoil surface due to the trailing edge separation. This is greater than it was for the 4-digit series, indicating a larger trailing edge separation. The most noticeable area of loss is again in the corner where the horseshoe vortex and trailing edge separation interact. In agreement with the increased trailing edge separation, this area of loss is noticeably larger than it was for the NACA 4-digit series. Another change from the 4-digit series is that the bending of low loss contours into the corner of the junction is no longer as obvious in this plane. At x/c=2.0 in Figure 4.27c, the low loss contours feeding the corner become noticeable again and the situation is similar to that witnessed for the 4-digit series.

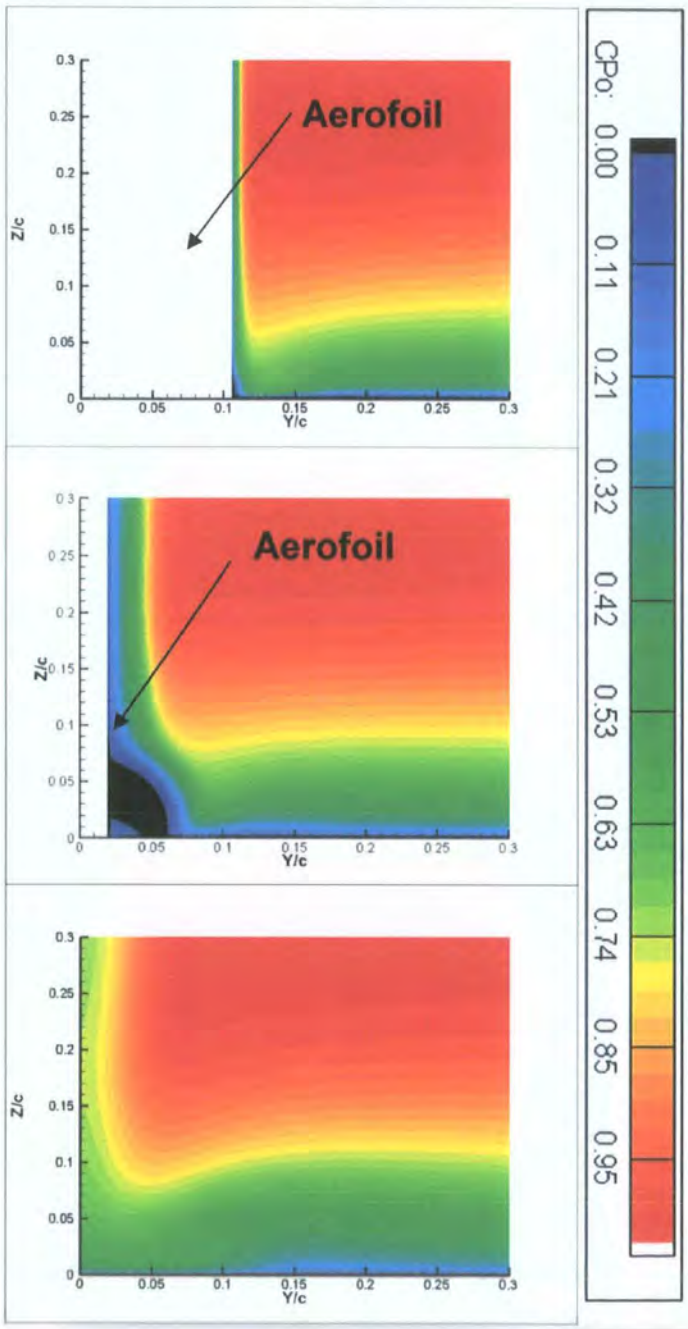

Figure 4.27: Stream wise development of total pressure coefficient through the test section in planes normal to the free stream direction at a) x/c=0.50, b) x/c=0.90, and x/c=2.0 for the NACA 66_4-021 aerofoil with $\delta^*/c=0.029$.

Looking at vorticity in Figure 4.28, the development of the horseshoe vortex and some explanation for the larger regions of loss seen in the corner of the aerofoil and plate from Figure 4.27b can be found. The horseshoe vortex (marked 'A' in Figure 4.28a) is once again most intense at the maximum thickness (x/c=0.50) in Figure 4.28a after propagating along from the leading edge. In this plane the less intense and more symmetric vortex core for the NACA 66-series is found more tightly packed into the corner than it was for the 4-digit series, which saw the vortex squashed against the plate surface; larger in its y-dimension, than in its z-dimension (see Figure 4.22). Rotation above the aerofoil surface is then created by flow entrained by the counter-clockwise rotation of the horseshoe vortex, which is similar to the 4-digit series; however, there is also an appreciable amount of counter rotation to the vortex noticeable along the plate surface as well, which was not seen for the 4-digit aerofoils. This rotation along the plate is seen in Figure 4.29a to be caused by fluid being ejected from the corner by the horseshoe vortex slowing the incoming flow. Above the horseshoe vortex and a horizontal line of $z/c \approx 0.08$, incoming fluid that is not effected by flow being ejected from the corner intersects the aerofoil surface and is turned in the –z-direction toward the plate, becoming part of the horseshoe vortex system in the corner.

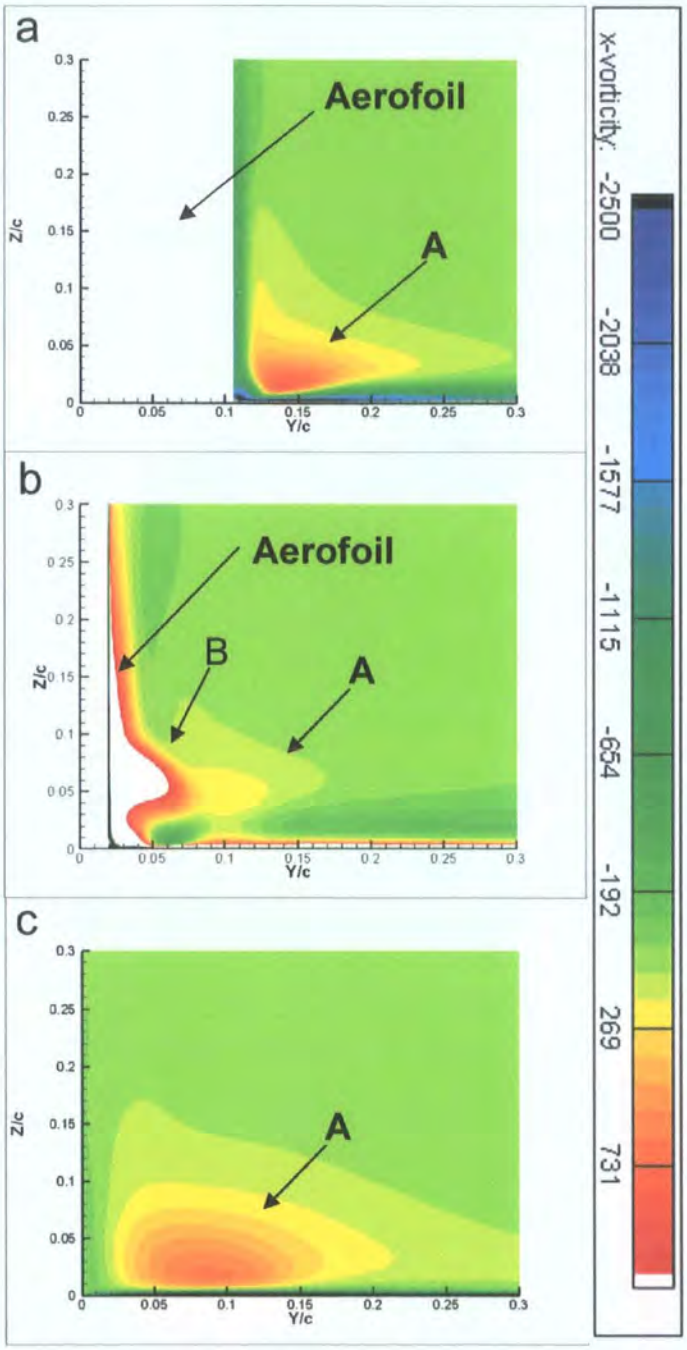

Figure 4.28: Stream wise development of vorticity through the test section in planes normal to the free stream direction at a) x/c=0.50, b) x/c=0.90, and x/c=2.0 for the 66_4-021 aerofoil with δ^*/c=0.029.

Looking at a plane further downstream (x/c=0.90) in Figure 4.28b, there is an increase in velocity magnitude (Figure 4.29b) toward the aerofoil surface just as there was for the 4-digit series as the aerofoil thickness decreases and flow moving downstream attempts to remain attached. As before, this inward flow imposes itself on the horseshoe vortex (marked A in Figure 4.28), overwhelming it, impeding fluid from exiting the corner, thereby reducing its intensity and shifting it toward the symmetry plane. As a result, the clockwise rotating fluid near the plate surface that was created by flow being ejected from the corner is no longer present; instead, the powerful flow toward the symmetry plane has created an area of counter-clockwise rotation near the plate surface. With the horseshoe vortex overwhelmed, the plane in

Figure 4.28 is dominated by newly created vorticity (marked 'B' in Figure 4.28b) at the aerofoil surface. To better understand this newly created formation, Figure 4.28b and Figure 4.29b have been re-created in Figure 4.30 at a different scale to help view the flow structure better by clearing up the vector field and the out of range vorticity

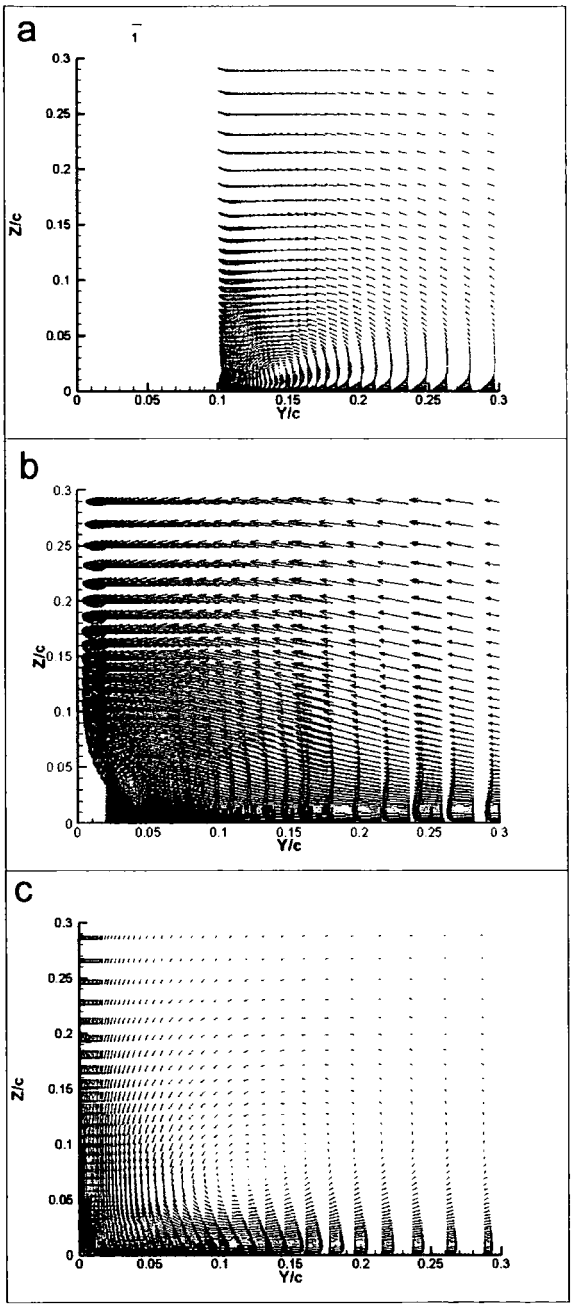

Figure 4.29: Stream wise development of velocity vectors through the test section in planes normal to the free stream direction at a) x/c=0.50, b) x/c=0.90, and x/c=2.0 for the 66_4-021 aerofoil with $\delta^*/c=0.029$.

Looking at Figure 4.30, not all the vorticity has been brought into range, but the values near the aerofoil surface are high enough that they will remove any definition from the plot contours if used. At this scale, the horseshoe vortex is no longer visible and all that is left visible is the rotation at the solid surfaces. As mentioned the inward flow creates a boundary layer of rotational fluid along the plate's surface. Above

this area, starting in the area marked 'C,' the inward flow has an upward (z) deflection. This flow continues toward z-axis where it impinges on the aerofoil surface and is turned in the –z-direction heading toward the favourable low pressure created by the trailing edge separation at the junction. This then creates the counter-clockwise rotation along the aerofoil surface seen in Figure 4.30. As the flow moves toward the plate along the aerofoil surface it is turned again in the corner and directed in the y-direction. As it is moving away from the aerofoil it then intersects the stronger incoming flow and the flow velocities are brought to zero at 'D' in Figure 4.30 creating the large area of loss in the corner of Figure 4.27b.

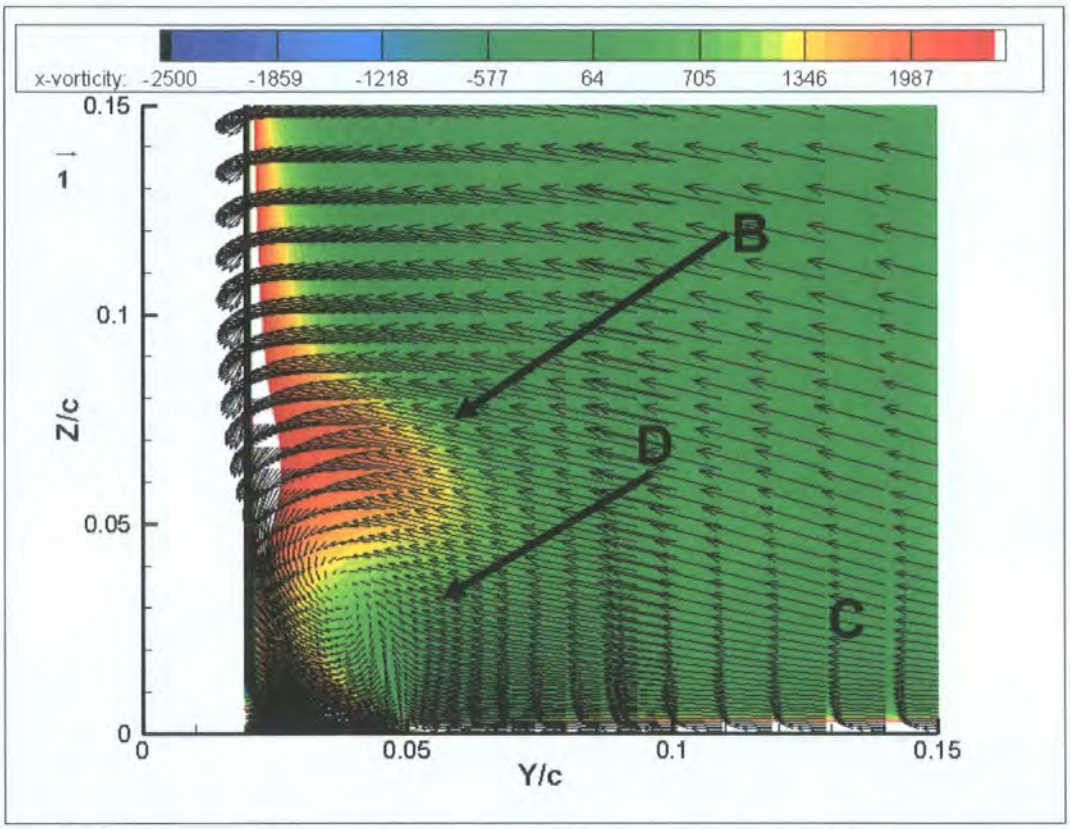

Figure 4.30: Stream wise vorticity and velocity vectors in a plane normal to the free stream at x/c = 0.90 for the NACA 66_4-021 aerofoil with $\delta^*/c=0.029$.

At the outlet plane (x/c=2.0) in Figure 4.27c low loss fluid from the free stream has mixed in with the large amount of loss that was seen in the corner in Figure 4.27b. The vorticity in the corner and along the aerofoil surface created by the trailing edge separation has disappeared and the prominent feature is once again the horseshoe vortex. Unlike the 4-digit series, the stronger incoming flow toward the aerofoil has had enough strength to re-energise the horseshoe vortex, not allowing it to dissipate as much as it moves downstream. Looking at the contours of the Figure 4.28c and vectors of Figure 4.29c it appears that the horseshoe vortex now has the majority of the plane in a counter clockwise rotation. This rotation around the vortex core then creates a thin clockwise rotational boundary layer along the plate in Figure 4.28c similar to that seen for the 4-digit aerofoils.

4.3.3.5 Comparison of flow mechanisms from each NACA series

The difference in the position of maximum thickness between the NACA series' creates little mentionable difference in the separation system described throughout the surveyed literature. However, the shape, concentration, and size of the two separations do depend on the type of aerofoil used. The combination of a narrower nose and a more gentle slope up to maximum thickness over 50% of the chord of the 66-series forms a smaller, less intense horseshoe vortex at the maximum thickness, and keeps it tucked tightly into the corner of the junction. After the maximum, the steeper decrease in thickness creates a larger trailing edge separation accompanied by an increased magnitude of inward flow toward the aerofoils symmetry plane. The opposite is true for the 4-digit series. The steep approach to maximum thickness creates a more intense, larger horseshoe vortex, but the shallow removal of the thickness makes less of a trailing edge separation and less inward flow toward the symmetry plane. Judging by the values of C_{Di} reported in Figure 4.11 and Figure 4.12, it is the larger trailing edge separation of the NACA 66-series aerofoils that creates slightly more interference. However, looking at Table 4.1 and Table 4.2 the viscous forces created on the plate are always similar, showing no advantage from the use of either profile.

4.3.4 Boundary Layer Variation

4.3.4.1 Effects of Boundary Layer Variation for the NACA 4-digit Aerofoils

Figure 4.31 through Figure 4.36 consist of plots of stream wise vorticity and velocity vectors at the aerofoils point of maximum thickness (x/c=0.30) in a plane normal to the flow direction for the selection of NACA 4-digit aerofoils in the 'Foil-Plate' configuration. Each figure contains four plots showing the development of the horseshoe vortex through each of the four boundary layer thicknesses.

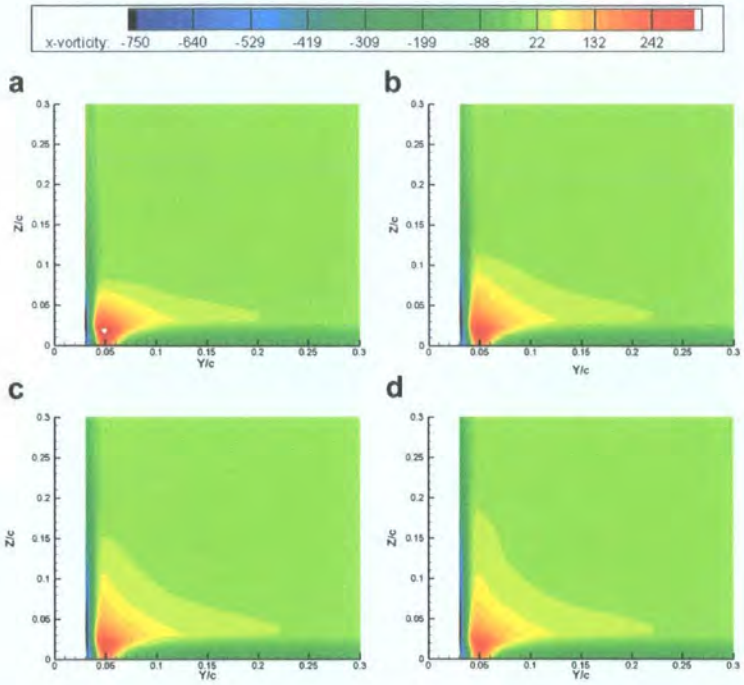

Figure 4.31: Stream wise vorticity in the yz-plane at x/c=0.30 for a NACA 0006 aerofoil for δ/c= a)0.009, b)0.015, c)0.021, and d)0.029.*

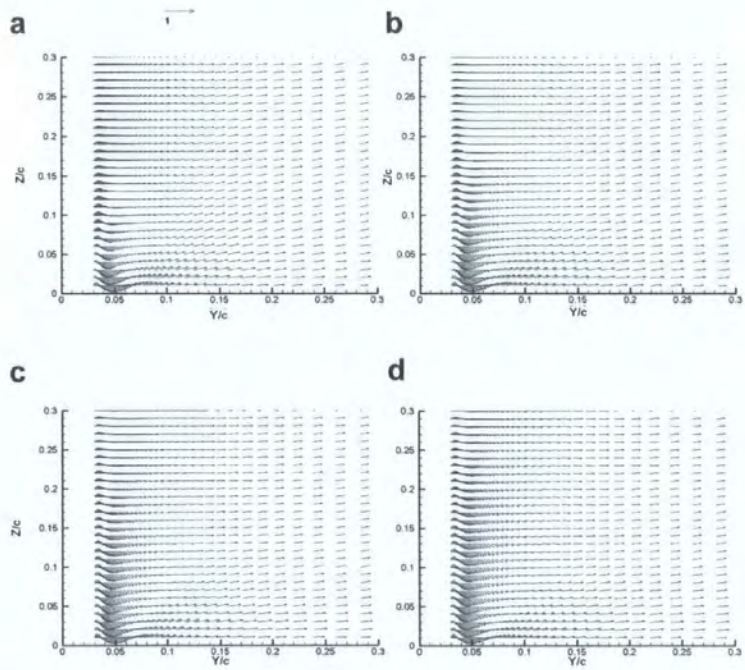

Figure 4.32: Velocity vectors in the yz-plane at x/c=0.30 for a NACA 0006 aerofoil for δ/c= a)0.009, b)0.015, c)0.021, and d)0.029.*

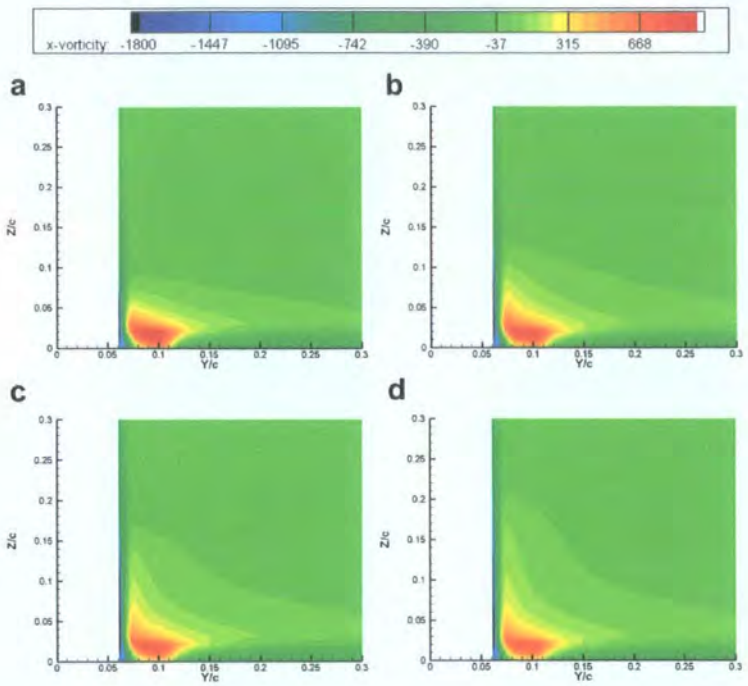

Figure 4.33: Stream wise vorticity in the yz-plane at x/c=0.30 for a NACA 0012 aerofoil for δ/c= a)0.009, b)0.015, c)0.021, and d)0.029.*

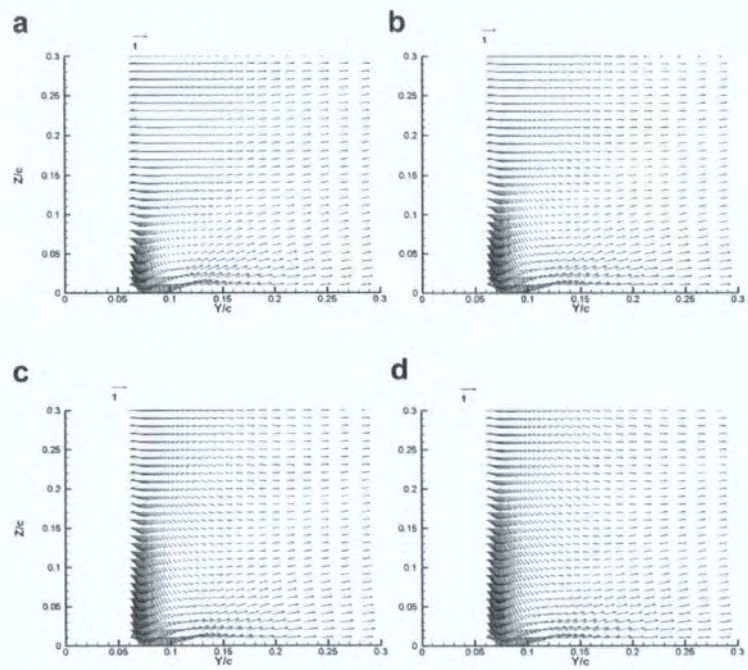

Figure 4.34: Velocity vectors in the yz-plane at x/c=0.30 for a NACA 0012 aerofoil for δ/c= a)0.009, b)0.015, c)0.021, and d)0.029.*

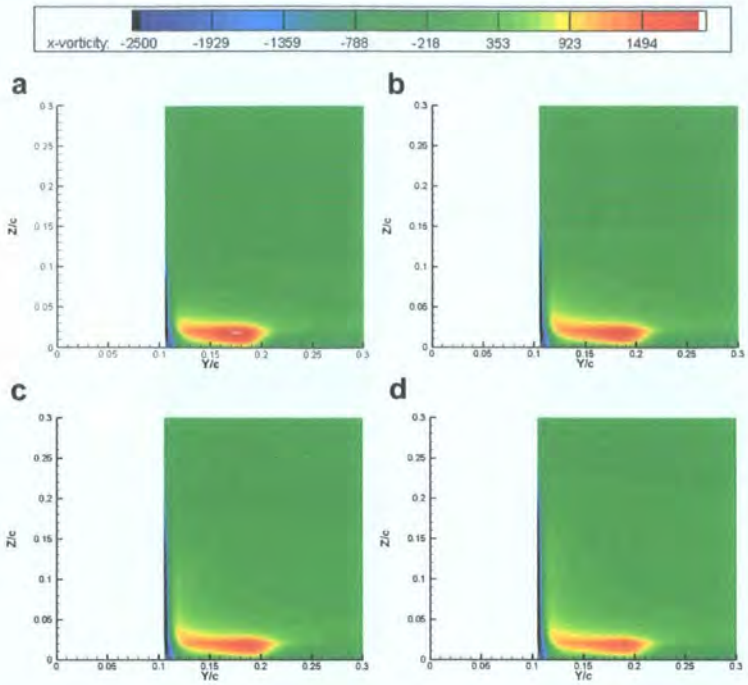

Figure 4.35: Stream wise vorticity in the yz-plane at x/c=0.30 for a NACA 0021 aerofoil for δ/c= a)0.009, b)0.015, c)0.021, and d)0.029.*

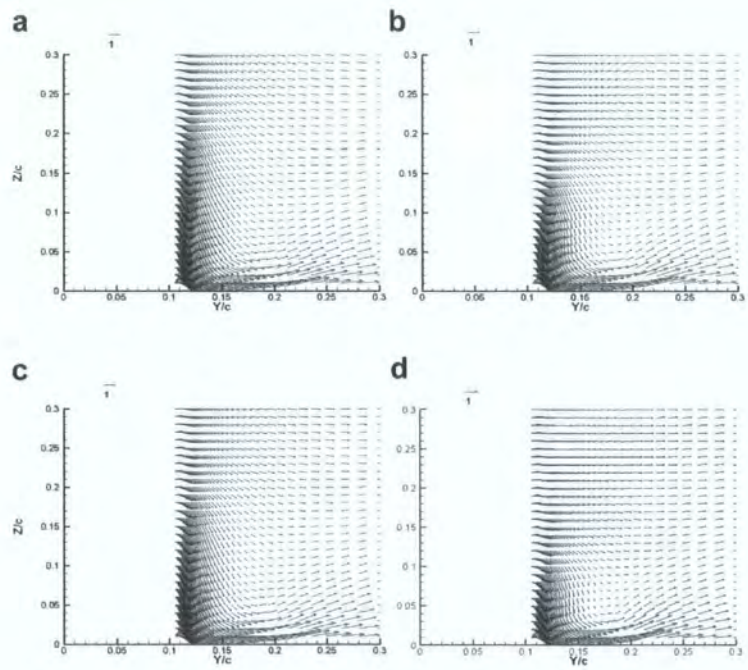

Figure 4.36: Velocity vectors in the yz-plane at x/c=0.30 for a NACA 0021 aerofoil for δ/c= a)0.009, b)0.015, c)0.021, and d)0.029.*

Throughout the range of T/c, the area of downward flow along the aerofoil's span, and hence the amount of fluid being entrained by the horseshoe vortex, increases with a growth of the boundary layer thickness. Also the influence of the rotational flow in the corner extends, entraining and ejecting, more fluid along the z and y axes, respectively, as the boundary layer grows. Accompanying this is a growth of the horseshoe vortex size, broadening as the inlet boundary layer thickness increases. Observing the vorticity

plots of Figure 4.31, Figure 4.33, and Figure 4.35 in increasing boundary layer order, the rotational field grows in both the y and z directions, with the core moving slightly away from the aerofoil in the y direction. The intensity at the vortex core, however, decreases with boundary layer growth; looking at the first (a) of each of the series of figures, there is a stronger concentration of vorticity than in the last of the series (d) for all aerofoil profiles. The increased intensity of the vortex in this case is due to the thinner boundary layer having a greater change in velocity per unit height. This then leads to a more intense vortex rolling up in front of the aerofoils leading edge at the stagnation point, which is responsible for the increased interference seen in Figure 4.11. For all cases the circulation of the trailing vortices will be the same, just over a different area. Another noticeable feature of the horseshoe vortex is that, as forecasted by Eckerle and Langston [Eckerle & Langston, 1987], it is approximately within one boundary layer disturbance thickness for each of the variations shown.

Figure 4.37 through Figure 4.42 show plots of C_{fx} and C_p on the plate for each of the NACA 4-digit aerofoils in the 'Foil-Plate' configuration for the four boundary layer thicknesses. For each of the T/c ratio, the area of low C_{fx} in front of the leading edge where the horseshoe vortex initially rolls up increases in size and decreases in magnitude, implying the formation of a larger vortex. Following the vortex around the seam, the maximum value of C_{fx} and minimum value of C_p in the region of the maximum thickness decrease, supporting the recognised reduction in vortex strength witnessed earlier in Figure 4.31 through Figure 4.36. Then at the rear of the aerofoil, the low skin friction area, indicating the size of the trailing edge separation, grows with increasing boundary layer thickness.

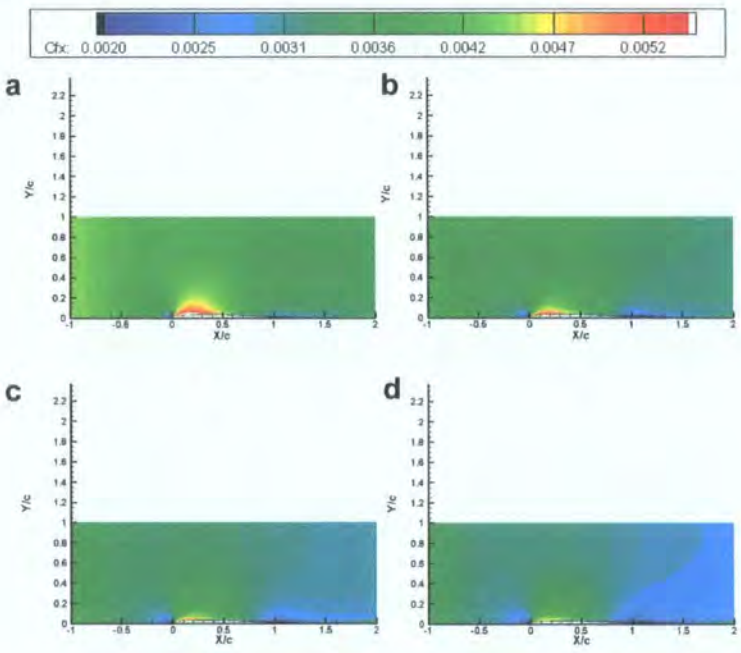

Figure 4.37: Skin friction coefficient on the plate when in junction with a NACA 0006 aerofoil for δ/c= a)0.009, b)0.015, c)0.021, and d)0.029.*

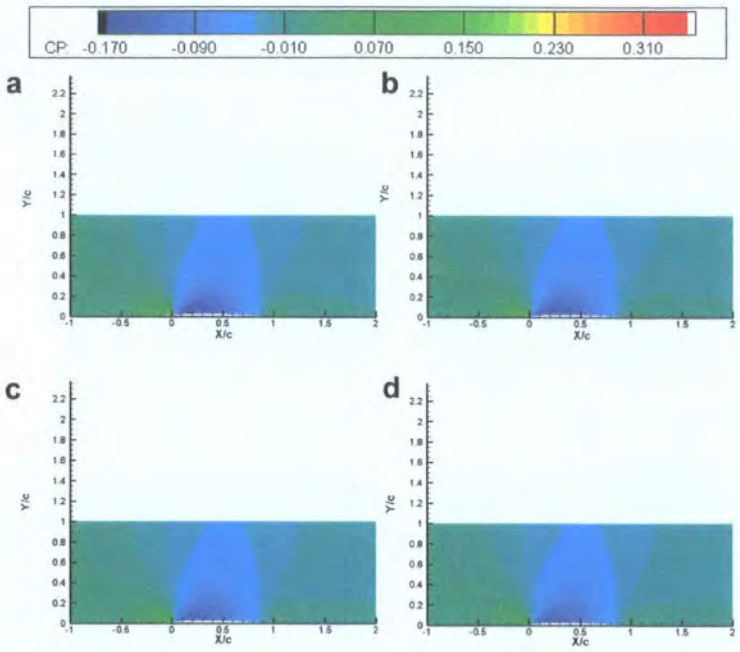

Figure 4.38: Pressure coefficient on the plate when in junction with a NACA 0006 aerofoil for δ/c= a)0.009, b)0.015, c)0.021, and d)0.029.*

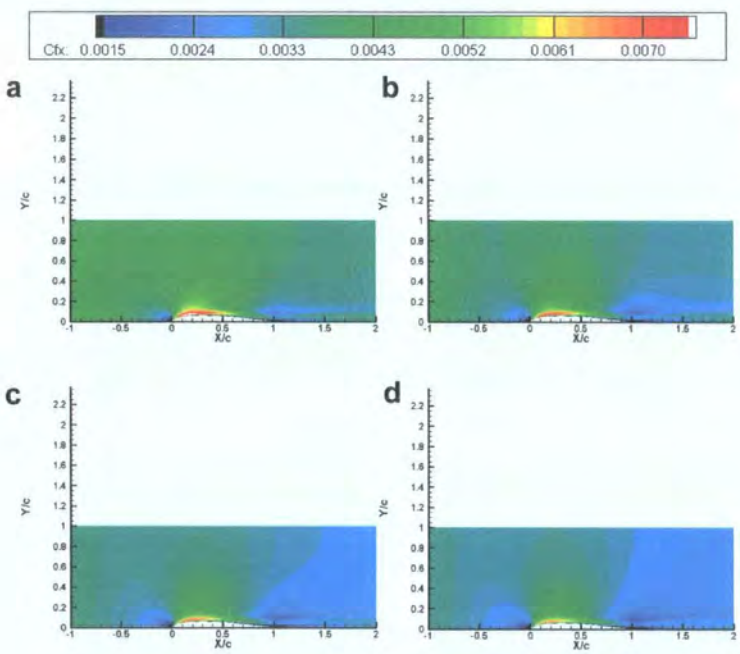

Figure 4.39: Skin friction coefficient on the plate when in junction with a NACA 0012 aerofoil for δ/c= a)0.009, b)0.015, c)0.021, and d)0.029.*

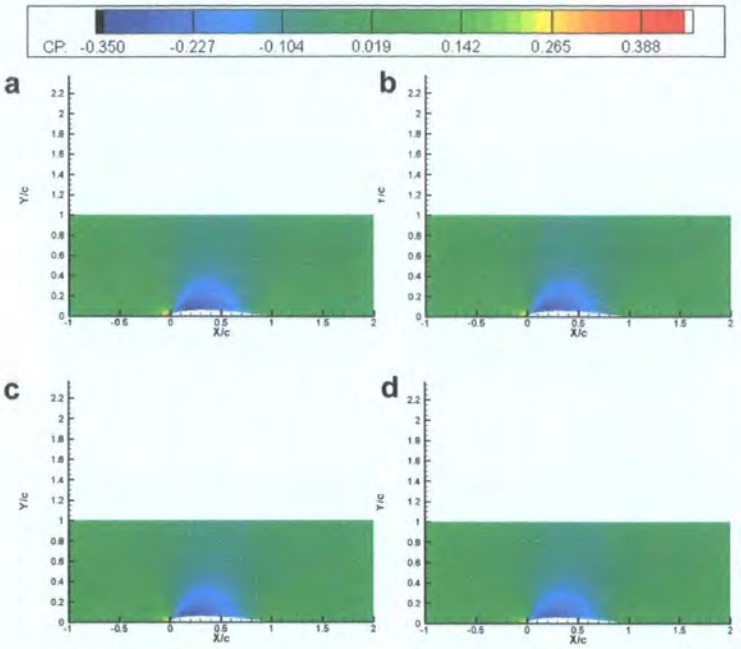

Figure 4.40: Pressure coefficient on the plate when in junction with a NACA 0012 aerofoil for δ/c= a)0.009, b)0.015, c)0.021, and d)0.029.*

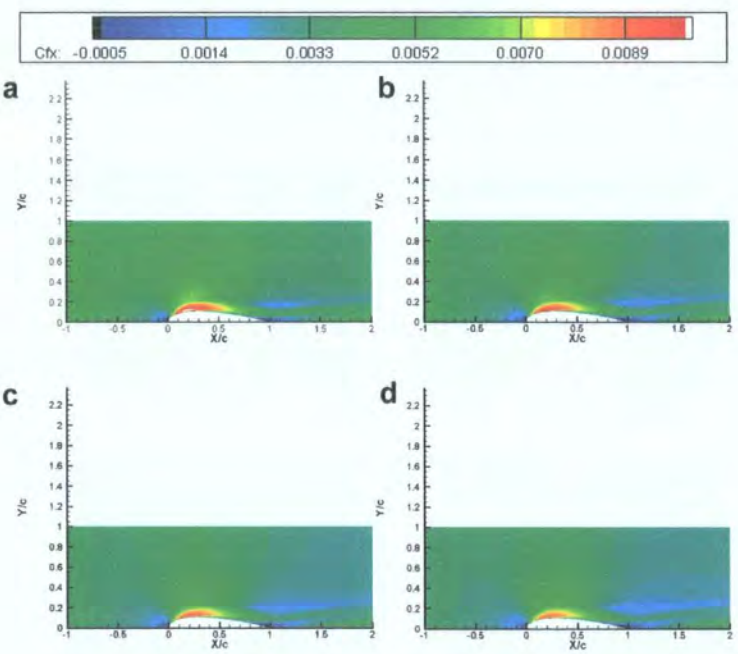

Figure 4.41: Skin friction coefficient on the plate when in junction with a NACA 0021 aerofoil for δ/c= a)0.009, b)0.015, c)0.021, and d)0.029.*

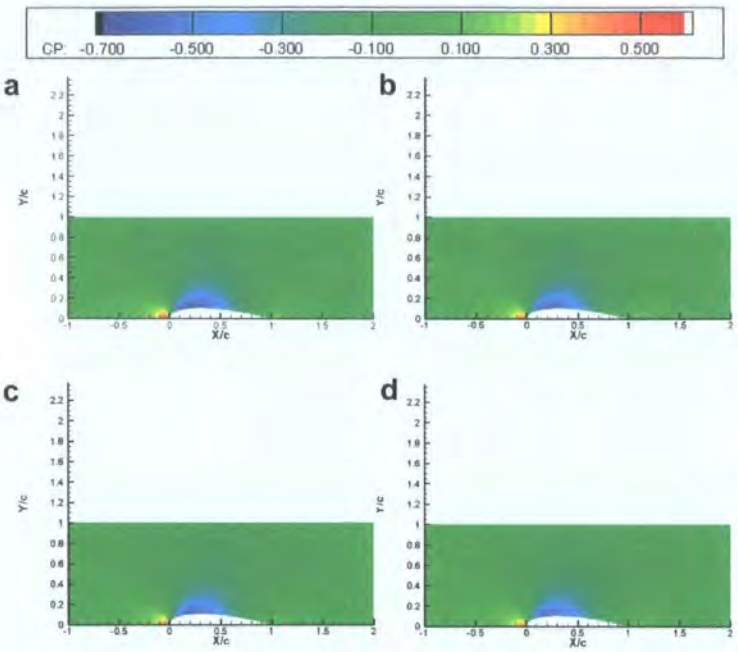

Figure 4.42: Pressure coefficient on the plate when in junction with a NACA 0021 aerofoil for δ/c= a)0.009, b)0.015, c)0.021, and d)0.029.*

4.3.4.2 *Effects of Boundary Layer Variation for the NACA 66-series Aerofoils*

Figure 4.43 through Figure 4.46 consist of plots of stream wise vorticity and velocity vectors in a plane normal to the direction of flow at the aerofoils point of maximum thickness (x/c=0.50) for the range of NACA 66-series aerofoils in the 'Foil-Plate' configuration. Each figure contains four plots showing the development of the horseshoe vortex through each of the four boundary layer thicknesses. The results of a varying inlet boundary layer for the NACA 66-series reinforce the trends witnessed for the NACA 4-digit series.

Observing Figure 4.43 and Figure 4.46 in increasing boundary layer thickness order (a through d), it can be seen once again that the intensity of the horseshoe vortex at the core decreases. Its size also increases with an increasing boundary layer, but its position does not move throughout the change of inlet boundary layer thicknesses as it did for the NACA 4-digit aerofoil. Also concurrent with the previous NACA series; the vortices can all be found within one boundary layer disturbance thickness. Looking at the velocity vectors of Figure 4.44 and Figure 4.46, the increase in size of the vortex caused by a larger boundary layer once again entrains more fluid from the free stream into the corner. However, the noticeable change is along the aerofoils surface, not above the plate. Above the plate the magnitude of the inward flow vectors does not noticeably increase. One of the differences in flow structure that was observed in Section 4.3.3.4 was the creation of rotational flow along the plate's surface by the flow being ejected from the corner turning the inward flow. Despite the increase in size of the horseshoe vortex, the inward flow (that does not increase with boundary layer thickness), and hence, the amount of rotation along the plate's surface does not change with an increased boundary layer thickness.

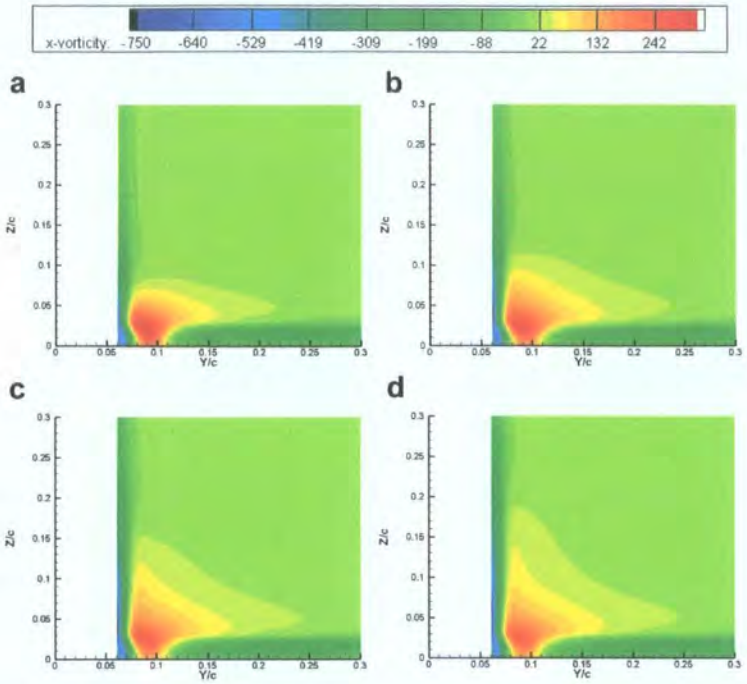

Figure 4.43: Vorticity in the yz-plane at x/c=0.50 for a NACA 66-012 aerofoil for four boundary layer displacement thicknesses of a)0.863mm, b)1.507mm, c)2.079mm, and d)2.860mm.

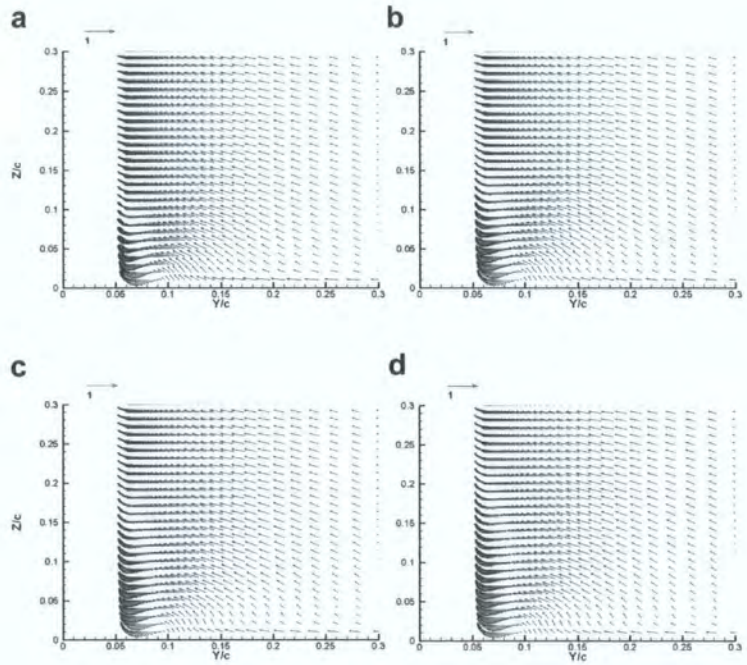

Figure 4.44: Velocity vectors in the yz-plane at x/c=0.50 for a NACA 66-012 aerofoil for four boundary layer displacement thicknesses of a)0.863mm, b)1.507mm, c)2.079mm, and d)2.860mm.

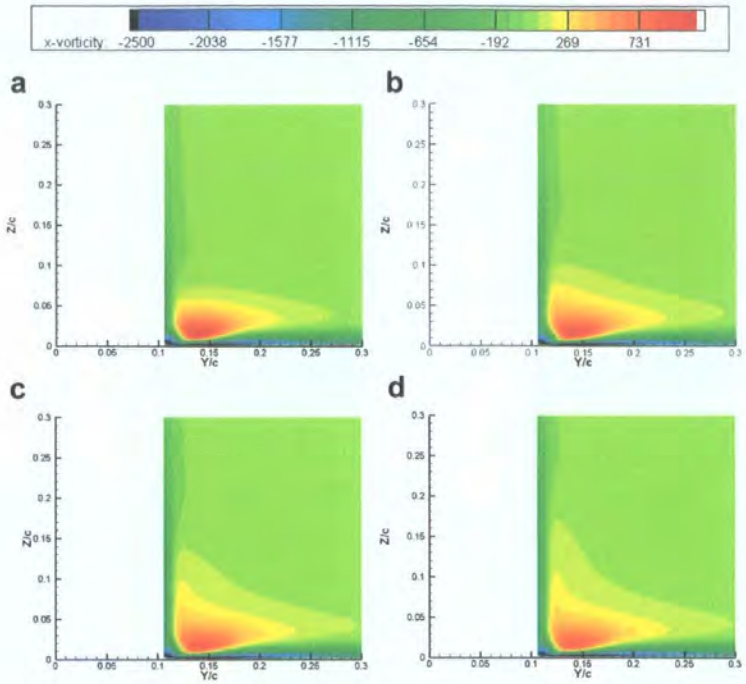

Figure 4.45: Vorticity in the yz-plane at x/c=0.50 for a NACA 66-021 aerofoil for four boundary layer displacement thicknesses of a)0.863mm, b)1.507mm, c)2.079mm, and d)2.860mm.

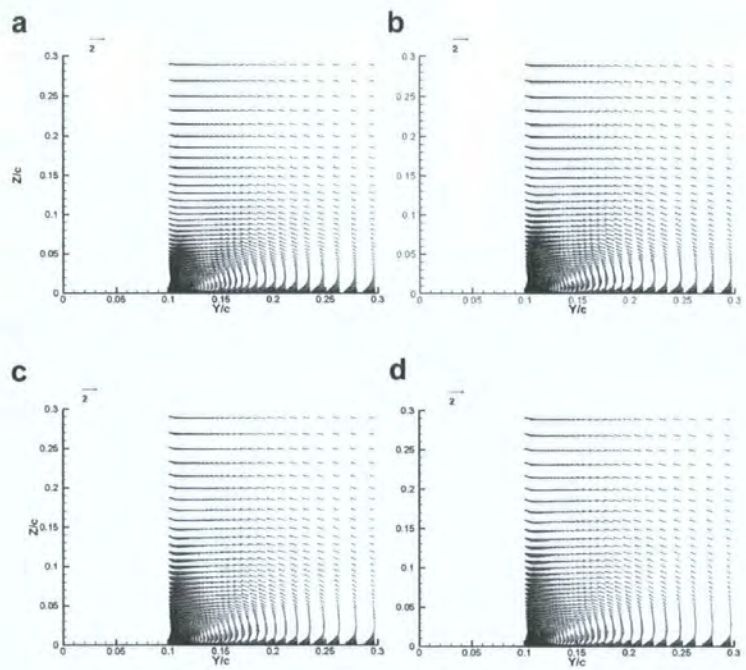

Figure 4.46: Velocity vectors in the yz-plane at x/c=0.50 for a NACA 66-021 aerofoil for four boundary layer displacement thicknesses of a)0.863mm, b)1.507mm, c)2.079mm, and d)2.860mm.

4.3.5 T/c Variation

4.3.5.1 Effects of T/c variation for the NACA 4-digit Aerofoils

It was shown earlier in Section 4.3.2, that aerofoil bluntness creates more interference than the previously discussed boundary layer thickness. To explore some of the reasons for this, Figure 4.47 through Figure 4.53 are presented showing various plots of C_{fx} and C_p on the plate as well as the aerofoil surface for the different T/c ratios of the NACA 4-digit aerofoils. Note that Sub-figure c from Figure 4.17, Figure 4.47, and Figure 4.49 is the same as sub-figure d in Figure 4.37 through Figure 4.41 and sub-figure c from Figure 4.48, Figure 4.50, and Figure 4.53 is the same as sub-figure d in Figure 4.38 through Figure 4.42.

Revisiting Section 4.3.3.2, the effects from the junction of a zero thickness aerofoil were minimal. A small scale separation slightly reducing skin friction on the plate, created by an interaction of the plate and aerofoil boundary layers was witnessed at the junction. This effect, when put on the scale of the changes created by the more blunt aerofoil profiles in Figure 4.11 is insignificant.

Immediately with placement of the thin profile of the NACA 0006 in Figure 4.47 and Figure 4.48 a more influential and different, separation at the junction is witnessed than for the 0width aerofoil. In Figure 4.47a&c and Figure 4.48a&c, respectively, the region of low and negative skin friction and high pressure in front of the aerofoil leading edge where the horseshoe vortex initially rolls up is now visible on the plate. In the vicinity of the front half of the aerofoil there is an area of high skin friction and low pressure where the flow begins to accelerate up to and around the point of the aerofoils maximum thickness. Then, following the junction downstream there is another area of low and negative skin friction starting at $x/c \approx 0.9$ where the trailing edge separation begins.

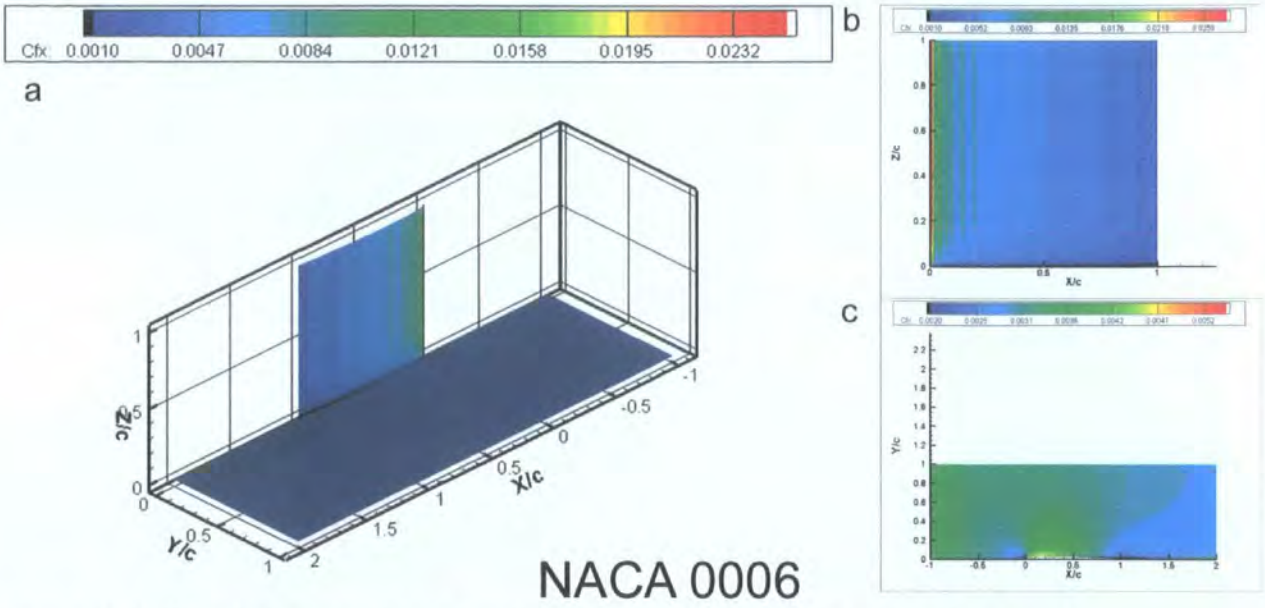

Figure 4.47: Skin friction coefficient contours for the NACA 0006 Foil-Plate case at δ/c=0.029 showing a) a three dimensional view of the junction, b) a two dimensional view of the aerofoil surface, and c) a two dimensional view of the flat plate.*

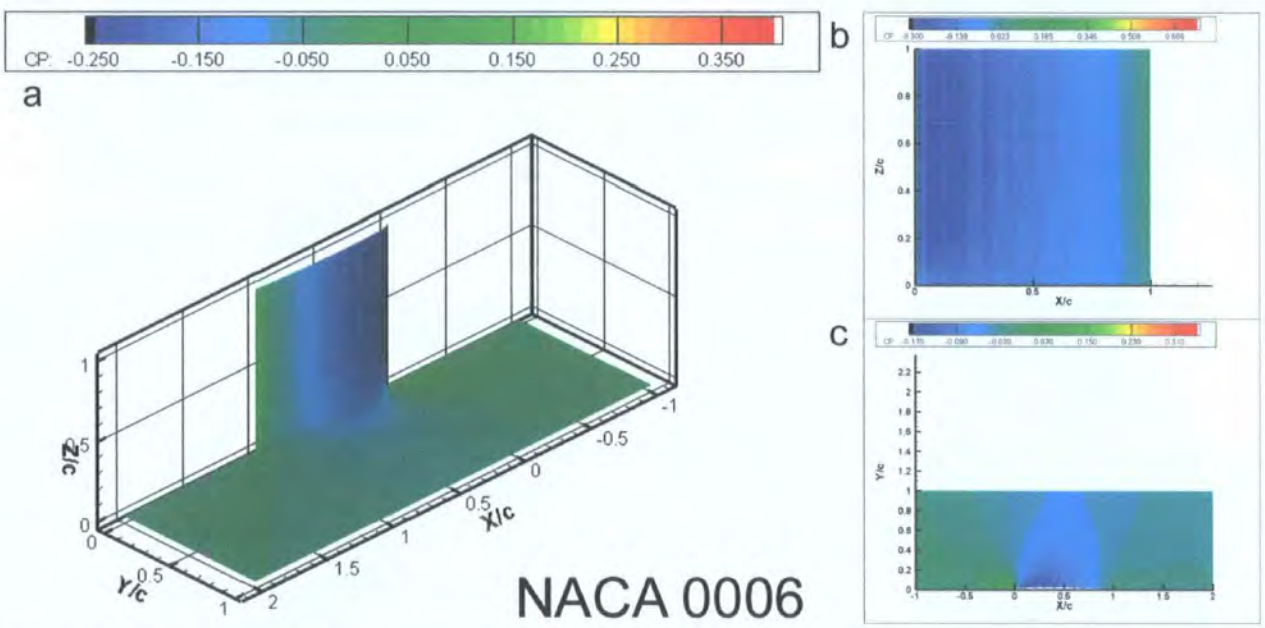

Figure 4.48: Pressure coefficient contours for the NACA 0006 Foil-Plate case at δ/c=0.029 showing a) a three dimensional view of the junction, b) a two dimensional view of the aerofoil surface, and c) a two dimensional view of the flat plate.*

Increasing the T/c ratio and observing the plots in Figure 4.49 and Figure 4.50 for the NACA 0012 aerofoil, the structure of the junction flow and its effects on the plate are similar to that of the NACA 0006, but they have gotten stronger and reach further around the junction. The area where the horseshoe vortex rolls up in front of the aerofoil grows in both physical size and magnitude with the increased bluntness. The same is true for the high friction and low pressure area where the flow accelerates around the aerofoils leading edge to the maximum thickness. Particularly interesting is the growth in size of the

low friction, high pressure area at the rear of the aerofoil, signifying a large jump in the size of the trailing edge separation. For the NACA 0006 aerofoil, the separation started x/c≈0.90; in this instance, for the NACA 0012, the separation starts at an earlier x/c≈0.80 in Figure 4.49 and extends creating the region of lower skin friction on the plate adjacent to the trailing edge separation.

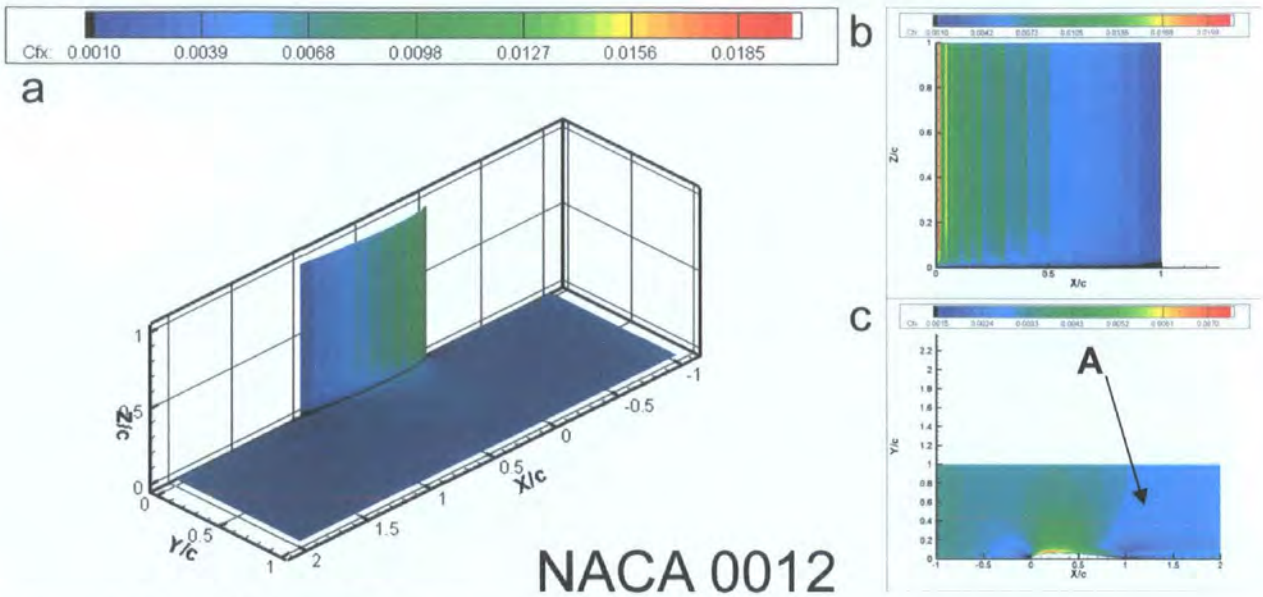

Figure 4.49: Skin friction coefficient contours for the NACA 0006 Foil-Plate case at δ/c=0.029 showing a)a three dimensional view of the junction, b)a two dimensional view of the aerofoil surface, and c)a two dimensional view of the flat plate.*

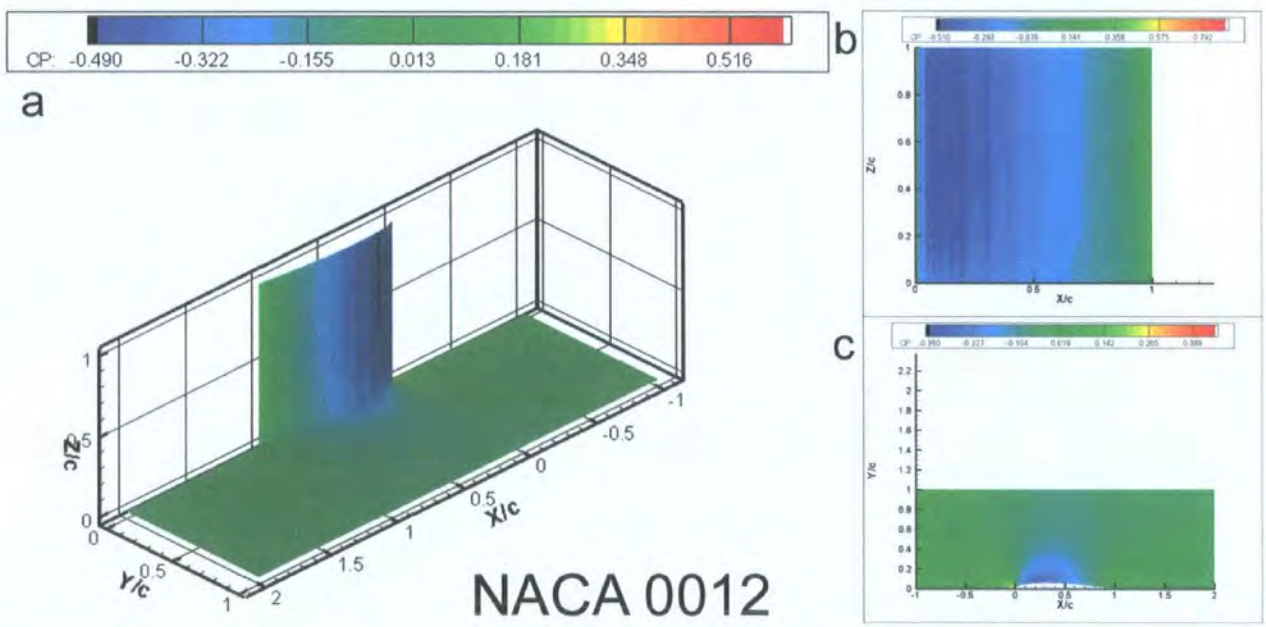

Figure 4.50: Pressure coefficient contours for the NACA 0012 Foil-Plate case with δ/c=0.029 showing a) a three dimensional view of the junction, b) a two dimensional view of the aerofoil surface, and c) a two dimensional view of the flat plate.*

Looking to Figure 4.51 and observing the plots in growing T/c ratio order, the horseshoe vortex has a higher maximum (local) vorticity for the thicker aerofoil profiles than for thinner aerofoil profiles. This is accompanied by a widening of the vortex shape along the y-axis, concurrent with the growing region of low skin friction seen in a comparison of the plates for the NACA 0006 and 0012 corresponding to Figure 4.47a&c and Figure 4.49a&c. In Figure 4.50c, the pressure distribution on the plate for the NACA 0012 aerofoils reflects this change. It is almost identical to that seen for the NACA 0006, just at a different scale, which would be expected due to the increase in strength and size of the vortex. The most notable difference created by a change in T/c ratio, however, occurs at the rear of the plate.

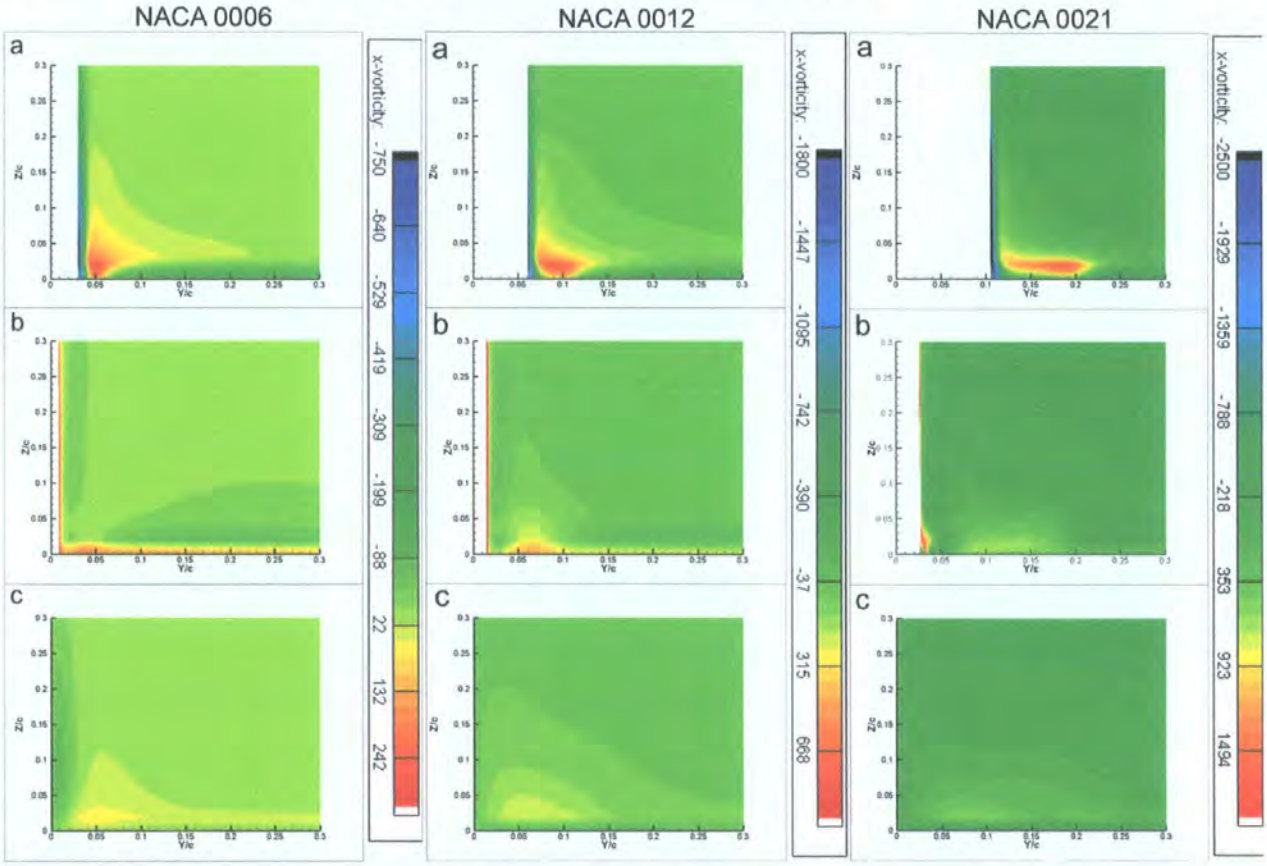

Figure 4.51: Stream wise vorticity in planes normal to the direction of flow at a) x/c=0.30, b)x/c=0.90, and c)x/c=2.0 for the NACA 4-digit aerofoils with δ/c=0.029.*

Increasing the T/c ratio again to 21% for the NACA 0021 and looking at C_{fx} and C_p in Figure 4.52 and Figure 4.53, respectively, the trend of growing effects seen on the plate in the areas at the aerofoil leading edge and maximum thickness due to the formation and passage of a larger horseshoe vortex continues. This is confirmed in Figure 4.51a with an increase in the intensity of the horseshoe vortex at its core. The increase in aerofoil thickness has also greatly increased the magnitude of velocity vectors flowing in toward the aerofoils surface in Figure 4.54b. For an aerofoil as thick as the NACA 0021, the combination of a larger trailing edge separation and stronger inward flow creates a small but, concentrated rotation in the corner, noticed earlier in Section 4.3.3.3. For the thinner aerofoils, this rotation does not occur to the same degree.

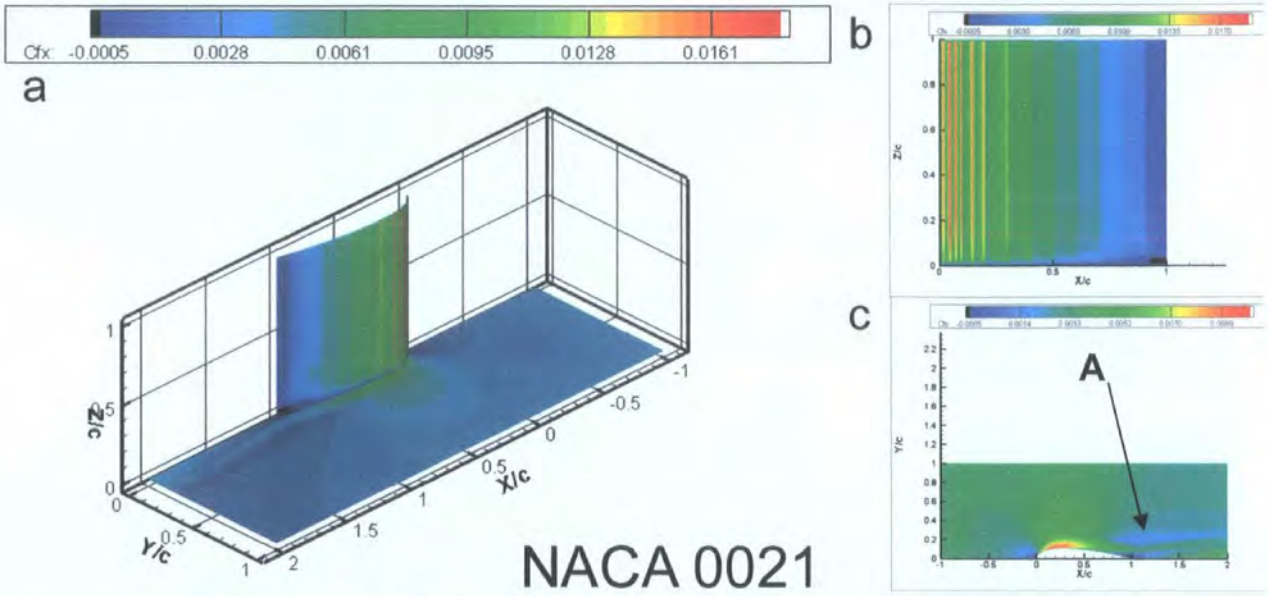

Figure 4.52: Skin friction coefficient contours for the NACA 0006 Foil-Plate case at δ/c=0.029 showing a) a three dimensional view of the junction, b) a two dimensional view of the aerofoil surface, and c) a two dimensional view of the flat plate.*

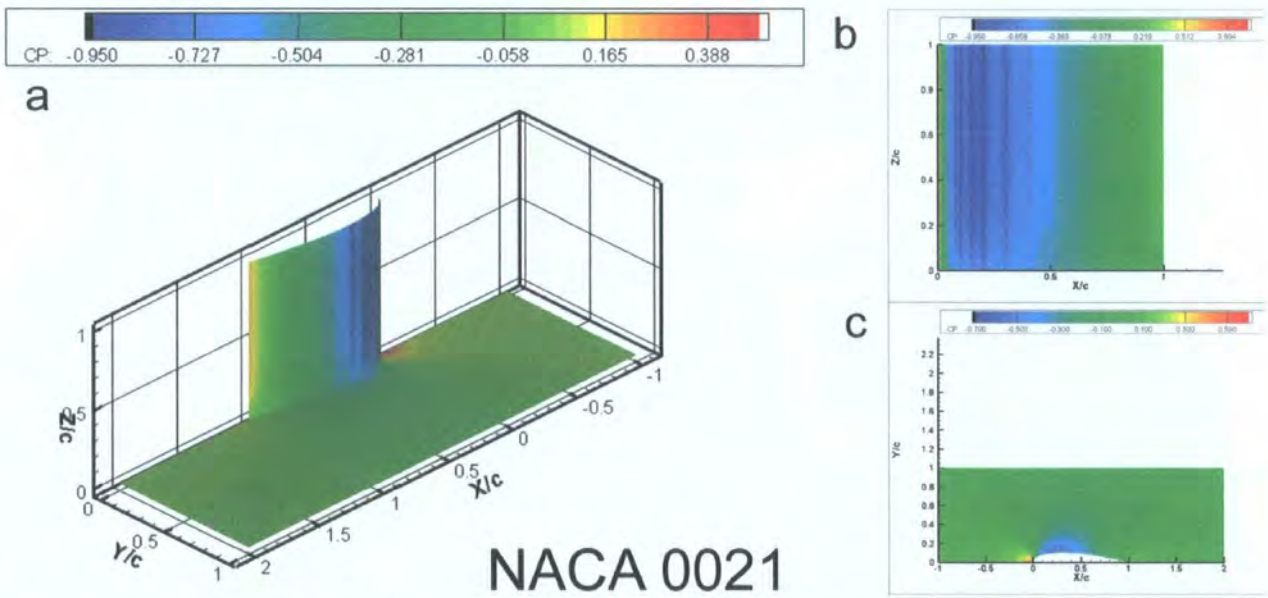

Figure 4.53: Pressure coefficient contours for the NACA 0021 Foil-Plate case at δ/c=0.029 showing a) a three dimensional view of the junction, b) a two dimensional view of the aerofoil surface, and c) a two dimensional view of the flat plate.*

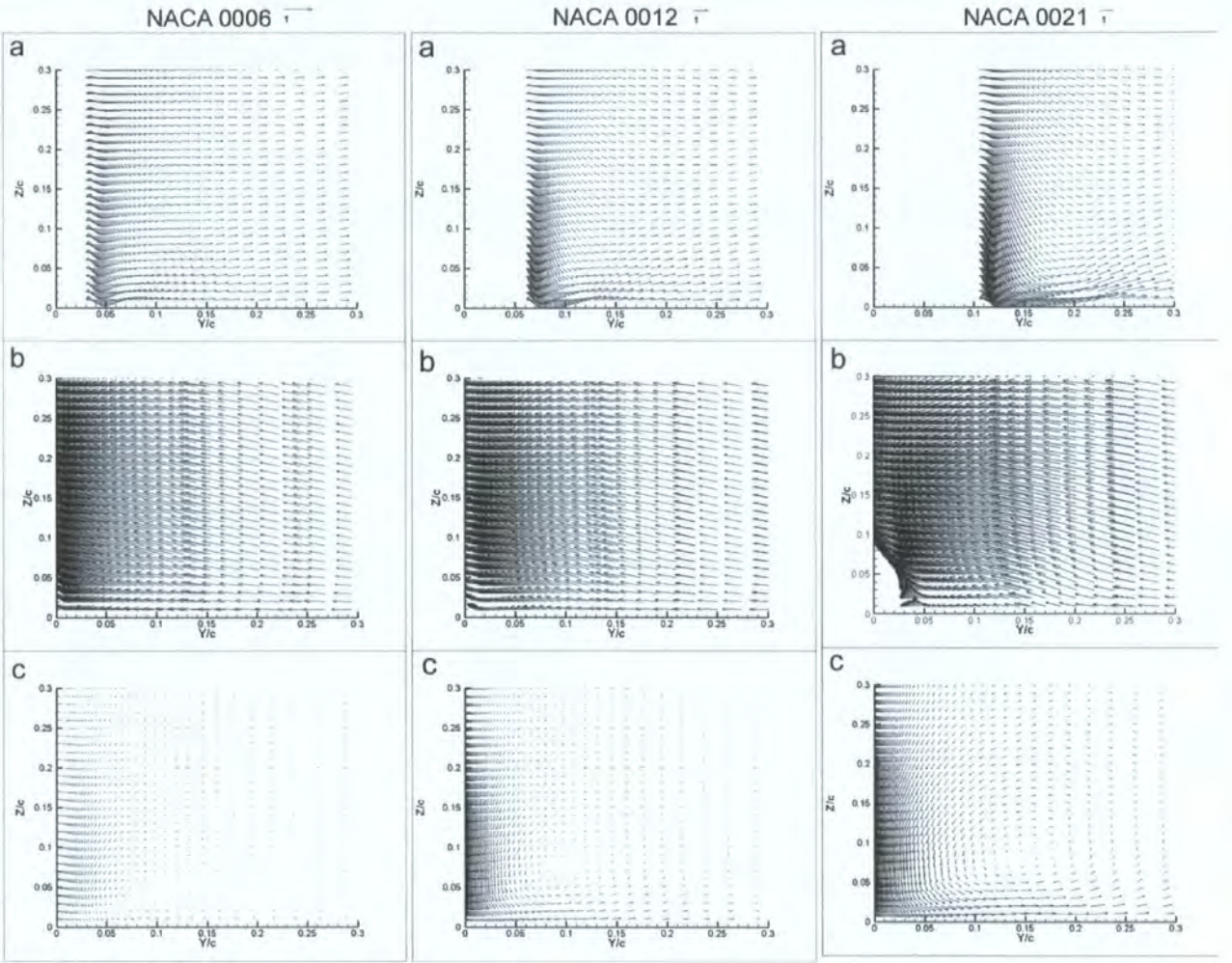

Figure 4.54: Velocity vectors in planes normal to the direction of flow at a) x/c=0.30, b)x/c=0.90, and c)x/c=2.0 for the NACA 4-digit aerofoils with δ/c=0.029.*

Another effect that was noticeable for the NACA 0012 (Figure 4.49c), but not the NACA 0006 (Figure 4.47c), and is now seen in Figure 4.52a&c for the NACA 0021 is an area of low skin friction adjacent to the area where the trailing edge separation has been witnessed, but further from the symmetry axis. This area, labelled 'A' in both Figure 4.49 for the NACA 0012 and Figure 4.52 for the NACA 0021 was explained earlier in the description of the flow structure for the NACA 4-digit aerofoils (Section 4.3.3.3); however, it is now seen that it increases with T/c ratios above 6% and otherwise is not present. Remembering Section 4.3.3.3 it was observed that the vortex was forced toward the plates surface as it propagated from the point of maximum thickness past the trailing edge and on toward the outlet. Looking now to Figure 4.49a and Figure 4.52a, the vortex path can be seen laid out as an area of increased skin friction extending downstream from just after the aerofoil maximum thickness to the outlet plane. Increasing the T/c ratio from 12% to 21% not only increased the size and strength of the horseshoe vortex, but also the size of the trailing edge separation, which then deflects the path of horseshoe vortex further from the symmetry plane as it exits the outlet plane.

For the NACA 0006 aerofoil the horseshoe vortex formation was weak and had almost completely dissipated by the time it reached the outlet plane (see Figure 4.54). For this same profile the trailing edge separation seen in Figure 4.55b by the amount of loss against the aerofoil surface (z-axis), is the smallest for the NACA 0006 and grows with increasing T/c ratio. Then in Figure 4.55c low loss fluid from the free stream is more easily mixed in behind the NACA 0006 aerofoil when compared to the thicker profiles. Increasing the T/c ratio makes this recovery more difficult because the horseshoe vortex and trailing edge separation are more prominent.

As further proof to the increasing strength of the horseshoe vortex, Figure 4.55a shows the low loss contours from the free stream bending further in towards the corner with an increase of T/c ratio. However, this does not help recover the loss behind the aerofoil due to the trailing edge separation seen in Figure 4.55b, instead it only adds more fluid to the junction increasing the skin friction in the area. The size and influence of the trailing edge separation determines the recovery behind the aerofoil.

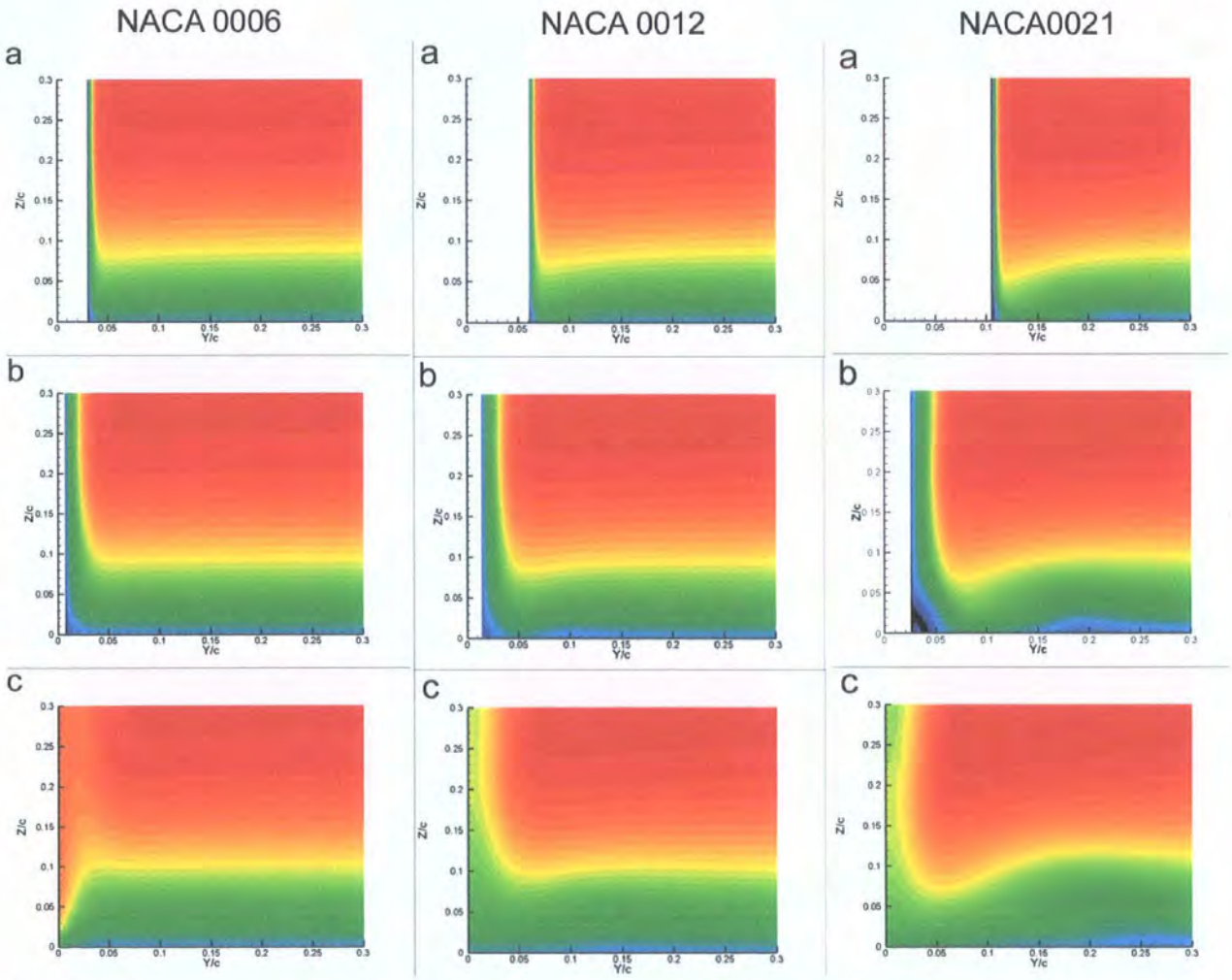

Figure 4.55: Total pressure coefficient in planes normal to the direction of flow at a) x/c=0.30, b)x/c=0.90, and c)x/c=2.0 for the NACA 4-digit aerofoils with δ/c=0.029.*

4.3.5.2 *Effects of T/c variation for the NACA 66-series Aerofoils*

Figure 4.56 through Figure 4.61 show changes due to growing T/c ratios of the NACA 66-series aerofoils. Although the effects of increasing T/c ratio for the NACA 66-series are similar to those seen for the NACA 4-digit series, the changes that an increase of T/c has on the differing features of the flow structure that were pointed out in Section 4.3.3.4 and 4.3.3.5 must be observed.

Comparing the effects at the leading edge and maximum thickness of increasing the T/c ratio from 12% to 21% in Figure 4.56 and Figure 4.57 only the magnitude, not the distribution of C_{fx} incurs a noticeable change. The same is also true for the C_p plots of Figure 4.58 and Figure 4.59: Pressure coefficient contours for the NACA 66-012 Foil-Plate case at $\delta^*/c=0.029$ showing a)a three dimensional view of the junction, b)a two dimensional view of the aerofoil surface, and c)a two dimensional view of the flat plate.

As was the case for the 4-digit aerofoils, this is due to the increased strength of the horseshoe vortex; however, unlike the 4-digit aerofoils a change in size of the vortex is not noticeable. Looking to Figure 4.60a the vortices are all the same size, but the 66_4-021 aerofoil exhibits a stronger concentration of vorticity at the core than the 66-012, confirming the trends seen in the plots of C_{fx}.

The obvious differences between the two are near the trailing edge of the aerofoil. The NACA 66-012 keeps the flow attached much better than the NACA 66_4 -021, creating a smaller trailing edge separation. The larger separation of the NACA 66_4-021 can be seen along the x-axis of Figure 4.57c as a small area of negative skin friction behind the aerofoil. It can also be seen that the separation for both aerofoils is larger than for similar T/c ratios of the 4-digit series and starts at an earlier value of x/c in Figure 4.56a&c and Figure 4.57a&c.

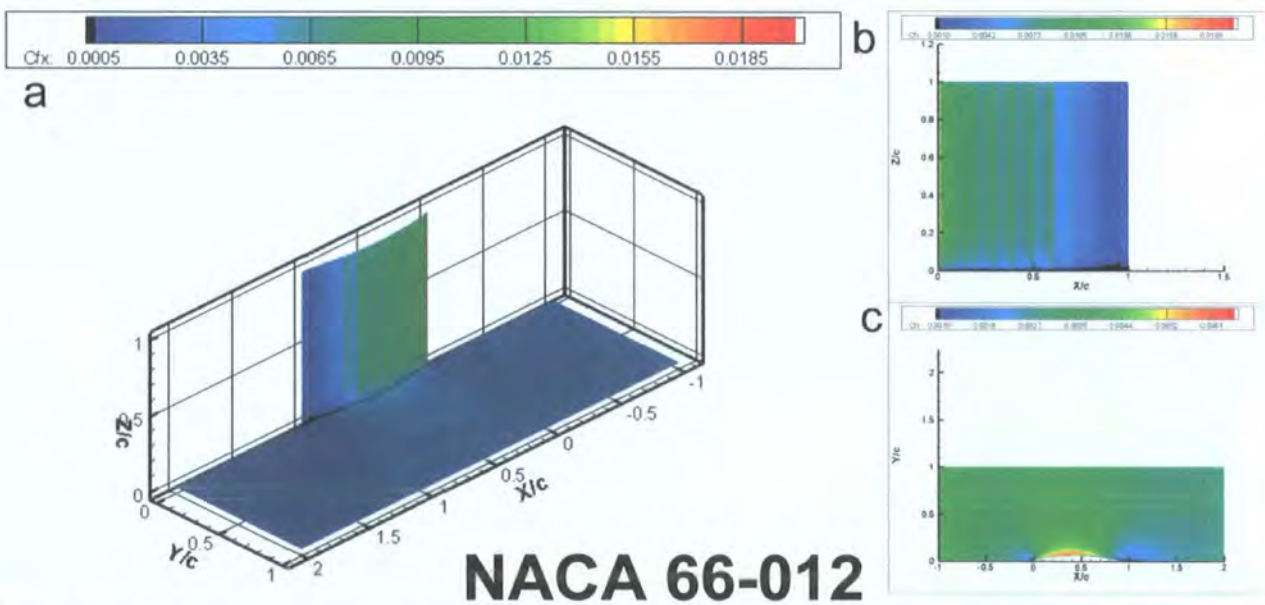

Figure 4.56: Skin friction coefficient contours for the NACA 66-012 Foil-Plate case at $\delta^*/c=0.029$ showing a)a three dimensional view of the junction, b)a two dimensional view of the aerofoil surface, and c)a two dimensional view of the flat plate.

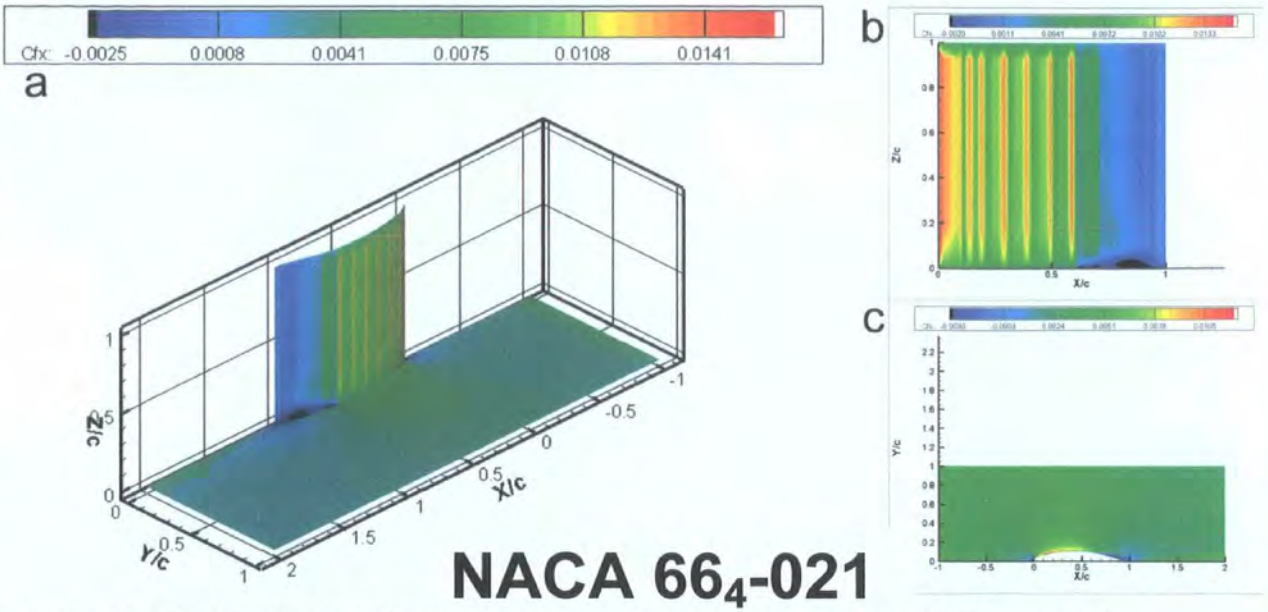

Figure 4.57: Skin friction coefficient contours for the NACA 66$_4$-021 Foil-Plate case at δ/c=0.029 showing a)a three dimensional view of the junction, b)a two dimensional view of the aerofoil surface, and c)a two dimensional view of the flat plate.*

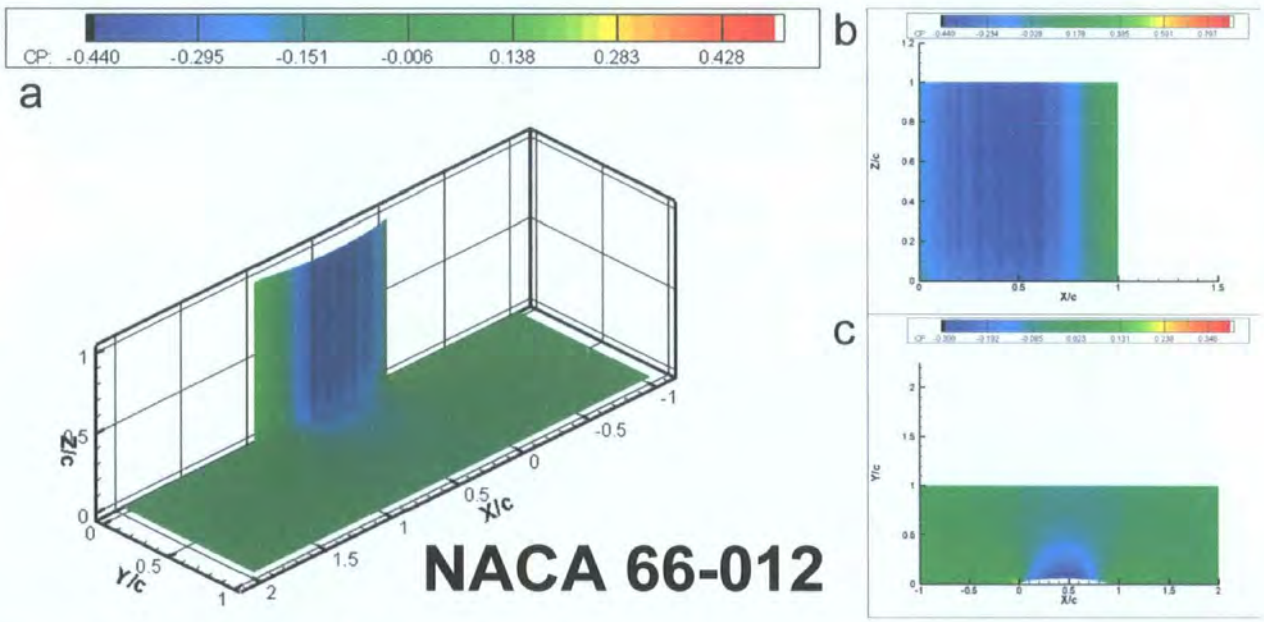

Figure 4.58: Pressure coefficient contours for the NACA 66-012 Foil-Plate case at δ/c=0.029 showing a)a three dimensional view of the junction, b)a two dimensional view of the aerofoil surface, and c)a two dimensional view of the flat plate.*

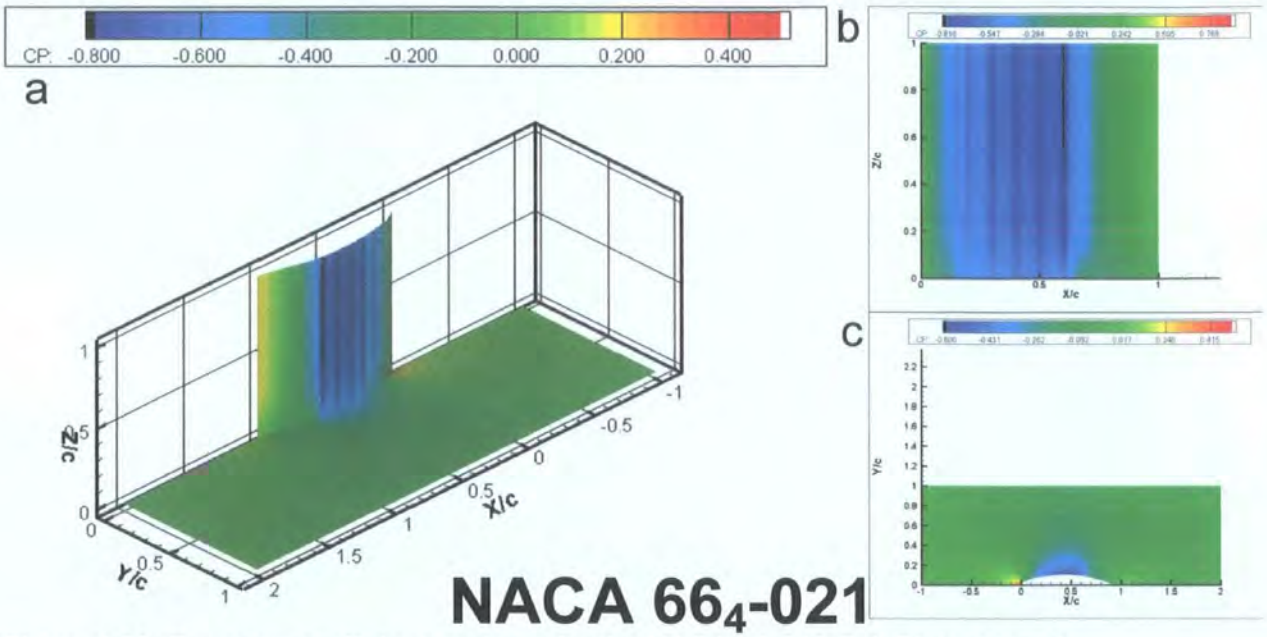

Figure 4.59: Pressure coefficient contours for the NACA 66-012 Foil-Plate case at δ/c=0.029 showing a)a three dimensional view of the junction, b)a two dimensional view of the aerofoil surface, and c)a two dimensional view of the flat plate.*

The reversed flow due to the larger trailing edge separation of the NACA 66_4-021 slows the fluid enough near the trailing end of the junction to allow the inward flow to create stronger vorticity (witnessed in Figure 4.60b), which is accompanied by increased loss along the aerofoil surface in the plots of CP_o (Figure 4.27b) . This large of an area of vorticity is not seen for the NACA 66-012 aerofoil. Also noticeable in the plots of CP_o is the increased vorticity strength of the NACA 66_4-021 bending low loss contours further into the corner of the junction.

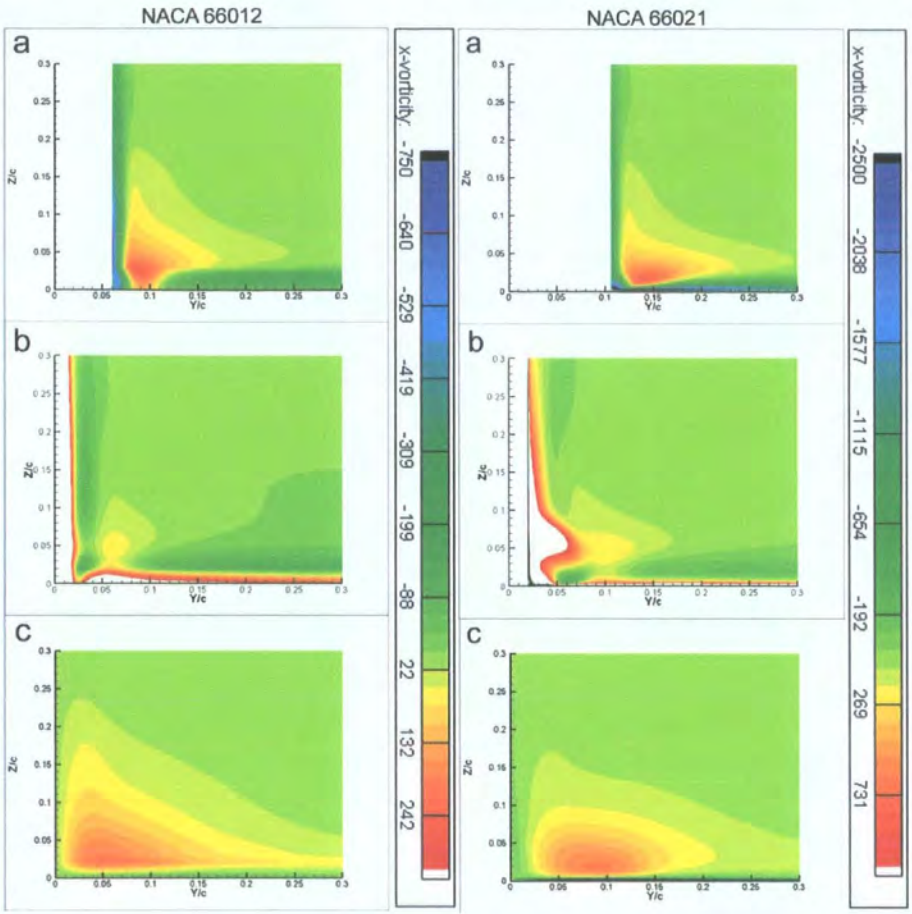

Figure 4.60: Stream wise vorticity in planes normal to the direction of flow at a) x/c=0.30, b)x/c=0.90, and c)x/c=2.0 for the NACA 66-series aerofoils with δ/c=0.029.*

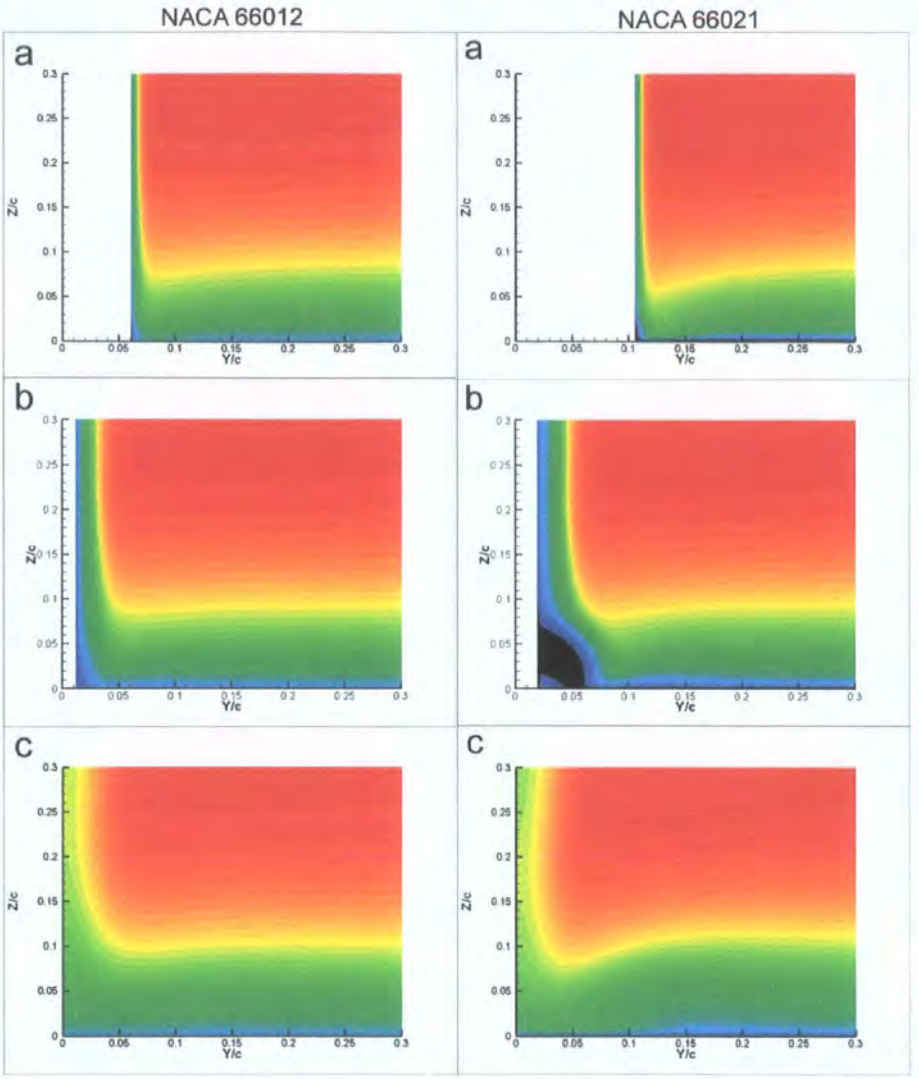

Figure 4.61: Total pressure coefficient in planes normal to the direction of flow at a) x/c=0.30, b)x/c=0.90, and c)x/c=2.0 for the NACA 66-series aerofoils with δ/c=0.029.*

4.4 SUMMARY

Throughout the progression of the junction flows for varying T/c ratios of the two differing NACA series it was first noticeable with the 0 width aerofoil that changes created by the junction were greater on the aerofoil surface when compared to the plate. Looking at the three dimensional plots of C_{fx} and C_p shown throughout the chapter, when both the plate and aerofoil are shown on the same scale, the greater variation of both C_{fx} and C_p is seen on the aerofoil surface, not the plate, suggesting that greater effects from the junction are seen on the aerofoil for all junctions of this type.

Looking back through the figures, the junction separation for an aerofoil of finite width (even one as slim as the NACA 0006) does not bear much resemblance to that for the 0width aerofoil. However, looking forward at trends over increasing T/c it is clear that with an increase of bluntness, the vortex strength, size, and influence grows. As was shown in the interference forces of Section 4.3.2, the difference created by a change in T/c ratio are much more pronounced than for a change of boundary layer thickness.

5 DISCUSSION

5.1 SUMMARY OF EFFECTS ON AERODYNAMIC FORCES

5.1.1 Ahmed Bluff Body

The measurements taken for the tested Ahmed bluff body are not representative of those taken by [Ahmed et al., 1984] during their initial parametric study of the model. Although it is difficult to discern without further exploration, it is thought that a large ground boundary layer ($\delta \approx 35$mm) has narrowed the air gap beneath the model and therefore altered the ground effect felt by the model, causing the backlight angle to stall early and switching the critical backlight angle to 27.5 degrees.

The Ahmed model saw a change in critical backlight angle from 27.5 to 30 degrees with the use of the Large Strut & All Stings. From all other support configurations, the critical backlight angle remained at 27.5 degrees. Across the range of backlight angles interference always manifested in an increase of drag on the model, the effect on lift, however, varied depending on support type and backlight angle. Overall the effects on C_D are at most approximately 10 counts with the exception of the spike in data shown at 30 degrees due to the alteration in critical angle created by the Large Strut & All Stings where the change is 125 counts. Across the range of backlight angles, support configurations using the wheel stings consistently reduce the amount of lift in a range of 40 to 80 counts. The struts on the other hand tend to increase lift. Prior to the critical angle the Small Strut has only a small effect on C_L, sometimes negligible.

Although it is commonly proposed that flow over the backlight would remain attached on a Fastback until the critical backlight angle was reached, some experimenters [Gilhome et al., 2001] [Strachan et al., 2004] have proposed that the presence of ground effect actually lowers the angle at which fluid will remain attached to the vehicle backlight to 15 degrees. It is further proposed that above 15 degrees the fluid separates at the backlight leading edge, but then re-attached further downstream.

It was noticed earlier in Section 3.2 that at angles less than 15 degrees the magnitudes of the effects from the supports would vary but they had a dependable trend on both lift and drag. It is certain that fluid flowing over the backlight in the strut wake will have less velocity than at the same location without any overhead strut present, but it is not clear how this creates an increase in both drag and lift on the model. With a lower velocity fluid flowing over the backlight near the centreline and behind the strut, the flow would be more likely to remain attached which would not help explain an increase in drag. Although further investigation would need to be undertaken, it is proposed that the presence of the strut, and in the case of the Large Strut, the actuator housing, forces flow into the c-pillar vortices. An increase of the size and strength of the vortices would then account for the increase of the measured aerodynamic forces seen from the overhead struts.

On the other hand, the lateral wheel stings affect flow at the under body and sides interfering with the already present base separation, increasing the drag and reducing the lift. Whether or not the stings induce a backlight separation cannot be confirmed. A combination of the support methods then sees the two effects compacted to further increase drag and slightly reduce the magnitude of the lift reduction. It is this combined affect that later pushes the critical backlight angle to 30 degrees.

At backlight angles greater than 20 degrees the addition of a natural backlight separation makes the effects of the support configurations becomes more ambiguous and the dependable trend disappears. At the critical backlight angle and beyond, however, there is an obvious change of the influence seen from both of the overhead struts that are known to interfere with the backlight separation.

5.1.2 Notchback

In Section 3.3.1, force measurements of model lift and drag reveal a sometimes small, but consistently increasing effect on both C_D and C_L from the use of an overhead strut. The effect of the Large Strut is consistently greater than the Small Strut, typically increasing C_D by 4 counts or more and C_L by 15 counts. The Small Strut has very little noticeable effect on lift, but effectively increases C_D by 3 counts. Because the Large strut affected lift, but the Small strut did not, and because the majority (approximately 95%) of the change in lift occurred at the rear of the vehicle, it is evident that the wake of the Large Strut's faired actuator housing is affecting flow over the rear of the model. It is proposed that the wake of the housing, in combination with the wake from the lower NACA 66_4-021 profiled portion of the strut, is creating a blockage effect and narrowing the passage for fluid in the jet above the rear portion of the model. This therefore increases the velocity in this area and lowers C_p on the rearward half of the model, generating lift.

Further in Section 3.3.1 the effects of individual pairs as well as a combination of pairs of stings is discussed. The most noticeable observation for all sting configurations was that the effects on C_D are not significant. The apparent effects, which are consistently less than force balance resolution, alternate sign and change magnitude, but are never obviously real. On the other hand, the use of the lateral wheel stings always increases C_L. The Front Stings create a small change of up to 4 counts, the Rear Stings follow next in the ranking with an effect of about 10 counts, and both pairs used together, comprising the 'All Stings' configuration follows with an approximately summed effect of 15 counts. The fact that the effect of both pairs combined is a sum of the effects of the two pairs when used alone shows little interaction, if any, between the two pairs of stings for this model.

5.1.3 Hatchback

5.1.3.1 Hatchback without the Roof Tailing Edge Deflector

Section 3.3.1 shows no effect outside of repeatability on C_D or C_L for the Small Strut on the Hatchback without the rear deflector. The Large Strut creates a more impressive change of 10 counts maximum on C_D and 35 counts maximum on C_L. For the different sting configurations, there is only an appreciable change in drag coefficient of 8 counts for the Rear Stings. The same is not true for lift coefficient which

sees the smallest effect from the rear stings of 10 counts and an opposite effect, reaching a maximum of -30 counts for the 'Front Sting' and 'All Sting' configurations. None of the effects on either lift or drag of the individual pairs of stings sum to provide the value of the effect for the two pairs when used together verifying an interaction between front and rear stings for this model.

5.1.3.2 *Hatchback with the Roof Trailing Edge Deflector*

With the flow deflector at the roof trailing edge the effects on the Hatchback model from the overhead struts are greater than they were without the deflector. Both still cause an increase in drag, but this time with the Small Strut raising the measurements to a maximum of 5 counts on C_D and 20 counts on C_L and the Large Strut raising the effect to 25 counts on C_D and just over 90 counts on C_L. The trend of increased effects with the deflector continues for the stings, but to a lesser degree. The only effects on drag once again come from the Rear Stings increasing C_D by about 10 counts. The effect on C_L follows the same trends as with the Hatchback without the deflector, with the Rear Stings increasing C_L to a maximum of 30 counts and the 'Front Stings' and 'All Stings' configurations reducing the measurement by about 40 counts. Once again the results of the front and rear pairs do not combine to the effect of 'All Stings,' showing an interaction between front and rear pairs.

5.1.3.3 *Effect of Roof Trailing Edge Deflector*

As mentioned the Hatchback is fitted with a flow deflector at the roof trailing edge that largely defines its wake structure and pressure forces felt by the model. At the end of Section 3.3.1 the effect on the model from adding the deflector is explored. Without the deflector, C_D and C_L are 13 and 118 counts greater, respectively, than they were with it. In agreement; with the deflector in place, the effect on C_D due to the Large Strut is 25 counts, without the deflector the effect is a lesser 7 counts. Similarly, the effect on C_L with the deflector is 93 counts, without it the effect is a lesser 33 counts. Because this sensitive vehicle component falls downstream of the strut junction the consequences are greater for the Hatchback with the deflector than they were for the Hatchback without the deflector. These results confirm that an overhead support can severely disrupt flow over the vehicle backlight. The change in the effect of the deflector with and without the stings is small amounting to less than 5 counts on both C_L and C_D showing that the stings do not have much interaction with flow over the roof trailing edge.

Perhaps surprisingly, the deflector effect actually reverses sign, becoming positive, when the supports are present (this is with the exception of the 'All Stings' configuration which still causes a slight decrease, but with a much smaller magnitude than in the baseline configuration). This draws the important conclusion that the effects of a shape change in the wind tunnel with supports may not be consistent to what will happen on the road, without supports when the same shape change is made. However, it must be mentioned that this flow deflector was designed specifically for this vehicle and this effect may not hold true for all models using wind deflecting devices at their roof trailing edges.

5.1.4 Open Wheel Racer (OWR)

Being that the OWR model is of a generic build and does not directly fit the scale dimensions or shape of any modern open wheel race car category it was used here to exhibit the common features witnessed on open wheel, open cockpit vehicle. Common to open wheel racers the model achieves down force using front and rear wings as well as profiled side pods and creates large amounts of drag with the exposed wheels, but it is not necessarily representative of any specific open wheel racer vehicle type.

In Section 3.4.1 the changes in drag and lift for the open wheel racer are outlined. The models exhibits a small, but real, negative reaction on C_D and positive reaction of 10 counts on C_L due to the Small Strut. This effect is then amplified for the Large Strut, increasing to 10 counts on C_D and a maximum of 55 counts on C_L. In general it would be assumed that interference from struts, stings, or both in combination would increase drag, but the drag is decreased by the supports, signifying that the supports are affecting some drag producing element of the vehicle. Because the support also produces a loss in down force a logical location for the interference is on the drag producing rear wing. This reduction in rear wing down force thus leads to a reduction in induced drag. The effects of the stings, however, are different. There is no significant effect of the stings on drag, but the apparent effect is positive. The effect of the stings increases lift by 15 counts without a strut and decreases lift by 9 counts when a strut is present. This perhaps shows the overwhelming effect of the strut on the rear wing or an interaction between the strut and stings for this model.

5.1.5 Closed Wheel Racer (CWR)

A typical closed wheel race car of this type should exhibit a lift balance of about 50% or 60% at the rear [Dominy, 2002]. However, for the model tested over a fixed ground the balance was always overly biased to the rear. By adjustment of rear wing incidence, body pitch angle and ride height, cooling duct flow, and front splitter plate size, the most realistic balance that could be achieved was 76%; however, this configuration was not used because it unrealistically lowered the amount of cooling flow altering the vehicles drag. A configuration with 80% rear balance provided a better compromise. The rearward biased lift balance was assumed due to the lack of a moving ground and the presence of boundary layers and stalled flow at the vehicle underside.

Outlined in Section 3.4.1, the maximum changes due to the Small Strut of -9 counts on C_D and 80 counts on C_L are smaller than the changes of -15 counts on C_D and 170 counts on C_L of the Large Strut. As with the OWR, the struts are affecting the drag and down force producing rear wing, thus decreasing drag and lift on the model. The more physically intrusive Large Strut creates more interference on the wing. One noteworthy aspect of the struts effects on C_D is that they diminish to less than repeatability for both the struts when they are used in combination with any of the sting configurations. For lift, however, the effect of the Small Strut remains the same and the effect of the Large Strut is halved when the stings are present. This shows a definite interaction between struts and stings, but a lesser interaction between a smaller strut and the stings when compared to the interaction of the larger strut ad the stings.

Looking more closely at the effects of the stings in the same section of Chapter 3; the Front Stings or Rear Stings alone can create a maximum effect of up to 12 counts, however, the effect can change sign depending on the size of overhead strut used. With All Stings in use, the effect is always negative despite the strut configuration, reaching a maximum of 26 counts and decreasing when the struts are added. The results show that the effects of individual pairs do not add up when All Stings are used, demonstrating an interaction between pairs of stings for the CWR. For lift coefficient the stings cause the greatest effect seen from an individual support component thus far. A front pair of stings can create up to a 175 count increase on C_L alone, then when combined with the rear stings the effect is pushed up to approximately 250 counts. The Rear Stings alone create a much lesser, but still significant effect of 20 counts on C_L. These effects are similar for all sting configurations when the stings are combined with the Small Strut, but when the Large Strut is used, the effects of the 'Front Sting' and 'All Sting' configurations decrease. The effect of the Rear Stings actually changes sign, growing to a greater negative magnitude of -50 counts. This change due to the presence of the Large Strut shows a powerful interaction between the Large Strut and stings for this model and is described later as due to the two supports types altering the vehicle base pressure in the region behind the rear wing and under floor tunnel exit.

The effects of the different sting configurations described above prove that the change in lift due to the use of All Stings is not an equal effort from both front and rear stings, but is instead mostly an effect from the front pair, slightly from the rear pair, and lastly from an interaction between the two. There is an extra effect that is 'switched on' when the sting pairs are combined. The fact that the rear stings have very little effect on lift is not surprising. Since the effects on lift due to wheel stings are due to an interaction of the sting wake with the flow over and under the vehicle's streamlined body, it makes sense that the front stings, whose wake must travel almost the entire distance of the vehicle, would have a greater effect than the rear stings, whose wake does not start until very close to the vehicle's rear end. The fact that the Large Strut & Rear Stings when used together cause an increase in down force, when all other support configurations on this model have witnessed a destruction of the models down force is likely from a favourable change to the base pressure at the tunnel exit caused by an interaction of the rear stings and Large Strut. This effect must not be present when the Front stings are used, impacting the entire side of the vehicle and the inlet to the under floor tunnels at the side skirts.

5.2 General Effects of Support Components Alone and in Combination

5.2.1 Passenger Vehicles and Bluff Bodies

Examining the effects of the support components individually before they are combined, the drag of the passenger vehicles is affected most by the larger overhead strut, not the smaller strut or the four lateral wheel stings. In fact, for the Notchback and Hatchback with the deflector drag is only affected by the strut and does not have a significant reaction to the use of the stings at all. For the Hatchback without the deflector, drag is still more affected by the strut, but sees a small effect from the stings as well. The

magnitude of this effect on drag, which is always positive for the passenger vehicles, is by far greatest for the Hatchback with the deflector, followed by the Hatchback without deflector and then the Notchback.

The effects on lift from the individual support components can alternate sign depending on the specific model and support configuration. The greatest effect was once again from the larger overhead strut on the Hatchback with the deflector, followed by the Hatchback without deflector, and then the Notchback. The stings created a decrease in lift for both versions of the Hatchback with the model fitted with the deflector feeling the greater effect. The Notchback felt an opposing, positive effect, but of a lesser magnitude than both the Hatchback models. The effects of the smaller overhead strut on both lift and drag were only significant for the Hatchback with the deflector, for the other two models the strut did not create effects outside of repeatability.

Combining the overhead struts with the lateral wheel stings for the passenger vehicles can cause a range of effects, but generally causes an interaction between the flow fields of the two supports and model that has a tendency to reduce the magnitude of the final effect. For the Ahmed model, Hatchback with the deflector, and Hatchback without the deflector, the individual effects of the overhead struts and lateral stings do not combine to equal the overall effect of the combined support methods. Also, the effects of both the overhead support struts decrease in the presence of the 'All Sting' configuration. Further to this point, in Section 5.1.3, both forms of the Hatchback model see that the effect of the Front Stings plus the effect of the Rear Stings does not sum to create the effect when the two pairs are used together (All Stings). These trends confirm that for a Hatchback vehicle type there is an additional interference effect that is introduced by the interaction of the different flow fields from an overhead strut, individual wheel stings, and the model itself. On the other hand the effect of an overhead strut for the Notchback is consistent across individual pairs (front and rear) of stings and the effect of the front and rear sting pairs appears to be reasonably summative, suggesting that there is a limited aerodynamic interaction between front and rear wheel sting pairs, as well as between stings and an overhead strut for a Notchback vehicle shape. These observations were presented in [Hetherington & Sims-Williams, 2004 & 2006].

Generalising the effects seen on the passenger vehicle models, the biggest effects from both the lift and drag data that were most frequently seen throughout the range of different support configuration were from the Large Strut when used alone. Other configurations that appeared in the top spot at least once for either lift or drag change were the 'Large Strut & All Stings' and the 'All Stings' configurations.

5.2.2 Motor Sport Vehicles

Overall, the effects from support interference on the motor sport models were of a much greater magnitude than the effects on the passenger vehicles. This is especially true for the CWR and its larger amount of attached flow when compared to the OWR. The aerodynamic performance of a closed wheeled race car such as this is created largely through ground effect and the flow over the body not separating, creating a large amount of down force [Hucho, 1998] and the side effect of induced drag. It was shown in Section 3.4.2 that the specific model used exhibits very few areas of separation; justly the larger the intrusion of a support or combination of supports, the larger the effect on the vehicle's performance.

For both motor sport vehicle models interference from any of the support configurations causes an increase in both drag and down force. Similar to the passenger vehicles, the OWR feels the greatest effect on lift and drag from the Large Strut with some small effects seen from both the 'Small Strut' and 'All Sting' configurations.

As mentioned, the CWR is unique, suffering the most from interference. The Large Strut & All Stings creates the largest increase in lift, but for drag the 'All Stings,' 'Small Strut & All Stings', and 'Large Strut & All Stings' are all tied for the greatest effect. Looking at the results for the individual components in Section 3.4.1 and comparing the effects of the overhead struts to the lateral stings it can be seen that once the flow field is disrupted and switched to this higher drag condition by the stings, the further intrusion of the struts (combined with the stings) will not create any further drag effect. Once the drag effect is created by the use of the stings, it cannot be made any more severe.

Simplifying the effects on the CWR and making some generalisations it seems the individual supports when used alone (Small Strut, Large Strut, Front Stings, and Rear Stings) have the smallest effects (which are still large relative to the effects on the passenger vehicles) but when they are combined, interactions, specifically between the front and rear pairs of stings, can create a more substantial decline in drag or increase in lift (loss of down force).

Remembering Section 3.4.1, the use of the stings with the OWR is not the same in the presence of the overhead strut and the effects of the individual component when used alone do not quite add up to their use together. Looking back to Section 5.1.5 there is a reduction in the effect of the stings when used in the presence of the strut, but it is small, only showing a weak interaction between the two types of supports for the OWR model.

5.3 Effects on Flow Structure

As presented in Section 3.3.1 the effect of the Large Strut is much greater on the Hatchback, when compared to the Notchback. In Section 3.3.2 it was shown for the Notchback that the support does largely re-arrange the wake structure, but this re-arrangement has little effect on the overall drag force felt by the vehicle. However, the CWR feels a much greater effect on lift than the OWR and it feels a change in drag, but without a change in wake structure. In Section 3.4.2 the CWR is described as having very powerful features in its wake that create the large amounts of down force seen in the model measurements. With the intrusion of supports, the intensity of the flow features is altered, but the form they take behind the model is not. The greater momentum of the flow surrounding the streamlined motor sport model is more difficult to disrupt when compared to the passenger vehicles. Therefore, the wake of the passenger vehicles is more susceptible to a change in structure, which may affect some other areas of vehicle aerodynamics, but does not have as much of an effect on vehicle performance as for the motor sport vehicles.

Common to a notchback vehicle shape, large flow separations were seen on the Notchback along the roof, trunk, and c-pillar trailing edges. However, the wake structure of this particular model was not

representative of the commonly accepted models seen for Notchback type vehicle. Carr [Carr, 1974] believed that flow separating at the roof trailing edge re-attached to the trunk, with some of the flow then travelling upstream supplying a transverse vortex in the notch and adding lift to the vehicle rear end. Hucho [Hucho, 1998] perpetuated this belief proposing that the re-attachment is caused by downwash created by c-pillar vortices, which are more common to fast back type vehicles. However, observing the centreline traverse it does not appear that downwash between the C-pillar vortices has forced the shear layer to re-attach to the trunk as predicted, at least not at the centre plane. Nouzawa [Nouzawa et al., 1990] also found a separation in this area, but believed that the transverse vortex had been bent into more of an arch-like shape by flow coming over the C-pillar and trunk sides. Jenkins [Jenkins, 2000] did not recognize a shear layer re-attachment or the formation of a transverse or arch vortex. Instead he believed that the shear layer extended downstream into the wake forced away from the trunk by up-flow from a pair of 'boot lid' vortices and inflow converging at the centre plane. However, none of these prescribed models is an exact fit to the separations seen around the rear of the Notchback model. Looking closely at the flow visualisations of Section 3.3.2 the flow pattern at the surface most closely resembles the unsteady hairpin vortex model as described by Gilhome et al. [Gilhome et al., 2001]. Yet, it is a much less symmetric version, to the extent that the hairpin vortex would have to be twisted so that the two contra rotating legs of the hairpin vortex sit one on top of the other at the left of the boot lid near the left C-pillar vortex.

This type of asymmetry is not unusual for notchbacks and has been witnessed by [Gaylard et al., 1998] on the simplified MIRA reference model and is explained further in [Gaylard et al., 2007]. It was also witnessed as part of the hairpin vortex system of [Gilhome et al.,2001], but was accredited to model asymmetry or flow inconsistency and was not further explored. Another short mention of such asymmetry can be found in [Cogotti, 1984], but is also not explained.

The existence of a not uncommon [Gaylard et al., 1998, 2007] asymmetric wake and the introduction of an additional area of separation from the use of an interfering support only added to the complexity of the flow field. The introduction of All Stings left the backlight separation asymmetric whereas the Large Strut created symmetry in the wake bringing it closer to the prescribed models in the literature.

For the Notchback the most noticeable effect is the Large Struts wake impinging on the backlight and trunk, forcing a more symmetric backlight separation. This is accompanied by a solid blockage effect (described earlier in Section 5.1.2) affecting the models rear lift. A similar effect is present in Section 3.4.2 for the CWR. Here the wake of the large strut is not seen impinging on the model body directly after the junction, but is witnessed further downstream on the rear wing. Results from both the CWR and OWR show a decrease in drag and a loss of down force combined with an increase in pitching moment, all of which are consistent with a reduction in the down force and induced drag of the rear wing. The wake of the strut that creates these effects will no doubt be present over the backlight of the Hatchback model causing the greater effects on the rear deflector that were discussed in Section 5.1.3.3 and the Ahmed model helping to change the critical backlight angle.

The stings create more lift than drag across the collection of models and that there is not much noticeable interaction between flow structures of the stings and struts for the Notchback (Section 5.1.2), also, the stings have a large effect on the rear deflector of the Hatchback (Section 5.1.3.3), and they have been proven to affect the under floor flow of the low riding CWR. These facts lead to the conclusion that the stings primarily affect flow at the vehicle underside.

In the case of the passenger vehicles, the stings will not be adding to the vehicle wake because there is no added drag with their addition and since there is no interaction with the overhead struts, for the Notchback or interaction with the rear deflector for the Hatchback, the stings must not be adding to the lower pressure above the vehicle, leaving the underside of the vehicle as the most likely location for a change in flow.

For the motor sport vehicles, the flow to the sides of the vehicle was observed as being much less disturbed than for the passenger vehicles in wake surveys of chapter 3. Judging by the flow patterns, the effect of the stings was altering the supply to the under floor along the side skirts. However, the sting wake was also stretched to the rear of the vehicle along the side, causing not only an interaction of front and rear sting, but also of the stings and the vehicles base pressures, which, in turn interfered with flow over the rear wing and flow from the overhead struts.

For the CWR, the wing creates down force by itself, but also helps pull fluid through the under floor nozzle-diffuser, creating even more down force. The pulling action comes from the low pressure induced by the wing at the tunnel exit; this helps reduce the amount of separation in the tunnel and increases the flow rate [Katz & Dykstra, 1992]. Because the effects from the wheel stings are also witnessed at the vehicle base behind the wing, the interaction of the two support types seen in the force measurements is an effect of the interaction of flow in this area. The large effects that were seen in the lift measurements from combinations of support types are due to the interaction of the stings' wakes affecting flow into the vehicle underside, as well as affecting the base pressure at the tunnel exit, combined with flow over the rear wing being altered by the presence of the strut wake. Observing changes at each of the three surface pressure stations for the vehicle under side in Section 3.4.2, there appears to be an equal division of the effect at all three stations, not just along the vehicle side, implying a more distributed effect. Also, in the force measurements of Section 3.3.1 and 3.4.1, most vehicles see a more equally distributed change in force between front and rear axles created by the stings than by the struts.

It is well known that there are many opportunities for separation around an open wheeled race car and these areas are even more exaggerated on this basic model. The model had very little ducting, no spoilers or vanes, and the front wing was a simple symmetric profiled element at nose height. The fact that the supports had less interaction on the vehicle with larger areas of separation supports the suggestion made by Page [Page et al., 2002], that there is less aerodynamic interference if a model is supported in a region of already disturbed flow.

Although it could not be proven through force measurements alone, the interaction of the flow fields for the different support types from the Ahmed model were probably at the vertical base where flow from

backlight and flow from the underside separate forming a recirculation region. Flow from the backlight will have been affected by the decreased momentum of the strut, whilst flow from the model underside will have been disrupted by the stings. Because the flow along the vehicle side was less disturbed, in the case for the CWR, the stings' wakes may also have stretched back affecting the formation of the C-pillar vortices.

5.4 CFD

Analysis of the results showed that increasing the plate boundary layer thickness increased the size of the horseshoe vortex around the seam of the joint, but decreased its strength, causing an increase of the interference effect. Increasing the thickness-to-chord ratio, or bluntness, of the intersecting aerofoil created an increased interference effect greater than that of increasing the plate boundary layer thickness. However, despite the obvious trends in these affects the overall magnitude of the interference was small and insignificant when non-dimensionalised based on a models frontal area. This leaves alterations of pressure and velocity in the support wake as the sole cause of interference.

Although the results tend to discredit the junction as a possible location for the creation of interference, the importance of junction flows has been well documented in both aerodynamics and hydrodynamics and should not be discounted too quickly. The separations at the junction found throughout the computational results agrees well with models proposed by [Simpson, 2001], [Paciorri et al., 2002], [Olcmen & Simpson, 1994], and [Davenport et al., 1990] amongst others mentioned in Section 1.7.1, but does not produce a magnitude of effects that seems to compare with those in the literature. One possible reason for this is the use of the one equation Spallart-Allmaras turbulence model. It has been mentioned that this model will perform poorly at the aerofoil trailing edge and that a y^+ value above the recommended value was used during the simulation, but it has also been shown to under predict the horseshoe vortex dimensions [Paciorri et al., 2002]. These failings in modelling the turbulence have then led to an insignificant contribution to interference from the junction; however, it is safe to say that the majority of interference arises from the presence of a supports wake.

5.5 CFD vs Experimental vs Hoerner for the Aerofoil-Plate Junction

Equation 1.10 based on Hoerner [Hoerner, 1965] predicts a junction drag of ΔC_D=0.007 for the NACA 66_4-021 strut used. Non-dimensionalising using the vehicle frontal area arrives at ΔC_D=0.0006. If this prediction is accurate then the drag change created at the junction amounts to approximately a quarter of the interference drag created by the strut when used on the Notchback or Hatchback without the deflector as a whole. This leaves influences of the strut wake on the downstream backlight separation as the greater cause of the interference effect. The amount of drag predicted at the junction then becomes even less of the total effect when compared to the larger interference drag values found for the Hatchback with the deflector. For the only other closed roof model, the CWR, the larger effect of the strut is actually

negative, so if any positive junction interference is witnessed, it is soon overcome by a greater negative interference from the strut wake impinging on flow at the drag producing rear wing.

The wheel stings are designed to support axles through the model wheels and are cylindrical at the model end. Equation 1.10 indicates that this blunt profile should result in a large junction drag of 0.070 on C_D per wheel sting, whereas the actual effects were smaller for all models tested. For all ground vehicle models flow in the area of the wheel supports suffers a large amount of disturbance due to the wheel rotation, wheel arch, vehicle underside, model mountings, and ground boundary layer; the lack of a correlation between measured and predicted effects is not surprising.

Comparing the predicted effects based on Hoerner to those measured for the plate in isolation, the magnitude of the effect is similar; however, the effects are of opposite sign. The plate in isolation saw a negative change in drag that was small and close to balance repeatability, whereas Hoerner predicts a positive change in drag. The presence of a gap beneath the aerofoil and the existence of reversed flow in the trailing edge separation near the junction is the likely cause of the discrepancy between the two. As discussed in Chapter 4, a laminar flow aerofoil of this thickness exhibits a large and influential trailing edge separation. This separation, combined with the horseshoe vortex from the leading edge of the junction, creates a region of reversed flow near the trailing edge of the junction that introduces low loss free stream fluid into the junction. The reversed flow is also visible in the flow visualisations of Section 3.5.1. However, the interference drag from the CFD simulations for this aerofoil, were still positive, but to a lesser magnitude than predicted by Hoerner. The discrepancies between the computational measurement of an isolated test case, predictions from literature, experimental measurements from an isolated test case, and experimental measurements from a full bodied test case show that there is not much rationale in evaluating interference from model supports considered in isolation. The small scale of the junction relative to that of the model (for these 25-40% models) precludes the possibility of predicting drag and lift changes on vehicle components downstream or the model-support configuration as a whole. The effects that can take place between the flow fields surrounding the model body and entire support system are much more significant than the effects local to the junction.

5.6 Isolated Rear Wing vs OWR

Overall the changes in drag and lift caused by placement of the NACA 66_4-021 strut upstream of the wing in isolation were greater than the changes found from interference of the strut on the complete vehicle. For certain rear wing incidences, the effects were comparable, but throughout the region of stall they were not. In isolation the wing had an undisturbed flow field; however, in position on the model as seen in Section 2.1, the wing fell downstream of the cockpit, roll cage, and engine intake, all of which severely disrupted the flow before it reached the wing. With placement of the strut into this region of already disturbed flow it is not surprising that there was a much smaller effect of the strut on the model. The results illustrate the importance of understanding and accounting for the effects between the wing and body of a motor sport vehicle, they also show that there is not much value of investigating interference

effects on a motor sport vehicles rear wing in isolation if it is used in a region of flow which is already disturbed.

5.7 GUIDELINES FOR FUTURE EXPERIMENTERS

It has been determined that using a single wide belt beneath a model will provide an accurate simulation of on-road conditions during wind tunnel testing, however, using this method will require the use of intrusive supports to hold the model in place and measure the aerodynamic forces. Results have shown that the complexity of interactions between struts, stings, and the model are highly vehicle dependent and preclude the possibility of developing a reliable correction. The results do, however, lead to suggestions for support-model coupling methods that minimise the magnitude of the interference effect and offer guidelines for the expected magnitudes of effects for the different vehicle types and struts tested.

5.7.1 Interference Reduction and Expected Effects

- Although there will inevitably be structural criteria placed upon a struts design to hold the model rigidly in place and reduce vibrations, the strut should be designed as a streamlined shape to minimise the bodies wake. This will help reduce the amount of interaction with the models flow field.

- Maintain a uniform support profile extending to the jet boundary. If a support is designed with a streamlined profile, this profile will be most effective if kept until outside the jet boundary. Interrupting the profile shape with the inclusion of other, frequently larger, components used for measurement or model adjustment creates a more complicated flow field and will result in further interference. Throughout the experiments performed for this investigation there has been a consistently smaller and sometimes insignificant effect seen from the Small Strut. This support is designed specifically to provide enough support for the model, but yet uses a thin, uniform profile to reduce its wake, jet blockage, and therefore reduce interference with the model. Reducing the overall size of the support present in the jet stream will also help maintain flow quality as a wind tunnel is infrequently designed with blockage from a model support as part of the design criteria.

- Support the model in areas of already disturbed flow. For most closed body vehicle types using a horizontal or angled strut approaching from behind, within the vehicle wake, where the flow is already disturbed will be advantageous.

- The use of overhead struts and wheel stings with motor sport vehicles will generate lift (remove down force) with a more substantial effect seen on a closed wheel, closed cockpit model.

- When a set of 4 wheel stings are the only support method used their effect is more equally distributed across the model length making them the most favourable support method for maintaining the lift balance.

- The use of an overhead strut can be expected to influence the backlight of passenger vehicles. Even a small streamlined strut will create a velocity deficiency in its wake affecting flow over the roof trailing edge, backlight, and boot if present. These effects will grow with increasing strut size. The use of an overhead strut has not been witnessed to directly influence the underside flow of passenger vehicles.

- The use of an overhead strut can be expected to influence the rear wings of motor sport vehicles.

- For a motor sport vehicle that relies on base pressure to accommodate the functioning of an under floor nozzle-diffuser an overhead strut will indirectly interfere with the under body flow by altering the base pressure behind and beneath the wing.

- The use of wheel support stings will disrupt flow around and through a vehicle's wheels. They can also be expected to disrupt flow beneath the model and at the model base.

- Although it may be the case for certain individual vehicles, it is never safe to assume that the effects of individual supports can be collected to give an overall effect of the supports when combined.

5.7.2 Magnitudes of Expected Effects for Vehicle Types

- Notchback/Fastback (backlight angles of 15-25 degrees): 5 to 10 count increase on C_D; 30 to 60 count +/-effect on C_L

- Squareback: 5 to 10 counts increase on C_D; 40 count decrease on C_L

- Hatchback: 20 count increase on C_D; 50 count increase on C_L

- Open wheel, open cockpit racer: 10 count reduction on C_D. 50 to 60 count increase on C_L

- Closed wheel, closed cockpit racer: 25 count reduction on C_D; 350 count increase on C_L.

These values were determined using mock supports with models mounted to a stationary ground plane. The presence of a moving ground could effectively alter these values.

Quoted values are using the popular configuration with an overhead strut and 4 wheel stings supporting each of the wheels.

6 CONCLUSION

Experiments were performed with a mock support configuration similar to that which would be used for moving ground testing, but with the range of models mounted on a fixed ground to an under floor balance. Different configurations of overhead struts and lateral wheel stings were then compared against a baseline configuration. To understand the importance of effects local to the junction a number of CFD simulations of an aerofoil intersecting a flat plate were performed and compared to experimental effects seen on the model-support configuration as well as an isolated test case of an aerofoil joined to a flat plate tested in the wind tunnel. Two isolated test cases were also performed; one testing an aerofoil shaped strut intersecting a flat plate to find the amount of interference that was introduced to the plate by the presence of the strut and another with an aerofoil shaped strut upstream from a motor sport vehicle rear wing to see the effects on the wing imposed by the strut wake.

6.1 Magnitude of Effects

The magnitude and sign of the effect of lateral and overhead supports was found to be highly vehicle dependent. From the array of model and support configurations tested a maximum change in drag of 25 counts (7% of the overall drag) was found from interference from a larger overhead strut alone for a Hatchback model fitted with a deflector at the roof trailing edge. For the other models tested typical drag changes ranged between -25 and +10 counts (1% to 3% change in the total drag for the model) for different support configurations. The changes in lift accompanied with these maximum changes in drag ranged from +30 counts for the passenger vehicles to +350 counts for one of the motor sport vehicles. Despite these maximum values, the changes in lift were not always positive, some models saw a decrease in lift by up to 30 counts.

6.2 Flow Changes from Overhead Struts

The intrusion of overhead supports can affect key areas of flow over the backlight of passenger vehicles, re-arranging the flow structure and having sometimes significant effects on lift, especially at the rear of the vehicle. The Ahmed bluff body can experience a significant amount of interference, altering the backlight flow and increasing the critical backlight angle. There are also associated changes in drag accompanying the reduction of flow momentum in the support wake. In the particular case of the Notchback vehicle tested within this project, the intrusion of the overhead strut forced the asymmetric backlight separation into a more symmetric structure with only a small associated change in drag and a change in lift at the rear of the vehicle. For motor sport vehicles the effect of an overhead strut is predominantly found to affect the performance of the vehicle's rear wing. Interference with the rear wing can also affect the wings interaction with the model that draws flow through the under floor tunnels. Typically changes caused by impingement of a strut wake on a rear wing create a loss of down force and a reduction in induced drag. For the above mentioned changes to passenger and motor sport vehicles, the interference effects created by an overhead strut, increase with strut size.

6.3 Flow Changes from Lateral Wheel Stings

For both vehicle types the intrusion of lateral wheel stings has little effect on drag, but can greatly alter vehicle lift. Finding the cause of the effect was challenging due to the presence of the ground boundary layer, but a lack of a change in drag and flow patterns on the upper surface of the vehicle, combined with greater pressure changes witnessed on a vehicles lower surface, lead to a conclusion that the stings primarily affect flow at the vehicle underside. Flow visualisation also witnessed the wake of the stings impinging on the vehicle sides. For motor sport vehicles in ground effect disruption of the flow in this area can alter portions of flow entering the vehicle underside.

6.4 Aerodynamic Interaction between Support Elements

For the Ahmed, Closed Wheel Racer, Hatchback with and without the deflector, and the Open Wheel Racer body shapes the effects of the overhead strut and front and rear wheel sting pairs were not summative, showing an extra effect that is created by the proximity of the flow fields to each other and the model. For the Notchback vehicle shape the effects were found to be consistently summative, showing that there was no interaction between the support types in the flow field surrounding this model. Consequently, the effect of one sting pair cannot be doubled and used to represent the amount of interference of both pairs across a symmetry line, thus, all four wheel stings must be used to determine interference and it is not safe to assume that the effects of a sting or sting pair is doubled on the other side or even opposite end of the vehicle.

6.5 Effect of Overhead Struts on the Impact of a Shape Change

Testing the Hatchback model with and without the roof trailing edge deflector and analysing the data to show the effect of the deflector itself on the models force measurements showed that the deflector can create an increase or a decrease in both drag and lift, depending on the type of support present during the wind tunnel test. This draws the important conclusion that the effects of a shape change in the wind tunnel with a support present may not be consistent to the effects that the same vehicle component will have on the road.

6.6 Strut Interference on an Isolated Wing

Results from the isolated test case with a strut upstream of a rear wing showed a much larger effect on the wing from the strut when in isolation than when it was placed on the model. This offered a testimony to the importance of designing a wing with the vehicle flow field in mind and showed that since the wing was subject to an entirely different flow field on the model, the results did not compare.

6.7 Isolated Junction

A turbulent boundary layer forming a horseshoe/necklace vortex as it encounters the leading edge of a blunt appendage mixed with a separation from the surface of the appendage will lead to an increase of

drag on an isolated junction due to a flow change created by either an increase in boundary layer thickness or aerofoil bluntness, with the latter having a more pronounced effect.

It has been shown that increasing the plate boundary layer thickness at a junction increases the size of the horseshoe vortex around the seam of the joint, but decreases its intensity. Increasing the T/c ratio will increase both the size and strength of the vortex. The trailing edge separation will grow larger with increasing boundary layer thickness, but more so with an increase of T/c ratio.

Because the majority of the interference created by the union is incurred on the foil surface, in the context of vehicle testing, the effect of the system of separations at a junction on a vehicle would be minimal. Instead, it is the changes to the vehicles natural flow created by the junction separations and the velocity deficit in the support wake that is of primary concern.

The reformation of the interference drag results from the computational work to apply to the vehicle arrived at interference values that were small and insignificant to the overall interference measured for the model-support configuration as a whole. Confirming this, experimental results from the isolated test case of an aerofoil intersecting a flat plate showed that the effect imposed on the plate by the strut was small when compared to the model drag. This verifies that it is the effects created by the wake of the supports, their interaction with vehicle components and each other, not local to the junction, that are paramount when in the context of supporting a vehicle above a moving ground plane.

6.8 Closing Remarks

The specifics of the support geometry, as well as model geometry local to the junction, and flow conditions (perhaps defined by vehicle elements or geometry upstream) were all important and determining factors into the amount of interference. The complexity of the observed aerodynamic interactions between different support types and the overall support configuration with the model itself prohibits the possibility of developing a reliable correction for interference. If an experimenter was to consistently test a common vehicle shape with a common strut, it could be possible to quantify the effects and make a possible correction in the form of an expected result. This could include being able to place the supports depending on the type of vehicle and the characteristics being investigated to reduce the interference, or it could manifest itself as an educated guess towards an indication of the likely magnitude of interference effects for different configurations. However, one could not be confident that small changes even within a specific vehicle category would feel the same effects or that vehicle components designed in the presence of these supports would serve the same function to the same magnitude when the supports are removed. Importantly, it has been shown that the effect of a typical shape change may be reversed in the presence of support interference.

This method would also not be able to predict the reversal of effects from shape changes to a vehicle. It would be more effective to use the results from this project as a kindling force to develop other, non-intrusive, means of support for wind tunnel models. Because of this, support interference should be

recognized as a factor in overall road to tunnel comparison error and should be considered against the benefits of moving ground testing.

7 FURTHER WORK

To further explore the phenomenon of support interference in ground vehicle wind tunnel testing and further confirm the results found throughout this project, additional investigations into interference could be performed.

It would be useful to explore different support approaches to the vehicle, specifically in areas where the flow is less sensitive or already separated, such as at an angle into the backlight of a passenger vehicle, or parallel to the direction of flow approaching motor sport vehicle in its wake. Concurrent with the results found here for the Open and Closed Wheel Racer a support have less effect if it is placed in an area of already separated flow.

It would also be interesting to see the effect of interference from the model-support configurations with the vehicle at yaw. At yaw an aerofoil shaped overhead strut will force the post strut flow down the centreline of the model, which is not the appropriate case for yawed flow. The flow should approach the model centreline at the chosen yaw angle.

To see if removing the struts from the test configuration completely is possible, an investigation into non-intrusive methods of model support above a moving ground, whilst still allowing for the possibility of force and moment measurements could prove invaluable.

Lastly, the determination of interference using mock supports but over a moving ground plane would be interesting. This could be done using a narrow belt beneath the car and in between its wheel track, and then mounting the vehicle using either an overhead strut only or lateral stings only. Mock versions of the support type not used (either struts or stings) could be put into place to see there effects with some portion of a moving ground present.

8 REFERENCES

Abbott IH & Von Doenhoff AE (1959), *Theory of Wing Selections,* Dover Publications Inc., New York, New York, 1959.

Ahmed SR, Ramm G, & Faltin G (1984), *Some Salient Features of the Time-Averaged Ground Vehicle Wake.* SAE Paper 840300, International Congress & Exposition, Detroit, Michigan, 1984.

AIAA (1998), *AIAA Guide for the Verification and Validation of Computational Fluid Dynamics Simulations.* AIAA G-077-1998, 1998.

Akehurst A (2003), *The Development of an Invisible Wind Tunnel Support Sting,* MEng Dissertation, Durham University, 2003.

Apsley DD & Leschziner MA (2001), *Investigation of Advanced Turbulence Models for Flow in a Generic Eing-Body Junction,* Flow, Turbulence, and Combustion 67: 25-55, Kluwer Academic Publishers, 2001.

Arnette S & Martinedale B (2000), *Advances in Wind Tunnel Aerodynamics for Motorsport Testing.* SAE Paper 2000-01-03549, SAE Motorsports Engineering Conference, Dearborn, Michigan, November 2000.

Arnette SA, Buchanan TD, & Zabat M (1999), *On Low-Frequency Pressure Pulsations and Static Pressure Distribution in Open Jet Automotive Wind Tunnels.* SAE Paper 1999-01-0813, 1999.

Barlow JB, Rae WH, & Pope A (1999), *Low Speed Wind Tunnel Testing.* John Wiley & Sons, New York, New York, 1999.

Bearman PW (1984), *Some Observations on Road Vehicle Wakes*, SAE 840301, 1984.

Borello G, Beccio S, Gollo G, & Quagliotti FB (2000), *Rolling Road Technology for Automotive High Speed Testing.* SAE Paper 2000-01-0353, SAE 2000 World Congress, Detroit, Michigan, March 2000.

Borello G, Beccio S, Limone S, Ferro G, Bergamini P, & Quagliotti FB (1999), *The Role of the Moving Ground for Automotive Wind Tunnel Testing on Race Cars.* SAE Paper 1999-01-0647, SAE World Congress, Detroit, Michigan, March 1999.

Buchhelm R, Unger R, Schenkel FK, Jousserandot P, Nishimura Y, Mercker E, & Wilsden DJ (1983), *Comparison Tests Between Major European and North American Automotive Wind Tunnels,* SAE Paper 830301, International Congress & Exposition, Detroit, Michigan, February, 1983.

Carney D, (2006) *Refreshing the Formula.* Automotive Engineering International, SAE Publications, Vol. 114, 5:64-66, May, 2006

Carr GW (1974), *Influence of Rear Body Shape on the Aerodynamic Characteristics of Saloon Cars.* MIRA Report 1974/2, 1974.

Cogotti A (1984), *Wake Surveys of Different Car-Body Shapes with Coloured Isopressure Maps,* SAE Paper 840299, 1984.

Cogotti A (1989), *A Strategy for Optimum Surveys of Passenger-Car Flow Fields*, SAE Paper 890374, 1989.

Davenport WJ & Simpson RL (1990), *An Experimental Investigation of the Flow Past an Idealised Wing-Body Junction.* VPI&SU Rep. VPI-AOE-172, Virginian Polytechnic Institute State University, Blacksburg, Virginia, 1990.

Davenport WJ & Simpson RL. (1987), *Some Time-Dependent Features of Turbulent Appendage-Body Junction Flows.* 16th International Symposium on Naval Hydrodynamics, Berkeley, CA, pp. 312-35. Washington, DC: Natl. Acad.

Davenport WJ, Agarwal NK, Dewitz MB, Simpson RL, & Poddar K (1990), *Effects of a Fillet on the Flow Past a Wing-Body Junction.* AIAA Journal, 28:2017-2024, 1990.

Davenport WJ, Dewitz MB, Agarwal NK, & Simpson RL (1992), *Effects of a Leading-Edge Fillet on the Flow past an Appendage-Body Junction.* AIAA Journal. 30:2177-2183, 1992.

Dominy RG & Hodson HP (1993) *An Investigation of Factors Influencing the Calibration of 5-Hole Probes for 3-D Flow Measurements*, ASME Journal of Turbomachinery, 115, 513-518, 1993.

Dominy RG (2002), *Sports Protoype Race Car Optimisation.* SAE Paper 2002-01-3286, SAE Motorsports Engineering Conference & Exhibition, Indianapolis, Indiana, 2002.

DSEurope (2002), *Sales Catalogue for Z-Folded Load Cells Series 500 QD with Internal A/D Electronics*, 2002.

Eckerle WA & Langston LS (1987), *Horseshoe Vortex Formation Around a Cylinder.* ASME Journal of Turbomachinery, Vol. 109, pp.278-285, 1987.

Eckert W, Singer N, & Vagt J (1992), *The Porsche Wind Tunnel Floor-Boundary-Layer Control – A Comparison with Road Data and Results from Moving Belt*, SAE Paper 920346, SAE International Congress, Detroit, Michigan, February, 1992.

Fago B, Lindner H, & Mahrenholtz O (1991), *The Effect of Ground Simulation on the Flow Around Vehicles in Wind Tunnel Testing.* Journal of Wind Engineering and industrial Aerodynamics, 38:47-57, 1991.

Fleming J, Simpson RL, & Davenport WJ (1991), *An Experimental Study of a Turbulent Wing-Body Junction and Wake Flow.* VPI&SU Report VPI-AOE-179, Virginian Polytechnic Institute State University, Blacksburg, Virginia, 1991.

Fleming J, Simpson RL, & Davenport WJ (1993), *An Experimental Study of a Turbulent Wing-Body Junction Flow.* Exp. Fluids 14:366-78, 1993.

Fluent (2006), *Fluent Online Help Manual.* Version: 3d, segregated, Spallart-Allmaras, 6.2.16, 2004, http://www.fluent.com/

Fox RW & McDonald AT (1998), *Introduction to Fluid Mechanics* (5th ed.), John Wiley & Sons, New York, NY, 1998.

Gallington R & Sisson G (1980), *Flow Visualisation Using a Computerised Data Acquisition System*, Second International Symposium on Flow Visualisation, Bochum.

Gaylard AP, Bickerton J, & Howell JP (1998), *Current Issues in the use of CFD to Predict Aerodynamic Characteristics of Car Shapes,* 2nd MIRA International Conference on Vehicle Aerodynamics, October, 1998.

Gaylard AP, Howell JP, & Garry KP (2007), *Observation of Flow Asymmetry Over the Rear of Notchback Vehicles,* SAE Publications, 2007.

Gilhome BR, Saunders JW, & Sheridan J (2001), *Time Averaged and Unsteady Near-Wake Analysis of Cars.* SAE Paper 2001-01-1040, World Congress, Detroit, Michigan, 2001.

Hetherington B & Sims-Williams DB (2004), *Wind Tunnel Model Support Strut Interference.* SAE Paper 2004-01-0806, SAE World Congress, Detroit Michigan, March, 2004.

Hetherington B & Sims-Williams DB (2006), *Support Strut Interference on Passenger and Racing Car Wind Tunnel Models.* SAE Paper 2006-01-0565, SAE World Congress, Detroit, Michigan, April, 2006.

Hoerner SF (1965), *Fluid-Dynamic Drag.* Published by the author, 1965.

Hoffman J, Martindale B, Arnette S, Williams J, & Wallis S (2003), *Development of Lift and Drag Corrections for Open Jet Wind Tunnel Tests for an Extended Range of Vehicle Shapes,* SAE Paper 2003-01-0934 (SP-1786), SAE World Congress, March, 2003.

Howell J & Hickman D (1997), *The Influence of Ground Simulation on the Aerodynamics of a Simple Car Model.* SAE Paper 970134, 1997.

Howell JP & Goodwin JC (1995), *The Influence of Ground Simulation on the Aerodynamics of Simple Car-Like Shapes with Underbody Roughness.* IMECHE C498/36/158, London, 1995.

Hucho WH (1998), *Aerodynamics of Road Vehicles.* Society of Automotive Engineers, Warrendale, PA, 1998.

Istvan H & Bearman PW (1994), *Effect of Ground Motion and Wind Turbulence on the Aerodynamic Force Coefficients of a Basic Bluff Body.* Royal Aeronautical Society Conference, Loughborough University of Technology, UK, July, 1994.

Jama H, Watkins S, & Dixon C (2006), *Reduced Drag and Adequate Cooling for Passenger Vehicles Using Variable Area Front Air Intakes.* SAE Paper 2006-01-0342, 2006.

Jenkins LN (2000), *An Experimental Investigation of the Flow over the Rear End of a Notchback Automobile Configuration.* SAE Paper 2000-01-0489, SAE World Congress, Detroit Michigan, March, 2000.

Katz J & Dykstra L (1992), *Effect of Wing/Body Interaction on the Aerodynamics of Two Generic Racing Cars.* SAE Paper 920349, SAE International Congress, Detroit, Michigan, February, 1992.

Katz J (1995), *Race Car Aerodynamics: Designing for Speed.* Robert Bentley Inc., Cambridge, Massachusetts, 1995.

Kessler JC & Wallis SB (1966), *Aerodynamic Test Techniques.* SAE Paper 600464, 1966.

Kieselbach RJF (1982a), *Streamline Cars in Germany. Aerodynamics in the Construction of Passenger Vehicles 1900-1945.* Kohlhammer Editors, Auto und Verk, Stuttgart. 1982.

Kieselbach RJF (1982b), *Streamline Cars in Europe and USA, Aerodynamics in the Construction of Passenger Vehicles 1900-1945*. Kohlhammer Editors, Auto und Verk, Stuttgart. 1982.

Kieselbach RJF (1983), *Aerodynamically Designed Commercial Vehicles 1931-1961. Built on the Chassis of: Daimler Benz, Krupp, Opel, Ford.* Kohlhammer Editors, Auto und Verk, Stuttgart. 1983.

Knowles R (2002), *Simulation and Experiments on an Isolated Racecar Wheel Rotating in Ground Contact.* 4th MIRA International Vehicle Aerodynamics Conference, October, 2002.

LaFleur RS & Langston LS (1993), *Drag Reduction of a Cylinder-Endwall Junction Using Ice Formation.* Journal of Fluids Engineering, 115: 26-32, 1993.

Landman D (2000), *Road Simulation for NASCAR Vehicles at the Langley Full-Scale Tunnel.* SAE Paper 2000-01-3550, SAE Motorsports Engineering Conference, Dearborn, Michigan, November 2000.

Lessard WB (2000), *Analysis of Post-Support and Wind Tunnel Wall Interference on Flow Field About Subsonic High-Lift High-Speed Research Configuration.* NASA TP-2000-210555, Hampton, Virginia, 2000.

Massey B (2006), *Mechanics of Fluids 8th Edition*, Taylor & Francis, London, England, 2006.

Mears AP, Dominy RG, & Sims-Williams DB (2002), *The Flow About an isolated Rotating Wheel – Effects of Yaw on Lift, Drag, and Flow Structure.* 4th MIRA International Vehicle Aerodynamics Conference, October, 2002.

Mercker E & Wiedemann J (1996), *On the Correction of Interference Effects in Open Jet Wind Tunnels,* SAE Paper 960671, Vehicle Aerodynamics: Wind Tunnels, CFD, Aeroacoustics, and Ground Transportation Systems, SAE SP-1145, SAE International Congress & Exposition, Detroit, Michigan, February, 1996.

Mercker E, Wiedemann J, & Wickern G (1999), *Aerodynamic Testing of Road Vehicles in Open Jet Wind Tunnels.* SAE SP-1465, 1999.

Moore J & Forlini TJ (1984), *A Horseshoe Vortex in a Duct,* ASME Transactions, Vol. 106:668-676, July, 1984.

Mueller R, Singer N, & Eckert W (1999), *Moving Belt with Distributed Suction in the Porsche Model Wind Tunnel,* SAE Paper 1999-01-0650, SAE International Congress, Detroit, Michigan, March, 1999.

Nouzawa T, Haruna S, Hiasa K, Nakamura T, & Sato H (1990), *Analysis of Wake Pattern for Reducing Aerodynamic Drag of Notchback Model,* SAE Paper 900318, International Congress & Exposition, Detroit, Michigan, 1990.

Olcmen MS, & Simpson RL (1994), *Influence of Wing Shapes on Surface Pressure Fluctuations at Wing-Body Junctions.* AIAA Journal, 32:6-15, 1994.

Paciorri R, Di Mascio A, & Favini B (2002), *A comparative Study of Turbulence Models for Junction Flow,* AIAA Paper 2002-2964, 32nd American Institute of Aeronautics & Astronautics Fluid Dynamics Conference and Exhibition, St. Louis, Missouri, June 2002.

Page M, Winkler J, Roberts N, Huschilt T, Smyth D, & Kane B (2002), *Recent Upgrades to the Swift 8ft x 9ft Rolling Road Wind Tunnel.* SAE Paper 02-MSEC-85, 2002.

Petroleum Museum (2006), *Texas Petroleum Museum Web Site.* 21 June, 2006. http://www.petroleummuseum.org/index.html.

Pininfarina (2006), *Aerodynamic and Aeroacoustic Research Center Web Site.* 26 July, 2006. http://arc.pininfarina.it/italiano//index_it.html.

Plint & Partners (1984), *TE44 Blower Tunnel and TE81 Three Component Balance Operators Manual.* Kennet Press Ltd., England, 1984.

Riegels FW (1961), *Aerofoil Sections: Results from Wind-Tunnel Investigations Theoretical Foundations,* Butterworths, London, 1961.

SensorTechnics (1994), *Instruction Manual for Signal Conditioned Precision Pressure Transducers series 103LP10D-PCB,* 1994.

Shizawa T, Honami S, & Yamamoto M (1996), *Experimental Study of Horseshoe Vortex at Wing/Body Junction with Attack Angle by Triple Hot-Wire.* AIAA-96-0323. 34th American Institute of Aeronautics & Astronautics Aerospace Science Meeting, Reno, 1996.

Simpson RL (2001), *Junction Flows.* Annual Review of Fluid Mechanics, 33:415-443, January, 2001.

Sims-Williams DB & Dominy RG (2002a), *The Design of a New Wind Tunnel for Vehicle Aerodynamics Research.* MIRA Vehicle Aerodynamics Conference, Warwick, UK, October 2002.

Sims-Williams DB & Dominy RG (2002b), *The Design of an Open-Jet Wind Tunnel for Model Testing,* SAE Paper 2002-01-3340, SAE Motorsport Engineering Conference, Indianapolis Indiana, December 2002.

Sims-Williams DB (2001), *Self Excited Aerodynamic Unsteadiness Associated with Passenger Cars.* PhD Thesis, Durham University, 2001.

Sims-Williams DB (2003), *Personal Correspondence*, Durham University, 2003.

Sims-Williams DB, Ryan A, & Crossland S (2000), DSW Software Manual, School of Engineering, Durham University, 2000.

Strachan RK, Knowles K, & Lawson NJ (2004), *A CFD and Experimental Study of an Ahmed Reference Model.* SAE Paper 2004-01-0442, World Congress, Detroit Michigan, 2004.

Sumantran V & Sovran G (1996), *Vehicle Aerodynamics: PT-49*, Society of Automotive Engineers Publications, Pennsylvania, 1996.

Tamai G (1999), *The Leading Edge: Aerodynamic Design of Ultra Streamlined Land Vehicles*, Robert Bentley Inc., Cambridge, Massachusetts, 1999.

Tetrault PA, Schetz JA, & Grossman B (2001), *Numerical Prediction of Interference Drag of Strut-Surface Intersection in Transonic Flow,* AIAA Journal, Vol. 39, No. 5, May, 2001.

Thomson WG & Wentz WH (1983), *Studies of Light-Twin Wing-Body Interference,* SAE Paper 830709, Business Aircraft Meeting & Exposition, Wichita, Kansas, April, 1983.

VintageRPM (2006), *Vintage Race Vehicles Home Page.* 21 June, 2006. http://www.vintagerpm.com/.

Walter JA & Patel VC (1996), *Measurements in Three-Dimensional Wake of a Surface-Mounted Wing-Like Symmetrical Ellipsoid.* Experimental Thermodynamics & Fluid Science 13:266-291, 1996.

Wickern G (2007), *Recent Literature on Wind Tunnel Test Section Interference Related to Ground Vehicle Testing.* SAE Paper 2007-01-1050, World Congress, Detroit, Michigan,, 2007.

Wickern G, Zwicker K, & Pfadenhauer M (1997), *Rotating Wheels – Their Impact on Wind Tunnel Test Techniques and on Vehicle Drag Results.* SAE Paper 970133, 1997.

Wiedemann J & Potthoff J (2003), *The New 5-Belt Road Simulation System of the IVK Wind Tunnels – Design and First Results,* SAE Paper 2003-01-0429, SAE World Congress, Detroit, Michigan, 2003.

Wildi J (1994), *Wind Tunnel Testing of Racing Cars – The Importance of the Road Simulation Technique,* Royal Aeronautical Society Conference, Loughborough University of Technology, Loughborough, England, July, 1994.

Wilson RA (2004), *CFD Investigation into Wind Tunnel Support Strut Interference,* 4H Final Year Project, Durham University, 2004.

A1 APPENDIX A

A1.1 CHOICE OF OVERHEAD STRUT PROFILE

The overhead struts used to purposefully interfere with the models' flow fields had to have the realistic geometry and stiffness of a strut that could be used to support a 25% to 40% model with an internal force balance above a moving ground plane. For this reason the design criteria for the strut being developed were: a stiffness equal to or greater than that of the existing support used in the Durham $2m^2$ tunnel for rolling road testing and a low drag to minimise the impact on vehicle components downstream.

A1.1.1 Calculation of Moments of Inertia in Bending and Torsion

To approximate the area and solve for the moments of inertia, the two dimensional aerofoil profile was split into smaller rectangular subdivisions using a left hand approximation. See Figure A1.1.

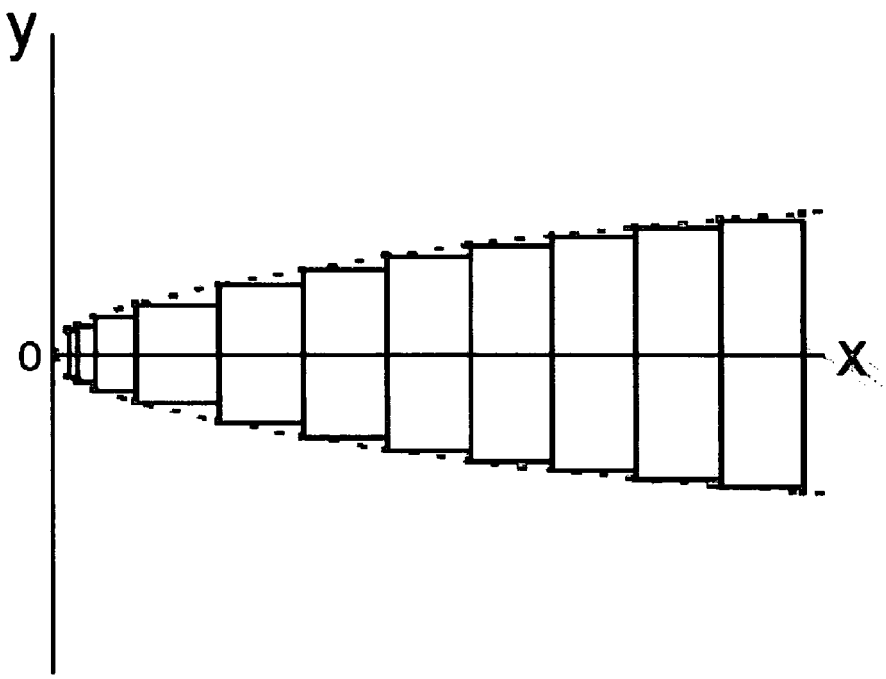

Figure A1.1: Example of rectangular subdivisions using left hand approximation.

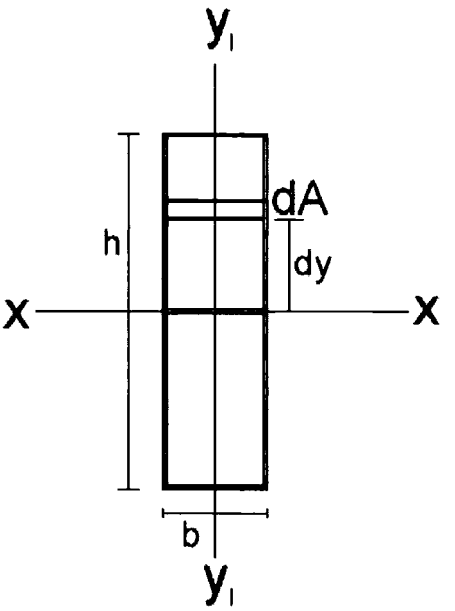

Figure A1.2: Axes and elemental area for rectangle with height (h) and base (b).

I_x of an area dA, with base (b) and height (dy), (Figure A1.2) is:

Equation A1.1

$$I_x = \int y^2 dA$$

Integrating with respect to h Equation A1.1 becomes:

Equation A1.2

$$I_x = \int_{-h/2}^{h/2} y^2 b dy = \frac{bh^3}{12}$$

Substituting $b = \Delta x$ and $h = 2y$ yields Equation A1.3 for the local moment of inertia about the x axis for an individual rectangular approximation. Because the aerofoil and approximated subdivisions share an axis, the total moment of inertia for the aerofoil (I_{xfoil}) is a sum of the local values for each individual rectangular approximation (Equation A1.4).

Equation A1.3

$$I_x = \frac{2\Delta x y^3}{3}$$

Equation A1.4

$$I_{xfoil} = \sum I_x$$

Similarly, I_y for an area dA, with height (h) and base (dx), is:

Equation A1.5

$$I_y = \int x^2 dA$$

Integrating with respect to b Equation A1.5 becomes:

Equation A1.6

$$I_y = \int_{-b/2}^{b/2} x^2 h dx = \frac{hb^3}{12}$$

In terms of the aerofoils coordinate system in Figure A1.1, $b = \Delta x$ and $h = 2y$, yielding:

Equation A1.7

$$I_y = \frac{y\Delta x^3}{6}$$

To find the moment of inertia for a rectangular subdivision (I_{yc}) about a y axis (y_c) that passes through the aerofoil centroid the parallel axis theorem (Equation A1.8) is used.

Equation A1.8

$$I_{yc} = I_y + Ad^2$$

Where A is the area of the rectangle and d is the distance between y_l and y_c. The total moment of inertia about the y-axis for the aerofoil (I_{yfoil}) is then the sum of all the values I_{yc} for the individual subdivisions (Equation A1.9).

Equation A1.9

$$I_{yfoil} = \sum I_{yc}$$

Because an aerofoil's chord is always larger than its maximum thickness, I_{yfoil} will always be larger than I_{xfoil} and was assumed sufficient once an appropriate I_{xfoil} was chosen.

To find the polar moment of inertia for one of the rectangular subdivisions the perpendicular axis theorem states that it will be a sum of the moments of inertia about the local axes x and y_l. So for each of the subdivisions the polar moment of inertia about their centroid will be:

Equation A1.10

$$I_p = I_x + I_y$$

To find I_{pfoil} about the aerofoils centroid the parallel axis theorem for polar moments of inertia was used:

Equation A1.11

$$I_{pfoil} = I_p + Ar^2$$

Where A is the area of the rectangle and r is the radius from the rectangles to the aerofoils centroid. Combining Equation A1.10 and Equation A1.11 yields an equation for I_{po} for each approximated rectangle about the aerofoils centroid:

Equation A1.12

$$I_{pfoil} = I_x + I_y + 2\Delta xyr^2$$

The values for each rectangle were then summed to give the total polar moment of inertia (I_{pfoil}) for a given aerofoil. Values for I_{xfoil}, I_{pfoil}, and sectional drag coefficient are reported in Table A1.1. Aerofoil coordinates and drag data used are provided by Riegels [Riegels, 1961].

Profile	Reynolds Number (10^{-4})	I_{xfoil} (mm^4)	I_{pfoil} (mm^4)	C_D (10^4)	$\left[\frac{C_D}{(I_{x100})^{1/4}}\right]^{-1}$	$\left[\frac{C_D}{(I_{p100})^{1/4}}\right]^{-1}$
Go 409	42	7923	447369	82	1151	3154
Go 410	42	13046	452873	101	1058	2568
Go 459	42	7879	458362	81	1163	3212
Go 460	42	32021	754448	109	1227	2704
NACA 0006	300	795	212308	44	1207	4879
NACA 0009	300	2684	320873	52	1384	4577
NACA 0012	200	6357	430367	62	1440	4131
NACA 0015	861	12424	542342	64	1650	4240
NACA 0018	784	21474	657364	70	1729	4068
NACA 0021	834	34111	775605	80	1699	3710
NACA 0025	879	57555	940577	93	1665	3349
NACA 0030	842	99468	1159146	117	1518	2804
NACA 63(1)-012	300	5761	321723	50	1742	4763
NACA 63(2)-015	300	11140	411498	53	1938	4779
NACA 63(3)-018	300	19046	492742	58	2025	4568
NACA 63(4)-021	300	29970	575451	63	2088	4372
NACA 63-006	300	734	167517	42	1239	4817
NACA 63-009	300	2455	249317	42	1676	5320
NACA 64(2)-015	300	11212	419951	54	1906	4714
NACA 64(3)-018	300	19144	502974	58	2028	4592
NACA 64(4)-021	300	30119	587822	62	2125	4466
NACA 64-006	300	737	170545	40	1302	5080
NACA 64-009	300	2464	253971	43	1638	5221
NACA 65(2)-015	300	11736	441599	50	2082	5156
NACA 65(4)-021	300	31576	616685	57	2339	4916
NACA 65-006	300	773	179574	35	1506	5882
NACA 66(1)-012	300	6700	389931	40	2262	6247
NACA 66(2)-015	300	12971	486011	46	2320	5740
NACA 66(215)-016	310	15699	519392	45	2487	5966
NACA 66(4)-021	300	35095	679236	52	2632	5521
NACA 66-006	300	851	197409	30	1800	7026
NACA 66-009	300	2846	294000	35	2087	6653

Table A1.1: Moments of inertia and drag data for known aerofoil profiles.

A1.1.2 Shape and Chord Length Choice

Once the moments of inertia for the given aerofoils were determined an appropriate profile had to be chosen. To manufacture a strut that is suitable for supporting 25% to 40% scale models while minimizing the amount of drag and therefore any impact on vehicle components downstream a profile with a minimal value of $C_D \times chord(c)$, but also meeting the required moment of inertia values from the previous rolling road support of $I_{xfoil} \cong 40{,}000\,\text{mm}^4$ and $I_{pfoil} \cong 700{,}000\,\text{mm}^4$ must be chosen.

The values reported in Table A1.1 are based on aerofoil profiles with a 100mm chord length. To find the moment of inertia (I_x or I_p) for a given profile, but at a different chord length Equation A1.13 is used.

Equation A1.13

$$I_{x,p} = I_{x,p100}\left(\frac{c}{100mm}\right)^4$$

Solving Equation A1.13 for c yields:

Equation A1.14

$$c = \left(\frac{I_{x,p}}{I_{x,p100}} \right)^{1/4} 100mm$$

Substituting into $C_D \times chord(c)$:

Equation A1.15

$$C_D c = 100 \left[\frac{C_D}{(I_{x,p100})^{1/4}} \right] (I_{x,p})^{1/4}$$

From Equation A1.15 I_x will have to be at least equal to the prescribed value of 40,000mm^4, and the quantities $\left[\frac{C_D}{(I_{x100})^{1/4}} \right]$ and $\left[\frac{C_D}{(I_{p100})^{1/4}} \right]$ remain as the only controllable variables, so to minimize $C_D c$, this value should be as small as possible. The candidate profiles with the top ten best values in both of these categories are presented in Table A1.2 and Table A1.3.

Profile	Reynolds Number (10^{-4})	I_{xfoil} (mm^4)	I_{pfoil} (mm^4)	C_D (10^4)	$\left[\frac{C_D}{(I_{x100})^{1/4}} \right]^{-1}$
NACA 64_3-018	300	19144	502974	58	2028
NACA 65_2-015	300	11736	441599	50	2082
NACA 66-009	300	2846	294000	35	2087
NACA 63_4-021	300	29970	575451	63	2088
NACA 64_4-021	300	30119	587822	62	2125
NACA 66_1-012	300	6700	389931	40	2262
NACA 66_2-015	300	12971	486011	46	2320
NACA 65_4-021	300	31576	616685	57	2339
NACA 66_{215}-016	310	15699	519392	45	2487
NACA 66_4-021	300	35095	679236	52	2632

Table A1.2: Highest values of $\left[\frac{C_D}{(I_{x100})^{1/4}} \right]^{-1}$

Profile	Reynolds Number (10^{-4})	I_{xfoil} (mm^4)	I_{pfoil} (mm^4)	C_D (10^4)	$\left[\frac{C_D}{(I_{p100})^{1/4}}\right]^{-1}$
NACA 65_2-015	300	11736	441599	50	5156
NACA 64-009	300	2464	253971	43	5221
NACA 63-009	300	2455	249317	42	5320
NACA 66_4-021	300	35095	679236	52	5521
NACA 66_2-015	300	12971	486011	46	5740
NACA 65-006	300	773	179574	35	5882
NACA 66_{215}-016	310	15699	519392	45	5966
NACA 66_1-012	300	6700	389931	40	6247
NACA 66-009	300	2846	294000	35	6653
NACA 66-006	300	851	197409	30	7026

Table A1.3: Highest values of $\left[\frac{C_D}{(I_{p100})^{1/4}}\right]^{-1}$

Cross referencing the data shows 5 likely candidates (matched with coloured text in Table A1.2 and Table A1.3) with large values of $\left[\frac{C_D}{(I_{x100})^{1/4}}\right]^{-1}$ and $\left[\frac{C_D}{(I_{p100})^{1/4}}\right]^{-1}$. The candidates have been placed in Table A1.4.

Profile	Reynolds Number (10^{-4})	I_{xfoil} (mm^4)	I_{pfoil} (mm^4)	C_D (10^4)	$\left[\frac{C_D}{(I_{x100})^{1/4}}\right]^{-1}$	$\left[\frac{C_D}{(I_{p100})^{1/4}}\right]^{-1}$
NACA 65_2-015	300	11736	441599	50	2082	5156
NACA 66-009	300	2846	294000	35	2087	6653
NACA 66_1-012	300	6700	389931	40	2262	6247
NACA 66_2-015	300	12971	486011	46	2320	5740
NACA 66_4-021	300	35095	679236	52	2632	5521

Table A1.4: Shape choice candidates

From this selection the profile with the highest values of I_{xfoil} and I_{pfoil} is the NACA 66_4-021. In order to find an appropriate chord to meet the stiffness requirements $I_{xfoil} \cong 40{,}000$ and $I_{pfoil} \cong 700{,}000$ Equation A1.14 is used with I_x and I_p equal to the required values and I_{x100} and I_{p100} equal to the values of I_{xfoil} and I_{pfoil}, respectively, found in the tables for the NACA 66_4-021

Solving this equation results in a chord of 103mm based on the bending requirement and 101mm based on the torsional requirement. The NACA 66_4-021 profile was designed with a chord of 100mm to approximately match the stiffness requirements for a steel strut to support a 25%-40% scale model while minimizing drag and thus wake interference with components downstream of the strut.

B1 APPENDIX B

B1.1 FORCE AND MOMENT MEASUREMENT

Due to the volume of measurements required throughout the course of this work an investigation into the efficiency and accuracy of force coefficient measurements was undertaken to determine an appropriate logging frequency, the force balance's repeatability, and the reliability of the taring function.

B1.1.1 Logging Frequency Choice

The logging frequency varies the duration of the sampling period; a longer period potentially offers more accuracy, whilst a shorter period reduces test time. Samples were taken at both 100Hz and 800Hz. The result is a collection of twenty readings with each reading comprising 2048 samples collected at the intended frequency on each channel. Of the twenty readings the first stands alone with each consecutive reading being an average of itself and the readings before it, making the twentieth reading an overall average of all readings for that frequency. Presumably, the first reading is the least accurate and the twentieth (overall average) is the most accurate. This overall average is then taken as the truest and most correct value and is used to determine which frequency allows coefficients to converge on it the quickest. According to Sims-Williams [Sims-Williams, 2003] the target repeatability was ±2 counts of the correct value. This level of accuracy in the coefficient would then also make the corresponding force or moment value acceptably accurate (2 counts of error in the drag coefficient will correspond to approximately 10 grams of error in the actual load used to calculate the force).

Figure B1.1 and Figure B1.2 show force and moment readings taken for the Notchback model without any interfering supports at 100Hz; Figure B1.3 and Figure B1.4 show the same tests, but at 800Hz. Comparison of the results shows no advantage in accuracy using the longer logging time of 100Hz. All tests converge to within 2 counts by approximately 10 readings for both frequencies. Justly the more time efficient logging frequency of 800Hz was proposed.

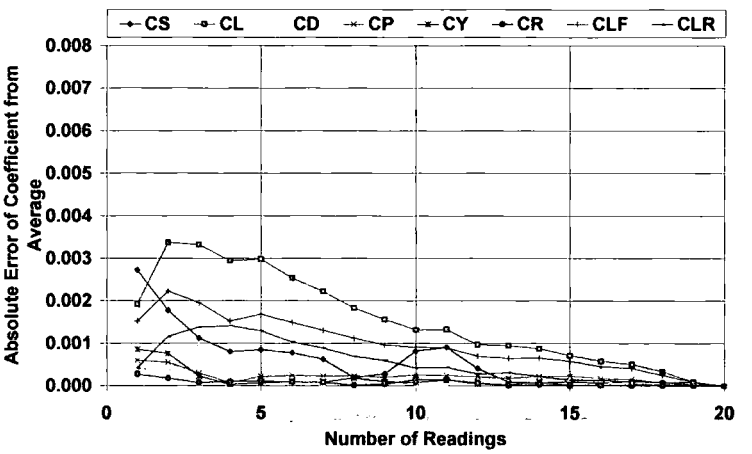

Figure B1.1: Absolute difference of twenty progressively averaged coefficients from an overall average of the twenty readings at 100Hz. Test 030225q.

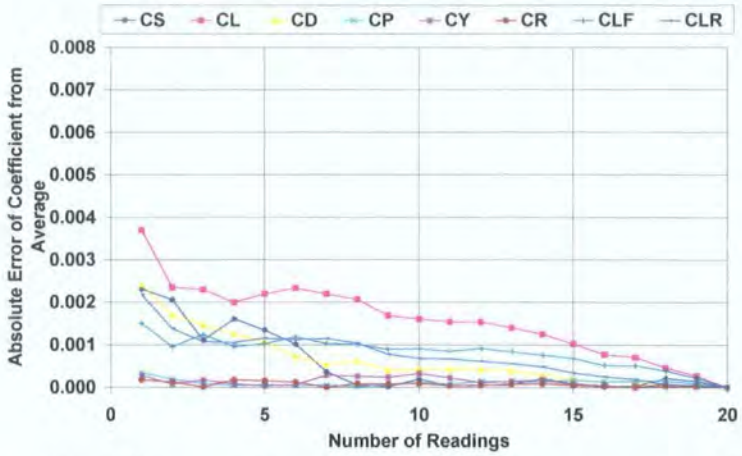

Figure B1.2: Absolute difference of twenty progressively averaged coefficients from an overall average of the twenty readings at 100Hz. Test 030226.

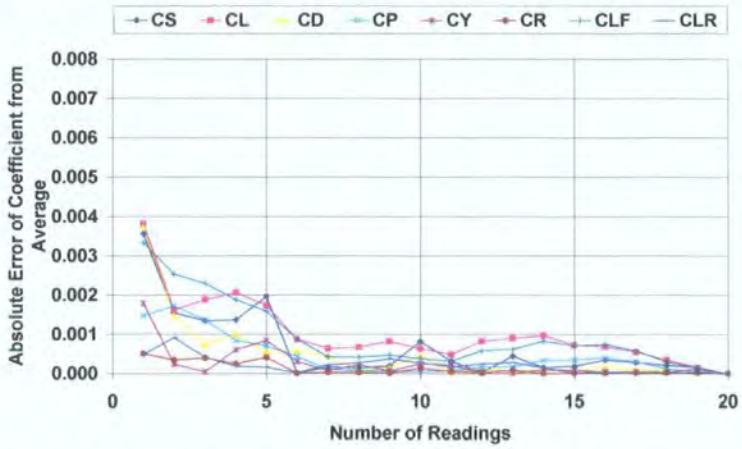

Figure B1.3: Absolute difference of twenty progressively averaged coefficients from an overall average of the twenty readings at 800Hz. Test 030218.

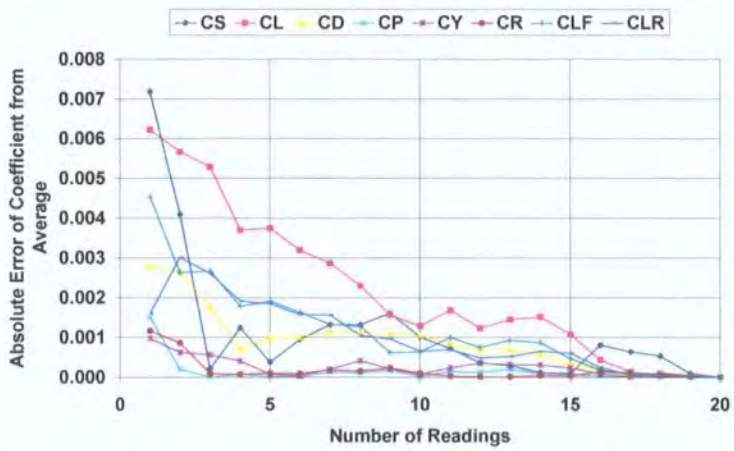

Figure B1.4: Absolute difference of twenty progressively averaged coefficients from an overall average of the twenty readings at 800Hz. Test 030224.

In order to confirm that 800 Hz was an appropriate data logging frequency one further test was performed. The test compared consecutive readings to an overall average derived from a larger collection of forty readings at 800 Hz with no load. The results, seen in Figure B1.5, once again converge to 0.002 on all coefficients within ten readings, validating the use of 10 sets of 2048 readings logged at 800Hz.

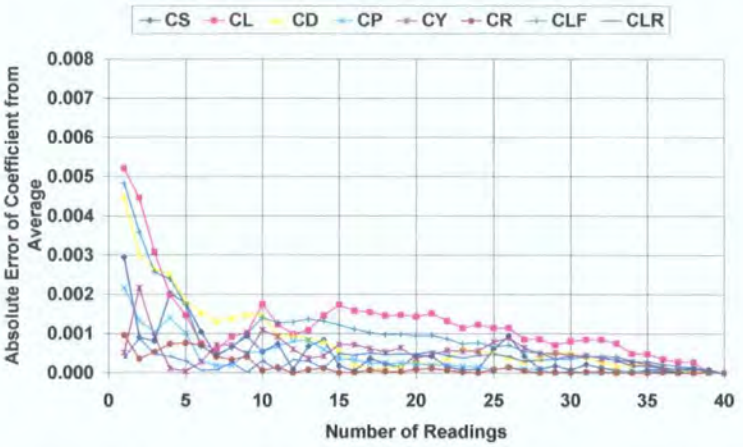

Figure B1.5: Absolute difference of forty progressively averaged coefficients from an overall average of the forty readings at 800Hz. Test 030311.

B1.1.2Tare Reliability

To discover the stability of the load cells in a static state, readings of 2048 samples were taken at the chosen logging frequency of 800 Hz to see the extent of the variation after a tare. The tests observed stability by taking twenty readings after a tare with the Notchback model mounted to the force balance, but without the presence of an aerodynamic load. Despite that there was no load, the measured forces were still converted to coefficients using the running conditions of the tunnel. The variation between consecutive readings is provided in graphical form in Figure B1.6 and the absolute difference from zero for each reading is shown in Figure B1.7. After a single tare the data shows that the lift components (C_L, C_{LR}, and C_{LF}) are the most unsteady and may be as far as 5 counts from the zero reading that they should report for the model without any load.

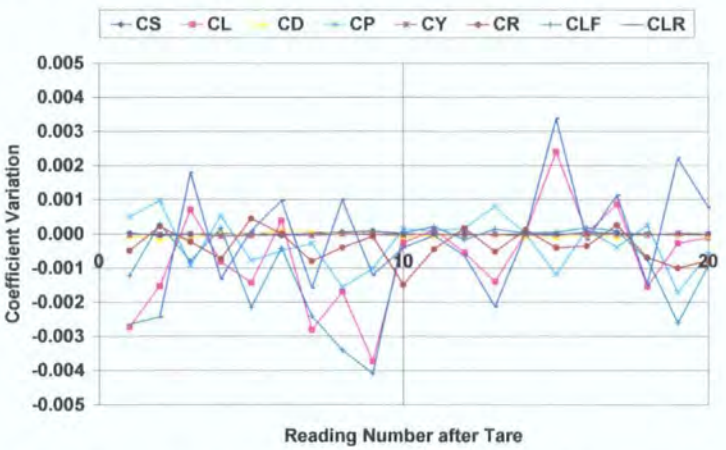

Figure B1.6: Coefficient variation after a tare with the model mounted but no aerodynamic load. Test 030313a.

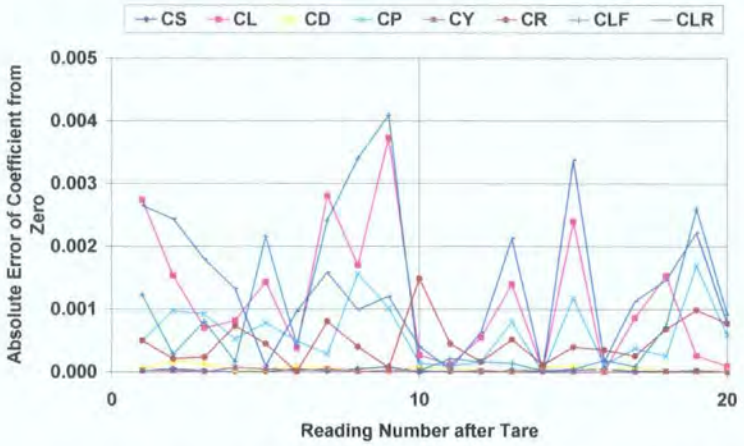

Figure B1.7: Absolute difference of coefficient values in Figure B1.6 from zero. Test 030313a

In another representation of the same data, Figure B1.8 shows the progressive averages converging on an overall average of the twenty readings taken. Observing the figure, an average from five readings will allow data to fall within 1 count of the overall average (Figure B1.8). Both of which are better than the prescribed allowable error of 2 counts. To keep time efficiency in mind, it was deemed that an average of ten readings would arrive at a reasonable tare with enough reliability as to not alter readings taken under load after the tare. Accordingly, the logging software tare function was setup to take ten readings and then average them, assigning this value as the new zero to use as a reference when a load is added.

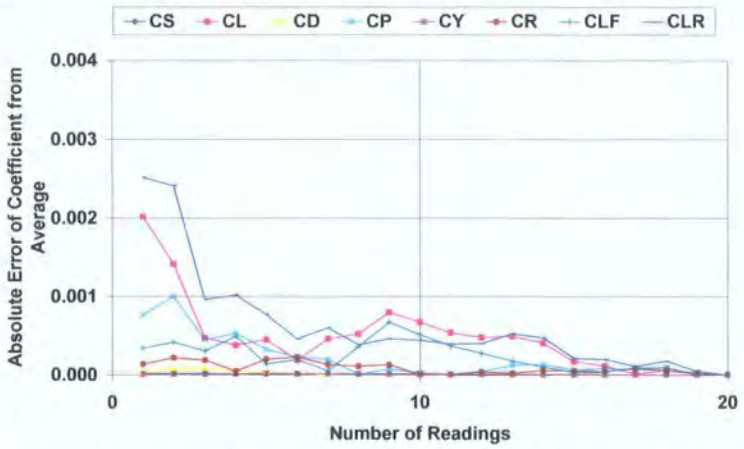

Figure B1.8: Absolute difference of coefficients from an overall average of twenty readings. Test 030313a.

Figure B1.9 illustrates the same testing method, but using the new logging program averaging 10 readings. The results show a vast improvement in tare accuracy, the readings converge to within 1 count of their average after one reading. Further tests were conducted using an unevenly weighted oscillator to shake the force balance and settle it before each tare, however, results proved to vary only a small amount from the case without the oscillator.

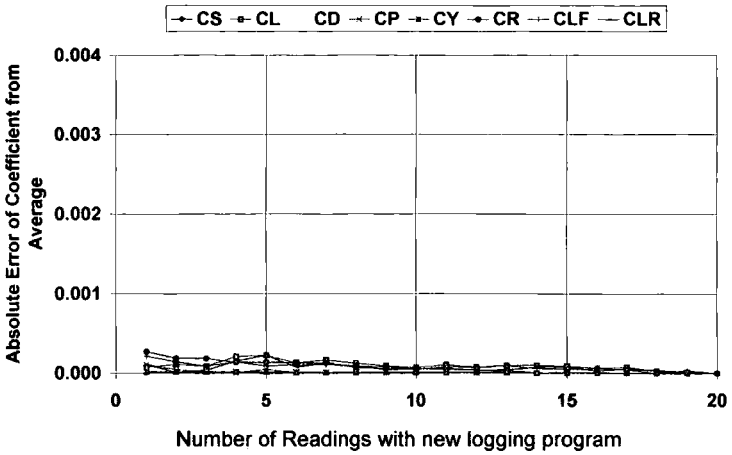

Figure B1.9: Absolute difference of coefficients from an overall average of twenty readings. Test 030313.

B1.1.3Force Balance Repeatability

To compensate for any variation in force balance measurements, a collection of readings needed to be taken and then averaged to dampen any fluctuations and arrive at a more accurate measurement. Although an average taken from the largest number of readings possible offers the most reliability, an effort was made to find the minimum number of readings for which the average will fall reasonably close to the 'correct' value in order to reduce test time. Also considered, is the limit of reliability available to see if there is an unavoidable amount of fluctuation. This achievable level of reliability and the acceptable amount of random error will determine the number of readings that must be averaged in order to consider a measurement practical.

The most 'correct' value used for comparison was taken from an overall average of just under 1000 readings taken at the decided 800 Hz and 2048 samples. To determine the minimum number of readings necessary, the Notchback model was tested without any interfering supports and progressive averages were taken and compared to the 'correct' value. The difference between each progressive average and the 'correct' value was plotted against the number of readings for three sets of data (Figure B1.10, Figure B1.11, and Figure B1.12) to see how many readings must be taken before their average falls within 2 counts of the 'correct' value.

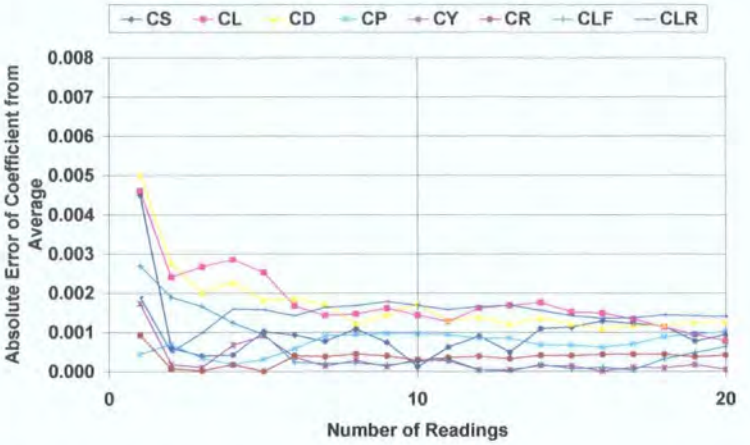

Figure B1.10: Absolute difference of twenty progressively averaged coefficients from the 'correct' value. Test 030218.

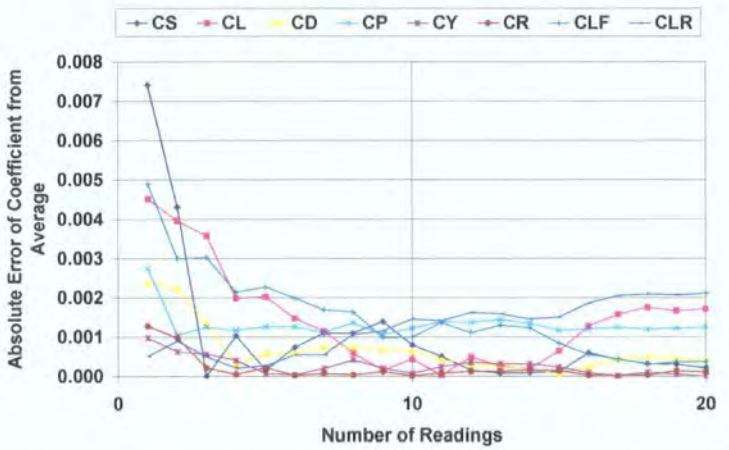

Figure B1.11: Absolute difference of twenty progressively averaged coefficients from the 'correct' value. Test 030224.

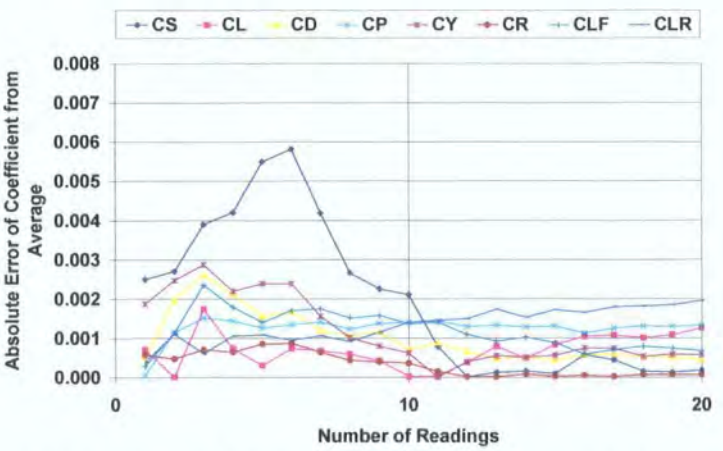

Figure B1.12: Absolute difference of twenty progressively averaged coefficients from the 'correct' value. Test 030225e.

In all three plots C_L, particularly C_{LR}, was the most unstable, having the greatest error after 20 progressively averaged readings in all three cases. To observe the stability of C_L (and all others) beyond twenty readings a set of forty readings was taken and plotted in the same manner to see if the measurement accuracy increases with the number of progressively averaged readings (Figure B1.13).

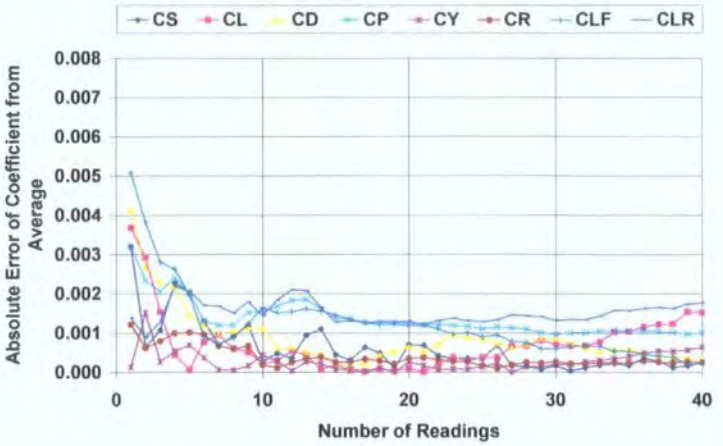

Figure B1.13: Absolute difference of forty progressively averaged coefficients from an overall correct average. Test 030311.

Observing Figure B1.13 the averages stay within 2 counts of error as desired, however, the accuracy of the coefficients; specifically the vertical components (C_P, C_{LF}, C_{LR}, and C_L), do not improve any further. The four sets of data shown in Figure B1.10 through Figure B1.13 arrived at an accuracy of 2 counts of an infinite average. Accordingly at least ten readings must be taken and averaged to safely say that the measurement is accurate to within 2 counts of the true coefficient value. A precise calculation of the data confirms that the balance arrives at repeatability within 2 counts on C_D and 3 counts on C_L when an average is taken of 10 readings of 2048 samples at 800Hz.

C1 APPENDIX C

C1.1 OVERHEAD STRUT MANUFACTURE

C1.1.1 Modular design

Because the strut was intended for use in two different configurations it had to be designed with an adaptable length, but still be able to mount to both the actuator housing and wind tunnel structure. There were also limitations placed on length by the capabilities of the milling machine used for manufacture.

In order to accommodate these requirements the aerofoil shaped strut was designed in modular parts, each part had the cross section of half an aerofoils two dimensional profile, split down its symmetry line. The design allowed the different parts to be joined together creating two different lengths and leaving one side of the part flat made mounting to the milling bed easier. In its final design the strut comprised a total of five parts, six of which were used for the 'Small Strut' configuration seen in Figure 2.8 and three of which were used for the 'Large Strut' configuration seen in Figure 2.10. Figure C1.1and Figure C1.3 show exploded isometric drawings of the parts assembled for the 'Small Strut' and 'Large Strut' configurations, respectively. The different parts have been colour coded to show their repeated use in the configurations. Also designed, but not shown were the two different mounting brackets used to mount the two struts to the wind tunnel. Figure C1.2 and Figure C1.4 depict the length dimensions of the struts. As mentioned in Section 2.2.1 and Appendix A, the struts have a 100mm chord and follow the profile of a NACA 66_4-021.

For clarification; when installed in the wind tunnel the 'Small Strut' stands alone as it is seen in this drawing with the exception of the mounting bracket and is named the 'Small Strut' because it creates a smaller wake. The 'Large Strut' is aptly named, not because of its length, which is actually shorter than the 'Small Strut', but because it is joined to a larger pitch and ride height actuator housing described in Section 2.2.1, and creates a larger wake than the 'Small Strut'.

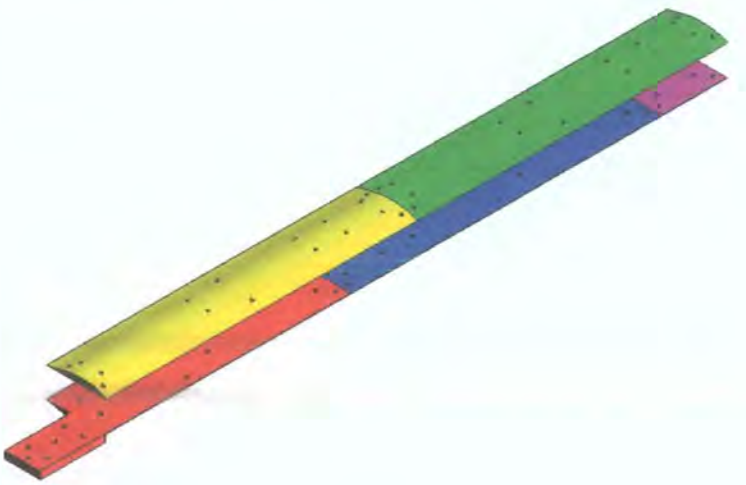

Figure C1.1: Small strut assembly drawing.

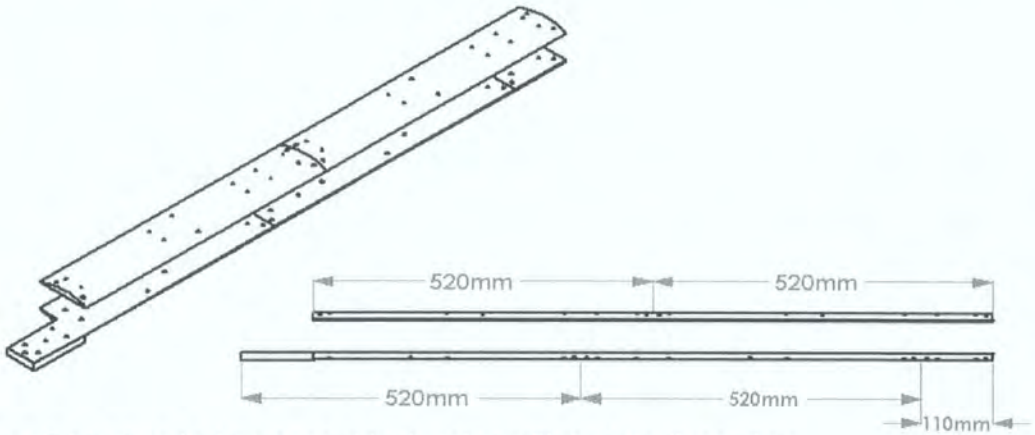

Figure C1.2: Small strut assembly drawing with length dimensions.

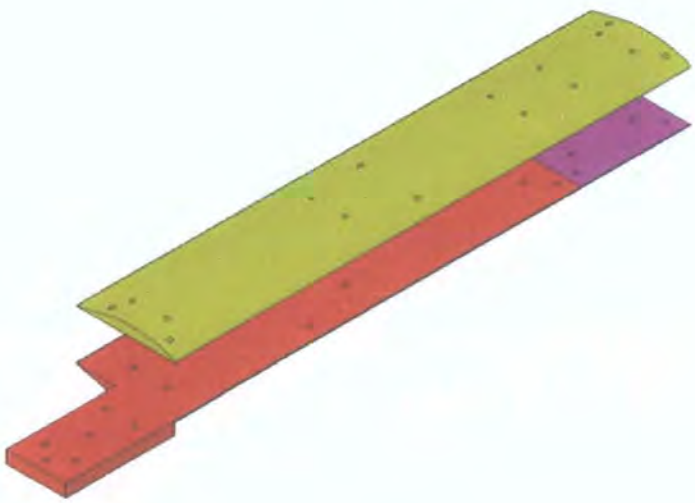

Figure C1.3: Large strut assembly drawing.

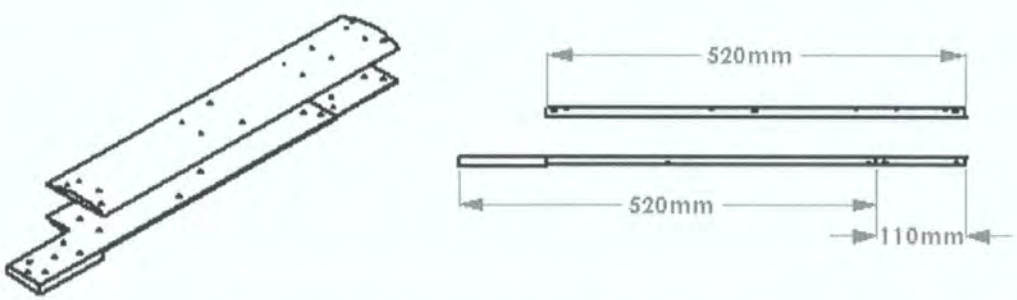

Figure C1.4: Large strut assembly drawing with length dimensions.

C1.1.2 Milling Program

To automatically guide the mill a program code had to be specifically written for input into the ANILAM 3000M CNC mill. This was a 3-axis machine that cut the aerofoils using a ball nose cutter. Coordinate values were taken from Riegels [Riegels 1961], but had to have offsets calculated to compensate for the cutting tools spherical end. These offset coordinates were then placed into the CNC program code.

Specific programs were written for milling the surface into the aerofoil profile, the tapped holes used for mounting the aerofoil to the mill, and the tappings/counter bores used to join the two aerofoil profile halves together. An example of the code used for one of the shorter strut components can be seen in Table C1.1

Dim Abs								
Unit MM								
Tool# 1								
Rapid	X	-16.000	Y	-116.000	Z	20.000		
Line	X	-16.000	Y	-116.000	Z	-16.000	Feed	150.000
Line	X	126.000	Y	-116.000	Z	-16.000		
Line	X	126.000	Y	-116.000	Z	6.000		
Line	X	126.000	Y	-102.000	Z	6.000		
Line	X	-16.000	Y	-102.000	Z	6.000		
Line	X	-16.000	Y	-102.000	Z	-0.126		
Line	X	126.000	Y	-102.000	Z	-0.126		
Line	X	126.000	Y	-100.750	Z	0.026	Feed	500.000
Line	X	-16.000	Y	-100.750	Z	0.026		
Line	X	-16.000	Y	-99.706	Z	0.162		
Line	X	126.000	Y	-99.706	Z	0.162		
Line	X	126.000	Y	-98.790	Z	0.297		
Line	X	-16.000	Y	-98.790	Z	0.297		
Line	X	-16.000	Y	-97.987	Z	0.436		
Line	X	126.000	Y	-97.987	Z	0.436		
Line	X	126.000	Y	-97.194	Z	0.600		
Line	X	-16.000	Y	-97.194	Z	0.600		
Line	X	-16.000	Y	-96.310	Z	0.808		
Line	X	126.000	Y	-96.310	Z	0.808		
Line	X	126.000	Y	-95.311	Z	1.064		
Line	X	-16.000	Y	-95.311	Z	1.064		
Line	X	-16.000	Y	-94.242	Z	1.352		
Line	X	126.000	Y	-94.242	Z	1.352		
Line	X	126.000	Y	-91.843	Z	2.018		
Line	X	-16.000	Y	-91.843	Z	2.018		
Line	X	-16.000	Y	-89.437	Z	2.707		
Line	X	126.000	Y	-89.437	Z	2.707		
Line	X	126.000	Y	-86.990	Z	3.419		
Line	X	-16.000	Y	-86.990	Z	3.419		
Line	X	-16.000	Y	-84.499	Z	4.150		
Line	X	126.000	Y	-84.499	Z	4.150		
Line	X	126.000	Y	-81.956	Z	4.894		
Line	X	-16.000	Y	-81.956	Z	4.894		
Line	X	-16.000	Y	-79.363	Z	5.640		
Line	X	126.000	Y	-79.363	Z	5.640		
Line	X	126.000	Y	-76.711	Z	6.380		
Line	X	-16.000	Y	-76.711	Z	6.380		
Line	X	-16.000	Y	-73.997	Z	7.103		
Line	X	126.000	Y	-73.997	Z	7.103		
Line	X	126.000	Y	-71.205	Z	7.799		
Line	X	-16.000	Y	-71.205	Z	7.799		
Line	X	-16.000	Y	-68.312	Z	8.453		
Line	X	126.000	Y	-68.312	Z	8.453		

Line	X	126.000	Y	-65.310	Z	9.043
Line	X	-16.000	Y	-65.310	Z	9.043
Line	X	-16.000	Y	-62.215	Z	9.538
Line	X	126.000	Y	-62.215	Z	9.538
Line	X	126.000	Y	-59.127	Z	9.908
Line	X	-16.000	Y	-59.127	Z	9.908
Line	X	-16.000	Y	-56.130	Z	10.163
Line	X	126.000	Y	-56.130	Z	10.163
Line	X	126.000	Y	-53.238	Z	10.328
Line	X	-16.000	Y	-53.238	Z	10.328
Line	X	-16.000	Y	-50.445	Z	10.428
Line	X	126.000	Y	-50.445	Z	10.428
Line	X	126.000	Y	-47.702	Z	10.483
Line	X	-16.000	Y	-47.702	Z	10.483
Line	X	-16.000	Y	-44.962	Z	10.497
Line	X	126.000	Y	-44.962	Z	10.497
Line	X	126.000	Y	-42.212	Z	10.469
Line	X	-16.000	Y	-42.212	Z	10.469
Line	X	-16.000	Y	-39.453	Z	10.398
Line	X	126.000	Y	-39.453	Z	10.398
Line	X	126.000	Y	-36.691	Z	10.281
Line	X	-16.000	Y	-36.691	Z	10.281
Line	X	-16.000	Y	-33.934	Z	10.118
Line	X	126.000	Y	-33.934	Z	10.118
Line	X	126.000	Y	-31.173	Z	9.912
Line	X	-16.000	Y	-31.173	Z	9.912
Line	X	-16.000	Y	-28.411	Z	9.659
Line	X	126.000	Y	-28.411	Z	9.659
Line	X	126.000	Y	-25.641	Z	9.360
Line	X	-16.000	Y	-25.641	Z	9.360
Line	X	-16.000	Y	-22.853	Z	9.008
Line	X	126.000	Y	-22.853	Z	9.008
Line	X	126.000	Y	-20.043	Z	8.601
Line	X	-16.000	Y	-20.043	Z	8.601
Line	X	-16.000	Y	-17.296	Z	8.146
Line	X	126.000	Y	-17.296	Z	8.146
Line	X	126.000	Y	-15.788	Z	7.871
Line	X	-16.000	Y	-15.788	Z	7.871
Line	X	-16.000	Y	-14.350	Z	7.592
Line	X	126.000	Y	-14.350	Z	7.592
Line	X	126.000	Y	-12.896	Z	7.290
Line	X	-16.000	Y	-12.896	Z	7.290
Line	X	-16.000	Y	-11.431	Z	6.966
Line	X	126.000	Y	-11.431	Z	6.966
Line	X	126.000	Y	-9.946	Z	6.615
Line	X	-16.000	Y	-9.946	Z	6.615
Line	X	-16.000	Y	-8.439	Z	6.233
Line	X	126.000	Y	-8.439	Z	6.233
Line	X	126.000	Y	-6.907	Z	5.817
Line	X	-16.000	Y	-6.907	Z	5.817
Line	X	-16.000	Y	-5.421	Z	5.383
Line	X	126.000	Y	-5.421	Z	5.383
Line	X	126.000	Y	-4.565	Z	5.118
Line	X	-16.000	Y	-4.565	Z	5.118
Line	X	-16.000	Y	-3.774	Z	4.865

Line	X	126.000	Y	-3.774	Z	4.865
Line	X	126.000	Y	-2.975	Z	4.597
Line	X	-16.000	Y	-2.975	Z	4.597
Line	X	-16.000	Y	-2.188	Z	4.325
Line	X	126.000	Y	-2.188	Z	4.325
Line	X	126.000	Y	-1.370	Z	4.032
Line	X	-16.000	Y	-1.370	Z	4.032
Line	X	-16.000	Y	-0.514	Z	3.712
Line	X	126.000	Y	-0.514	Z	3.712
Line	X	126.000	Y	0.379	Z	3.360
Line	X	-16.000	Y	0.379	Z	3.360
Line	X	-16.000	Y	1.306	Z	2.974
Line	X	126.000	Y	1.306	Z	2.974
Line	X	126.000	Y	2.263	Z	2.551
Line	X	-16.000	Y	2.263	Z	2.551
Line	X	-16.000	Y	3.267	Z	2.078
Line	X	126.000	Y	3.267	Z	2.078
Line	X	126.000	Y	4.292	Z	1.560
Line	X	-16.000	Y	4.292	Z	1.560
Line	X	-16.000	Y	5.232	Z	1.053
Line	X	126.000	Y	5.232	Z	1.053
Line	X	126.000	Y	5.962	Z	0.635
Line	X	-16.000	Y	5.962	Z	0.635
Line	X	-16.000	Y	6.699	Z	0.184
Line	X	126.000	Y	6.699	Z	0.184
Line	X	126.000	Y	7.579	Z	-0.400
Line	X	-16.000	Y	7.579	Z	-0.400
Line	X	-16.000	Y	8.357	Z	-0.965
Line	X	126.000	Y	8.357	Z	-0.965
Line	X	126.000	Y	9.020	Z	-1.487
Line	X	-16.000	Y	9.020	Z	-1.487
Line	X	-16.000	Y	9.491	Z	-1.884
Line	X	126.000	Y	9.491	Z	-1.884
Line	X	126.000	Y	9.983	Z	-2.325
Line	X	-16.000	Y	9.983	Z	-2.325
Line	X	-16.000	Y	10.397	Z	-2.718
Line	X	126.000	Y	10.397	Z	-2.718
Line	X	126.000	Y	10.812	Z	-3.134
Line	X	-16.000	Y	10.812	Z	-3.134
Line	X	-16.000	Y	11.214	Z	-3.562
Line	X	126.000	Y	11.214	Z	-3.562
Line	X	126.000	Y	11.722	Z	-4.145
Line	X	-16.000	Y	11.722	Z	-4.145
Line	X	-16.000	Y	12.661	Z	-5.376
Line	X	126.000	Y	12.661	Z	-5.376
Line	X	126.000	Y	13.682	Z	-7.026
Line	X	-16.000	Y	13.682	Z	-7.026
Line	X	-16.000	Y	14.755	Z	-9.379
Line	X	126.000	Y	14.755	Z	-9.379
Line	X	126.000	Y	15.452	Z	-11.687
Line	X	-16.000	Y	15.452	Z	-11.687
Line	X	-16.000	Y	15.718	Z	-13.010
Line	X	126.000	Y	15.718	Z	-13.010
Rapid	X	126.000	Y	15.718	Z	20.000
Rapid	X	-16.000	Y	16.000	Z	20.000

Line	X	-16.000	Y	16.000	Z	-16.000
Line	X	126.000	Y	16.000	Z	-16.000
Rapid	X	126.000	Y	16.000	Z	20.000
Rapid	X	0.000	Y	0.000	Z	20.000
EndMain						

Table C1.1: Example of CNC program code.